University of Bologna

DEPARTMENT OF ELECTRICAL ENGINEERING
FACULTY OF ENGINEERING

Ph. D. in Electrical Engineering
XIX year
POWER ELECTRONICS, MACHINES AND DRIVES (ING-IND/32)

Control of Matrix Converters

Ph. D. Thesis:

Luca Zarri

Tutor:

Prof. Giovanni Serra

Ph. D. Coordinator:

Prof. Francesco Negrini

Final Dissertation in 2007

Contents

Preface

A matrix converter (MC) is an array of controlled semiconductor switches that directly connect each input phase to each output phase, without any intermediate dc link.

The main advantage of MCs is the absence of bulky reactive elements, that are subject to ageing, and reduce the system reliability. Furthermore, MCs provide bidirectional power flow, nearly sinusoidal input and output waveforms and controllable input power factor. Therefore MCs have received considerable attention as a good alternative to voltage-source inverter (VSI) topology.

The development of MCs started when Alesina and Venturini proposed the basic principles of operation in the early 1980's [1].

Afterwards the research in this fields continued in two directions. On the one hand there was the need of reliable bidirectional switches, on the other hand the initial modulation strategy was abandoned in favor of more modern solutions, allowing higher voltage transfer ratio and better current quality.

In the original Alesina and Venturini's theory the voltage transfer ratio was limited to 0.5, but it was shown later that, by means of third harmonic injection techniques, the maximum voltage transfer ratio could be increased up to 0.866, a value which represents an intrinsic limitation of three-phase MCs with balanced supply voltages [2].

A new intuitive approach towards the control of matrix converters, often

defined “indirect method”, was presented in [3]. According to this method the MC is described as a virtual two stage system, namely a 3-phase rectifier and a 3-phase inverter connected together through a fictitious DC-link. The indirect approach has mainly the merit of applying the well-established space vector modulation (SVM) for VSI to MCs, although initially proposed only for the control of the output voltage [4]. The SVM was successively developed in order to achieve the full control of the input power factor, to fully utilize the input voltages and to improve the modulation performance [5], [6].

A general solution of the modulation problem for MCs was presented in [7], based on the concept of “Duty-Cycle Space Vector”, that allows an immediate comprehension of all the degrees of freedom that affect the modulation strategies.

Meanwhile, several studies were presented about the bidirectional switches necessary for the construction of a matrix converter. The bidirectional switches were initially obtained combining discrete components [8]. Then, as the interest toward matrix converter increased, some manufacturers produced power modules specifically designed for matrix converter applications [9]. As regards the hardware components, the switches are usually traditional silicon IGBTs, but also other solutions have been recently tested, such as MCTs or IGBTs with silicon carbide diodes. The performance of the switches has been compared in [10]-[13].

Another problem that the researchers have dealt with is the current commutation between the bidirectional switches. The absence of free-wheeling diodes obliges the designer to control the commutation in order to avoid short circuits and over voltages. A comparison among several solutions has been done in [14], [15] and [16].

To obtain a good performance of the matrix converter, it is necessary also the design of a L-C filter to smooth the input currents and to satisfy the EMI requirements [17]. It has been shown that the presence of a resonant L-C filter could determine instability phenomena that can prevent the matrix converter to deliver the rated power to the load [18]. A possible remedy for this problem consists in filtering the input voltage before calculating the duty-cycles. In this way it is possible to increase the stability power limit and to obtain the maximum voltage transfer ratio.

All this aspects are considered in the next chapters. In particular, Chapter 1 gives an overview of the basic principles of matrix converters. Chapter 2 summarises the most important modulation strategies for matrix converter, whereas Chapter 3 proposes two novel modulation techniques that allows obtaining a better performance in terms of number of commutations and current distortion.

Chapter 4 and 5 concern the stability problem. In those Chapters the unstable behaviour of matrix converter is explained and some solutions are proposed.

Chapter 6 analyses in details the quality of the input currents. Finally, Chapter 7 presents and assesses a complete electric drive for induction motor based on matrix converter.

Chapter 1

Fundamentals of Matrix Converters

Abstract

The matrix converter has several attractive features and some companies have shown a particular interest in its commercial exploitation. These chapter presents an introduction to its technology and theory. After a brief historical review, the basic hardware solutions for the development of matrix converters are described. A notable part of the chapter is dedicated to the comparison between matrix converter and back-to-back converter.

1.1. Structure of Matrix Converter

Basically, a matrix converter (MC) is composed by 9 bidirectional switches, as shown in Fig. 1.1, where each dot of the grid represents a connection between the output and the input terminals.

The converter is usually fed at the input side by a three phase voltage source and it is connected to an inductive load at the output side.

The schematic circuit of a matrix converter feeding a passive load is shown in Fig. 1.2. The system is composed by the voltage supply, an L-C input filter, the MC and a load impedance.

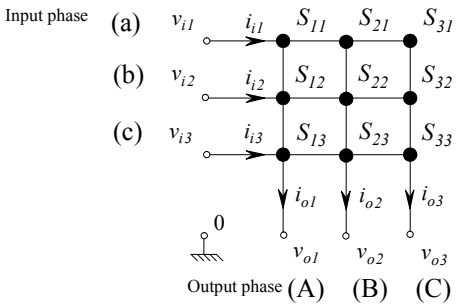

Fig. 1.1 - Basic scheme of matrix converters.

A. Input Filter

The input filter is generally needed to smooth the input currents and to satisfy the EMI requirements. A reactive current flows through the input filter capacitor, leading to a reduction of the power factor, especially at low output power. As a consequence, the capacitor is chosen in order to ensure at least a power factor of 0.8 with 10% of the rated output power. After the selection of the capacitor, the input filter inductance of the matrix converter can be chosen in order to satisfy the IEEE Recommended Practices and Requirements for Harmonic Control in Electrical Power Systems (IEEE Std. 519-1992).

B. Bidirectional Switches

The MC requires bidirectional switches with the capability to block the

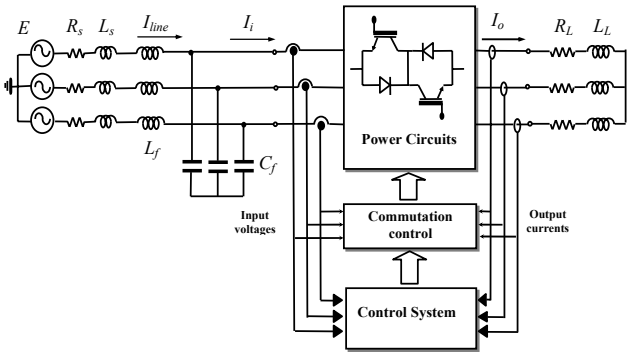

Fig. 1.2 - Complete scheme of a MC system.

voltage and to conduct the current in both directions. There are two main topologies for bi-directional switches, namely the common emitter anti-parallel IGBT configuration and the common collector anti-parallel IGBT configuration.

The common emitter arrangement is represented in Fig. 1.3(a). As can be seen, two IGBTs are connected with two diodes in an anti-parallel configuration. The diodes provide the reverse blocking capability.

The complete connection scheme of the common emitter arrangement is shown in Fig. 1.4. The main advantage of this solution is that the two IGBTs can be driven with respect the same point, i.e. the same common emitter, that can be considered as a local ground for the bidirectional switch. On the other hand, each bidirectional switch requires an insulated power supply, in order to ensure a correct operation and, hence, a total of nine insulated power supplies is needed. The power supplies must be insulated because, as a bidirectional switch is turned on, the common emitter assumes the potential of an input phase. Therefore, it is not possible for all the bidirectional switches to be driven with respect to the same common point.

Fig. 1.3 - Bidirectional switches. (a) common emitter configuration. (b) common collector configuration.

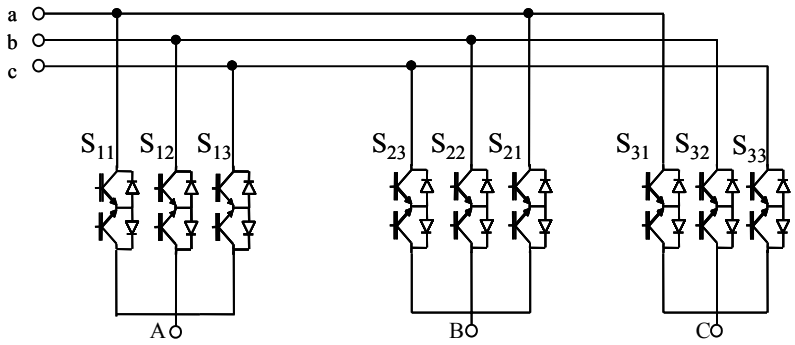

Fig. 1.4 - Complete scheme of the power stage using common emitter arrangement.

The common collector arrangement is presented in Fig. 1.3(b). The IGBTs are now arranged in a common collector configuration. In this case, only six insulated power supplies are needed. In fact, three IGBTs have the emitter connected to the input phase *a*. This common point can be considered as a local ground for them. Furthermore, three other IGBTs have the emitter connected to the output phase *A*. Once again, this point has the meaning of a local ground, that has to be insulated from the previous one. The same happens for the couples of phases *b*-*B* and *c*-*C*, thus concluding that six insulated power supplies are necessary. The complete connection scheme of the common collector arrangement is shown in Fig. 1.5.

From a commercial point of view, it is worth noting that several manufacturers have already produced integrated power modules for MC. The traditional solution consists of a single power module containing the switches corresponding to one leg of the converter. However, it is possible to find also modules containing the whole power stage of the converter (EUPEC).

Another interesting solution proposed by International Rectifier is represented in Fig. 1.6. In this case each module contains three IGBTs connected to one input phase and three IGBTs connected to the corresponding output phase [19].

The arrangement shown in Fig. 1.6 is particularly suitable for the common collector configuration and allows a simplification of the control circuit layout, since each power module requires only two insulated supplies to be driven. The traditional solution, instead, requires four of the six insulated

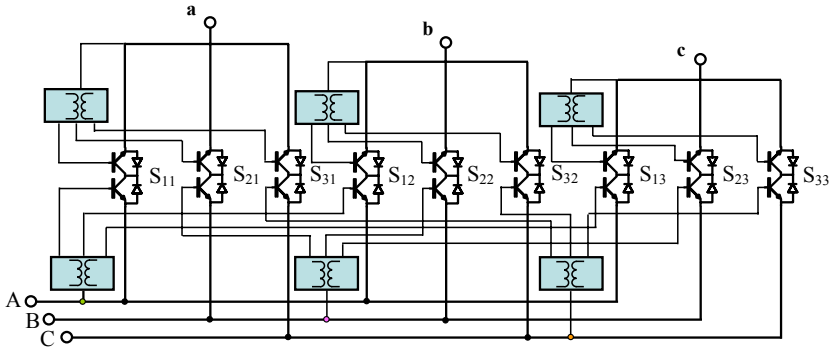

Fig. 1.5 - Complete scheme of the power stage using common collector arrangement.

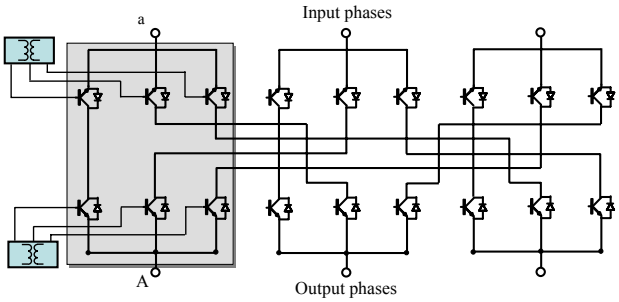

Fig. 1.6 - Scheme of the power stage based on modules manufactured by International Rectifier Corporation.

voltages that are necessary for the common collector configuration [20].

C. *Current Commutation*

Matrix converters have not free-wheeling diodes, unlike traditional voltage source inverters. This makes the current commutation between switches a difficult task, because the commutation has to be continuously controlled. The switches have to be turned on and turned off in such a way as to avoid short circuits and sudden current interruptions.

Many commutation strategies have been already studied. The most common solution is the "4-step commutation", that requires information about the actual current direction in the output phases. The four step sequence is shown in Fig. 1.7, that refers to the general case of current commutation from a bidirectional switch *a* to a bidirectional switch *b*.

In the beginning both IGBT of switch *a* are enabled. In the first step, the

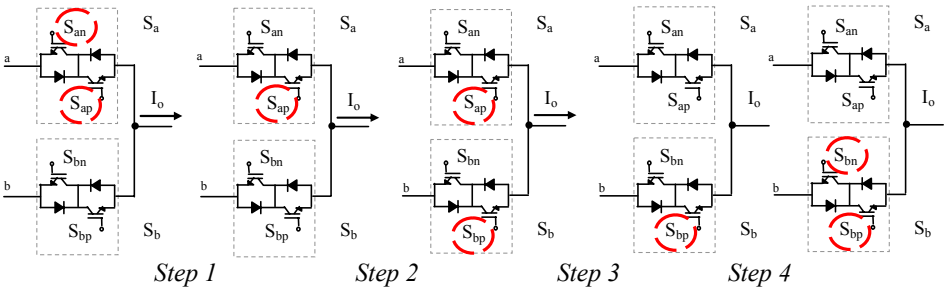

Fig. 1.7 - Four step commutation sequence.

IGBT S_{an}, which is not conducting the load current, is turned off. In the second step, the IGBT S_{bp}, that will conduct the current, is turned on. As a consequence, both switches a and b can conduct only positive currents and short circuits are prevented. Depending upon the instantaneous input voltages, after the second step, the conducting diode of switch a is subject to the voltage v_{ab}. If $v_{ab} < 0$, then the diode is reverse biased and a natural commutation takes place. Otherwise, if $v_{ab} \geq 0$, a hard commutation happens when, in the third step, IGBT S_{ap} is turned off. Finally, in the fourth step, the non-conducting switch S_{bn} is enabled to allow the conduction of negative currents. During a period of the input voltage, the natural commutation occurs in 50% of all commutations and therefore this current commutation has earned the name "semisoft switching".

Apart the 4-step commutation, other commutation strategies have been proposed. In particular, a "3-step commutation strategy" is described in [14] and [15]. The basic principle is that, combining the measurements of the input voltages to those of the output currents, the control logic can always perform the current commutation avoiding one step. In this way the commutation time is reduced and the current quality improves.

D. Converter Protections

Due to the lack of free-wheeling paths for the currents, a number of protection strategies should be adopted to prevent the damage of the converter. Protections against over-load, short-circuit and over-voltage are usually implemented.

The over-load protection is performed directly by the control logic, that turns off all the switches when the load current is greater than the rated one. This solution is not satisfactory in order to avoid the damage of the switches if a load short-circuit happens, because the latency time of the DSP depending on the cycle period is too high. Therefore, the protection against the short circuit consists in the monitoring of the collector-emitter voltage of all the IGBTs comprised in the power modules.

It is worth noting that it is not possible to simply turn off all the switches, otherwise the inductive load current have no closing path. The most common solution to this problem is to add a diode bridge clamp across the input and the output sides of the converter, shown in Fig. 1.8. The small capacitor of

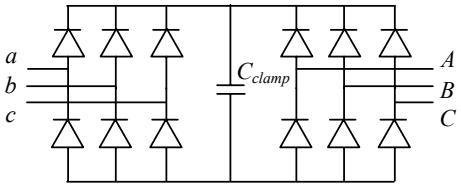

Fig. 1.8 - Clamp circuit for the protection of the matrix converter.

the clamp is designed to store the energy corresponding to the inductive load current.

In addition the voltage across the capacitor is continuously measured. In fact fault conditions are more frequently caused by instability phenomena at the input of the converter or wrong switch commutations rather than short circuits of the load. When the voltage across the capacitor becomes greater than a limit value, the over-voltage protection should stop the converter.

It is possible to show that some diodes of the clamp can be replaced by the diodes already present in the bidirectional switches if they are connected in the common-emitter configuration. In this way, instead of 12 clamp diodes, only 6 diodes are necessary. However, this solution requires three additional insulated voltage supplies for the drivers to guarantee a correct operation. Further details can be found in [17].

Another protection issue is that MC is less immune to power grid disturbances than other converter. In hoisting applications, short-term braking capability during a power outage is needed until the mechanical brake engages or to perform a more effective combined braking.

A method to provide short-term braking capability during a power outage for MCs was presented in [20]. It includes a braking chopper in the clamp circuit, which allows a notable reduction of the capacitor size. The power flow in the clamp circuit is reduced by increasing the harmonic content in the motor currents, thus causing higher motor losses.

1.2. Input Current Modulation Strategies

The MC allows the control not only of the output voltages, but also of the phase angle of the input current vector.

There are several possible solutions for the modulation of the input current vector that basically differ in the direction along which the current

vector is modulated. This direction can be represented introducing the vector $\overline{\psi}$ with arbitrary magnitude, here named modulation vector. For any strategy it is

$$\overline{\psi} \cdot j\bar{i}_i = 0 \tag{1.1}$$

where $\bar{i}_i$ is the input current vector.

Any input current modulation strategy is completely defined once the modulation vector $\overline{\psi}$ is known. In fact, the input current can be expressed as a function of the modulation vector, the power absorbed by the converter and the input voltage.

The power absorbed by the converter can be written as follows:

$$p_i = \frac{3}{2}\overline{v}_i \cdot \bar{i}_i \,. \tag{1.2}$$

Then, combining (1.1) and (1.2) leads to the following expression of the input current vector:

$$\bar{i}_i = \frac{2}{3}\frac{p_i}{\overline{v}_i \cdot \overline{\psi}}\overline{\psi} \tag{1.3}$$

where p_i is the power delivered to the load.

If the switches are assumed ideal and the converter power losses are neglected, the input power is equal to the power delivered to the load p_o. As a consequence, (1.3) becomes as follows:

$$\bar{i}_i = \frac{2}{3}\frac{p_o}{\overline{v}_i \cdot \overline{\psi}}\overline{\psi} \,. \tag{1.4}$$

As can be seen from (1.4) the input current space vector depends on the output power level, the input voltage vector and the modulation vector.

The simplest input current modulation strategy (Strategy A) is to maintain the input current vector in phase with the actual input voltage vector, determining instantaneous unity input power factor. For instance, Fig. 1.9 shows the behaviour of a 10-kW matrix converter. As is possible to see, the line current is nearly sinusoidal and is kept in phase with the input line-to-neutral voltage.

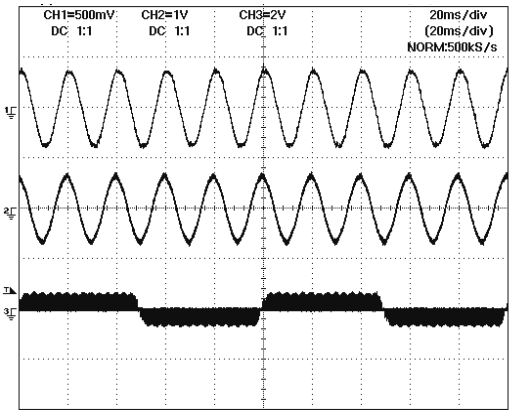

Fig. 1.9 - Experimental tests: stable steady state operation. Upper track: line current (20 A/div). Middle track: input line-to-neutral voltage (400 V/div). Lower track: load line-to-line voltage (600 V/div).

In case of input voltage disturbances, Strategy A produces non-sinusoidal input currents having the lowest total RMS value.

In [21] it has been demonstrated that a better performance in terms of input current distortion can be achieved if the input current vector is dynamically modulated around the input voltage vector (Strategy B), or is modulated to be in phase with the positive sequence fundamental component of the input voltage vector (Strategy C). Theoretical and experimental results obtained comparing these input current modulation strategies are given in [22] and [23]. As a conclusion, it can be noted that Strategy B has to be preferred in the case of unbalanced sinusoidal input voltages because allows unbalanced, but sinusoidal, input currents to be obtained. Strategy C performs better in presence of input voltage distortions. It is possible to demonstrate that Strategy C represents the optimal modulation strategy which determines the lowest total RMS value of the input current disturbance. It will be pointed out that Strategy C has also a stabilizing effect on the converter operation. This aspect will be clarified in the next paragraph.

1.3. Instability Phenomena

The simplest modulation strategy is based on detecting the zero crossing

of one input voltage for synchronizing the input current modulation. This control technique performs correctly if an ideal power supply is assumed (i.e. balanced and sinusoidal supply voltages), but in presence of input voltage disturbances, these are reflected on the output side determining low order voltage harmonics, as the matrix converter has no internal energy storage. Considering unbalanced non-sinusoidal input voltages, the magnitude and the angular velocity of the input voltage vector are not constant. Then, a simple synchronization with the input voltages is no longer applicable but the input voltages must be measured at each cycle period, in order to calculate the duty-cycles necessary to generate balanced and sinusoidal output voltages.

However, the compensation of the input voltage disturbances leads to a closed loop control that might cause instability phenomena when the matrix converter output power exceeds a limit value. Typical waveforms of the line current, the output voltage and the input line-to-line voltage during unstable operation are shown in Fig. 1.10 for a 10-kW MC.

Here is a qualitative explanation of the instability phenomena. Let's suppose that a voltage disturbance is temporarily applied to the converter input, thus leading to a variation of the input current. It is worth noting that this current variation is proportional to the output power. The current harmonics with frequencies close to the resonant frequency of the LC input

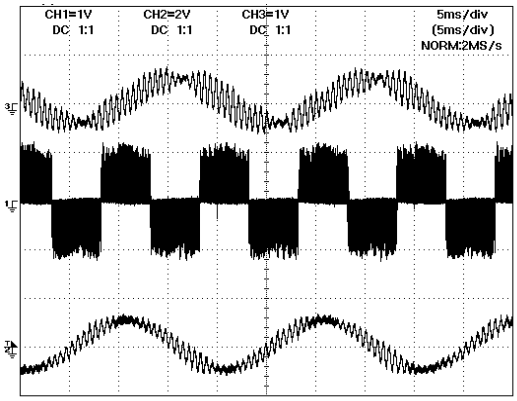

Fig. 1.10 - Experimental test: unstable steady state operation. Upper track: line current (10A/div). Middle track: line to line output voltage (400 V/div). Lower track: line to line input voltage (400 V/div).

filter are amplified and their effect is to reinforce the input voltage disturbance. If the output power is small, this reinforcement action is weak and after the disturbance has vanished, the converter returns to the normal steady state operation. Otherwise, if the output power is high enough, the reinforcement action is sufficient to establish self-sustained oscillations in the input voltages, even after the initial disturbance has vanished. In this case, the system reaches a new steady state operation, but the converter does not work correctly, because the input currents and voltages are remarkably distorted.

It is interesting to note that these oscillations have the form of "beatings", namely they are composed by at least two separate harmonics with close frequencies.

A first attempt to determine the stability power limit was done in [18], where the stability is evaluated by analyzing the migration of the eigenvalues of a small-signal model of the system. The power limit results as follows:

$$P_{lim} = \frac{3}{2} V_i^2 C_f \sqrt{\frac{R_s^2}{L_T^2} + 4\omega_i^2} \tag{1.5}$$

where V_i is the amplitude of the input voltage vector, ω_i the input angular frequency, and L_T is the sum of filter and line inductances.

For a prefixed value of the input filter resonance frequency, (1.5) emphasizes that, in order to increase the power limit, high values of the capacitance C_f and low values of the inductance L_f should be preferred.

Furthermore, the control of MCs is usually done with digital microprocessors whose calculations are performed within a finite cycle period. The digital controller samples the input voltages in the beginning of the cycle period, but applies the new configurations only during the subsequent cycle period, thus determining a delay of one cycle period. It has long been known that a time delay could remarkably modify the system stability. The effect of the time delay was addressed in [24]. In this case the stability power limit depends not only on the line and filter parameters, but also on the load impedance and on the cycle period T_p.

Some methods have been proposed to increase the stability power limit, such as the addition of a damping resistance across the filter inductor. In [25] and [26] it has been shown that the power limit can be sensibly improved if

the calculation of the duty-cycles is carried out by filtering the matrix converter input voltages of the MC by means of a digital low-pass filter. For example, the continuous-time equation of a possible filter applied to the input voltage vector is the following one:

$$\frac{d\overline{v}_{if}}{dt} = \frac{\overline{v}_i - (1 - j\omega_i\tau)\overline{v}_{if}}{\tau} \tag{1.6}$$

where $\overline{v}_{if}$ is the filtered input voltage vector.

By increasing the time constant τ of the low-pass filter is possible to increase the limit voltage. The only drawback is that the filter may affect to some extent the capability of the control system to compensate the effect of input voltage disturbances on the load currents.

1.4. Comparison between MC and Back-to-back Converter

To obtain the favours of market, MC should overcome the performance of the other competitors in terms of cost, size and reliability. The most important alternative to MC is the back-to-back converter, whose scheme is shown in Fig. 1.11.

The MC has been already compared with the back-to-back converter obtaining some important but not conclusive results. The comparison is extremely difficult due to the high number of system parameters (i.e. input filter and load parameters, switching frequency, output frequency,

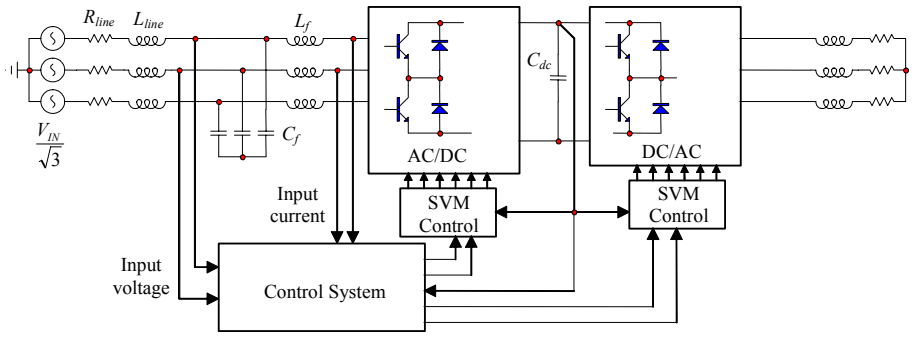

Fig.1.11 - Schematic drawing of the back-to-back converter.

modulation strategies, etc.) and to the inherent differences between the two converter topologies, such as the maximum voltage transfer ratio. For instance, the MC is able to generate balanced and sinusoidal output voltages, whose amplitude can be regulated from zero to approximately 87% of the input voltage amplitude. The output voltage of the back-to-back converter instead is related to the DC-link voltage, and can be equal or even greater than the input voltage [26].

The switching frequencies of the two converters are related to the adopted modulation strategies and should be chosen with care in order to make a fair comparison. Furthermore, both converters need an input filter to reduce the input current harmonics, and the filter parameters are strictly related to the switching frequency.

In [27]- [28] the comparison between the two topologies is performed in terms of total switch losses, by evaluating the converter efficiency for given operating conditions. On the other hand, it has been clearly emphasized that in matrix converters the switch losses are not equally shared among the switches, being the distribution related to the output frequency. Thus, considering only the total switch losses as the key-parameter for the comparison may be misleading.

In [29] the comparison between matrix and back-to-back converters is performed by evaluating the maximum output power that each converter is able to deliver to the load for different output frequency. The comparison is carried out assuming the same types of IGBTs and diodes for both converters. The maximum output power is determined taking into account the thermal limit of each switch on the basis of a thermal model. All the parameters needed for the comparison are shown in Tab. 1.1.

The performance of the two converter topologies has been tested for different values of the output frequency in the range 0-150 Hz. The voltage has been changed with the frequency according to the well-known constant V/Hz law for induction motor drives. Thus, the output voltage is varied proportionally to the frequency until 50Hz. For higher frequencies the phase to phase output voltage is kept constant, i.e. 330V and 380V for the MC and the back-to-back converter respectively. At low frequencies, the output voltage has been changed in order to compensate the voltage drop on the stator winding resistance.

TABLE 1.1 – SYSTEM PARAMETERS

Parameters	Back to Back	Matrix Converter
V_{IN}	380 V(RMS), 50 Hz	380 V(RMS), 50 Hz
R_{line}	0.11Ω	0.11Ω
L_{line}	0.167mH	0.167mH
V_{DC}	600V	-
C_{DC}	200μF	-
C_f	25μF (Y)	40 μF (Y)
L_f	1.00 mH	0.35 mH
R_{jc}	0.64 °C/W	0.64 °C/W
C_j	31.2 mJ/°C	31.2 mJ/°C
θ_{case}	70flC	70flC
f_{sw}	6.6kHz (ac-dc),16kHz (dc-ac)	8kHz
$\cos \varphi_{load}$	0.8	0.8
V_{out}	f_{out}< 50 Hz , const. V/Hz f_{out}> 50 Hz , V_{out} = 380 V	f_{out}< 50 Hz , const. V/Hz f_{out}> 50 Hz, V_{out} = 330 V
Diodes	HFA16PB120	HFA16PB120
IGBTs	IRG4PH50U	IRG4PH50U

The maximum output power achievable by the two converters as a function of the output frequency is summarized in Fig. 1.12. It is evident that the output power of MC is always higher than that of back-to-back converter, showing a decrease around 50 and 100 Hz.

Fig. 1.13 shows the load current corresponding to the maximum output power as a function of the output frequency, for the matrix and the back-to-back converters. In this figure the better performance of the matrix converter in terms of maximum output current is evident, especially in the low output frequency range. The reason of so low values of the output current for the back-to back converter is that, at low frequency, the output current is not equally shared among the six switches. This situation is similar to the one occurring when the matrix converter operates at 50 Hz. On the contrary, the matrix converter is able to deliver high currents at low frequency because these currents are equally shared among the 18 switches.

In order to make a fair comparison, one should take into account that the

two converter topologies are realized with a different number of switches (i.e. 18 for the matrix converter and 12 for the back-to-back converter). For this purpose two more significant quantities have been introduced, which represent the maximum output power per switch and the corresponding output current per switch. These new quantities are represented in Figs. 1.14 and 1.15 respectively.

Fig. 1.14 shows that the output power per switch of the MC is always lower than that of back-to-back converter, except for frequency values ranging from 0 to about 30 Hz. On the other hand, it can be seen from Fig. 1.15 that the load current per switch of the matrix converter is always higher than that of the back-to-back converter, except for frequency values around 50 Hz.

From Figs. 1.14 and 1.15 it can be concluded that in terms of maximum

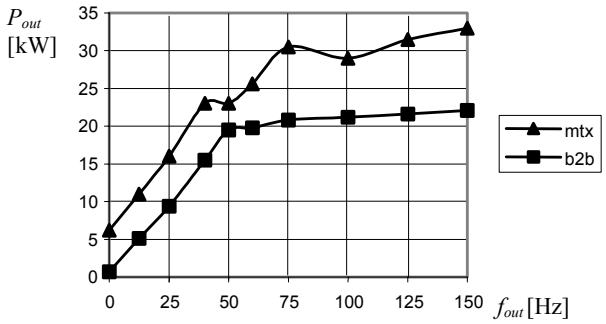

Fig. 1.12 - Maximum output power as a function of the output frequency.

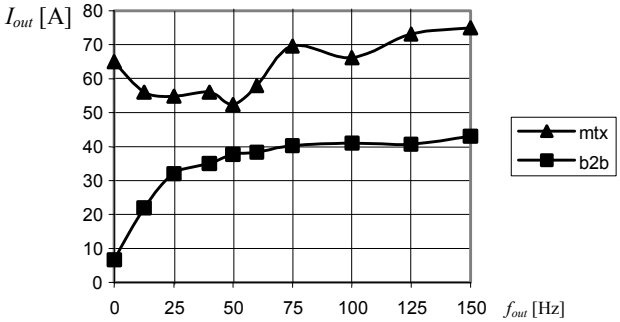

Fig. 1.13 - Maximum output current as a function of the output frequency.

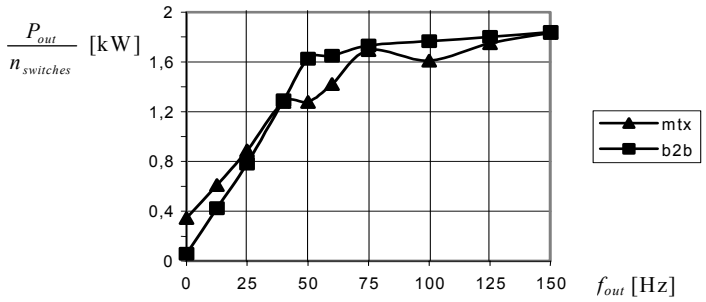

Fig. 1.14 - Maximum output power per switch as a function of the output frequency.

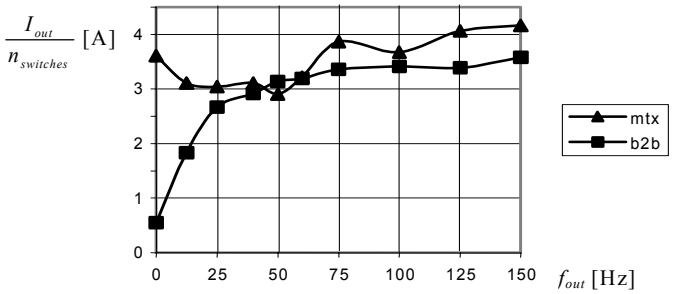

Fig. 1.15 - Maximum output current per switch as a function of the output frequency.

output power per switch the two converter topologies show practically the same performance, whereas in terms of output current per switch the matrix converter should be preferred to the back-to-back converter particularly in the low output frequency range.

These results could be usefully employed in the choice of the converter topology for drive systems, once the operating conditions and the over-load capability were specified in details.

1.5. Conclusion

MCs provides some interesting features, such as compactness and sinusoidal waveform of the input and output currents. However, there are some potential disadvantages of MC technology that have so far prevented its commercial exploitation. During the last two decades, several of these problems were solved. In particular, the commutation problem between two bidirectional switches was solved with the development of multistep

commutation strategies and new power modules designed for MC application have been manufactured.

Chapter 2

Modulation Strategies

Abstract

In this chapter a novel representation of the switches state of a three-phase to three-phase matrix converter is presented. This approach, based on the space vector representation, simplifies the study of the modulation strategies, leading to a complete general solution and providing a very useful unitary point of view. The already-established strategies can be considered as particular cases of the proposed general solution. Using this approach it can be verified that the SVM technique coincides with the general solution of the modulation problem of matrix converter. This technique can be considered the best solution for the possibility to achieve the highest voltage transfer ratio and to optimize the switching pattern through a suitable use of the zero configurations.

2.1. Introduction

The complexity of the matrix converter topology makes the study and the determination of suitable modulation strategies a hard task.

Two different mathematical approaches have been considered in the past

to face this problem, namely the Modulation Duty-Cycle Matrix (MDCM) approach and the Space Vector Modulation (SVM) approach.

The MDCM approach has been initially used in order to put the matrix converter theory on a strong mathematical foundation and several fundamental papers have been published.

A first strategy based on MDCM and proposed by Alesina and Venturini (in the following AV method), allowing the full control of the output voltages and of the input power factor, has been derived in [1]. The maximum voltage transfer ratio of the proposed algorithm is limited to 0.5 and the input power factor control requires the knowledge of the output power factor.

The inclusion of third harmonics in the input and output voltage waveforms has been successfully adopted in [30] to increase the maximum voltage transfer ratio up to 0.866, a value which represents an intrinsic limitation of the three-phase to three-phase matrix converter, with balanced supply voltages and balanced output conditions. In [2], the same technique has been extended with input power factor control leading to a very powerful modulation strategy (in the following optimum AV method).

The scalar control modulation algorithm proposed in [31], although based on a different approach, leads to performance similar to that obtained by using the optimum AV method.

A sensible increase of the maximum voltage transfer ratio up to 1.053 is a feature of the Fictitious DC Link algorithm, presented in [3]. This strategy considers the modulation as a two steps process, namely rectification and inversion. The higher voltage transfer ratio is achieved to the detriment of the waveform quality of the input and output variables.

The SVM approach, initially proposed in [4] to control only the output voltages, has been successively developed in [6], [8], [21], [32] in order to completely exploit the possibility of matrix converters to control the input power factor regardless the output power factor, to fully utilize the input voltages, and to reduce the number of switch commutations in each cycle period. Furthermore, this strategy allows an immediate comprehension of the modulation process, without the need for a fictitious DC link, and avoiding the addition of the third harmonic components.

In this chapter a new general and complete solution to the problem of the modulation strategy of three-phase matrix converters is presented. This

solution has been obtained using the Duty-Cycle Space Vector (DCSV) approach, which consists of a representation of the switches state by means of space vectors. In this way, the previously mentioned strategies can be considered as particular cases of the proposed one.

A review of the well-established modulation techniques is presented in Paragraph 2.2. Then, in Paragraph 2.4, the new approach is illustrated in order to determine a generalized modulation technique.

From this unitary point of view, some modulation techniques are described and compared with reference to maximum voltage transfer ratio, number of commutations and ripple of the input and output quantities. It should be noted that the analysis is concerned with modulation techniques that do not utilize information about the output currents.

Finally, it is emphasized that the generalized SVM technique, obtained by using more than one zero configuration in each cycle period, represents the general solution to the problem of the modulation strategy for matrix converters.

2.2. Duty-cycle Matrix Approach

The basic scheme of three-phase matrix converters has been already represented in Fig. 1.1.

The switching behaviour of the converter generates discontinuous output voltage waveforms. Assuming inductive loads connected at the output side leads to continuous output current waveforms. In these operating conditions, the instantaneous power balance equation, applied at the input and output sides of an ideal converter, leads to discontinuous input currents. The presence of capacitors at the input side is required to ensure continuous input voltage waveforms.

In order to analyze the modulation strategies, an opportune converter model is introduced, which is valid considering ideal switches and a switching frequency much higher than input and output frequencies. Under these assumptions, the higher frequency components of the variables can be neglected, and the input/output quantities are represented by their average values over a cycle period T_c.

The input/output relationships of voltages and currents are related to the

states of the nine switches, and can be written in matrix form as

$$\begin{bmatrix} v_{o1} \\ v_{o2} \\ v_{o3} \end{bmatrix} = \begin{bmatrix} m_{11} & m_{12} & m_{13} \\ m_{21} & m_{22} & m_{23} \\ m_{31} & m_{32} & m_{33} \end{bmatrix} \begin{bmatrix} v_{i1} \\ v_{i2} \\ v_{i3} \end{bmatrix} \tag{2.1}$$

$$\begin{bmatrix} i_{i1} \\ i_{i2} \\ i_{i3} \end{bmatrix} = \begin{bmatrix} m_{11} & m_{21} & m_{31} \\ m_{12} & m_{22} & m_{32} \\ m_{13} & m_{23} & m_{33} \end{bmatrix} \begin{bmatrix} i_{o1} \\ i_{o2} \\ i_{o3} \end{bmatrix} \tag{2.2}$$

with

$$0 \le m_{hk} \le 1, \quad h = 1,2,3, \quad k = 1,2,3. \tag{2.3}$$

The variables m_{hk} are the duty-cycles of the nine switches S_{hk} and can be represented by the duty-cycle matrix $\boldsymbol{m}$. In order to prevent short-circuit on the input side and ensure uninterrupted load current flow, these duty-cycles must satisfy the three following constraint conditions:

$$m_{11} + m_{12} + m_{13} = 1 \tag{2.4}$$

$$m_{21} + m_{22} + m_{23} = 1 \tag{2.5}$$

$$m_{31} + m_{32} + m_{33} = 1. \tag{2.6}$$

The determination of any modulation strategy for the matrix converter, can be formulated as the problem of determining, in each cycle period, the duty-cycle matrix that satisfies the input-output voltage relationships (2.1), the required instantaneous input power factor, and the constraint conditions (2.3)-(2.6). The solution of this problem represents a hard task and is not unique, as documented by the different solutions proposed in literature.

It should be noted that in order to completely determine the modulation strategy it is necessary to define the switching pattern, that is the commutation sequence of the nine switches. The use of different switching patterns for the same duty-cycle matrix $\boldsymbol{m}$ leads to a different behaviour in terms of number of switch commutations and ripple of input and output quantities.

A. Alesina-Venturini 1981 (AV method)

A first solution, obtained by using the duty-cycle matrix approach, has been proposed in [1]. This strategy allows the control of the output voltages and input power factor, and can be summarized in the following equation, valid for unity input power factor ($\alpha_i = \beta_i$)

$$m_{hk} = \frac{1}{3}\left\{1 + 2\,q\cos\left[\alpha_o - (h-1)\frac{2\pi}{3}\right]\cos\left[\beta_i - (k-1)\frac{2\pi}{3}\right]\right\}. \qquad (2.7)$$

Assuming balanced supply voltages and balanced output conditions, the maximum value of the voltage transfer ratio q is 0.5. This low value represents the major drawback of this modulation strategy.

The allocation of the switch states within a cycle period is not unique and different switching patterns lead to different input-output ripple performance. A typical double-sided switching pattern usually adopted is represented schematically in Fig. 2.1.

As is possible to see, by using this modulation technique, 12 switch commutations occur in each cycle period (a commutation takes place when the value of h or k in m_{hk} changes).

B. Alesina-Venturini 1989 (Optimum AV method)

In order to improve the performance of the previous modulation strategy in terms of maximum voltage transfer ratio, a second solution has been presented in [2]. In this case the modulation law can be described by the following relationship

$$m_{hk} = \frac{1}{3}\left\{1 + 2\,q\cos\left[\beta_i - \frac{2\pi(k-1)}{3}\right]\cdot\right.$$

$$\cdot\left[\cos\left(\alpha_o - \frac{2\pi(h-1)}{3}\right) - \frac{\cos(3\alpha_o)}{6} + \frac{\cos(3\beta_i)}{2\sqrt{3}}\right] -$$

$$\left. - \frac{2}{3\sqrt{3}}\,q\left[\cos\left(4\beta_i - (k-1)\frac{2\pi}{3}\right) - \cos\left(2\beta_i + (k-1)\frac{2\pi}{3}\right)\right]\right\}. \qquad (2.8)$$

In particular, the solution given in (2.8) is valid for unity input power

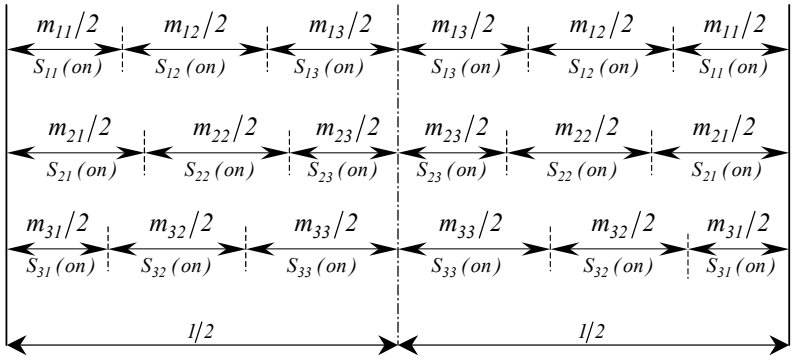

Fig. 2.1 – Double-sided switching pattern in a cycle period T_p.

factor ($\alpha_i = \beta_i$), and the maximum voltage transfer ratio q is 0.866.

It should be noted that in [2] a complete solution, valid for values of the input power factor different from unity, has been also derived. The corresponding expressions for m_{hk} are very complex and require the knowledge of the output power factor.

2.3. Space Vector Approach

A. Vectors of MC

The Space Vector Approach is based on the instantaneous space vector representation of input and output voltages and currents.

Among the 27 possible switching configurations available in three-phase matrix converters, 21 only can be usefully employed in the SVM algorithm, and can be represented as shown in Tab. 2.1.

The first 18 switching configurations determine an output voltage vector $\bar{v}_o$ and an input current vector $\bar{i}_i$, having fixed directions, as represented in Figs. 2.2(a) and (b), and will be named “active configurations”. The magnitude of these vectors depends upon the instantaneous values of the input line-to-line voltages and output line currents respectively.

The last 3 switching configurations determine zero input current and output voltage vectors and will be named “zero configurations”.

The remaining 6 switching configurations have each output phase

TABLE 2.1 - SWITCHING CONFIGURATIONS USED IN THE SVM ALGORITHM.

Switch configuration	Switches On			v_o	α_o	i_i	β_i
+1	S_{11}	S_{22}	S_{32}	$2/3\ v_{12i}$	0	$2/\sqrt{3}\ i_{o1}$	$-\pi/6$
−1	S_{12}	S_{21}	S_{31}	$-2/3\ v_{12i}$	0	$-2/\sqrt{3}\ i_{o1}$	$-\pi/6$
+2	S_{12}	S_{23}	S_{33}	$2/3\ v_{23i}$	0	$2/\sqrt{3}\ i_{o1}$	$\pi/2$
−2	S_{13}	S_{22}	S_{32}	$-2/3\ v_{23i}$	0	$-2/\sqrt{3}\ i_{o1}$	$\pi/2$
+3	S_{13}	S_{21}	S_{31}	$2/3\ v_{31i}$	0	$2/\sqrt{3}\ i_{o1}$	$7\pi/6$
−3	S_{11}	S_{23}	S_{33}	$-2/3\ v_{31i}$	0	$-2/\sqrt{3}\ i_{o1}$	$7\pi/6$
+4	S_{12}	S_{21}	S_{32}	$2/3\ v_{12i}$	$2\pi/3$	$2/\sqrt{3}\ i_{o2}$	$-\pi/6$
−4	S_{11}	S_{22}	S_{31}	$-2/3\ v_{12i}$	$2\pi/3$	$-2/\sqrt{3}\ i_{o2}$	$-\pi/6$
+5	S_{13}	S_{22}	S_{33}	$2/3\ v_{23i}$	$2\pi/3$	$2/\sqrt{3}\ i_{o2}$	$\pi/2$
−5	S_{12}	S_{23}	S_{32}	$-2/3\ v_{23i}$	$2\pi/3$	$-2/\sqrt{3}\ i_{o2}$	$\pi/2$
+6	S_{11}	S_{23}	S_{31}	$2/3\ v_{31i}$	$2\pi/3$	$2/\sqrt{3}\ i_{o2}$	$7\pi/6$
−6	S_{13}	S_{21}	S_{33}	$-2/3\ v_{31i}$	$2\pi/3$	$-2/\sqrt{3}\ i_{o2}$	$7\pi/6$
+7	S_{12}	S_{22}	S_{31}	$2/3\ v_{12i}$	$4\pi/3$	$2/\sqrt{3}\ i_{o3}$	$-\pi/6$
−7	S_{11}	S_{21}	S_{32}	$-2/3\ v_{12i}$	$4\pi/3$	$-2/\sqrt{3}\ i_{o3}$	$-\pi/6$
+8	S_{13}	S_{23}	S_{32}	$2/3\ v_{23i}$	$4\pi/3$	$2/\sqrt{3}\ i_{o3}$	$\pi/2$
−8	S_{12}	S_{22}	S_{33}	$-2/3\ v_{23i}$	$4\pi/3$	$-2/\sqrt{3}\ i_{o3}$	$\pi/2$
+9	S_{11}	S_{21}	S_{33}	$2/3\ v_{31i}$	$4\pi/3$	$2/\sqrt{3}\ i_{o3}$	$7\pi/6$
−9	S_{13}	S_{23}	S_{31}	$-2/3\ v_{31i}$	$4\pi/3$	$-2/\sqrt{3}\ i_{o3}$	$7\pi/6$
0_1	S_{11}	S_{21}	S_{31}	0	-	0	-
0_2	S_{12}	S_{22}	S_{32}	0	-	0	-
0_3	S_{13}	S_{23}	S_{33}	0	-	0	-

connected to a different input phase. In this case the output voltage and input current vectors have variable directions and cannot be usefully used to synthesise the reference vectors.

B. SVM Technique

The SVM algorithm for matrix converters presented in this paragraph has the inherent capability to achieve the full control of both output voltage vector and instantaneous input current displacement angle [6], [8], [21], [32].

At any sampling instant, the output voltage vector $\overline{v}_o$ and the input current displacement angle φ_i are known as reference quantities (Figs. 2.3(a) and 2.4(b)). The input line-to-neutral voltage vector $\overline{v}_i$ is imposed by the

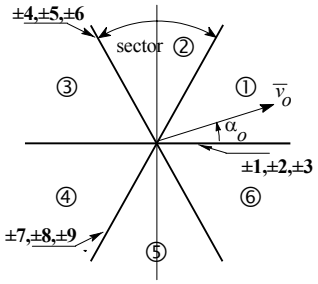

Fig. 2.2(a) - Direction of the output line-to-neutral voltage vectors generated by the active configurations.

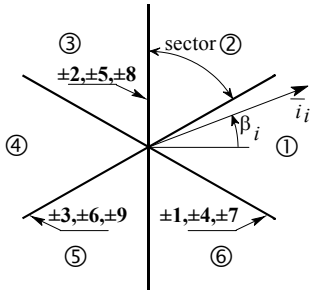

Fig. 2.2(b) – Directions of the input line current vectors generated by the active configurations.

source voltages and is known by measurements. Then, the control of φ_i can be achieved controlling the phase angle β_i of the input current vector.

In principle, the SVM algorithm is based on the selection of 4 active configurations that are applied for suitable time intervals within each cycle period T_p. The zero configurations are applied to complete T_p.

In order to explain the modulation algorithm, reference will be made to Figs. 2.3(a) and (b), where $\overline{v}_o$ and $\overline{i}_i$ are assumed both lying in sector 1, without missing the generality of the analysis.

The reference voltage vector $\overline{v}_o$ is resolved into the components $\overline{v}_o^{'}$ and $\overline{v}_o^{''}$ along the two adjacent vector directions. The $\overline{v}_o^{'}$ component can be

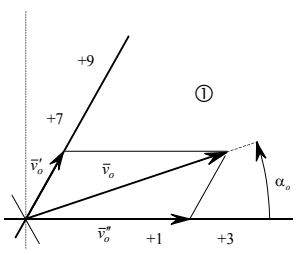

Fig. 2.3(a) - Output voltage vectors modulation principle.

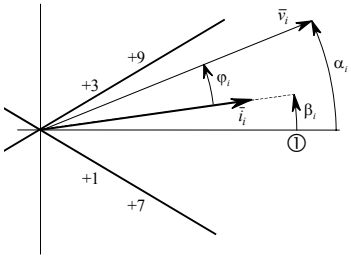

Fig. 2.3(b) - Input current vectors modulation principle.

synthesised using two voltage vectors having the same direction of $\bar{v}_o'$. Among the six possible switching configurations (±7, ±8, ±9), the ones that allow also the modulation of the input current direction must be selected. It is verified that this constraint allows the elimination of two switching configurations (+8 and -8 in this case). Among the remaining four, we assume to apply the positive switching configurations (+7 and +9). The meaning of this assumption will be discussed later in this paragraph. With similar considerations the switching configurations required to synthesise the $\bar{v}_o''$ component can be selected (+1 and +3).

Using the same procedure it is possible to determine the four switching configurations related to any possible combination of output voltage and input current sectors, leading to the results summarized in Tab. 2.2.

Four symbols (I, II, III, IV) are also introduced in the last row of Tab. 2.2 to identify the four general switching configurations, valid for any combination of input and output sectors.

Now it is possible to write, in a general form, the four basic equations of the SVM algorithm, which satisfy, at the same time, the requirements of the reference output voltage vector and input current displacement angle. With reference to the output voltage vector, the two following equations can be written:

TABLE 2.2 – SELECTION OF THE SWITCHING CONFIGURATIONS FOR EACH COMBINATION OF OUTPUT VOLTAGE AND INPUT CURRENT SECTORS.

		Sector of the output voltage vector											
		1 or 4				2 or 5				3 or 6			
Sector of the input current vector	1 or 4	+9	+7	+3	+1	+6	+4	+9	+7	+3	+1	+6	+4
	2 or 5	+8	+9	+2	+3	+5	+6	+8	+9	+2	+3	+5	+6
	3 or 6	+7	+8	+1	+2	+4	+5	+7	+8	+1	+2	+4	+5
		I	II	III	IV	I	II	III	IV	I	II	III	IV

$$\bar{v}_o' = \bar{v}_o^I \delta^I + \bar{v}_o^{II} \delta^{II} = \frac{2}{\sqrt{3}} v_o \cos(\tilde{\alpha}_o - \frac{\pi}{3}) e^{j[(K_v-1)\pi/3+\pi/3]} \tag{2.9}$$

$$\bar{v}_o'' = \bar{v}_o^{III} \delta^{III} + \bar{v}_o^{IV} \delta^{IV} = \frac{2}{\sqrt{3}} v_o \cos(\tilde{\alpha}_o + \frac{\pi}{3}) e^{j[(K_v-1)\pi/3]} . \tag{2.10}$$

With reference to the input current displacement angle, two equations are obtained by imposing to the vectors $\left(\bar{i}_i^I \delta^I + \bar{i}_i^{II} \delta^{II}\right)$ and $\left(\bar{i}_i^{III} \delta^{III} + \bar{i}_i^{IV} \delta^{IV}\right)$ to have the direction defined by β_i. This can be achieved by imposing a null value to the two vectors component along the direction perpendicular to $e^{j\beta_i}$ (i.e. $j e^{j\beta_i}$), leading to

$$\left(\bar{i}_i^I \delta^I + \bar{i}_i^{II} \delta^{II}\right) \cdot j e^{j\tilde{\beta}_i} e^{j(K_i-1)\pi/3} = 0 \tag{2.11}$$

$$\left(\bar{i}_i^{III} \delta^{III} + \bar{i}_i^{IV} \delta^{IV}\right) \cdot j e^{j\tilde{\beta}_i} e^{j(K_i-1)\pi/3} = 0 . \tag{2.12}$$

In (2.9)-(2.12) $\tilde{\alpha}_o$ and $\tilde{\beta}_i$ are the output voltage and input current phase angle measured with respect to the bisecting line of the corresponding sector, and differ from α_o and β_i according to the output voltage and input current sectors. In these equations the following angle limits apply

$$-\frac{\pi}{6} < \tilde{\alpha}_o < +\frac{\pi}{6}, \qquad -\frac{\pi}{6} < \tilde{\beta}_i < +\frac{\pi}{6} . \tag{2.13}$$

δ^I, δ^{II}, δ^{III}, δ^{IV} are the duty-cycles (i.e. $\delta^I = t^I/T_p$) of the 4 switching configurations, K_v=1,2,..,6 represents the output voltage sector and K_i=1,2,…,6 represents the input current sector. $\bar{v}_o^I, \bar{v}_o^{II}, \bar{v}_o^{III}, \bar{v}_o^{IV}$ are the output voltage vectors associated respectively with the switching configurations I, II, III, IV given in Tab. 2.2. The same formalism is used for the input current vectors.

Solving (2.9)-(2.12) with respect to the duty-cycles, after some tedious manipulations, leads to the following relationships [21]:

$$\delta^I = (-1)^{K_v+K_i} \frac{2}{\sqrt{3}} q \frac{\cos(\tilde{\alpha}_o - \pi/3)\cos(\tilde{\beta}_i - \pi/3)}{\cos\varphi_i} \tag{2.14}$$

$$\delta^{II} = (-1)^{K_v+K_i+1}\frac{2}{\sqrt{3}}q\frac{\cos(\tilde{\alpha}_o - \pi/3)\cos(\tilde{\beta}_i + \pi/3)}{\cos\varphi_i} \tag{2.15}$$

$$\delta^{III} = (-1)^{K_v+K_i+1}\frac{2}{\sqrt{3}}q\frac{\cos(\tilde{\alpha}_o + \pi/3)\cos(\tilde{\beta}_i - \pi/3)}{\cos\varphi_i} \tag{2.16}$$

$$\delta^{IV} = (-1)^{K_v+K_i}\frac{2}{\sqrt{3}}q\frac{\cos(\tilde{\alpha}_o + \pi/3)\cos(\tilde{\beta}_i + \pi/3)}{\cos\varphi_i}. \tag{2.17}$$

Equations (2.14)-(2.17) have a general validity and can be applied for any combination of output voltage sector K_v and input current sector K_i.

It should be noted that, for any sector combinations, two of the duty-cycles calculated by (2.14)-(2.17) assume negative values. This is due to the assumption made of using only the positive switching configurations in writing the basic equations (2.9)-(2.12). A negative value of the duty-cycle means that the corresponding negative switching configuration has to be selected instead of the positive one.

Furthermore, for the feasibility of the control strategy, the sum of the absolute values of the four duty-cycles must be lower than unity

$$\left|\delta^{I}\right| + \left|\delta^{II}\right| + \left|\delta^{III}\right| + \left|\delta^{IV}\right| \le 1. \tag{2.18}$$

The zero configurations are applied to complete the cycle period.

By introducing (2.14)-(2.17) in (2.18), after some manipulations, leads to the following equation

$$q \le \frac{\sqrt{3}}{2}\frac{\left|\cos\varphi_i\right|}{\cos\tilde{\beta}_i\cos\tilde{\alpha}_o}. \tag{2.19}$$

Equation (19) represents, at any instant, the theoretical maximum voltage transfer ratio, which is dependent on the output voltage and input current phase angles and the displacement angle of the input current vector. It is useful to note that, in the particular case of balanced supply voltages and balanced output voltages, the maximum voltage transfer ratio occurs when (2.19) is a minimum (i.e. when $\cos\tilde{\beta}_i$ and $\cos\tilde{\alpha}_o$ are equal to 1), leading to

$$q \le \frac{\sqrt{3}}{2}\left|\cos\varphi_i\right|. \qquad (2.20)$$

Assuming unity input power factor, (2.20) gives the well-known maximum voltage transfer ratio of matrix converters 0.866.

Using the SVM technique, the switching pattern is defined by the switching configuration sequence. With reference to the particular case of output voltage vector lying in sector 1 and input current vector lying in sector 1, the switching configurations selected are, in general, 0_1, 0_2, 0_3, +1, -3, -7, +9. It can be verified that there is only one switching configuration sequence characterized by only one switch commutation for each switching configuration change, that is 0_3, -3, +9, 0_1, -7, +1, 0_2. The corresponding general double-sided switching pattern is shown in Fig. 2.4.

The use of the three zero configurations leads to 12 switch commutations in each cycle period. It should be noted that the possibility to select the duty-cycles of three zero configurations gives two degrees of freedom, being $\delta_{01} + \delta_{02} + \delta_{03} = 1 - \delta_1 - \delta_3 - \delta_7 - \delta_9$. This two degrees of freedom can be utilized to define different switching patterns, characterized by different behaviour in terms of ripple of the input and output quantities. In particular, the two degrees of freedom might be utilized to eliminate one or two zero

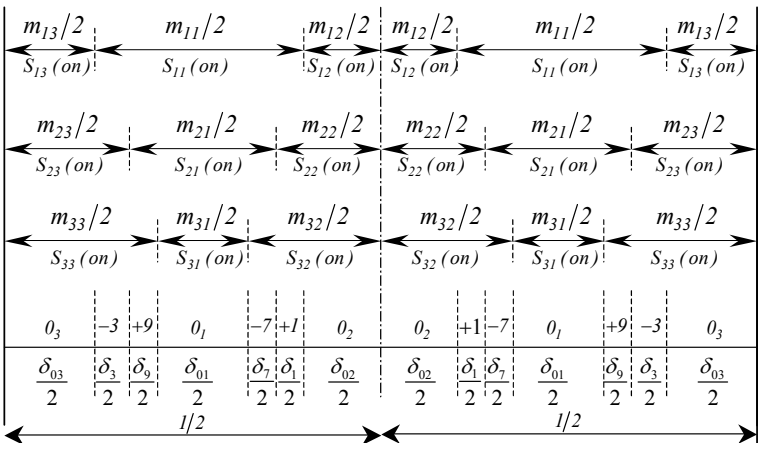

Fig. 2.4 – Double-sided switching pattern in a cycle period T_p.

configurations, affecting also the number of commutations in each cycle period.

In the following, reference will be made to 2 particular cases of SVM techniques. The first one, called "Symmetrical SVM" (SSVM), utilizes all the three zero configurations in each cycle period, with equal duty-cycles. As a consequence 12 switch commutations occur in each cycle period. The second one, called "Asymmetrical SVM" (ASVM), utilizes only one of the three zero configurations, that is the configuration located in the middle of each half of the switching pattern (configuration 0_1 in Fig. 2.4). In this way, the switches of one column (in this case the first one of Fig. 1) of the matrix converter do not change their state, and the number of switch commutations in each cycle period is reduced to 8 (S_{11} is always on, S_{12} and S_{13} are always off in Fig. 2.4).

2.4. New Duty-Cycle Space Vector Approach

A new and very efficient mathematical approach for the analysis of matrix modulation techniques can be developed by using the space vector notation, and introducing the concept of "duty-cycle space vector".

The three duty-cycles m_{11}, m_{12} and m_{13} in the first row of the modulation duty-cycle matrix, can be represented by the duty-cycle space vector $\overline{m}_1$, defined by the following transformation equation:

$$\overline{m}_1 = \frac{2}{3}\left(m_{11} + m_{12} e^{j\frac{2\pi}{3}} + m_{13} e^{j\frac{4\pi}{3}} \right). \tag{2.21}$$

Taking into account the constraint condition (2.4), the inverse transformations are

$$m_{11} = \frac{1}{3} + \overline{m}_1 \cdot e^{j0} \tag{2.22}$$

$$m_{12} = \frac{1}{3} + \overline{m}_1 \cdot e^{j\frac{2\pi}{3}} \tag{2.23}$$

$$m_{13} = \frac{1}{3} + \overline{m}_1 \cdot e^{j\frac{4\pi}{3}} \quad . \tag{2.24}$$

A similar transformation can be introduced for the second and third row of the modulation duty-cycles matrix (2.1), defining respectively $\overline{m}_2$ and $\overline{m}_3$. In general we can write:

$$\overline{m}_\ell = \frac{2}{3}\left(m_{\ell 1} + m_{\ell 2} e^{j\frac{2\pi}{3}} + m_{\ell 3} e^{j\frac{4\pi}{3}} \right) \qquad \ell = 1,2,3 \tag{2.25}$$

$$m_{hk} = \frac{1}{3} + \overline{m}_h \cdot e^{j(k-1)\frac{2\pi}{3}} \qquad h = 1,2,3,\ k = 1,2,3\,. \tag{2.26}$$

In order to explain the meaning of this new duty-cycle space vector approach, the geometrical representation of $\overline{m}_1$ in d-q plane will be discussed.

Taking the constraints (2.3) into account, it can be realized that all the acceptable values for $\overline{m}_1$ are inside a region, represented in Fig. 2.5 by the equilateral triangle ABC. In fact, the acceptable values for m_{11} are inside the region delimited by the two vertical parallel lines obtained by solving (2.22) for $m_{11} = 0$ and $m_{11} = 1$, respectively. In the same way, two regions

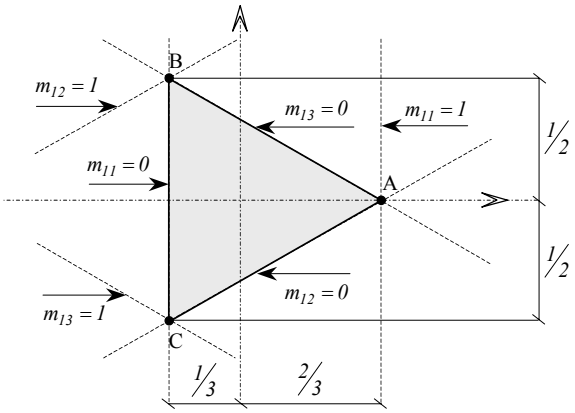

Fig. 2.5 – Geometrical representation of the validity domain for $\overline{m}_1$.

delimited by two parallel lines can be defined with reference to m_{12} and m_{13}. The intersection among the three regions lead to the triangular domain ABC of Fig. 2.5, which includes all the possible values for $\overline{m}_1$, and then any combination of m_{11}, m_{12} and m_{13}.

The position of the space vector $\overline{m}_1$ inside the triangle determines the number of switch commutations of S_{11}, S_{12} and S_{13} in a cycle period.

Switching patterns with four commutations, as shown in the first row of Fig. 2.4, are represented by values of $\overline{m}_1$ inside the triangle. Switching patterns with only two commutations are represented by values of $\overline{m}_1$ lying on the triangle sides, being one switch always off. In fact, each triangle side is defined by a null value of m_{11} or m_{12} or m_{13}. Switching patterns with no commutations, are represented by values of $\overline{m}_1$ coinciding with the triangle vertexes, being in this case two switch always off, and one switch always on.

The duty-cycle space vectors $\overline{m}_1$, $\overline{m}_2$ and $\overline{m}_3$ can be usefully employed, instead of the duty cycle matrix $\boldsymbol{m}$, in order to describe the switches state of the matrix converter in each cycle period. It should be noted that, using this notation, the three constraint conditions (2.4)-(2.6) are intrinsically satisfied.

Then, the input-output relationships (2.1) and (2.2) can be rewritten in the following form

$$\overline{v}_o = \frac{\overline{v}_i}{2}\left(\overline{m}_1^* + \overline{m}_2^* e^{j\frac{2\pi}{3}} + \overline{m}_3^* e^{j\frac{4\pi}{3}}\right) + \frac{\overline{v}_i^*}{2}\left(\overline{m}_1 + \overline{m}_2 e^{j\frac{2\pi}{3}} + \overline{m}_3 e^{j\frac{4\pi}{3}}\right) \quad (2.27)$$

$$\overline{i}_i = \frac{\overline{i}_o}{2}\left(\overline{m}_1 + \overline{m}_2 e^{j\frac{4\pi}{3}} + \overline{m}_3 e^{j\frac{2\pi}{3}}\right) + \frac{\overline{i}_o^*}{2}\left(\overline{m}_1 + \overline{m}_2 e^{j\frac{2\pi}{3}} + \overline{m}_3 e^{j\frac{4\pi}{3}}\right). \quad (2.28)$$

The previous equations suggest to define three new variables $\overline{m}_d$, $\overline{m}_i$, $\overline{m}_o$ as functions of $\overline{m}_1$, $\overline{m}_2$, $\overline{m}_3$, using the following direct transformation equations

$$\overline{m}_d = \frac{1}{3}\left(\overline{m}_1 + \overline{m}_2 e^{j\frac{2\pi}{3}} + \overline{m}_3 e^{j\frac{4\pi}{3}}\right) \quad (2.29)$$

$$\overline{m}_i = \frac{1}{3}\left(\overline{m}_1 + \overline{m}_2\, e^{j\frac{4\pi}{3}} + \overline{m}_3\, e^{j\frac{2\pi}{3}}\right) \tag{2.30}$$

$$\overline{m}_o = \frac{1}{3}\left(\overline{m}_1 + \overline{m}_2 + \overline{m}_3\right). \tag{2.31}$$

The quantities $\overline{m}_d$, $\overline{m}_i$, $\overline{m}_o$ may be considered as direct, inverse and zero component of the duty-cycle space vectors $\overline{m}_1$, $\overline{m}_2$ and $\overline{m}_3$.

The inverse transformation equations are:

$$\overline{m}_1 = \overline{m}_d + \overline{m}_i + \overline{m}_o \tag{2.32}$$

$$\overline{m}_2 = \overline{m}_d\, e^{j\frac{4\pi}{3}} + \overline{m}_i\, e^{j\frac{2\pi}{3}} + \overline{m}_o \tag{2.33}$$

$$\overline{m}_3 = \overline{m}_d\, e^{j\frac{2\pi}{3}} + \overline{m}_i\, e^{j\frac{4\pi}{3}} + \overline{m}_o \ . \tag{2.34}$$

Substituting (2.32) - (2.34) in (2.27) and (2.28) yields:

$$\overline{v}_o = \frac{3}{2}\overline{v}_i\, \overline{m}_i^* + \frac{3}{2}\overline{v}_i^*\, \overline{m}_d \tag{2.35}$$

$$\overline{i}_i = \frac{3}{2}\overline{i}_o\, \overline{m}_i + \frac{3}{2}\overline{i}_o^*\, \overline{m}_d \ . \tag{2.36}$$

The relationships (2.35) and (2.36) represent the input-output relationships of three-phase matrix converters in a very useful and compact form. A similar formalism for representing the input-output relationships of voltages and currents has been presented in [33].

2.5. Generalized Modulation Strategy

The problem of determining a modulation strategy is completely defined by solving with respect to $\overline{m}_d$ and $\overline{m}_i$ the following equations

$$\overline{v}_{o,ref} = \frac{3}{2}\overline{v}_i\, \overline{m}_i^* + \frac{3}{2}\overline{v}_i^*\, \overline{m}_d \tag{2.37}$$

$$\left(\overline{i}_o\, \overline{m}_i + \overline{i}_o^*\, \overline{m}_d\right) \cdot j\, \overline{\psi}_{ref} = 0 \tag{2.38}$$

being the phase angle of $\overline{\psi}_{ref}$ the desired phase angle for the input current space vector and $\overline{v}_{o,ref}$ the desired output voltage vector.

The first equation is clearly related to the output voltage control requirement, whereas the second equation is written so as to satisfy the required input power factor.

It can be noted that only the variables $\overline{m}_d$ and $\overline{m}_i$ appear in (2.37) and (2.38). As a consequence the variable $\overline{m}_o$ can assume any arbitrarily chosen value, without affecting the average value of the reference quantities.

The general solution of the system of equations (2.37) and (2.38), valid for any value of the parameter λ, is

$$\overline{m}_d = \frac{\overline{v}_{o,ref}\,\overline{\psi}_{ref}}{3\left(\overline{v}_i \cdot \overline{\psi}_{ref}\right)} + \frac{\lambda}{\overline{v}_i^{*}\,\overline{i}_o^{*}} \tag{2.39}$$

$$\overline{m}_i = \frac{\overline{v}_{o,ref}^{*}\,\overline{\psi}_{ref}}{3\left(\overline{v}_i \cdot \overline{\psi}_{ref}\right)} - \frac{\lambda}{\overline{v}_i^{*}\,\overline{i}_o} \quad . \tag{2.40}$$

The parameter λ, together with $\overline{m}_o$, yields three degrees of freedom, which can be utilized in defining any type of modulation strategy.

The general solution given in (2.39) and (2.40) includes all the already-known modulation strategies as particular cases.

As it is possible to see, the parameter λ can be utilized only if the phase angle of $\overline{i}_o$ is known in each cycle period. Here this parameter is not utilized and is set to zero, then (2.39) and (2.40) can be rewritten as:

$$\overline{m}_d = \frac{q}{3\,\cos\varphi_i}\, e^{j\alpha_o}\, e^{j\beta_i} \tag{2.41}$$

$$\overline{m}_i = \frac{q}{3\,\cos\varphi_i}\, e^{-j\alpha_o}\, e^{j\beta_i} \quad . \tag{2.42}$$

Taking into account (2.32) - (2.34), (2.41) and (2.42) leads to:

$$\overline{m}_\ell = \frac{2}{3} q \frac{\cos\left[\alpha_o - (\ell - 1)\frac{2\pi}{3}\right]}{\cos\varphi_i} e^{j\beta_i} + \overline{m}_o \qquad l = 1,2,3\,. \qquad (2.43)$$

Equation (2.43) allows the determination, in each cycle-period, of the values of the three duty-cycle space vectors $\overline{m}_1$, $\overline{m}_2$, $\overline{m}_3$, as function of the voltage transfer ratio q, the output voltage phase angle α_o, the input current phase angle β_i, and the input power factor $\cos\varphi_i$.

These equations can be analyzed using their geometrical representation in the d-q plane. The three quantities $\overline{m}_1$, $\overline{m}_2$ and $\overline{m}_3$ given in (2.43) lie on a segment of variable length, rotating and translating within the triangular domain as function of time, as represented in Fig. 2.6(a). The position of the three duty-cycle space vectors $\overline{m}_1$, $\overline{m}_2$ and $\overline{m}_3$ on the segment depends on the output voltage vector sector. The situation illustrated in Fig. 2.6(a) refers to output voltage and input current vectors lying in their corresponding sectors 1. The length of the segment depends on the voltage transfer ratio, the instantaneous input power factor, and the output voltage phase angle, whereas its orientation is given by the input current phase angle.

The position of any segment connecting the three duty-cycle space vectors

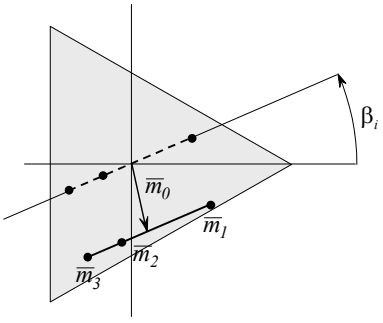

Fig. 2.6(a) – Geometrical representation of the segment connecting $\overline{m}_1$, $\overline{m}_2$ and $\overline{m}_3$.

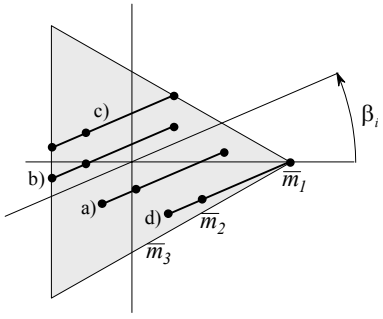

Fig. 2.6(b) – Geometrical representation of four typical positions of the segment connecting $\overline{m}_1$, $\overline{m}_2$ and $\overline{m}_3$.

can be arbitrarily changed by means of $\overline{m}_o$, with the constraint that it has to remain completely within the triangular region. The choice of $\overline{m}_o$ provides two degrees of freedom, affecting the modulation features in terms of maximum voltage transfer ratio, number of switch commutations and ripple of the input/output quantities.

For given values of α_o, β_i and φ_i, the maximum achievable value for the voltage transfer ratio depends on how long can be the segment without crossing the triangle boundary. The maximum length depends on the position of the segment within the triangle and, as a consequence, from the selected value of $\overline{m}_o$.

As already mentioned, the number of switch commutations in a cycle period depends on the position of $\overline{m}_1$, $\overline{m}_2$ and $\overline{m}_3$ with respect to the triangle boundaries and vertexes, and then once again on $\overline{m}_o$. Four different typical positions may occur, which are represented in Fig. 2.6(b).

When the segment is completely within the triangle (case a)) the values of the nine duty-cycles m_{hk} are within the interval [0,1]. Then 12 switch commutations occur in a cycle period. In the case b), $\overline{m}_3$ lies on the triangle boundary. Then $m_{31} = 0$ and, as a consequence, the number of switch commutations in the cycle period is reduced to 10, being the switch S_{31} always off.

In the case c), $\overline{m}_1$ and $\overline{m}_3$ lie both on the boundaries of the triangle leading to $m_{13} = 0$ and $m_{31} = 0$, with only 8 switch commutations in the cycle period.

The same number of switch commutations occur in case d) where $\overline{m}_1$ coincides with a vertex of the triangle. In this condition $m_{11} = 1$, $m_{12} = 0$ and $m_{13} = 0$, then the switches S_{12} and S_{13} are always off whereas the switch S_{11} is always on. These concepts will be discussed with further details in Chapter 3.

At last, it is worthy to note that different values of $\overline{m}_o$ yield the same average values for the input/output quantities in a cycle period, but they

determine different switching patterns and, as a consequence, different performance in terms of ripple.

Substituting (2.43) in (2.26), leads to:

$$m_{hk} = \frac{1}{3} + \frac{2}{3} q \frac{\cos\left[\alpha_o - (l-1)\frac{2\pi}{3}\right]\cos\left[\beta_i - (k-1)\frac{2\pi}{3}\right]}{\cos\varphi_i} + \overline{m}_o \cdot e^{j(k-1)\frac{2\pi}{3}} \quad (2.44)$$

where h=1,2,3 k=1,2,3.

This equation is a new and compact solution to the problem of determining the modulation law for matrix converters. Equation (2.44) may be considered also a direct generalization of the solution corresponding to the AV method and the optimum AV method.

2.6. Comparison of the Modulation Strategies

Any modulation strategy can be represented using the DCSV approach and analyzed from a new unitary point of view. In this way, a fair comparison can be carried out in terms of voltage limits, number of switch commutation, and ripple of the input/output quantities.

In order to do this it is sufficient to determine, for each modulation technique, the expression of $\overline{m}_o$, being $\overline{m}_d$ and $\overline{m}_i$ prefixed by the reference quantities, namely q, $\cos\varphi_i$, α_o and β_i. Then, by using (2.43) it is possible to evaluate the trajectories of the three duty-cycle space vectors $\overline{m}_1$, $\overline{m}_2$, $\overline{m}_3$, and the movement of the corresponding segment within the triangular domain. In Fig. 2.7 some examples are shown with reference to operating conditions characterized by input and output frequency of 50 Hz and 25 Hz respectively, with a voltage transfer ratio of 0.5.

A. Alesina-Venturini 1981

Substituting (2.7) in (2.25), and then the obtained equation in (2.31), leads to:

$$\overline{m}_o = 0\,. \quad (2.45)$$

The movement of the segment connecting $\overline{m}_1$, $\overline{m}_2$ and $\overline{m}_3$ is emphasized

in Fig. 2.7(a), whereas the trajectories of the three duty-cycle space vectors are shown in Figs. 2.7(b), (c) and (d) respectively.

Fig. 2.7(a) shows six numbered segments, which have been obtained in six successive time instants, equally spaced by 20 electrical degrees (with reference to the input quantities). The ends of these segments draw the trajectories of $\overline{m}_1$ and $\overline{m}_3$, as shown in Figs. 2.7(b) and 2.7(d), respectively. The numbered points in Figs. 2.7(b) – (d) refer to the corresponding segment positions of Fig 2.7(a).

In this modulation strategy the two degrees of freedom related to the choice of $\overline{m}_o$ are not utilized, then the segment substantially rotates around the origin of the axis. In this way the performance in terms of maximum voltage transfer ratio are very poor as emphasized in Fig. 2.11(a). In this figure the surface representing the maximum voltage transfer ratio is shown as function of the instantaneous values of α_o and β_i, with unity input power factor. Owing to the symmetry, the analysis has been restricted to values of α_o and β_i within the intervals $\left[0^o,120^o\right]$ and $\left[-30^o,90^o\right]$ respectively.

The lower and the higher values are 0.5 and 1, respectively. The lower value 0.5 determines the maximum voltage transfer ratio achievable in balanced sinusoidal operating conditions, as also shown by the trajectories of Fig. 2.7.

As far as the number of commutations are concerned, it can be noted that the trajectories of $\overline{m}_1$, $\overline{m}_2$ and $\overline{m}_3$ remain completely within the

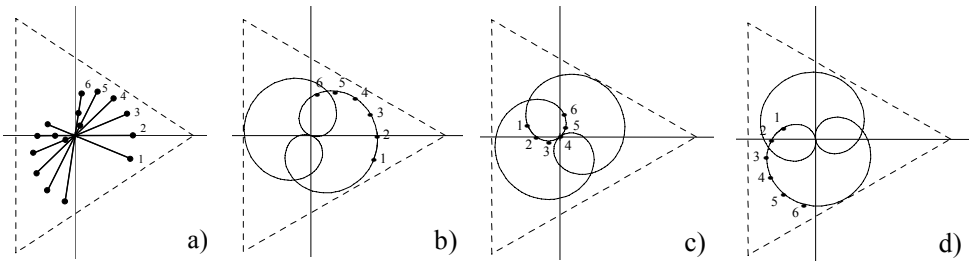

Fig. 2.7 – Segment position a), trajectory of $\overline{m}_1$ b), $\overline{m}_2$ c) and $\overline{m}_3$ d) obtained by using AV strategy with: $q = 0.5$, $f_1 = 50\,Hz$, $f_2 = 25\,Hz$.

boundary of the triangular region, without touching the triangle sides. As a consequence, using this modulation technique, 12 switch commutations occur in each cycle period.

It should be noted that the AV method does not provide any degree of freedom, then the performance in terms of ripple of the input/output quantities is intrinsically prefixed.

B. Alesina-Venturini 1989

Substituting (2.8) in (2.25) and then, the equation so obtained in (2.31), leads to:

$$\overline{m}_0 = \frac{q}{18}\left[- e^{j\beta_i}\left(e^{j3\alpha_o} + e^{-j3\alpha_o}\right) - \frac{1}{\sqrt{3}} e^{j4\beta_i} + \frac{7}{\sqrt{3}} e^{-j2\beta_i} \right]. \qquad (2.46)$$

As is possible to see, the presence of the zero component $\overline{m}_0$ of the duty-cycle space vectors determines a rotation and a translation of the segment in the d-q plane. This movement is emphasized in Fig. 2.8(a), whereas the trajectories of the three duty-cycle space vectors $\overline{m}_1$, $\overline{m}_2$ and $\overline{m}_3$, are shown in Figs. 2.8(b), (c) and (d), respectively. The maximum voltage transfer ratio can be sensibly improved owing to this particular choice of $\overline{m}_o$, as shown in Fig. 2.11(b). The lower and the higher values are 0.866 and 0.945 respectively. The increase of the lower value to 0.866 has to be considered a great advantage of this optimum AV method with reference to the basic AV method, despite of a small reduction of the higher value.

Also in this case, the trajectories of $\overline{m}_1$, $\overline{m}_2$ and $\overline{m}_3$ remain completely

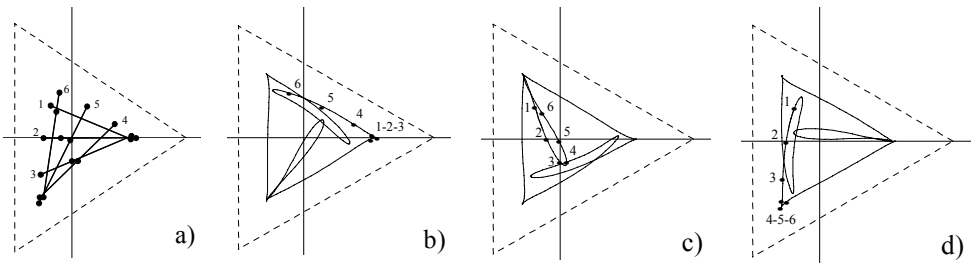

Fig. 2.8 – Segment position a), trajectory of $\overline{m}_1$ b), $\overline{m}_2$ c) and $\overline{m}_3$ d) obtained by using optimum AV strategy with: $q = 0.5$, $f_1 = 50\,Hz$, $f_2 = 25\,Hz$.

within the boundary of the triangular region, without touching the triangle sides, leading to 12 switch commutations in each cycle period.

Furthermore, as in AV method, the optimum AV method does not provide any degree of freedom, then the performance in terms of ripple of the input/output quantities is intrinsically prefixed.

C. SVM Technique

In order to achieve the expression of $\overline{m}_o$ for the SVM technique, reference is made to Tab. 2.1, Tab. 2.2 and (2.14)-(2.17). In the case of output voltage vector and input current vector both lying in their corresponding sectors 1, after some manipulations, it is possible to obtain the following equation

$$\overline{m}_0 = \frac{2q}{3\sqrt{3}\cos\varphi_i}\left[\sin\left(\tilde{\beta}_i - \tilde{\alpha}_o\right)e^{-j\frac{\pi}{3}} - \sin\left(\tilde{\beta}_i + \tilde{\alpha}_o\right)e^{j\frac{\pi}{3}}\right] + \\ + \frac{2}{3}\left(\delta_{01} + \delta_{02}\, e^{j\frac{2\pi}{3}} + \delta_{03}\, e^{j\frac{4\pi}{3}}\right). \qquad (2.47)$$

Owing to the presence of the last term in (2.47), the value of $\overline{m}_0$ depends on the particular selection of the zero configuration duty-cycles, leading to two degrees of freedom.

With simple considerations it is possible to demonstrate that these degrees of freedom correspond to the two degrees of freedom of the segment represented in Fig. 2.6(a), which can translate anywhere within the triangular region.

As a consequence, the SVM technique should not be considered a particular modulation strategy, but indeed a synthesis of all the possible modulation strategies. In fact, the AV and the optimum AV techniques can be derived by the SVM technique with an opportune choice of δ_{01}, δ_{02} and δ_{03}, in each cycle period.

The movement of the segment related to SSVM technique is illustrated in Fig. 2.9(a), whereas the trajectories of the three duty-cycle space vectors $\overline{m}_1$, $\overline{m}_2$ and $\overline{m}_3$ are shown in Figs. 2.9(b), (c) and (d), respectively. As is possible to see, comparing Figs. 2.8 and Figs. 2.9, the behaviour of the SSVM technique is quite similar to the behaviour of the optimum AV method. The

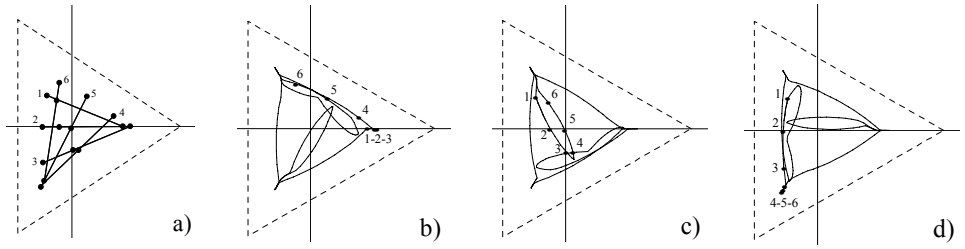

Fig. 2.9 – Segment position a), trajectory of $\overline{m}_1$ b), $\overline{m}_2$ c) and $\overline{m}_3$ d) obtained by using SSVM strategy with: $q = 0.5$, $f_1 = 50\,Hz$, $f_2 = 25\,Hz$.

segment moves, without discontinuity, completely within the triangular region, leading to 12 switch commutations in each cycle period.

The movement of the segment obtained using the ASVM technique is illustrated in Fig. 2.10(a), whereas the trajectories of the three corresponding duty-cycle space vectors $\overline{m}_1$, $\overline{m}_2$ and $\overline{m}_3$ are shown in Figs. 2.10(b), (c) and (d), respectively. This kind of movement is quite different from that obtained using SSVM. The segment rotates around one of its ends, cantered on a vertex of the triangle, which is determined by the actual sector of the input current vector. Then, the position of the segment instantaneously changes as the input current vector crosses the sector boundary. In this way, 8 switch commutations occur in each cycle period.

With regard to the voltage transfer ratio, it is easy to demonstrate, with geometrical consideration, that the maximum voltage transfer ratio achievable with optimal positioning of the segment within the triangular region equals the maximum voltage transfer ratio of the SVM technique

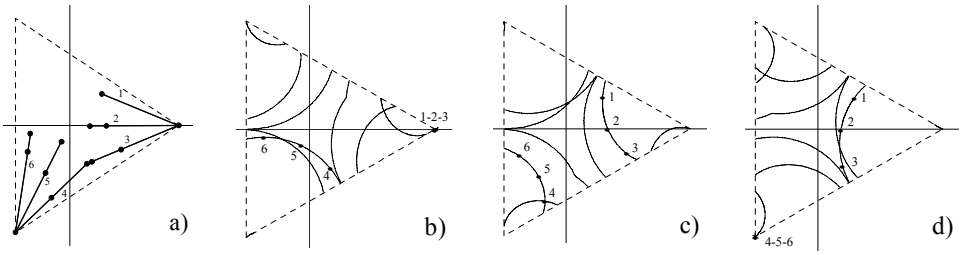

Fig. 2.10 – Segment position a), trajectory of $\overline{m}_1$ b), $\overline{m}_2$ c) and $\overline{m}_3$ d) obtained by using ASVM strategy with: $q = 0.5$, $f_1 = 50\,Hz$, $f_2 = 25\,Hz$.

shown in (2.19). Then, from this point of view, the SVM technique can be considered the optimal solution.

This result is clearly emphasized in Fig. 2.11(c). The lower and the higher values are 0.866 and 1.155 respectively. The lower value is the same as in optimum AV, but the higher value is sensibly increased. This feature is very important with reference to the possibility to apply over-modulation techniques.

Finally, it should be noted that the SVM technique, owing to the 2 degrees of freedom related to the three zero configuration duty-cycles, allows different switching patterns to be used and, as a consequence, different performance in terms of the RMS value of the output currents and input voltages ripple to be obtained.

2.7. Conclusion

The analysis of the three-phase to three-phase matrix converter modulation strategies represents a hard task. Some solutions, proposed in the literature and using different theoretical approaches, have been here briefly reviewed.

A new representation of the switches state of the matrix converter, based on the Duty-Cycle Space Vector approach, has been presented. Using this approach it has been demonstrated that three degrees of freedom are available in defining the modulation law, allowing the control of the instantaneous values of the output voltages and input power factor. The

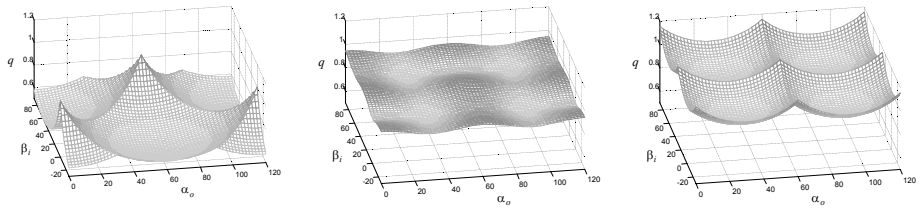

Fig. 2.11 – Surfaces representing the instantaneous maximum voltage transfer ratio q as a function of α_o and β_i for unity input power factor.

a) AV method, b) optimum AV method, c) SVM method.

degrees of freedom reduce to only two if no information about the output currents is used.

A compact and general solution to modulation problem of the matrix converter, which includes the already-established modulation strategies as particular cases, has been derived.

A useful geometrical representation of the duty-cycle space vector has been presented. It provides a unitary point of view and simplifies the comparison between different modulation strategies in terms of maximum voltage transfer ratio, switching frequency and ripple of the input/output quantities.

Owing to its intrinsic two degrees of freedom, SVM technique represents the general solution of the matrix converter modulation problem, and can be considered the best solution for the possibility to achieve the highest voltage transfer ratio and to optimize the switching pattern through a suitable use of the zero configurations.

Chapter 3

Advanced Modulation Strategies

Abstract

The performance of matrix converters is strictly related to the modulation strategy adopted to control the state of the switches. In the first part of this chapter a novel modulation strategy, based on the measurement of the output currents, is presented and discussed. The proposed strategy allows obtaining sinusoidal input and output currents, like the well-known Space Vector Modulation or Alesina-Venturini Modulation. However, compared to those modulation strategies, it requires a lower number of switch commutations for cycle period, thus leading to a sensible reduction of the converter switching losses and of the effects related to the switching dead time. Furthermore, the maximum voltage transfer ratio can be preserved.

In the second part of the chapter an analytical approach to predict the current ripple in an inductive load fed by a matrix converter controlled with Space Vector Modulation is presented. The analysis aims at determining the

optimal modulation strategy that minimizes the rms value of the load current ripple. The minimization procedure is based on the analysis of the locus described by the current ripple in the d-q reference frame. As a result, a set of equations which allows the on-line calculation of the optimal SVM switching pattern is found. It has been verified that it is possible to obtain a current ripple lower than that of traditional SVM strategies, and with a reduced number of commutations. Experimental results are provided to confirm the theoretical approach.

3.1. Introduction

While the main features of the modulation theory for VSI are well-established, the research on the modulation strategies for matrix converters are still in progress.

Several solutions have been presented in Chapter 2. Each of them shows different features in terms of number of switch commutations in a cycle period and utilization of the input voltage.

To discuss this issue, it is convenient to introduce the concept of Branch Switch Overs (BSOs). The number of BSO of a branch is defined as the number of its state changes in a cycle period.

The voltage transfer ratio of Alesina and Venturini's original theory, by means of third harmonic injection techniques, can be increased up to 0.866, a value which represents an intrinsic limitation of three-phase matrix converters with balanced supply voltages [1].

The Optimum Alesina-Venturini method requires 12 BSOs per cycle period [2].

The Scalar Control Algorithm proposed in [31], based on a different approach, leads to similar performance.

In [34] a double-sided SVM strategy with 9 BSOs was proposed. Later, in [35], it was shown that a proper selection of the switch sequence could reduce the number of BSOs from 9 to 8 without deteriorating the performance of the modulation strategy. Finally, in [36] a modified SVM strategy was proposed in order to reduce the switch losses. This strategy can be applied only for voltage transfer ratio lower than 0.5.

A comparison between different types of modulation strategies can be

found in [7], [37]-[39], showing that the "indirect approach" for matrix converter, initially preferred for its simplicity, is now partially replaced by modern direct theories, that allow an immediate understanding of the modulation process, without the need of a fictitious DC link.

The general and complete direct solution of the control problem of matrix converters, described in Chapter 2, was originally presented in [7]. This solution is based on the Duty-Cycle Space Vector (DCSV) approach, which consists in the representation of the switch states by means of space vectors.

This approach has the advantage to emphasize all the parameters affecting the performance of the modulation strategy, such as the common mode voltage and the output currents.

It should be noted that the modulation techniques cited above do not utilise any information about the output currents. The main reason is that, at a first glance, a modulation strategy avoiding the use of current sensors, is desirable.

However, in several applications involving electric motor drives, the load currents must be monitored and directly controlled. In these cases, the current sensors are required without regard to the type of converter feeding the motor, and the current measurement can be used also for improving the performance of the modulation strategy.

Exploiting the features of the DCSV approach, a novel modulation strategy based on the measurement of the output currents is proposed and analysed in the first part of this chapter. Compared with the well-established strategies, its main advantage is the reduction of the number of BSOs in a cycle period from 8 to 6, thus decreasing the switch losses and the effects of the switch dead time [40],[41].

Furthermore, this advantage is obtained without deteriorating the quality of the input/output voltages and currents and preserving the maximum voltage transfer ratio.

3.2. Duty-Cycle Space Vector Approach

The matrix converter input-output relationships can be easily expressed introducing the concept of "Duty-Cycle Space Vector" exposed in Chapter 2. According to this principle, the duty-cycles m_{11}, m_{12} and m_{13} of the three

switches S_{11}, S_{12}, S_{13} of the first branch of the converter shown in Fig. 1.1 can be represented by the space vector $\overline{m}_1$ given by (2.1).

The geometrical representation of $\overline{m}_1$ in the d-q plane shows that all the acceptable values for $\overline{m}_1$ are inside the region represented in Fig. 3.1 by the equilateral triangle ABC. It can be noted that the distances between $\overline{m}_1$ and the triangle sides directly represent the values of the duty-cycles m_{11}, m_{12} and m_{13}.

The position of the space vector $\overline{m}_1$ inside the triangle determines the number of switch commutations of S_{11}, S_{12} and S_{13} in a cycle period, and consequently defines the number of BSOs of the first branch.

Furthermore, modern modulation strategies are usually "double-sided" or "symmetrical", meaning that the turn-on sequence of the switches is completed in the first half of the cycle period and it is repeated with inverse order in the second half of the cycle period. In such a way, useless commutations can be avoided, if the switch state at the beginning of the current cycle period is equal to the switch state at the end of the previous cycle period.

If $\overline{m}_1$ lies inside the triangle, all the duty-cycles are expected to be greater than zero and the corresponding number of BSOs for a double-sided turn-on sequence of the switches is 4. For instance, a possible symmetrical sequence for the switches S_{11}, S_{12} and S_{13} concerning the first output phase could be

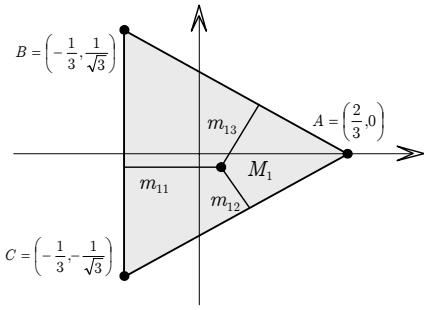

Fig. 3.1 – Graphical meaning of the duty-cycle space vector $\overline{m}_1$.

$S_{11} \rightarrow S_{12} \rightarrow S_{13} \rightarrow S_{12} \rightarrow S_{11}$, where each arrow corresponds to one BSO.

If $\overline{m}_1$ lies on a triangle side, then at least one duty-cycle among m_{11}, m_{12}, m_{13} is zero. This means that the corresponding switch never turns on during the cycle period and the number of BSOs reduces to 2.

Finally, if $\overline{m}_1$ is on a triangle vertex, two duty-cycles are zero. In this case the number of BSOs is zero, because the state of the branch never changes during the cycle period.

The same considerations can be carried out for the second and the third branch of the converter in Fig. 1.1, introducing the duty-cycle space vectors $\overline{m}_2$ and $\overline{m}_3$ respectively. The number of BSOs can be derived in general form as shown in Tab. 3.1.

3.3. Generalized Modulation Strategy

The problem of determining a modulation strategy is completely defined by (2.39) and (2.40), here reported for convenience:

$$\overline{m}_d = \frac{\overline{v}_{o,ref}\,\overline{\psi}_{ref}}{3\left(\overline{v}_i \cdot \overline{\psi}_{ref}\right)} + \frac{\lambda}{\overline{v}_i^{*}\,\overline{i}_o^{*}} \tag{2.39'}$$

$$\overline{m}_i = \frac{\overline{v}_{o,ref}^{*}\,\overline{\psi}_{ref}}{3\left(\overline{v}_i \cdot \overline{\psi}_{ref}\right)} - \frac{\lambda}{\overline{v}_i^{*}\,\overline{i}_o} \tag{2.40'}$$

being the phase angle of $\overline{\psi}_{ref}$ the desired phase angle for the input current space vector and $\overline{v}_{o,ref}$ the desired output voltage vector.

The parameter λ together with $\overline{m}_o$ yield three degrees of freedom, which can be utilized in defining any type of modulation strategy.

After the calculation of $\overline{m}_d$ and $\overline{m}_i$ by means of (2.39)-(2.40), (2.32)-(2.34)

TABLE 3.1 – NUMBER OF BSOS OF THE K-TH BRANCH FOR A DOUBLE-SIDED SWITCHING PATTERN.

Position of $\overline{m}_k$ (k=1,2,3)	Number of BSOs
Inside the triangle	4
On a triangle side	2
On a triangle vertex	0

can be used to determine $\overline{m}_1$, $\overline{m}_2$ and $\overline{m}_3$. As is possible to see, the parameter λ can be utilized as a degree of freedom only if the phase angle of $\bar{i}_o$ is known in each cycle period, otherwise it should be set to 0.

Finally, from $\overline{m}_1$, $\overline{m}_2$ and $\overline{m}_3$, one obtains the duty-cycles of the matrix converter switches, which can be used as input commands for the converter, by means of (2.26).

Taking (2.39) and (2.40) into account, (2.32) - (2.34) lead to:

$$\overline{m}_k = \frac{2}{3}\frac{\overline{v}_{o,ref}\cdot e^{j(k-1)\frac{2\pi}{3}}}{\overline{v}_i\cdot\overline{\psi}_{ref}}\overline{\psi}_{ref} + j\frac{2\lambda}{v_i^2\, i_o^2}\left[\bar{i}_o\cdot j\, e^{j(k-1)\frac{2\pi}{3}}\right]\overline{v}_i + \overline{m}_0 \qquad k=1,2,3. \quad (3.1)$$

Equation (3.1) can be rewritten in a more compact form as follows:

$$\overline{m}_k = \overline{A}_k + \lambda\,\overline{B}_k + \overline{m}_o \quad (3.2)$$

where

$$\overline{A}_k = \frac{2}{3}\frac{\overline{v}_{o,ref}\cdot e^{j(k-1)\frac{2\pi}{3}}}{\overline{v}_i\cdot\overline{\psi}_{ref}}\overline{\psi}_{ref} \quad (3.3)$$

$$\overline{B}_k = j\frac{2}{v_i^2\, i_o^2}\left[\bar{i}_o\cdot j\, e^{j(k-1)\frac{2\pi}{3}}\right]\overline{v}_i\,. \quad (3.4)$$

As can be seen in (3.3) - (3.4), $\overline{A}_k$ and $\overline{B}_k$ can be calculated using reference and measured quantities.

Equation (3.1), which allows the determination of the values of the three duty-cycle space vectors $\overline{m}_1$, $\overline{m}_2$, $\overline{m}_3$ in each cycle-period, can be analyzed using a geometrical representation in the d-q plane.

Assuming $\lambda = 0$, a value implicitly adopted for defining the modulation laws in [1]–[6], [34]-[39] the three quantities $\overline{m}_1$, $\overline{m}_2$ and $\overline{m}_3$ lie on a line segment. The segment length depends on the voltage transfer ratio, the instantaneous input power factor, and the output voltage phase angle, whereas its orientation is given by the input current phase angle.

The line segment can be arbitrarily moved within the triangle by varying

$\overline{m}_o$. This provides two degrees of freedom, affecting the maximum voltage transfer ratio, the total number of BSOs in a cycle period and the ripple of the input/output quantities. Four typical positions can be defined for the segment, already shown in Fig. 2.6(b):

a) the line segment is completely inside the triangle. In this case the total number of BSOs is 12 (4 BSOs for each branch);

b) one end point of the line segment lies on a triangle side. In this case the total number of BSOs is 10 (2 BSOs for one branch and 4 BSOs for the others);

c) both the end points of the line segment lie on triangle sides. The total number of BSOs is 8 (two branches present 2 BSOs and the other one presents 4 BSOs);

d) one end point of the line segment coincides with a triangle vertex. The total number of BSOs is 8 (one branch does not present any BSO, each one of the others presents 4 BSOs).

These results are summarised in Tab. 3.2.

It is important to note that the already-known modulation strategies can be reviewed according to the DCSV approach. For instance, Optimal Alesina-Venturini Modulation Strategy and the particular type of SVM that uses 3 zero vectors belong to case a) and present 12 BSOs.

The SVM that uses 2 zero vectors belongs to case b) and presents 10 BSOs. The SVM that uses 1 zero vector belongs to case c) or d) and presents 8 BSOs.

3.4. Modulation Strategy with Minimum BSOs

In this paragraph, a novel approach, that makes use of the parameter λ in order to reduce the total number of BSOs in a cycle period, is discussed. As

TABLE 3.2
TOTAL NUMBER OF BSOS FOR DOUBLE-SIDED SWITCHING PATTERN WITH REFERENCE TO FIG. 3.1

Case	Total number of BSOs
a)	12
b)	10
c)	8
d)	8

is possible to see from (2.39) and (2.40), if the phase angle of $\bar{i}_o$ is known in each cycle period, the parameter λ can be utilized as a further degree of freedom. In particular, as is possible to see from (3.1), the parameter λ moves $\overline{m}_1$, $\overline{m}_2$ and $\overline{m}_3$ along straight lines that are perpendicular to the input voltage space vector. It will be shown that, with an opportune selection of the value of the parameters λ and $\overline{m}_0$, it is always possible to move one duty-cycle space vector to a triangle vertex and at least another one to a triangle side.

Thus the total number of BSOs in a cycle period is reduced to only 6. In this way a significant reduction of the switching frequency with respect to the already-known modulation strategies is achieved.

Here, the basic principle of the modulation strategy is summarised with reference to the example shown in Fig. 3.2.

The value of $\overline{m}_o$ can be selected in order to move the segment so that one of its ends coincides with one vertex of the triangle, defined on the basis of the input current direction. In this way one of the duty-cycles space vector ($\overline{m}_1$ in the example) is fully determined, because its position is known.

Starting from an initial null value of λ and varying the value of this parameter, $\overline{m}_2$ and $\overline{m}_3$ migrate from their initial positions along two straight lines (r and s). By an appropriate selection of $\overline{m}_o$, it is possible to keep the

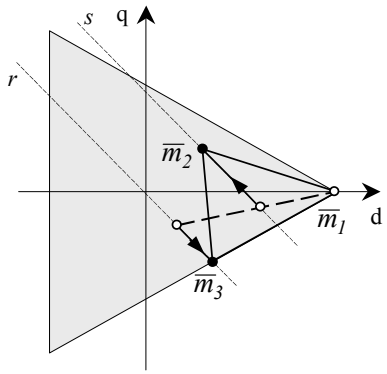

Fig.3.2 – Example of migration of $\overline{m}_1$, $\overline{m}_2$ and $\overline{m}_3$ due to a non-null value of λ.

position of $\overline{m}_1$ unchanged for any value of λ. Thus the values of λ bringing $\overline{m}_2$ or $\overline{m}_3$ on a triangle side can be found. From a geometrical point of view, this can be done finding the six values of λ corresponding to the intersections between the straight lines *r* and *s*, expressed in a parametric form, with the straight lines to which the triangle sides belong.

Among these six values, let λ_p be the minimum among the positive values and λ_n the maximum among the negative ones. It is worth noting that values of λ external to the interval $[\lambda_n, \lambda_p]$ lead $\overline{m}_2$ or $\overline{m}_3$ out of the triangle, which represents the validity domain.

To reduce the number of BSOs, λ can assume indifferently the values λ_n or λ_p. Once the values of λ and $\overline{m}_o$ are defined, it is possible to determine $\overline{m}_2$ and $\overline{m}_3$, thus giving the complete solution of the modulation problem with only 6 BSOs.

The algorithm for the selection of λ and $\overline{m}_o$ in the general case is presented in Appendix A.

3.5. Simulation Results

To verify the analytical approach, the behaviour of the proposed modulation strategy has been tested with numerical simulation for a system composed by a non-ideal supply, an input L-C filter and a matrix converter feeding a three-phase symmetrical R-L passive load. The basic scheme of the system is shown in Fig. 3.3 and the values of the system parameters are reported in Tab. 3.3.

The behaviour of the proposed modulation strategy has been also compared with some well-established modulation strategies based on SVM.

Figs. 3.4, 3.5 and 3.6 represent the waveform of the input voltage (a), the line current (b) and the output current (c) for three different modulation strategies, namely the SVM that uses one zero vector placed at the beginning of the cycle period (8 BSOs), the SVM that uses two zero vectors placed at the beginning and in the middle of the switching period (10 BSOs), and the new modulation strategy (6 BSOs). The simulations have been carried out for

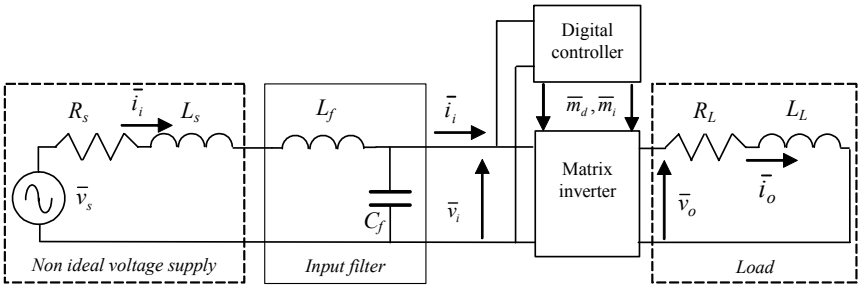

Fig. 3.3 - Basic matrix converter scheme using the space vector notation.

a cycle period T_p of 200 μs, that is generally sufficient for the implementation of the control algorithm.

As can be seen, the new modulation strategy determines practically the same current and voltage ripple as the SVM with one zero vector, while the SVM with two zero vectors performs better than the other modulation techniques.

To make a fair comparison, the cycle period should be changed in order to cause the same BSOs per second for each modulation strategy. As a consequence, a cycle period of 250 μs has been assumed for the SVM with two zero vectors, while a cycle period of 150 μs has been used for the new modulation strategy. The behaviour of these modulation strategies is shown in Fig. 3.7 and 3.8 respectively. The cycle period for the SVM with one zero vector has been kept unchanged.

As can be seen, although the new modulation has only 6 BSOs, its performance is comparable with the SVM with 10 BSOs, and is better than the SVM with 8 BSOs.

TABLE 3.3
SYSTEM PARAMETERS

Supply
V_S(rms) = 220 V, $\omega_S = 2\pi$ 50 rad/s, $R_S = 0.25\ \Omega$, L_S=0.4 mH
Filter
$L_f = 0.6$ mH, $C_f = 10.0$ μF
Load
$R_l = 10\ \Omega$, $L_l = 20$ mH, $\omega_o = 2\pi$ 25 rad/s

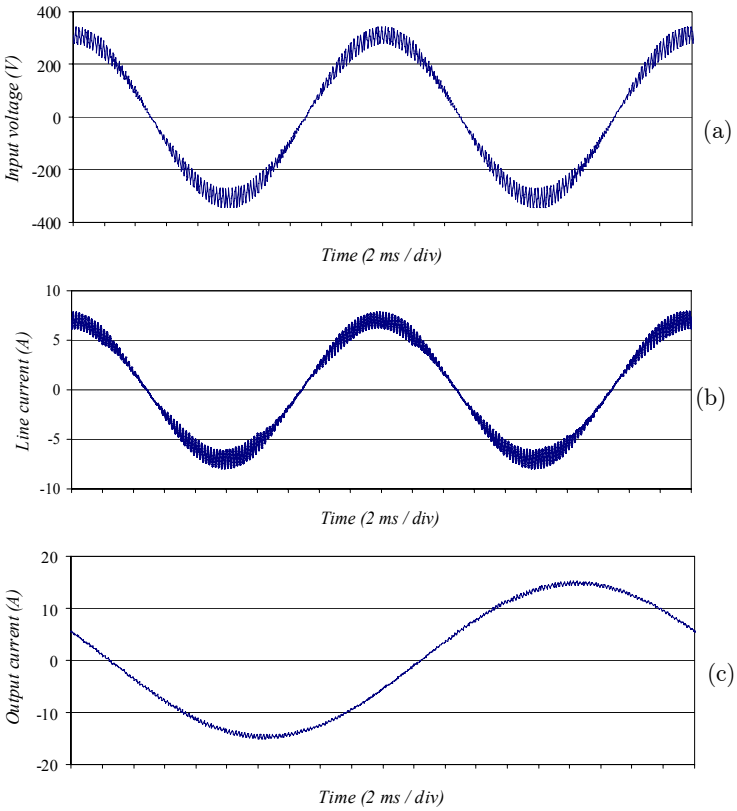

Fig. 3.4 - SVM with one zero vector placed at the beginning of the cycle period (8 BSOs). Cycle period of 200 μs. (a) input voltage, (b) line current, (c) output current.

Furthermore, the reduction of the number of BSOs allows to limit the effects related to the switch dead-time.

3.6. Preliminary Conclusion

A new modulation strategy for matrix converters, based on the output current sensing and characterized by only 6 BSOs for cycle period, has been presented. The reduced number of BSOs leads to a sensible reduction of the converter switching losses and of the effects related to the switch dead time, without deteriorating the quality of the input/output voltages and currents.

The modulation strategy has been developed using the Duty-Cycle Space

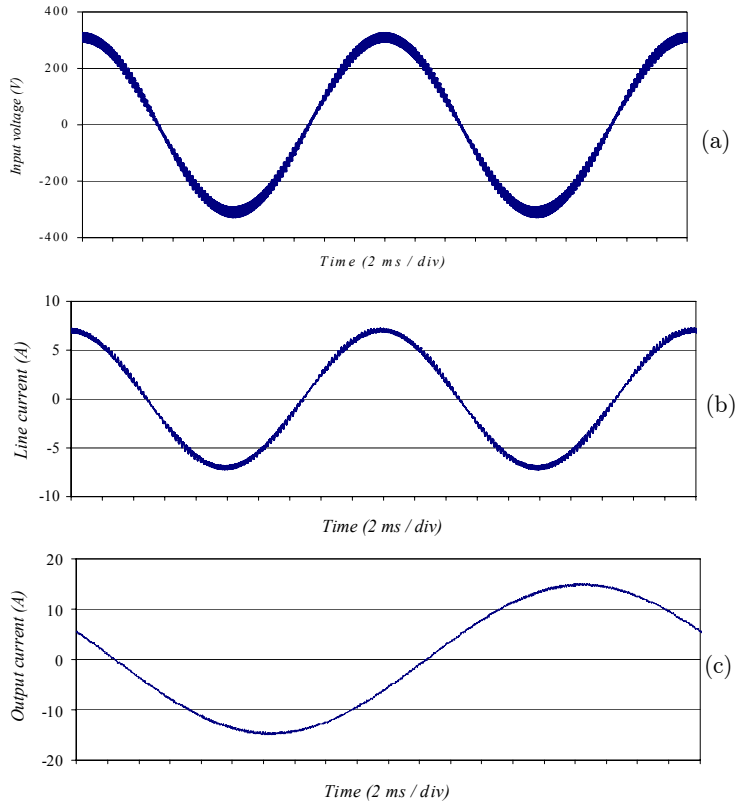

Fig. 3.5 - SVM with two zero vectors placed at the beginning and at the middle of the cycle period (10 BSOs). Cycle period of 200 μs. (a) Input voltage, (b) line current, (c) output current.

Vector Theory, which allows, through a simple and direct geometrical representation, an immediate comprehension of the modulation basic principles.

The performance of the new modulation strategy and of the well-known SVM, in terms of ripple of input and output quantities, has been analyzed by means of realistic numerical simulations. The comparison has been carried out assuming either the same cycle period or the same switching frequency. The obtained results clearly emphasize the effectiveness of the proposed modulation strategy.

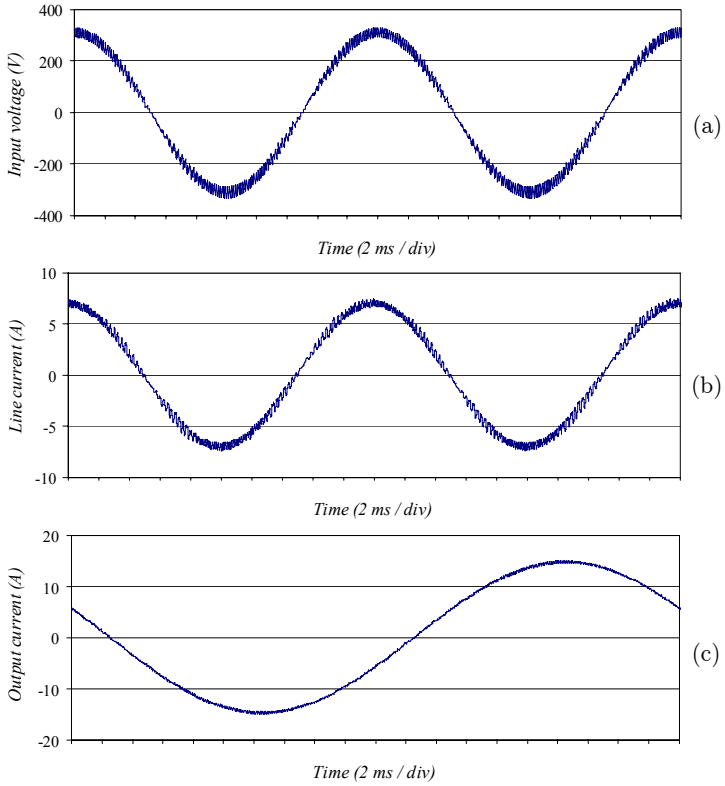

Fig. 3.7 - SVM with two zero vectors placed at the beginning and at the middle of the cycle period (10 BSOs). Cycle period of 250 μs. (a) Input voltage, (b) line current, (c) output current.

3.7. Optimisation of SVM: an Overview

In Chapter 2 a direct approach for SVM has been presented. This algorithm allows balanced and sinusoidal output voltages to be generated, even under unbalanced non-sinusoidal supply conditions. The algorithm is based on the instantaneous space vector representation of input and output voltages and currents. It analyses all the possible switching configurations available in three-phase MCs, and does not need the concept of a virtual DC link.

Furthermore, the arrangement of the three zero voltage vectors of MCs in

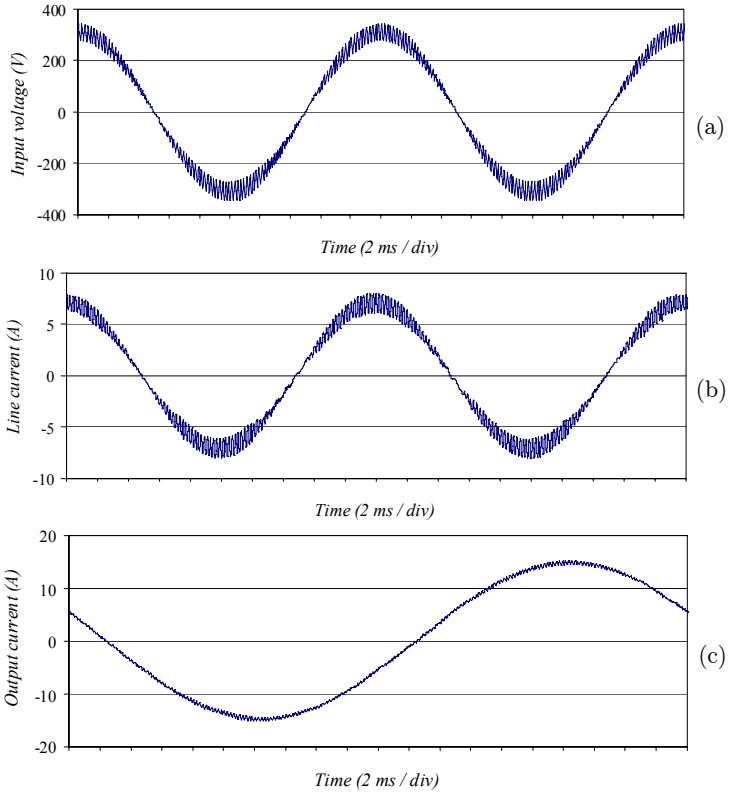

Fig. 3.6 - New modulation strategy (6 BSOs). Cycle period of 200 μs. (a) Input voltage, (b) line current, (c) output current.

the switching pattern offers some degrees of freedom that the designer can usefully utilize to improve the modulation strategy.

The remaining paragraphs of this chapter will discuss the relationship existing between the rms value of the current ripple and the arrangement of the zero voltage vectors. In fact, a widely-used method to evaluate the relative merits of different modulation techniques is to calculate the rms value of the load current ripple, which is strongly related to torque ripple and motor heating.

Finally a method for predicting the minimum rms value of the load current ripple in each cycle period is presented. The result of the analysis consists of very simple equations, which can be used in digital control systems for the on-line implementation of the optimal modulation technique.

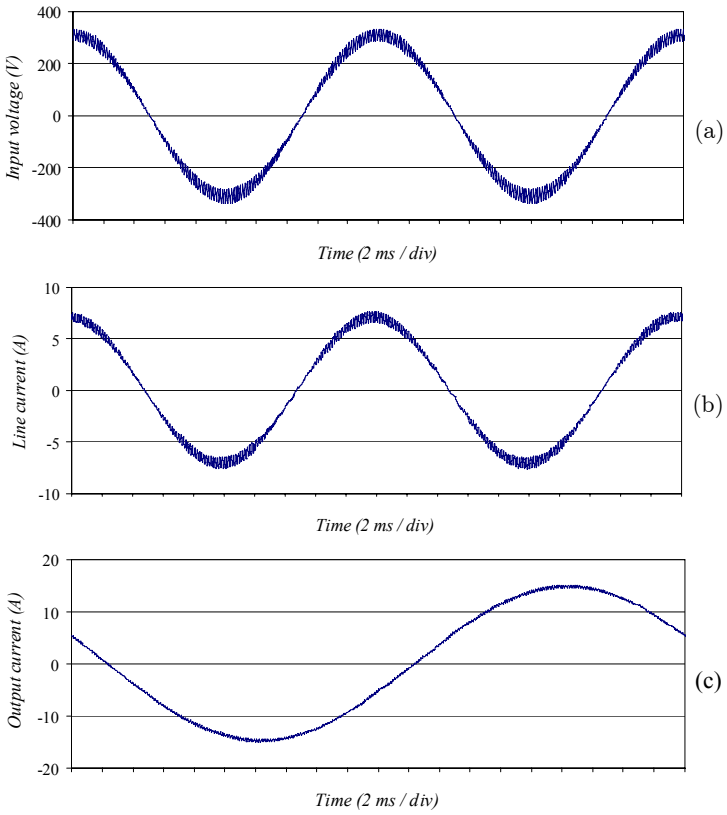

Fig. 3.8 - New modulation strategy (6 BSOs). Cycle period of 150 μs. (a) Input voltage, (b) line current, (c) output current.

This technique produces a current ripple lower than that of traditional SVM strategies for MCs and, in operating conditions with high values of the modulation index, it produces also a reduction of the number of commutations.

3.8. SVM for MCs

A. Basic Principles

The SVM algorithm for MCs is able to synthesize the reference output voltage vector $\overline{v}_{o,ref}$ and to control the phase angle of the input current vector selecting 4 non-zero configurations, applied for suitable time intervals

within the cycle period T_p. The three zero configurations available in MCs are applied to complete T_p.

Therefore, the reference output voltage can be written as follows:

$$\overline{v}_{o,ref} = \delta_1\overline{v}_1 + \delta_2\overline{v}_2 + \delta_3\overline{v}_3 + \delta_4\overline{v}_4 \tag{3.5}$$

where $\overline{v}_1$, $\overline{v}_2$, $\overline{v}_3$ and $\overline{v}_4$ are the output voltage vectors corresponding to the 4 selected configurations, and δ_1, δ_2, δ_3 and δ_4 are the duty-cycles, defined as

$$\delta_k = \frac{T_k}{T_p},\ k=1,2,3,4. \tag{3.6}$$

In (3.6), T_1, T_2, T_3 and T_4 are the time intervals of application of $\overline{v}_1$, $\overline{v}_2$, $\overline{v}_3$ and $\overline{v}_4$.

Once δ_1, δ_2, δ_3 and δ_4 are found, it is necessary to define the switching pattern, namely the turn-on and turn-off sequence of the switches.

B. Degrees of freedom in the switching patterns

It is a general principle that, once the reference output voltage vector and the input current displacement angle are given, the SVM univocally determines the switching pattern. In fact, among all possible switching sequences involving $\overline{v}_1$, $\overline{v}_2$, $\overline{v}_3$, $\overline{v}_4$ and the three zero vectors, there is only one commutation sequence characterized by only one switch commutation for each switching configuration change.

The SVM algorithm can be simplified to some extent taking advantage of its symmetries if the *d-q* plane is divided into 6 sectors for the output voltage vectors and the input current vectors as shown in Figs. 2.2(a)-(b). Hence, in the following, the input voltage vector and the reference output voltage vector are assumed in sector 1. In addition it is assumed that the goal of the control system is to keep the input current in phase with the input voltage vector, leading to unity input power factor.

Fig. 3.9 shows the switching sequence corresponding to the case of Fig. 2.2(a)-(b). As can be seen, the use of the three zero configurations leads to 12 switch commutations in each cycle period. It should be noted that the possibility to select the duty-cycles of three zero configurations gives only two

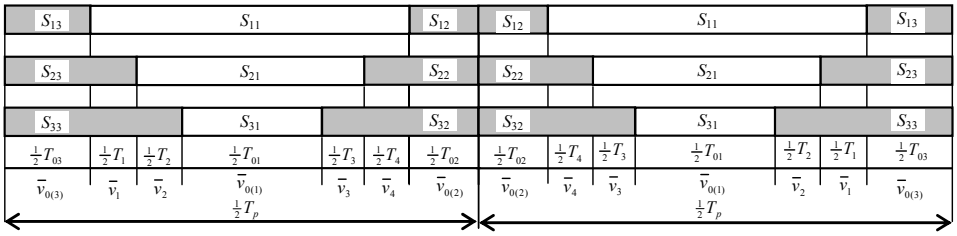

Fig. 3.9 – Double-sided switching pattern in a cycle period T_p, with reference to the case shown in Fig. 2.

degrees of freedom, being

$$\delta_{01} + \delta_{02} + \delta_{03} = 1 - \delta_1 - \delta_2 - \delta_3 - \delta_4 \tag{3.7}$$

where δ_{01}, δ_{02} and δ_{03} are the duty-cycles of the 3 zero voltage vectors $\bar{v}_{0(1)}$, $\bar{v}_{0(2)}$ and $\bar{v}_{0(3)}$. These two degrees of freedom will be used to define different switching patterns, characterized by different behaviour in terms of ripple of the input and output quantities. The two degrees of freedom might be utilized also to eliminate one or two zero configurations, affecting also the number of commutations in each cycle period.

In the following, the switching frequency f_s is defined as the total number of BSOs per second.

The traditional SVM strategies considered in this chapter and their switching frequencies are reported in Tab. 3.4.

Strategies 1-3 are characterized by only one zero configuration for each half of the switching pattern. Using these strategies the number of switch commutations in each cycle period is 8. A particular case is Strategy 1, which uses only the zero configuration located in the middle of each half of the switching pattern (vector $\bar{v}_{0(1)}$ in Fig. 3.9). In this way, the switches of one column (in this case the first one of Fig. 1.1) of the MC do not change their state (S_{11} is always on, S_{12} and S_{13} are always off in Fig. 3.3).

Strategies 4–6 use two zero configurations, determining 10 commutations in a cycle period.

Finally, Strategy 7 is characterized by the fact that all zero configurations are used with equal duty-cycles. As a consequence, 12 switch commutations

TABLE 3.4 – STRATEGIES FOR SVM

Strategy number	Defining equation	Switching frequency
1	$\delta_{02} = \delta_{03} = 0$	$f_s = 8/T_p$
2	$\delta_{01} = \delta_{03} = 0$	$f_s = 8/T_p$
3	$\delta_{01} = \delta_{02} = 0$	$f_s = 8/T_p$
4 (Asymmetrical)	$\delta_{02} = \delta_{03}, \quad \delta_{01} = 0$	$f_s = 10/T_p$
5	$\delta_{01} = \delta_{03}, \quad \delta_{02} = 0$	$f_s = 10/T_p$
6	$\delta_{01} = \delta_{02}, \quad \delta_{03} = 0$	$f_s = 10/T_p$
7 (Symmetrical)	$\delta_{01} = \delta_{02} = \delta_{03}$	$f_s = 12/T_p$

occur in each cycle period.

3.9. Analysis of the Load Current Ripple

If the reference voltage vector $\bar{v}_{o,ref}$ could be ideally applied to the load, the corresponding current would be $\bar{i}_{o,ref}$. However, the actual value of the output voltage $\bar{v}_o$ differs from $\bar{v}_{o,ref}$ because $\bar{v}_o$ can assume only a finite number of values. Hence, it is possible to define the output voltage and current ripple vectors as follows

$$\bar{v}_{rip} = \bar{v}_o - \bar{v}_{o,ref} \tag{3.8}$$

$$\bar{i}_{rip} = \bar{i}_o - \bar{i}_{o,ref} \tag{3.9}$$

where $\bar{i}_o$ is the actual value of the load current vector, and $\bar{i}_{o,ref}$ is its mean value over the cycle period. According to the principles of the SVM technique, the mean value of $\bar{v}_{rip}$ during a cycle period T_p is zero.

For an inductive load, the high frequency relationship between $\bar{v}_{rip}$ and $\bar{i}_{rip}$ can be written as follows

$$\frac{d\bar{i}_{rip}}{dt} = \frac{\bar{v}_{rip}}{L_L} \tag{3.10}$$

where L_L is the load inductance.

Also the current ripple has zero mean value in a cycle period. Taking (3.6) into account, it is possible to determine the locus described in the stationary *d-q* reference frame by the vector $\bar{i}_{rip}$ during T_p. Fig. 3.10 shows the locus obtained with reference to the switching pattern of Fig. 3.9.

At the beginning of the cycle period, $\bar{i}_{rip}$ is zero, corresponding to the point *O*, origin of the reference frame. After a time interval $T_{03}/2$, during which the zero vector $\bar{v}_{0(3)}$ is applied to the load, $\bar{i}_{rip}$ reaches point *A* and the current ripple vector changes by the quantity $\overline{AO}$ given by

$$\overline{AO} = -\frac{\delta_{03} T_p}{2L_L} \bar{v}_{o,ref} . \tag{3.11}$$

During the second interval of length $\frac{1}{2} T_1$, the vector $\bar{v}_1$ is applied to the load and $\bar{i}_{rip}$ changes by the quantity $\overline{BA}$ given by

$$\overline{BA} = \frac{\delta_1 T_p}{2L_L} \left(\bar{v}_1 - \bar{v}_{o,ref} \right), \tag{3.12}$$

thus reaching the point *B*. The ripple vector $\bar{i}_{rip}$ reaches the points *C*, *D*, *E* and *F* in sequence (corresponding to the application of the vectors $\bar{v}_2$, $\bar{v}_{0(1)}$, $\bar{v}_3$ and $\bar{v}_4$ shown in Fig. 3.9). After the application of the vector $\bar{v}_{0(2)}$, $\bar{i}_{rip}$

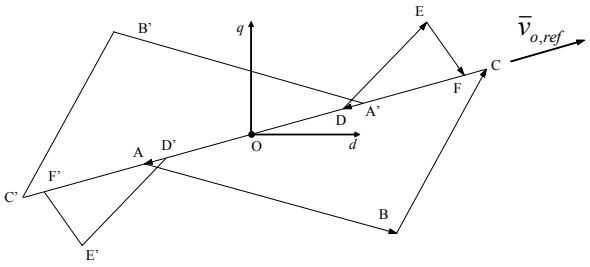

Fig. 3.10 – Locus described by the current ripple vector in the *d-q* plane.

reaches the point O again in the middle of the cycle period. Afterwards, $\bar{i}_{rip}$ symmetrically covers the second half of the locus passing through F', E', D' C', B', A' and finally returns to O.

It is worth noting that the length of the segments AO, DC and OF is proportional to δ_{01}, δ_{02} and δ_{03} respectively. Therefore, the shape of the locus depends on the splitting of the total time δ_0. For example, Fig. 3.11 shows the locus of the load current ripple for the same case of Fig. 3.10, but with $\delta_{02} = 0$ (C coincides with D). As can be seen, it is rather different from the one shown in Fig. 3.10, and the overall ripple is likely greater.

3.10. Optimal Space Vector Modulation Strategy

The parameter that is commonly used to represent the distortion of the current waveform is the rms value of its ripple, defined as

$$I_{rip,rms} = \sqrt{i^2_{o1,rip,rms} + i^2_{o2,rip,rms} + i^2_{o3,rip,rms}} \,. \tag{3.13}$$

where $i_{o1,rip,rms}$, $i_{o2,rip,rms}$ and $i_{o3,rip,rms}$ are the rms values of the ripple of the three load currents.

As the locus described by $\bar{i}_{rip}$ is symmetrical with respect to the origin of the reference frame, the rms value of the current ripple, in terms of the space vector $\bar{i}_{rip}$, can be written as follows:

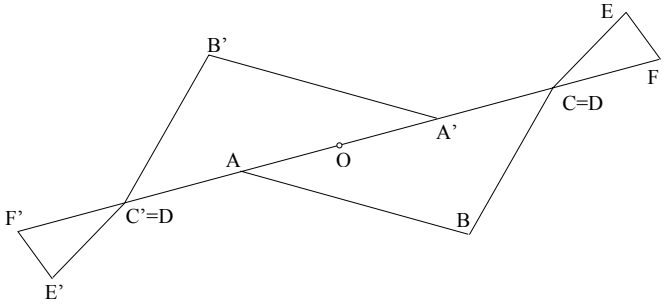

Fig. 3.11 – Locus described by the current ripple vector in the d-q plane for the case $\delta_{02} = 0$.

$$I_{rip,rms}^2 = \frac{3}{T_p}\int_0^{\frac{T_p}{2}} i_{rip}^2 dt\,. \tag{3.14}$$

In order to determine the operating conditions that minimize the current ripple, a geometrical analysis of the locus described in the *d-q* reference frame is necessary. Owing to the symmetry, the analysis can be focused only on the figure with vertexes *OABCDEFO* shown in Fig. 3.10, that corresponds to the first half of the cycle period. Moreover, the figure can be decomposed in two separate triangles, namely the triangles *ABC* and *DEF*.

Hence, the integral in (3.10) can be divided into two terms, each one corresponding to a different triangle, as follows:

$$\int_0^{\frac{T_p}{2}} i_{rip}^2 dt = \int_{ABC} i_{rip}^2 dt + \int_{DEF} i_{rip}^2 dt\,. \tag{3.15}$$

The length of the sides of the triangles is shown in Tab. 3.5. It is worth noting that the times necessary to cover the sides *AC* and *DF*, namely $\frac{1}{2}\delta' T_p$ and $\frac{1}{2}\delta'' T_p$, are "virtual" since they do not correspond to a specific switching interval. However, they can be calculated as shown in Appendix B as a function of the two fictitious duty-cycles δ' and δ'', that depend on δ_0 but are independent of δ_{01}, δ_{02} and δ_{03} separately.

As a first step, it is interesting to calculate the average value of the current ripple for both triangles, as follows:

$$\overline{G'O} = \frac{1}{T_{ABC}}\int_{ABC} \bar{i}_{rip} dt \tag{3.16}$$

TABLE 3.5 – LENGTH OF THE SIDES OF THE TRIANGLES ABC AND DEF

$\overline{BA}$	$\frac{\delta_1 T_p\left(\bar{v}_1 - \bar{v}_{o,ref}\right)}{2L_L}$	$\overline{ED}$	$\frac{\delta_3 T_p\left(\bar{v}_3 - \bar{v}_{o,ref}\right)}{2L_L}$
$\overline{CB}$	$\frac{\delta_2 T_p\left(\bar{v}_2 - \bar{v}_{o,ref}\right)}{2L_L}$	$\overline{FE}$	$\frac{\delta_4 T_p\left(\bar{v}_4 - \bar{v}_{o,ref}\right)}{2L_L}$
$\overline{AC}$	$-\frac{\delta' T_p \bar{v}_{o,ref}}{2L_L}$	$\overline{DF}$	$-\frac{\delta'' T_p \bar{v}_{o,ref}}{2L_L}$

$$\overline{G''O} = \frac{1}{T_{DEF}} \int_{DEF} \bar{i}_{rip} dt \tag{3.17}$$

where T_{ABC} and T_{DEF} are the total times required to cover the triangles ABC ed DEF, defined as

$$T_{ABC} = \tfrac{1}{2} T_p \left(\delta_1 + \delta_2 + \delta'\right) \tag{3.18}$$

$$T_{DEF} = \tfrac{1}{2} T_p \left(\delta_3 + \delta_4 + \delta''\right). \tag{3.19}$$

It is worth noting that T_{ABC} and T_{DEF} are independent of the duty-cycles δ_{01}, δ_{02} and δ_{03} as well. Obviously, their sum is equal to half the cycle period, i.e.

$$T_{ABC} + T_{DEF} = \tfrac{1}{2} T_p \,. \tag{3.20}$$

It can be verified that (3.16) and (3.17) are similar to the equations used to calculate the centre of gravity of a mechanical system with respect to the point O, origin of the reference frame. Like in mechanics, the positions of the points G' and G'' are independent from the point O. Hence, it is convenient to refer $\bar{i}_{rip}$ to G' and G''. For the triangle ABC, the current ripple $\bar{i}_{rip}$ can be written introducing the new space vector $\bar{i}'$ defined as follows:

$$\bar{i}_{rip} = \bar{i}' + \overline{G'O} \,. \tag{3.21}$$

Since $\overline{G'O}$ is the average value of $\bar{i}_{rip}$ over ABC, the average value of $\bar{i}'$ over T_{ABC} is zero. Similarly, for the triangle DEF, the current ripple can be expressed introducing the new space vector $\bar{i}''$, whose average value is zero in the time interval T_{DEF}, as follows:

$$\bar{i}_{rip} = \bar{i}'' + \overline{G''O} \,. \tag{3.22}$$

Substituting (3.21) and (3.22) in (3.14) leads to the following result:

$$\int_0^{\frac{T_p}{2}} i_{rip}^2 dt = T_{ABC} \left|\overline{G'O}\right|^2 + T_{DEF} \left|\overline{G''O}\right|^2 + \int_{ABC} i'^2 dt + \int_{DEF} i''^2 dt \,. \tag{3.23}$$

The two integral terms in (3.23) are independent from the duty-cycles δ_{01},

δ_{02} and δ_{03}. Therefore the rms value of the current ripple is minimum when both vectors $\overline{G'O}$ and $\overline{G''O}$ have the minimum length. This condition is achieved when the projections of G' and G'' on the line AF coincide with the point O, as shown in Fig. 3.12.

For the application of this basic principle it is useful to introduce the parameters λ and μ defined as

$$\lambda = \frac{T_{03}}{T_{ABC}} \tag{3.24}$$

$$\mu = \frac{T_{02}}{T_{DEF}}. \tag{3.25}$$

The geometrical condition shown in Fig. 3.12, after some analytical developments, leads to the following optimal values for λ and μ:

$$\lambda_{opt} = (\operatorname{sgn}\delta')\left[\frac{1}{2} + \frac{\delta_1\delta_2(\delta_1 - \delta_2)}{4\delta'(\delta_1^2 + \delta_2^2 + \delta_1\delta_2)}\right] \tag{3.26}$$

$$\mu_{opt} = (\operatorname{sgn}\delta'')\left[\frac{1}{2} + \frac{\delta_3\delta_4(\delta_4 - \delta_3)}{4\delta''(\delta_3^2 + \delta_4^2 + \delta_4\delta_3)}\right]. \tag{3.27}$$

The mathematical procedure used to obtain (3.26) and (3.27) is similar to that applied in [42] for traditional VSIs.

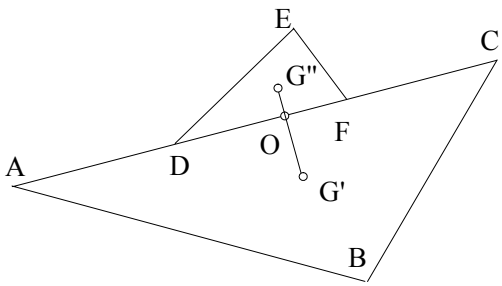

Fig. 3.12 – Half of the locus described by the current ripple vector in the condition of minimum ripple.

The optimal values for δ_{03} and δ_{02} are

$$\delta_{03,opt} = min\left\{max-\lambda_{opt}\left|\delta'\right|,0'',\delta_0\right\} \tag{3.28}$$

$$\delta_{02,opt} = min\left\{max-\mu_{opt}\left|\delta''\right|,0'',\delta_0\right\} \tag{3.29}$$

and $\delta_{01,opt}$ is given by

$$\delta_{01,opt} = \delta_0 - \delta_{02,opt} - \delta_{03,opt}. \tag{3.30}$$

Equations (3.28) and (3.29) ensure that $\delta_{03,opt}$ and $\delta_{02,opt}$ are positive and lower than δ_0. However, since $\delta_{02,opt}$ and $\delta_{03,opt}$ are found minimizing the two distances $\left|\overline{G'O}\right|$ and $\left|\overline{G''O}\right|$ separately, it can happen that the condition

$$\delta_{01,opt} > 0 \tag{3.31}$$

is not satisfied. In this case, it is necessary to assume

$$\delta_{01,opt} = 0 \tag{3.32}$$

and (3.28) and (3.29) are replaced by the following equations:

$$\delta_{03,opt} = min\left\{max-\lambda\left|\delta'\right|\left(\delta' + \delta_1 + \delta_2\right) + \right.$$
$$\left. + \left(\delta'' + \delta_4 + \delta_3\right)\left(\delta_0 - \mu\left|\delta''\right|\right),0,\delta_0\right\} \tag{3.33}$$

$$\delta_{02,opt} = \delta_0 - \delta_{03,opt}\ . \tag{3.34}$$

3.11. Simulation Results

To characterize the behaviour of the modulation strategies, it is opportune to introduce an appropriate quality index. This quality index could be the mean value of the $I^2_{rip,rms}$ evaluated over the range $[0,2\pi]$ of the phase angles α and β of the output and input voltage vectors. The index is defined as follows:

$$Q = \frac{1}{2\pi}\int_0^{2\pi}\frac{1}{2\pi}\int_0^{2\pi} I^2_{rip,rms}(\alpha,\beta)d\alpha\, d\beta\,. \tag{3.35}$$

Fig. 3.13 shows the behaviour of Q as a function of the modulation index

q, namely the ratio between the magnitudes of the output and the input voltage vectors. Fig. 3.13 has been normalized with respect to the value of Q for $q = \sqrt{3}/2$ using the optimal modulation strategy. It can be noted that the behaviour of the optimal strategy is better than that of the other strategies for any value of q. In addition, the optimal modulation is superior to Strategy 7 in terms of mean switching frequency, for high values of q. In fact, in these operating conditions the optimal strategy tends to perform like Strategy 4. This is confirmed in Fig. 3.14, where the switching frequency, expressed in p.u. of the switching frequency of Strategy 7 is plotted as function of q for the different types of modulation strategies.

3.12. Experimental Results

In order to verify the theoretical approach, a prototype of a three-phase to three-phase MC has been used to supply a linear passive R-L load. The MC is realized using the FM35E12KR3 IGBT module produced by EUPEC. The control algorithm is implemented on the platform C6711, a floating-point digital signal processor provided by Texas Instruments. The switching frequency of the SVM strategies is 12.5 kHz, corresponding to a cycle period

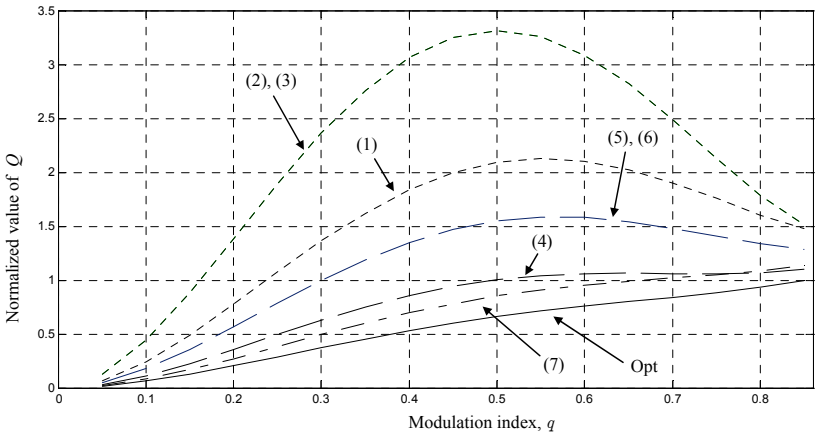

Fig. 3.13 - Behavior of the quality index Q as a function of the modulation index q for Strategies (1)-(7) and for the optimal strategy (Opt). All curves are normalized with respect to the value of Q for $q = \sqrt{3}/2$ using the optimal modulation strategy.

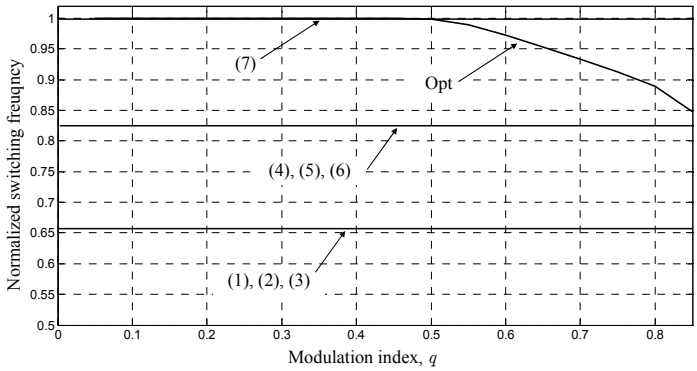

Fig. 3.14 - Behaviour of the switching frequency for all the modulation strategies in p.u. of the switching frequency of Strategy 7.

of 80 μs. The converter is fed by a voltage transformer with variable voltage transfer ratio to adjust the input voltage to a value of about 110 V rms. A L-C filter is connected at the input side of the converter. The parameters of filter, supply and load correspond to those reported in Tab. 3.6.

Fig. 3.15 shows the behaviour of the traditional modulation strategies and of the optimal strategy in terms of squared rms value of the load current ripple. The rms value of the ripple has been determined by sampling the current waveforms and considering only the high frequency harmonics. As can be seen, the optimal modulation exhibits the lowest ripple, and the behaviour of the curves is similar to that predicted in Fig. 3.13.

3.13. Conclusion

A geometrical approach for the analysis of the load current ripple in SVM for MCs has been presented. The proposed method has been applied to define

TABLE 3.6
SYSTEM PARAMETERS.

Supply	Filter	Load
V_S = 110 V(rms),	L_f = 1.16 mH	R_L = 8.3 Ω
ω_i = 2π 50 rad/s,	C_f = 4.5 μF	L_L = 1.3 mH,
R_S = 0.2 Ω, L_S=0.70 mH	R_f = 300 Ω	ω_o = 2π 100 rad/s

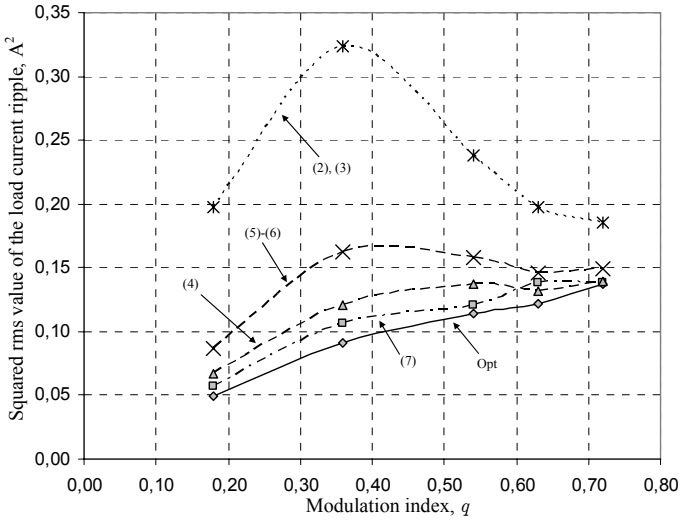

Fig. 3.15 - Experimental tests. Square of the rms value of the load current ripple as a function of the modulation index ρ for different modulation strategies.

the optimal SVM technique, characterized by the minimum rms value of the load current ripple in each cycle period and, as a consequence, over the fundamental period. The explicit equations to calculate the duty-cycles of the three zero voltage vectors and then the determination of the switching pattern of the optimal SVM technique have been presented.

The performance of the optimal modulation strategy has been compared with that of the most commonly used modulation techniques. As a result, the optimal strategy performs better than the other modulation strategies in terms of current ripple. In addition, for high values of the modulation index, the optimal strategy shows a switching frequency that is ≈15% lower than that of the modulation strategy that uses three zero vectors.

Experimental tests have been performed emphasizing the behaviour of the different modulation strategies and confirming the results predicted by the theoretical approach.

Chapter 4

Stability of Matrix Converter

Abstract

Input filters are usually adopted in electrical drives in order to improve the input current quality and to reduce the input voltage distortion. These filters can determine instabilities, depending on the converter topology and drive control strategy.

Matrix converters perform a direct coupling between two ac sources without the need of energy storage components. This characteristic, together with the presence of L-C input filters and the feedforward compensation of the input voltage disturbances, may determine unstable operation as the power delivered to the load exceeds a limit value.

In this chapter the stability of an electrical drive fed by a three-phase to three-phase matrix converter is analyzed considering two different input filter structures. A state average model of the whole system, assuming a constant power load, is proposed. The stability of the system is evaluated by analyzing the migration of eigenvalues of the system, which is linearized around the operating point. The analytical approach allows the determination of relationships showing the maximum output power of the matrix converter as a function of the parameters of power supply and input filter.

4.1. Introduction

The presence of filters, at the input side of a power converter, can determine instabilities depending on the drive control strategy and the converter topology [43]-[45]. This problem becomes evident if the converter is controlled with fast closed loops, as it happens in controlled rectifiers [46], in Field Oriented Control (FOC) and in Direct Torque Control (DTC) drives [47]-[48], thus leading to constant power operation.

The use of matrix converters increases the problems of instability, owing to the absence of an intermediate dc-link with energy storage capability and the reduced size of the input filters [49], [50].

Several control techniques for matrix converters have been proposed in literature [1] , [2], [5], [7], [13], [21], [32]. Among these the most simple is the one based on detecting the zero crossing of one input voltage for synchronizing the input current modulation strategy, under the assumption of ideal supply (i.e. balanced and sinusoidal supply voltages). In this case any input voltage disturbance is reflected on the output voltages determining low order harmonics.

It is possible to compensate these effects by monitoring the input voltages and, consequently, calculating the duty-cycles necessary to generate balanced and sinusoidal output voltages. However, this type of feedforward compensation of the input voltage perturbations might lead to instability phenomena as the matrix converter output power exceeds a maximum limit that is related to the grid impedance and the input L-C filter parameters [18].

Firstly in this chapter two input filter topologies are considered, and the different effects on system stability are emphasized. It has been verified that standard design methods of input filters for matrix converters lead to filter parameters that may determine instability phenomena at very low power levels.

Then, it is shown that the power limit can be increased if the duty-cycles of the switching configurations are calculated using input voltages filtered by a digital low-pass filter implemented in a synchronous reference frame. As a consequence, the capability of the matrix converter to compensate input voltage disturbances is affected to some extent, but the stability limits can be sensibly improved.

In order to investigate the stability improvement achievable by using

filtered input voltages, a theoretical analysis based on a state variable average model is proposed. The stability of the whole system, including the grid impedance, the input L-C filter and a passive load, is evaluated by analyzing the migration of eigenvalues of the linearized state matrix. The analytical approach allows the determination of the maximum voltage transfer ratio of the matrix converter, and then of the maximum output power, as function of the time constant of the digital low-pass input voltage filter.

Firstly the validity of the analytical approach has been verified by numerical simulations in which the matrix converter switches are assumed as ideal switches. Then, more accurate models of the power switches have been considered using a general-purpose simulator of electronic circuits. The transition from stable to unstable operation of the matrix converter has been verified changing the operating conditions.

The most important contribution of this study is the analytical approach proposed for the analysis of matrix converter stability, which makes it possible to demonstrate the existence of possible unstable operating conditions and to find out a simple method for extending the stability power range.

Numerical simulations have been performed showing the validity of the analytical approach.

4.2. Mathematical Model Using L-C Filter

The whole system, which is composed by a non-ideal supply, a second order L-C filter and a matrix converter operating at constant power, is represented as shown in Fig. 4.1.

The input current modulation strategy generally maintains a constant displacement angle between the input line-to-neutral voltage space vector and the input current space vector. In this case the input current modulation strategy can be expressed as

$$\overline{\psi}_{ref} = \overline{v}_i \, e^{-j\varphi} \tag{4.1}$$

where $\overline{\psi}_{ref}$ is the space vector defining the direction along which the input current is modulated.

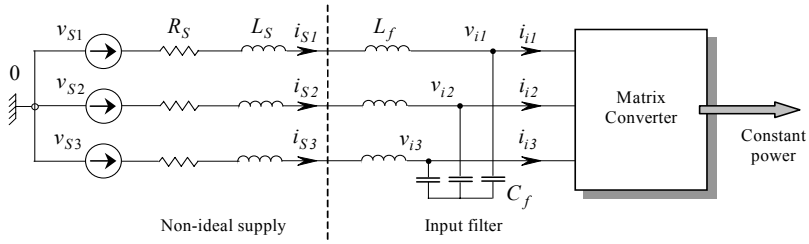

Fig. 4.1 - Basic scheme of the system analyzed.

In the following, the analytical developments are carried out neglecting the effects of the switching harmonics, considering for the output voltages and input currents their average values over a switching interval.

The system equations, written using the space vector notation, are

$$\overline{v}_S = R_S \, \overline{i}_S + L_T \frac{d\overline{i}_S}{dt} + \overline{v}_i \tag{4.2}$$

$$\overline{i}_f = C_f \frac{d\overline{v}_i}{dt} \tag{4.3}$$

$$\overline{i}_S = \overline{i}_f + \overline{i}_i \tag{4.4}$$

$$\overline{i}_i = \frac{2}{3} \frac{P_o \, \overline{\Psi}_{ref}}{\overline{v}_i \cdot \overline{\Psi}_{ref}} \tag{4.5}$$

where $L_T = L_S + L_f$ and P_o is the constant output power.

Equation (4.5) is valid supposing that the converter is ideal, without power losses. In this case the output power is equal to the input power and the input current is perfectly modulated.

From (4.2)-(4.5) it is possible to derive the nonlinear state space equations in a synchronous reference frame, which can be expressed as

$$\frac{d\overline{i}_S}{dt} = -\left(\frac{R_S}{L_T} + j\,\omega_i \right) \overline{i}_S - \frac{1}{L_T} \overline{v}_i + \frac{1}{L_T} \overline{v}_S \tag{4.6}$$

$$\frac{d\overline{v}_i}{dt} = \frac{1}{C_f} \overline{i}_S - j\,\omega_i \, \overline{v}_i - \frac{1}{C_f} \overline{i}_i \tag{4.7}$$

being ω_i the supply angular frequency.

It should be noted that the system behaviour depends on the adopted input current modulation strategy. This is emphasized by the presence in (4.5) of the space vector $\overline{\psi}_{ref}$.

Assuming for $\overline{\psi}_{ref}$ the expression given in (4.1) and using (4.5) leads for (4.7) the following new form:

$$\frac{d\overline{v}_i}{dt} = \frac{1}{C_f}\bar{i}_S - j\,\omega\,\overline{v}_i - \frac{1}{C_f}\frac{\frac{2}{3}P_o\,e^{-j\varphi}}{\overline{v}_i^{*}\cos\varphi}. \tag{4.8}$$

This equation can be further simplified assuming $\varphi = 0$, which represents unity input power factor.

4.3. Steady-State Operating Conditions

In the synchronous reference frame and in steady-state conditions, the variables $\overline{v}_i$, $\overline{v}_S$ and $\bar{i}_S$ assume the corresponding constant values $\overline{V}_i$, $\overline{V}_S$ and $\bar{I}_S$. As a consequence, (4.6) and (4.8) become

$$0 = -\left(\frac{R_S}{L_T} + j\,\omega\right)\bar{I}_S - \frac{1}{L_T}\overline{V}_i + \frac{1}{L_T}\overline{V}_S \tag{4.9}$$

$$0 = \frac{1}{C_f}\bar{I}_S - j\,\omega\,\overline{V}_i - \frac{2\,P_o\,e^{-j\varphi}}{3\,C_f\,\overline{V}_i^{*}\cos\varphi}. \tag{4.10}$$

These equations can be solved with respect to $\bar{I}_s$ and $\overline{V}_i$. It can be verified that the solution exists only if the output power P_o of the matrix converter satisfies the following inequality, written in the particular case of $\varphi = 0$:

$$P_{S1} < P_o < P_{S2} \tag{4.11}$$

where

$$P_{S1}, P_{S2} = \frac{3}{4} \frac{V_S^2}{\omega^2 \left[L_T \left(1 - \omega^2 L_T C_f\right) - R_S^2 C_f \right]^2} \cdot \cdot \left\{ - R_S \mp \sqrt{R_S^2 + \omega^2 \left[L_T \left(1 - \omega^2 L_T C_f\right) - R_S^2 C_f \right]^2} \right\} \quad (4.12)$$

The power limit expressed by (4.12) represents the well-known maximum power that can be exchanged between a power source with internal impedance and a load.

The positive value P_{S2} refers to motor behaviour, whereas the negative value P_{S1} represents a limit during regenerative braking.

4.4. Stability Analysis

Assuming the d-q synchronous reference frame with the d-axis along the direction of the vector $\overline{V}_i$, and linearizing (4.6) and (4.8) around the steady-state operating point, leads to the following state equations:

$$\begin{bmatrix} \frac{d\Delta i_{Sd}}{dt} \\ \frac{d\Delta i_{Sq}}{dt} \\ \frac{d\Delta v_{id}}{dt} \\ \frac{d\Delta v_{iq}}{dt} \end{bmatrix} = \begin{bmatrix} -\frac{R_S}{L_T} & \omega_i & -\frac{1}{L_T} & 0 \\ -\omega_i & -\frac{R_S}{L_T} & 0 & -\frac{1}{L_T} \\ \frac{1}{C_f} & 0 & \frac{A_d}{V_i^2} & \frac{A_q}{V_i^2} + \omega_i \\ 0 & \frac{1}{C_f} & \frac{A_q}{V_i^2} - \omega_i & -\frac{A_d}{V_i^2} \end{bmatrix} \begin{bmatrix} \Delta i_{Sd} \\ \Delta i_{Sq} \\ \Delta v_{id} \\ \Delta v_{iq} \end{bmatrix} \quad (4.13)$$

where

$$A_d = \frac{2}{3} \frac{P_o}{C_f}, \; A_q = -\frac{2}{3} \frac{P_o}{C_f} tg\,\varphi .$$

The analysis of the eigenvalues of the state matrix in (4.13) leads to the following simple stability conditions:

$$-P_1 < P_o < P_1 \quad (4.14)$$

and

$$-P_2 < P_o < P_2 \tag{4.15}$$

where

$$P_1 = \frac{3}{2} V_i^2 \left|\cos\varphi\right| C_f \sqrt{\left(\frac{R_S^2}{L_T^2} + 4\,\omega_i^2\right)} \tag{4.16}$$

$$P_2 = \frac{3}{2} V_i^2 \left|\cos\varphi\right| \sqrt{\frac{\left(1 - \omega^2\, L_T\, C_f\right) + R_S^2\, \omega_i^2\, C_f^2}{R_S^2 + \omega_i^2\, L_T^2}}\,. \tag{4.17}$$

The relationship (4.14), which is usually more restrictive than (4.15), defines a limit value for the output power of the matrix converter as function of the system parameters. It can be noted that the best condition, in terms of maximum power limit, is obtained with unity input power factor.

The output power limit given in (4.16) is not related in any way to the output power limit given in (4.12), that is concerned with steady-state operating conditions. Instead, P_1 is a power limit, usually much lower than P_{S2}, determined by dynamic operating conditions.

It should be noted that the maximum output power limits given by (4.16) and (4.17) do not depend on the switching frequency of the matrix converter. In fact, the analysis has been carried out assuming an infinitely high switching frequency. Then, increasing the switching frequency does not prevent the system from becoming unstable.

The proposed approach demonstrates that instability phenomena are not determined by the interaction between the filter and the switching harmonics, as it could appear from analyzing the behaviour of the input quantities as the instability occurs.

The results obtained in terms of output power limits are valid for the input current modulation strategy given in (4.1). Changing the input current modulation strategy leads to different output power limits.

Equation (4.16) is a simple expression that can be useful to understand the effect of the input filter parameters on the system stability.

For a prefixed value of the input filter resonance frequency, (4.16) emphasizes that, in order to increase the power limit, high values of the capacitance C_f and low values of the inductance L_f should be preferred. On the other hand, high values of the capacitance deteriorate the input power

factor. In order to overcome this problem, a different filter structure should be considered.

4.5. Mathematical Model Using R-L-C Filter

The relationship (4.16) emphasizes the positive effect of the line resistance on the system stability. Obviously, it is not possible to add a damping resistance in series with the L-C input filter, because this solution would seriously degrade the efficiency.

A better solution is to add a resistance in parallel with L_f, so that, in practice, only the high frequency current harmonics flow through the damping resistance [51].

The structure of the R-L-C type filter is shown in Fig. 4.2. In order to show the effectiveness of this filter, the stability analysis has been carried out in the same way as in Paragraph 4.4, but considering the third order R-L-C filter.

The nonlinear state space equations of the whole system, in a synchronous reference frame, can be written as

$$\frac{d\bar{i}_S}{dt} = -\left(\frac{1}{\tau_S} + j\,\omega\right)\bar{i}_S - \frac{1}{L_S}\,\bar{v}_i + \frac{R_f}{L_S}\,\bar{i}_{Lf} + \frac{1}{L_S}\,\bar{v}_S \tag{4.18}$$

$$\frac{d\bar{v}_i}{dt} = \frac{1}{C_f}\,\bar{i}_S - j\,\omega\,\bar{v}_i - \frac{1}{C_f}\,\frac{\frac{2}{3}P\,\bar{\Psi}_{ref}}{\bar{v}_i \cdot \bar{\Psi}_{ref}} \tag{4.19}$$

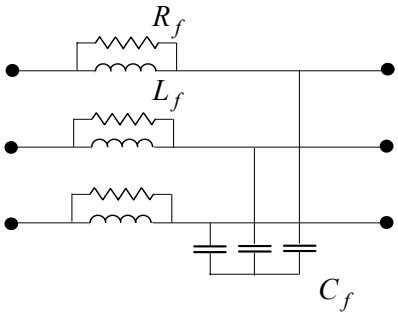

Fig. 4.2 – Topology of the R-L-C type input line filter.

$$\frac{d\bar{i}_{Lf}}{dt} = \frac{R_f}{L_f}\bar{i}_S - \left(\frac{R_f}{L_f} + j\,\omega\right)\bar{i}_{Lf} \tag{4.20}$$

being $\tau_S = \dfrac{L_S}{\left(R_S + R_f\right)}$.

Linearizing (4.18)-(4.20) around the steady-state operating point and decomposing in *d-q* components, leads to the following state equation, valid for $\varphi = 0$.

$$\begin{bmatrix} \frac{d\Delta i_{Sd}}{dt} \\ \frac{d\Delta i_{Sq}}{dt} \\ \frac{d\Delta v_{id}}{dt} \\ \frac{d\Delta v_{iq}}{dt} \\ \frac{d\Delta i_{Lfd}}{dt} \\ \frac{d\Delta i_{Lfq}}{dt} \end{bmatrix} = \begin{bmatrix} -\frac{1}{\tau_S} & \omega_i & -\frac{1}{L_S} & 0 & \frac{R_f}{L_S} & 0 \\ -\omega_i & -\frac{1}{\tau_S} & 0 & -\frac{1}{L_S} & 0 & \frac{R_f}{L_S} \\ \frac{1}{C_f} & 0 & \frac{A_d}{V_i^2} & \omega_i & 0 & 0 \\ 0 & \frac{1}{C_f} & -\omega_i & -\frac{A_d}{V_i^2} & 0 & 0 \\ \frac{R_f}{L_f} & 0 & 0 & 0 & -\frac{R_f}{L_f} & \omega_i \\ 0 & \frac{R_f}{L_f} & 0 & 0 & -\omega_i & -\frac{R_f}{L_f} \end{bmatrix} \begin{bmatrix} \Delta i_{Sd} \\ \Delta i_{Sq} \\ \Delta v_{id} \\ \Delta v_{iq} \\ \Delta i_{Lfd} \\ \Delta i_{Lfq} \end{bmatrix} \tag{4.21}$$

The stability of the system described by (4.21) cannot be easily developed in analytical form. Then, a numerical approach has been used. With reference to the system defined in Tab. 4.1, the position of the dominant eigenvalue is evaluated as function of the matrix converter output power, for different values of the filter damping resistance R_f . The results are shown in Fig. 4.3.

TABLE 4.1 - SYSTEM PARAMETERS

Supply	
$V_S = 220$ V(rms),	$\omega_i = 2\pi\ 50$ rad/s
$R_S = 0.25\ \Omega$,	$L_S = 0.4$ mH.
Filter	
$L_f = 0.6$ mH,	$C_f = 10.0\ \mu$F.
Load	
$R_L = 10\ \Omega$,	$L_L = 20$ mH.

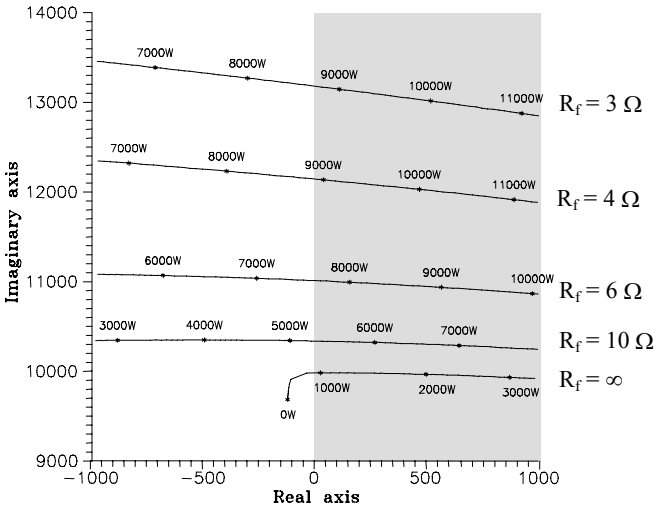

Fig. 4.3 – Position of the dominant eigenvalue in the complex plane as function of the matrix converter output power.

As is possible to see, the introduction of the damping resistance improves significantly the system stability. The power limit, which is of about 1 kW for $R_f = \infty$ (L-C input line filter), can be increased up to a maximum value of about 9 kW by decreasing R_f down to 4Ω. A further reduction of the damping resistance is not useful, because it reduces the corresponding power limit.

4.6. Simulation Results

In order to verify the consistency of the proposed analytical approach, the behaviour of the system composed by a non-ideal supply, an input line filter and a matrix converter feeding a three-phase symmetrical R-L passive load, has been tested by numerical simulation.

The simulation takes into account the switching behaviour of the matrix converter and the delay related to the digital implementation of the control algorithm.

The values of the system parameters have already been shown in Tab. 4.1.

The control strategy adopted for the matrix converter is the SVM

technique, with double-sided switching pattern and cycle period of 80 μs [7].

The behaviour of the system has been analysed at two different power levels by changing the magnitude of the output voltages.

The results obtained, with unity input power factor, are presented in Figs. 4.4 and 4.5.

Fig. 4.4(a) shows the steady-state waveform of the input voltage of the matrix converter with an output to input voltage ratio of 50/220, corresponding to an output power of 670 W. The steady-state waveforms of line current and load current are illustrated in Figs. 4.4(b) and (c),

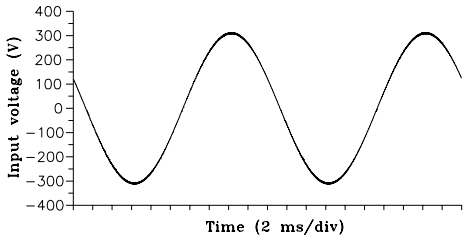

Fig. 4.4(a) - Matrix converter input line to neutral voltage, P=670 W.

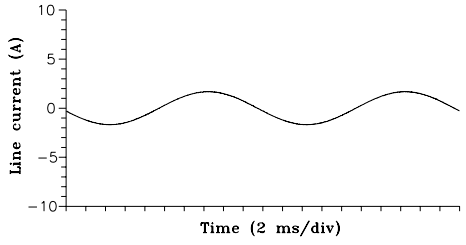

Fig. 4.4(b) - Line current.

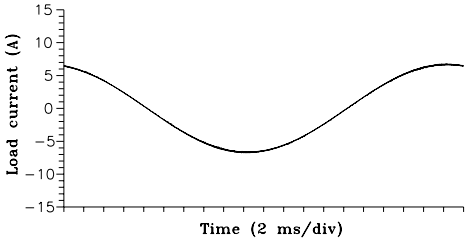

Fig. 4.4(c) - Load current.

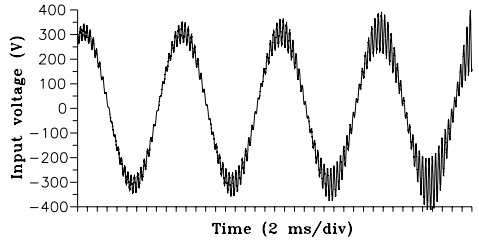

Fig. 4.5(a) - Matrix converter input line to neutral voltage, P=1500 W.

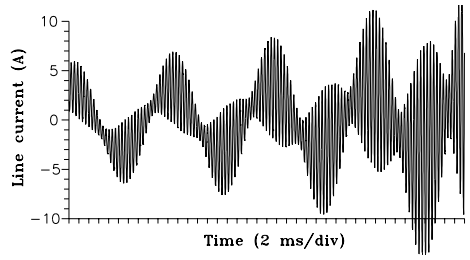

Fig. 4.5(b) - Line current.

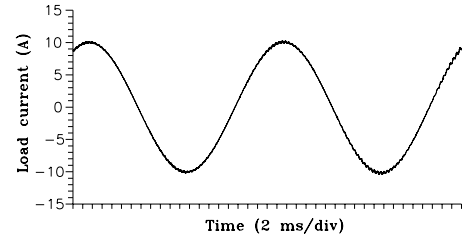

Fig. 4.5(c) – Load current.

respectively.

As is possible to see, all the waveforms are sinusoidal and characterized by a small ripple, due to the high switching frequency of the matrix converter.

Fig. 4.5(a) shows the transient waveform of the input voltage of the matrix converter with an output to input voltage ratio of 74/220, corresponding to a theoretical output power of 1500 W. The transient waveforms of line current and load current are illustrated in Figs. 4.5(b) and (c), respectively.

As is possible to see in Figs. 4.5(a) and (b), in these operating conditions the waveforms of voltage and current at the input side are heavily distorted, showing large oscillations at a frequency close to the resonance frequency of the input filter.

This behaviour is due to the predicted instability phenomena that occur when the output power exceeds the stability range limits defined by (4.14)-(4.17), even if the switching frequency (12.5 kHz) is much higher than the resonance frequency of the input filter (1.6 kHz).

These results can be justified on the basis of the proposed stability analysis. With reference to the values of the system parameters, shown in Tab. 4.1, (4.16) gives a power limit of 970 W.

In the first case (Figs. 4.4), the power delivered to the load is lower than the power limit, and the system is stable. In the second case (Fig. 4.5), the output power is higher than the power limit, and the system becomes unstable. Any small perturbation, as the switching effects of the matrix converter, causes the system to leave steady-state operating conditions.

It should be noted that, initially, in spite of the large oscillations at the input side, the waveform of the load current is nearly sinusoidal, as can be seen from Fig. 4.5(c). The fast adaptation of the duty-cycles, based on on-line measurement of the input voltages, allows the control of the output voltages to be maintained.

In order to emphasize the improvements that can be reached by changing the input line filter structure, the system behaviour has been evaluated with a damping resistance of 4 Ω.

The results obtained with an output to input voltage ratio of 170/220 (P_o = 8000 W) are shown in Fig. 4.6.

Fig. 4.6(a) shows the input voltage waveform of the matrix converter,

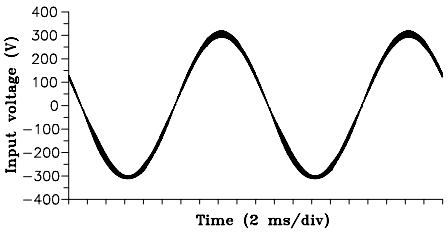

Fig. 4.6(a) – Matrix converter input line to neutral voltage, P=8000 W, $R_f = 4\ \Omega$.

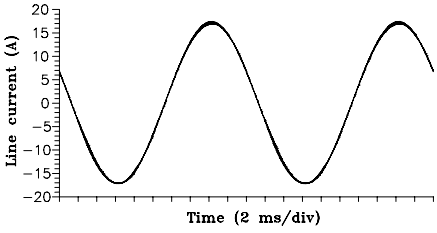

Fig. 4.6(b) – Line current.

whereas the line current waveform is illustrated in Fig. 4.6(b). According to the results shown in Fig. 4.3, this operating condition is stable and all the waveforms are practically sinusoidal.

As can be seen, the damping resistance in the input line filter, which determines negligible power losses, strongly increases the system power limit.

4.7. Use of a Digital Input Filter

In the following it will be shown that the power limit can be sensibly improved if the calculation of the duty-cycles is carried out filtering the matrix converter input voltages by means of a digital low-pass filter implemented in a reference frame synchronous with the fundamental component of the input voltage vector.

The modulation strategy is such that the input current vector is kept in phase with the filtered input voltage vector instead of the actual voltage vector. Therefore, the modulation vector $\overline{\psi}_{ref}$ is defined by

$$\overline{\psi}_{ref} = \overline{v}_{if} \,. \tag{4.22}$$

The system scheme is the same shown in Fig. 4.1. It is important to note that, due to phase lag of the digital input filter, it is not possible to suppose that the matrix converter delivers a constant power to the load during the transients. Therefore, it is necessary to consider the behaviour of the load and not only that of the voltage source.

As usual, the analytical developments are carried out neglecting the effects of the switching harmonics, considering for the output voltages and input currents their average values over a switching interval.

The system equations, in terms of space vectors, can be written for convenience in different reference frames as summarized in Tab. 4.2.

The equations for the input side of the matrix converter, written in a reference frame rotating at the supply angular frequency ω_i are given by (4.6) and (4.7).

The equation representing the behaviour of the first order low-pass filter applied to the input voltage is

$$\frac{d\overline{v}_{if}}{dt} = \frac{1}{\tau}\overline{v}_i - \frac{1}{\tau}\overline{v}_{if} \tag{4.23}$$

where τ is the time constant of the input voltage filter. It can be noted that this filter, being implemented on a synchronous reference frame, does not introduce any attenuation and phase shift on the fundamental component of the input voltage.

The equation for the output side of the matrix converter is written in a reference frame rotating at the output angular frequency ω_o as follows:

$$\frac{d\bar{i}_o}{dt} = -\left(\frac{R_L}{L_L} + j\,\omega_o\right)\bar{i}_o + \frac{1}{L_o}\overline{v}_o \ . \tag{4.24}$$

The input-output relationships of the matrix converter, written using the duty-cycle space vectors $\overline{m}_d$ and $\overline{m}_i$, are as follows:

$$\overline{v}_o = \frac{3}{2}\overline{v}_i\,\overline{m}_i^* + \frac{3}{2}\overline{v}_i^*\,\overline{m}_d \tag{4.25}$$

TABLE 4.2 – SYNCHRONOUS REFERENCE FRAMES

Variables	Angular speed of the reference frame
Input variables	ω_i
Output variables	ω_o
$\overline{m}_d$	$\omega_i + \omega_o$
$\overline{m}_i$	$\omega_i - \omega_o$

$$\bar{i}_i = \frac{3}{2}\bar{i}_o\,\overline{m}_i + \frac{3}{2}\bar{i}_o^*\,\overline{m}_d\,. \tag{4.26}$$

In (4.25) and (4.26) the duty-cycle space vector $\overline{m}_d$ is defined in a reference frame rotating at the angular speed $\omega_i + \omega_o$, and the duty-cycle space vector $\overline{m}_i$ in a reference frame rotating at the angular speed $\omega_i - \omega_o$.

The problem of the determination of the duty-cycle space vectors is completely solved by the following equations, valid under the assumption that the measured input voltages are filtered as shown in (4.22):

$$\overline{m}_d = \frac{\overline{v}_{o,ref}}{3\,\overline{v}_{if}^*} \tag{4.27}$$

$$\overline{m}_i = \frac{\overline{v}_{o,ref}^*}{3\,\overline{v}_{if}^*}\,. \tag{4.28}$$

In order to study the stability of the system it is opportune to linearize the system equations around a steady-state operating point corresponding to balanced and sinusoidal supply voltages.

A. Steady-State Operating Conditions with Balanced and Sinusoidal Supply Voltages

In steady-state operating conditions, the variables $\bar{v}_S$, $\bar{i}_S$, $\bar{v}_i$, $\bar{i}_i$, $\bar{v}_{if}$, $\bar{v}_{o,ref}$, $\bar{v}_o$, $\bar{i}_o$, $\overline{m}_d$ and $\overline{m}_i$, expressed in their synchronous reference frames, assume the constant values $\overline{V}_S$, $\bar{I}_S$, $\overline{V}_i$, $\bar{I}_i$, $\overline{V}_{if}$, $\overline{V}_o$, $\bar{I}_o$, $\overline{V}_{o,ref}$, $\overline{M}_d$, $\overline{M}_i$.

It is worth noting that the phase angles of $\overline{V}_i$ and $\overline{V}_{o,ref}$ can be arbitrarily chosen.

Assuming for $\overline{V}_i$ and $\overline{V}_{o,ref}$ the following values $\overline{V}_i = V_i$, $\overline{V}_{o,ref} = V_{o,ref}$, and solving the system equations (4.6),(4.7), (4.23) – (4.28) leads to the following solution:

$$\overline{V}_{if} = V_i \tag{4.29}$$

$$\overline{M}_d = \frac{q}{3} \tag{4.30}$$

$$\overline{M}_i = \frac{q}{3} \tag{4.31}$$

$$\overline{V}_o = q\,V_i \tag{4.32}$$

$$\bar{I}_o = \frac{q\,V_i}{\overline{Z}_o} \tag{4.33}$$

$$\bar{I}_i = \frac{R_L}{Z_L^2}\,q^2\,V_i \tag{4.34}$$

$$\bar{I}_S = \left(j\,\omega_i\,C_f + \frac{R_L}{Z_L^2}\,q^2 \right) V_i \tag{4.35}$$

$$\overline{V}_S = \left(1 + j\,\omega_i\,C_f\,\overline{Z}_S + \frac{R_L\,\overline{Z}_S}{Z_L^2}\,q^2 \right) V_i \tag{4.36}$$

where $\overline{Z}_L = R_L + j\,\omega_L\,L_L$ and $\overline{Z}_S = R_S + j\,\omega_i\,L_T$. As usual, the variable $q = V_{o,ref}/V_i$ is the voltage transfer ratio.

From the previous equations it can be noted that the filtered input voltage is equal to the input voltage itself, as well as the output voltage is equal to the corresponding reference value. This means that, in these operating conditions, the digital low-pass filter does not affect the output voltage.

B. Small Signal Equations

The linearization of the system equations (4.22)–(4.28) around the steady-state operating point defined by (4.29)– (4.36) leads to the following system of small signal equations:

$$\frac{d\Delta\bar{i}_S}{dt} = -\left(\frac{R_S}{L_T} + j\,\omega_i \right) \Delta\bar{i}_S - \frac{1}{L_T}\,\Delta\bar{v}_i + \frac{1}{L_T}\,\Delta\bar{v}_S \tag{4.37}$$

$$\frac{d\Delta\overline{v}_i}{dt} = \frac{1}{C_f}\Delta\bar{i}_S - j\,\omega_i\,\Delta\overline{v}_i - \frac{1}{C_f}\Delta\bar{i}_i \tag{4.38}$$

$$\frac{d\Delta\bar{i}_o}{dt} = \left(-\frac{R_L}{L_L} - j\,\omega_o\right)\Delta\bar{i}_o + \frac{1}{L_L}\Delta\overline{v}_o \tag{4.39}$$

$$\frac{d\Delta\overline{v}_{if}}{dt} = \frac{1}{\tau}\Delta\overline{v}_i - \frac{1}{\tau}\Delta\overline{v}_{if} \tag{4.40}$$

$$\Delta\overline{v}_o = \frac{3}{2}\Delta\overline{v}_i\,\overline{M}_i^* + \frac{3}{2}\Delta\overline{v}_i^*\,\overline{M}_d + \frac{3}{2}V_i\,\Delta\overline{m}_i^* + \frac{3}{2}V_i\,\Delta\overline{m}_d \tag{4.41}$$

$$\Delta\bar{i}_i = \frac{3}{2}\Delta\bar{i}_o\,\overline{M}_i + \frac{3}{2}\Delta\bar{i}_o^*\,\overline{M}_d + \frac{3}{2}\bar{I}_o\,\Delta\overline{m}_i + \frac{3}{2}\bar{I}_o^*\,\Delta\overline{m}_d \tag{4.42}$$

$$6\,\overline{M}_d\left(1\cdot\Delta\overline{v}_{if}\right) + 3\,\Delta\overline{m}_d\,V_i = q\,\Delta\overline{v}_{if} \tag{4.43}$$

$$6\,\overline{M}_i\left(1\cdot\Delta\overline{v}_{if}\right) + 3\,\Delta\overline{m}_i\,V_i = q\,\Delta\overline{v}_{if}\quad. \tag{4.44}$$

4.8. Stability Analysis

Resolving (4.37)–(4.44) into the d–q components leads to the following state equations:

$$\frac{d\boldsymbol{x}}{dt} = \boldsymbol{A}\,\boldsymbol{x} \tag{4.45}$$

being

$$\boldsymbol{x} = \left[\Delta i_{Sd} \quad \Delta i_{Sq} \quad \Delta v_{id} \quad \Delta v_{iq} \quad \Delta i_{od} \quad \Delta i_{oq} \quad \Delta v_{ifd} \quad \Delta v_{ifq}\right]^T \tag{4.46}$$

$$\boldsymbol{A} = \begin{bmatrix} -\frac{R_S}{L_T} & \omega_i & -\frac{1}{L_T} & 0 & 0 & 0 & 0 & 0 \\ -\omega_i & -\frac{R_S}{L_T} & 0 & -\frac{1}{L_T} & 0 & 0 & 0 & 0 \\ \frac{1}{C_f} & 0 & 0 & \omega_i & -\frac{q}{C_f} & 0 & K & 0 \\ 0 & \frac{1}{C_f} & -\omega_i & 0 & 0 & 0 & 0 & -K \\ 0 & 0 & \frac{q}{L_L} & 0 & -\frac{R_L}{L_L} & \omega_o & -\frac{q}{L_L} & 0 \\ 0 & 0 & 0 & 0 & -\omega_o & -\frac{R_L}{L_L} & 0 & 0 \\ 0 & 0 & \frac{1}{\tau} & 0 & 0 & 0 & -\frac{1}{\tau} & 0 \\ 0 & 0 & 0 & \frac{1}{\tau} & 0 & 0 & 0 & -\frac{1}{\tau} \end{bmatrix} \tag{4.47}$$

where

$$K = \frac{q^2}{C_f} \Re_e \left[\frac{1}{\overline{Z}_L} \right]. \tag{4.48}$$

The stability limit of the matrix converter can be evaluated by analyzing the eigenvalues of the state matrix $\boldsymbol{A}$, through a numerical approach.

This approach demonstrates the existence of a limit value for the voltage transfer ratio, above which the real part of at least one eigenvalue becomes positive and the linear system is unstable. For this purpose the voltage transfer ratio has been used to represent the maximum power that the matrix converter is able to deliver to the load, as a function of the time constant τ of the digital low-pass voltage filter. With reference to the system parameters defined in Tab. 4.1, the results of the stability analysis are summarized in Fig. 4.7, with reference to the case of $\omega_o = 2\pi$ 25 rad/s.

As is possible to see, a significant improvement of the system stability can be achieved by applying the digital low-pass filter to the input voltage values used for the calculation of the duty-cycles. In this case, a value 0.4 ms for the filter time constant τ allows the theoretical maximum voltage transfer ratio

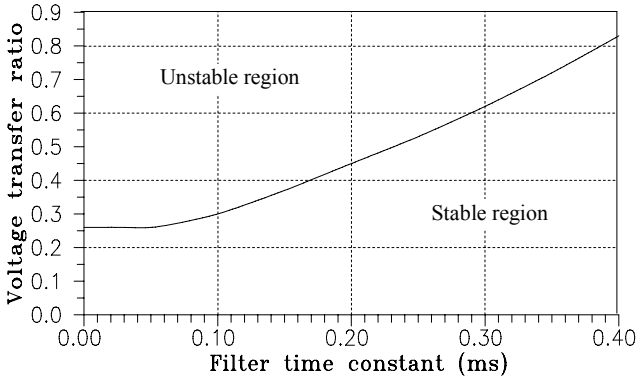

Fig. 4.7 - Stability limit of the matrix converter voltage transfer ratio as function of the filter time constant τ.

to be practically achieved.

The proposed approach can be useful in the design of the digital input filter, providing an accessible method of checking for the occurrence of instabilities.

The digital filter time constant can be increased in order to ensure the system stability for any operating condition, but as a counterpart a high value of τ reduces the capability of the control system to compensate the input voltage perturbations. These aspects will be analyzed in details in the next paragraph.

4.9. Analysis of the Output Voltage Distortion

In presence of input voltage disturbances, depending on the strategy used to control the matrix converter, the output voltages might be more or less affected by distortions. In this paragraph, the analysis is focused on the effects introduced on the output voltages by the presence of the digital low-pass filter.

For this purpose, balanced and sinusoidal output voltages are assumed as reference, and a small input voltage disturbance is superimposed to balanced and sinusoidal input voltages. The input voltage disturbance is defined by

$$\Delta\overline{v}_i = \overline{V}_{iH}\, e^{j\omega_H t} \quad . \tag{4.49}$$

The variable $\overline{V}_{iH}$ determines the amplitude and the phase angle of the disturbance harmonic component, whereas ω_H defines the corresponding angular frequency with respect to the input reference frame.

Solving (4.40), (4.41), (4.43) and (4.44), and introducing (4.49), leads to the following expression for the output voltage disturbance of the matrix converter:

$$\Delta\overline{v}_o = \frac{q}{2}\left[\overline{V}_{iH}\left(\frac{j\,\omega_H\,\tau}{1+j\omega_H\tau}\right)e^{j\,\omega_H\,t} + \overline{V}_{iH}^{*}\left(\frac{-j\,\omega_H\,\tau}{1-j\omega_H\tau}\right)e^{-j\,\omega_H\,t}\right] \tag{4.50}$$

This equation can be considered as the transfer function between the output and input voltage disturbances. The output voltage disturbance consists of two harmonic components having the angular frequency ω_H and $-\omega_H$, respectively, in the output reference frame. The two harmonic components have the same amplitude, which is related to the input voltage disturbance, the voltage transfer ratio and the digital low-pass filter time constant.

Actually, the two ratios containing ω_H and $-\omega_H$ are the analytical expressions of two high-pass filter. As a consequence, high frequency input voltage disturbances are reflected on the output side, whereas low frequency input voltage disturbances are attenuated as function of the filter time constant. For high values of τ ($\tau \to \infty$) the input disturbances are completely transferred to the output side. If the action of the low-pass filter is eliminated ($\tau = 0$), the output voltages are balanced and sinusoidal even in presence of input voltage disturbances.

4.10. Computer Simulations of a MC with Input Digital Filter

In order to verify the analytical approach, the behaviour of the system composed by a non-ideal supply, an input L-C filter and a matrix converter feeding a three-phase symmetrical R-L passive load, has been tested by numerical simulations. The switches of the matrix converter have been assumed as ideal switches.

The simulation takes into account the switching behaviour of the matrix converter and the delay related to the digital implementation of the control algorithm.

The values of the system parameters are that of Tab. 4.1, and are the same used in Fig. 4.7.

The control strategy adopted for the matrix converter is the SVM technique, with a double-sided switching pattern and a cycle period of 80 μs [7].

The behaviour of the system, in terms of stability, has been analyzed for different values of the voltage transfer ratio and of the time constant of the digital low-pass input filter.

The results obtained are presented in Figs. 4.8, 4.9, and 4.10.

Fig. 4.8(a) shows the steady-state waveform of the input voltage of the matrix converter, with a voltage transfer ratio of 0.2, and with $\tau = 0$. The steady-state waveforms of the line current and load current are illustrated in Figs. 4.8(b) and (c), respectively.

As is possible to see, all the waveforms are sinusoidal and characterized by a small ripple, due to the high switching frequency of the matrix converter.

Fig. 4.9(a) shows the waveform of the input voltage of the matrix converter with a voltage transfer ratio of 0.35, and with $\tau = 0$. The waveforms of a line current and a load current are illustrated in Figs. 4.9(b) and (c), respectively. In these operating conditions the input voltage and current waveforms are heavily distorted, showing large oscillations at a frequency practically equal to the resonance frequency of the input L-C filter.

This behaviour is due to the predicted instability phenomena that occur when the voltage transfer ratio exceeds the stability limits shown in Fig. 4.7, even if the switching frequency (12.5 kHz) is much higher than the resonance frequency of the input L-C filter (1.6 kHz).

These results are in agreement with the stability limits determined by the proposed analysis. Fig. 4.7 gives a voltage transfer ratio limit of 0.27 for the system under study, with $\tau = 0$.

In the first case (Fig. 4.8), the voltage transfer ratio is lower than the limit value, and the system is stable. In the second case (Fig. 4.9), the voltage transfer ratio is higher than the limit value, and the system becomes unstable.

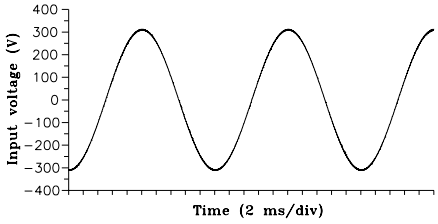

Fig. 4.8(a) - Matrix converter input line to neutral voltage, q=0.2, τ=0 ms.

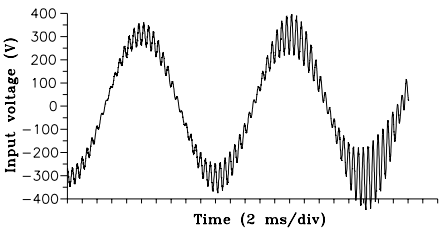

Fig. 4.9(a) - Matrix converter input line to neutral voltage, q=0.35, τ=0 ms.

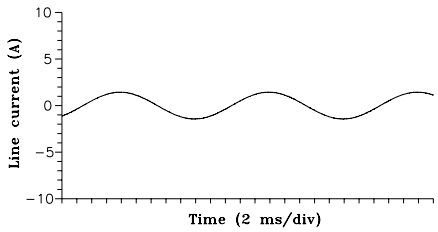

Fig. 4.8(b) - Line current, q=0.2, τ=0 ms.

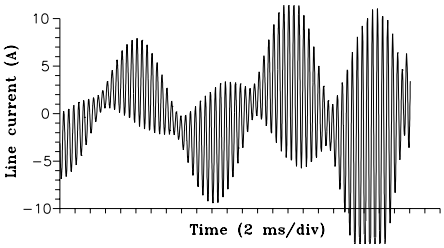

Fig. 4.9(b) - Line current, q=0.35, τ=0 ms.

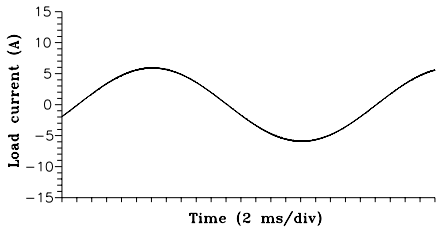

Fig. 4.8(c) - Load current, q=0.2, τ=0 ms.

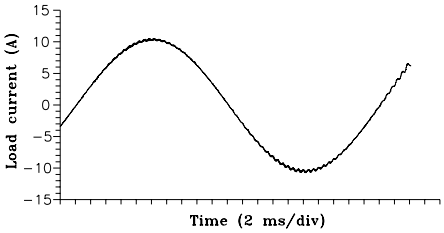

Fig. 4.9(c) - Load current, q=0.35, τ=0 ms.

Any small perturbation due to the switching effects, or coming from input/output side, causes the system to leave the stable and steady-state operating conditions.

It should be noted that, initially, in spite of the large oscillations at the input side, the waveform of the load current is nearly sinusoidal, as can be seen in Fig. 4.9(c), because of the fast adaptation of the duty-cycles, based on the on-line measurement of the input voltages.

Fig. 4.10(a) shows the steady-state waveform of the input voltage of the matrix converter with an output to input voltage transfer ratio of 0.55, with $\tau = 0.4\ ms$. The steady-state waveforms of the line current and load current

are illustrated in Figs. 4.10(b) and (c), respectively.

As is possible to see, all the waveforms are sinusoidal and characterized by a small ripple. This result demonstrates the effectiveness of the digital low-pass filter in terms of stability.

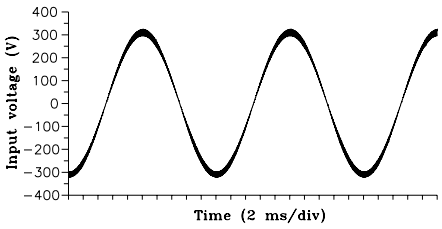

Fig. 4.10(a) - Matrix converter input line to neutral voltage, q=0.55, τ=0.4 ms.

In order to emphasize the behaviour of the control system under operating conditions characterized by input voltage distortion, a negative sequence fundamental component has been superimposed to the positive sequence fundamental component of the supply voltages. The amplitude of the negative sequence is 10% of the positive sequence amplitude.

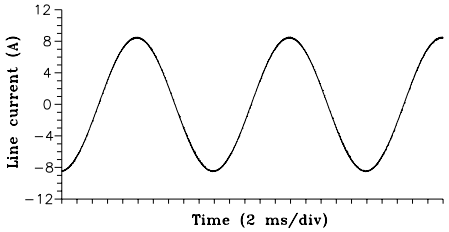

Fig. 4.10(b) - Line current, q=0.55, τ=0.4 ms.

Firstly, the system behaviour has been evaluated without the digital low-pass input voltage filter ($\tau = 0$). The waveforms of the input voltage and output current, obtained with a voltage transfer ratio of 0.2, are shown in Figs. 4.11(a) and (d), respectively. Figs. 4.11(b) and (e) represent the locus described by the input voltage and load current space vectors, respectively.

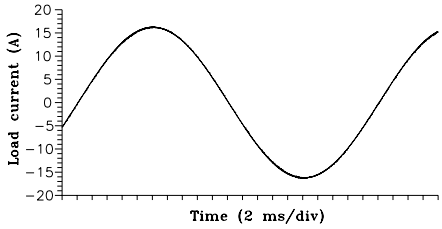

Fig. 4.10(c) - Load current, q=0.55, τ=0.4 ms.

The corresponding harmonic spectra in p.u. of the fundamental component are shown in Figs. 4.11(c) and (f). These results demonstrate that the control system is stable and is able to completely compensate the input voltage disturbance.

As a second step, the system behaviour has been verified in presence of the digital low-pass input voltage filter, with $\tau = 0.4$ ms. The results obtained

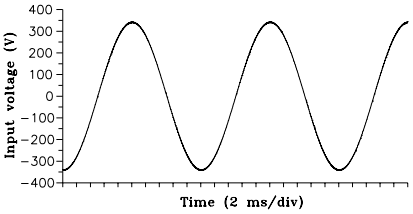

Fig. 4.11(a) - Matrix converter input line to neutral voltage, q=0.2, τ=0 ms (unbalance degree 10%).

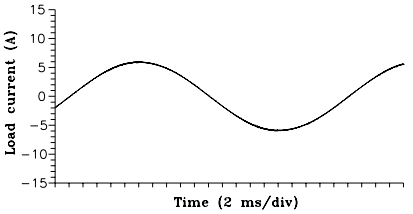

Fig. 4.11(d) - Load current, q=0.2, τ=0 ms (unbalance degree 10%)

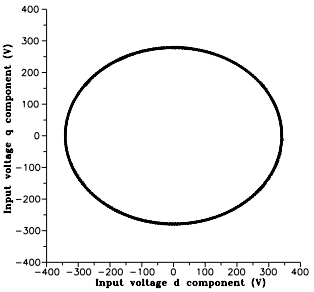

Fig. 4.11(b) - Locus of the matrix converter input line to neutral voltage space vector.

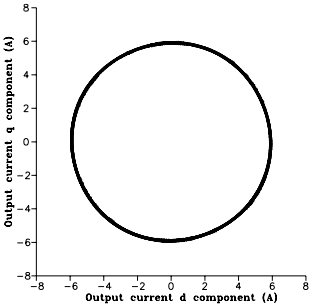

Fig. 4.11(e) - Locus of the load current space vector.

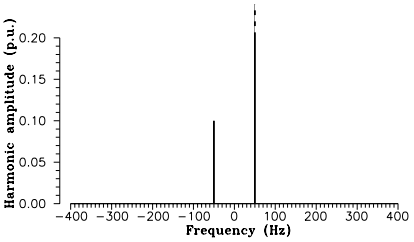

Fig. 4.11(c)- Spectrum of the matrix converter input line to neutral voltage space vector.

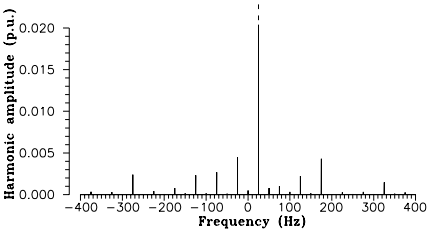

Fig. 4.11(f) - Spectrum of the load current space vector.

are shown in Figs. 4.12(a)-(f).

In this case the stability of the system would be improved, but the capability to compensate the input voltage disturbance is reduced.

Figs. 4.12(d)-(f) clearly show that the load current is characterized by the presence of harmonic components, according to the theoretical results expressed by (4.50).

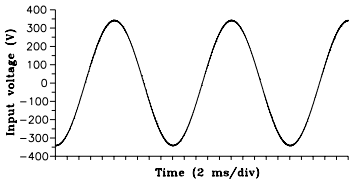

Fig. 4.12(a) – Matrix converter input line to neutral voltage, q=0.2, τ=0.4 ms (unbalance degree 10%).

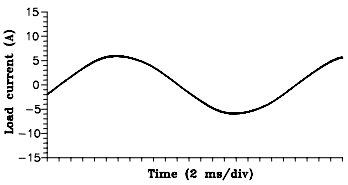

Fig. 4.12(d) – Load current, q=0.2, τ=0.4 ms (unbalance degree 10%).

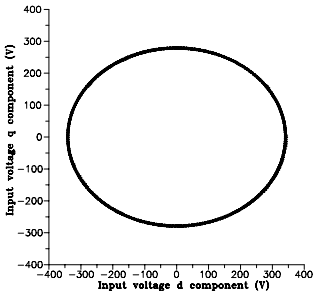

Fig. 4.12(b) – Locus of the matrix converter input line to neutral voltage space vector.

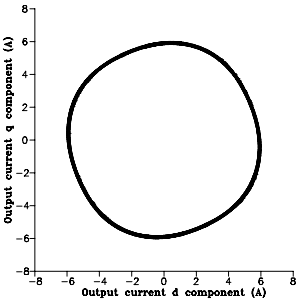

Fig. 4.12(e) – Locus of the load current space vector.

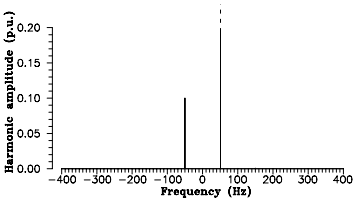

Fig. 4.12(c)–Spectrum of the matrix converter input line to neutral voltage space vector.

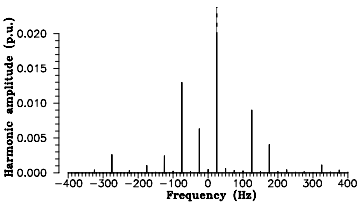

Fig. 4.12(f) – Spectrum of the load current space vector.

A further simulation has been carried out considering as input voltage perturbation a 5^{th} harmonic component, having amplitude of 10% of the fundamental component.

The system behaviour has been firstly evaluated without the digital low-pass input voltage filter ($\tau = 0$), and then in presence of the filter.

The results obtained are illustrated in Figs. 4.13 and 4.14, respectively. In the case of $\tau = 0$ (Fig. 4.13) the system compensate the input voltage disturbance and the load current is practically sinusoidal.

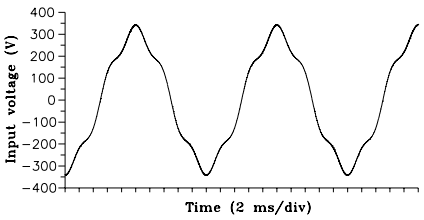

Fig. 4.13(a) - Matrix converter input line to neutral voltage, q=0.2, τ=0 ms (10% 5^{th} harmonic).

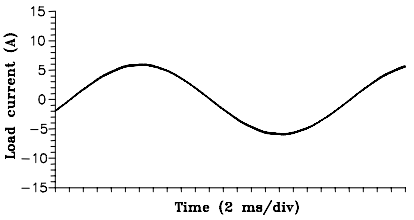

Fig. 4.13(d) - Load current, q=0.2, τ=0 ms (10% 5^{th} harmonic).

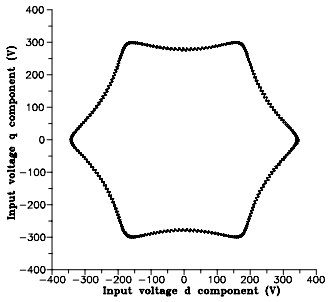

Fig. 4.13(b) - Locus of the matrix converter input line to neutral voltage space vector.

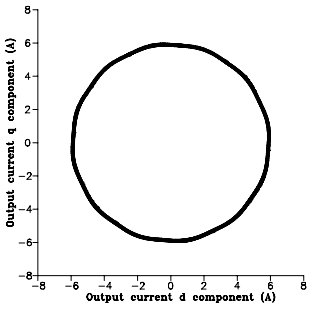

Fig. 4.13(e) - Locus of the load current space vector.

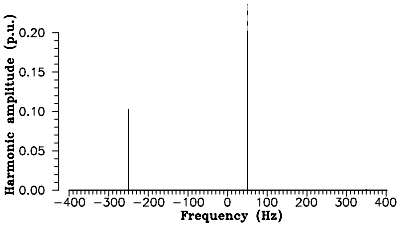

Fig. 4.13(c)-Spectrum of the matrix converter input line to neutral voltage space vector.

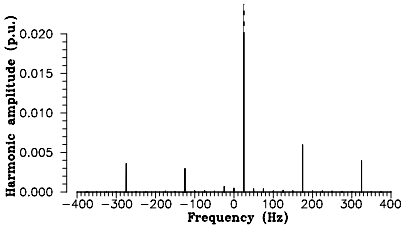

Fig. 4.13(f) - Spectrum of the load current space vector.

In the case of τ = 0.4 ms (Fig. 4.14) the input voltage disturbance is partially reflected at the output side, and the output current is characterized by the presence of harmonic components, as predicted by (4.50) and shown in Fig. 4.14(f).

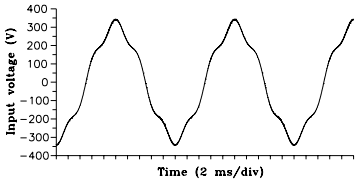

Fig. 4.14(a) – Matrix converter input line to neutral voltage, q=0.2, τ=0.4 ms. (10% 5th harmonic)

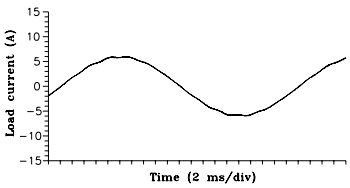

Fig. 4.14(d) – Load current, q=0.2, τ=0.4 ms. (10% 5th harmonic)

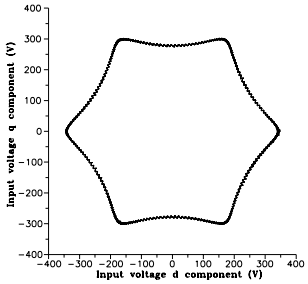

Fig. 4.14(b) – Locus of the matrix converter input line to neutral voltage space vector.

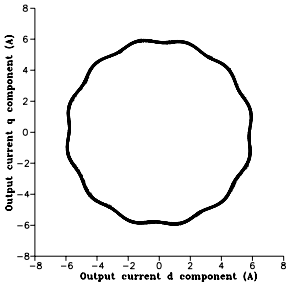

Fig. 4.14(e) – Locus of the load current space vector.

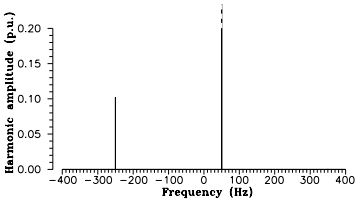

Fig. 4.14(c)– Spectrum of the matrix converter input line to neutral voltage space vector.

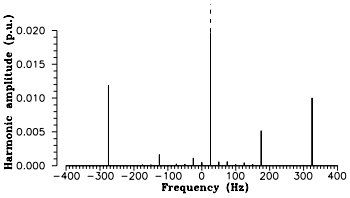

Fig. 4.14(f) – Spectrum of the load current space vector.

4.11. Important Remarks About Stability

Actually, stability issues of power converters and electrical drives have been already discussed in several papers [43]-[47]. With reference to matrix converters it is worth noting that the possibility of unstable behaviour is not inherent in matrix converter operation, but rather related to the control algorithm implementation. It has been previously mentioned that it is

opportune to calculate the duty-cycles of the switching configurations on the basis of the instantaneous values of the input voltages when studying the operation of matrix converters under unbalanced and distorted supply voltages. The feedforward action of this type of control is the main potential reason of the instability phenomena. It has been also shown that the power limit can be sensibly improved if the calculation of the duty-cycles is carried out using filtered values of the matrix converter input voltages.

In practical applications, the instability phenomena could be not observed if the voltage measurement is performed at the input of the L-C filter, rather than at the input of the converter. In this case the system stability is improved because the filtering action performed by the proposed digital filter is replaced, to some extent, by the filter inductance L_f. Actually, instability is not eliminated, but only moved towards higher power levels.

However, it can be noted that the voltage measurement at the L-C filter input is not an optimal solution owing to the following reasons:

- The L-C filter is usually designed in order to satisfy EMC requirements rather than to guarantee the system stability. In addition, it determines a sensible phase-shift in the measured voltage at the fundamental frequency, which can deteriorate the output voltage since the duty-cycles are not calculated on the basis of the actual voltage.

- The digital filter, instead, can be tuned so that the system shows the best performance and, in addition, it is implemented in the synchronous reference frame, thus introducing no phase shift at the fundamental frequency.

- If the matrix converter is connected to a weak network, the filter inductance can be omitted because the grid inductance is sufficient for the filter requirements; it is then possible to avoid the presence of a bulky component. In this case the matrix converter stability can be improved only by using the digital low-pass filter applied to the voltages measured across the filter capacitors.

The effects introduced by digital controllers, such as the sample and hold circuit and the switching period delay, also affect the stability of matrix converters. The digital controller samples the input voltages at the beginning of the cycle period, then calculates the duty-cycles of the switching configurations that will be applied at the beginning of the next cycle period,

thus determining a delay of one cycle. It has long been known that a time delay could remarkably modify the stability of the drive system.

The proposed analytical approach does not take into account the effect of the control delay and therefore it gives reliable results only for low values of the cycle period. The value of 80μs adopted in the numerical simulations is sufficient for the implementation of the control algorithm and provides results in good agreement with the theoretical analysis. In [52] it has been clearly emphasized the influence of the cycle period width on the stability of the drive system.

A further issue, relevant for the system stability, is the energy losses in the input filter and in the converter switches, which influence the damping capability of the drive system. In fact the energy losses can reduce the voltage and current oscillations so improving the system stability.

For this purpose the behaviour of the matrix converter has been also verified using the electronic circuit analysis program MICRO-CAP 7.0. In this program it is possible to use more accurate models of the power switches and then to improve the simulation reliability. The models adopted for IGBTs and diodes are MICRO-CAP general models: IGBT type IRG4PH50U, diode type HFA16PB120.

The matrix converter control technique and the system parameters are the same used in the previous paragraph.

Fig. 4.15 shows the transition from stable to unstable operation of the matrix converter obtained increasing the voltage transfer ratio q, for a given value of the filter time constant (τ=0.2 ms). The upper traces represent the input and output current waveforms, the medium trace is the voltage measured at the input side of the L-C filter, and the bottom trace is the voltage measured across the filter capacitance. As can be seen, the system is stable for q=0.3 and unstable for q=0.7, in perfect agreement with Fig. 4.7.

For q=0.5 the system shows a stable behaviour, although the voltage transfer ratio is slightly greater than the stability limit of Fig. 4.7. This can be explained by the damping introduced by the energy losses and the effect of the cycle period delay.

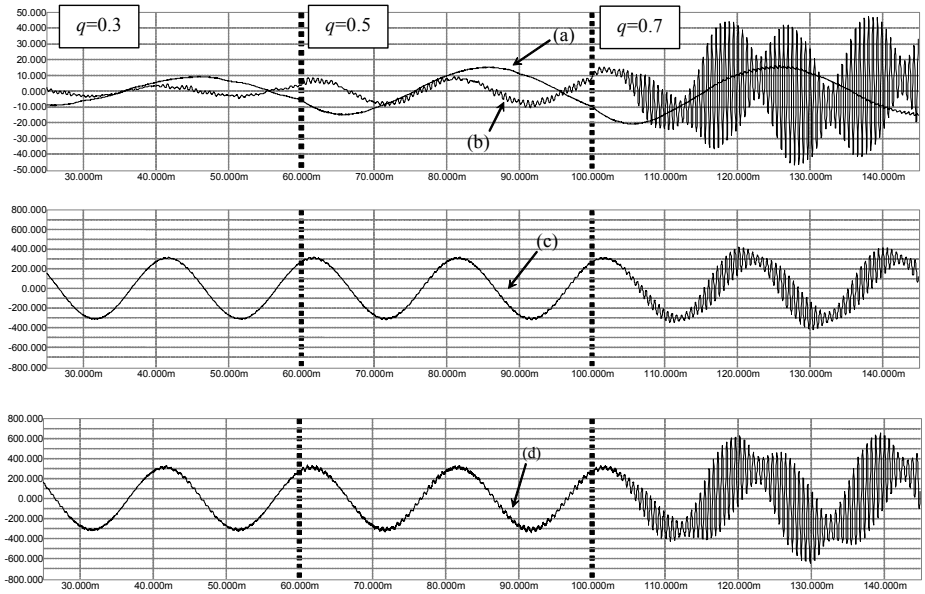

Fig. 4.15 - Transition from stable to unstable operation changing q from 0.3 to 0.5 and then to 0.7, with τ=0.2 ms. a) output current, b) input current, c) filter input voltage, d) matrix converter input voltage.

4.12. Conclusion

The MC can be considered as a current source at the input side, then a L-C filter topology is needed to smooth the input currents and to satisfy the EMI requirements. A reactive current flows through the input filter capacitor of the matrix converter, which causes a reduction of the power factor especially at low output power. As a consequence, the capacitor should be chosen in order to ensure at least a power factor of 0.8 with 10% of the rated output power. After the selection of the capacitor, the input filter inductance can be selected in order to satisfy the IEEE Recommended Practices and Requirements for Harmonic Control in Electrical Power Systems (IEEE Std. 519-1992).

If the input filter is well designed, current harmonics at frequencies greater or equal to the switching frequency are smoothed to a certain extent. On the

other hand, current harmonics at a frequency close to the resonance frequency of the filter could be amplified determining oscillations of the voltage across the capacitor, which in turn have a negative effect on the MC behaviour leading to possible unstable operating conditions.

In order to increase the system stability it is possible to add a damping resistance in parallel with the filter inductance. A suitable value of this resistance allows the high frequency current harmonics to close through the source leading to lower oscillations of the capacitor voltage. The damping effect and then the stability limit increases while reducing the value of the resistance. Unfortunately, this solution is effective for improving the MC stability but it is of detriment for the EMI requirements. Therefore, a compromise should be find between stability and input current quality.

A different approach which avoids the need of damping resistances is to calculate the duty cycles of the MC switching configurations by means of input voltage values filtered by a low-pass filter implemented in a synchronous reference frame. This method has been proved to be very effective for increasing the power limit and is included in the control scheme of the MC analyzed in this chapter.

In this chapter a method for the stability analysis of matrix converters has been proposed. For this purpose a variable state average model of the whole system, including the grid impedance, the input L-C filter and the load, has been derived, and the stability of the system has been evaluated by analyzing the migration of the eigenvalues of the linearized state matrix.

By using the proposed approach, the maximum output power can be calculated as function of the digital low-pass filter time constant, for given values of the grid impedance, input L-C filter parameters and load. Simulation results have been performed showing the validity of the proposed method for low values of the cycle period, and emphasizing the improvement of the power limit achievable by changing the time constant of the digital low-pass filter.

Chapter 5

Advanced Models for Stability Analysis

Abstract

In this chapter a theoretical analysis of the stability of matrix converters is presented with the aim of predicting possible critical operating conditions. It is verified that all the system parameters affect more or less the stability, including the delay introduced by the digital controller and the power losses. The theoretical analysis is supported by numerical simulations and experimental results carried out on a matrix converter prototype.

5.1. Introduction

In chapter 4, MC stability has been investigated through a small signal analysis of the whole system composed by the power grid, the input filter, the MC and the load. It has been shown that the power limit is related to all

system parameters, and in particular to the grid impedance and the input L-C filter parameters.

In addition, the analysis has been further developed showing that the power limit can be increased if the duty-cycles of the switching configurations are calculated using input voltages filtered by a digital low-pass filter implemented in a synchronous reference frame. Using this filter the capability of the matrix converter to compensate input voltage disturbances is affected to some extent, but the stability limit can be sensibly improved. It has been also verified that including a damping resistance in the input filter allows a significant increase of the stability limit.

However, up to now, the analysis has neglected that the control of matrix converter is usually achieved with a digital microprocessor, whose calculations are performed within a finite cycle period. The digital processor samples the input voltages and determines the configuration of the matrix converter switches that are modified at the beginning of the next cycle period, thus determining one cycle delay.

It has long been known that a time delay could remarkably modify the system stability.

The analytical approach proposed in Chapter 4 does not take into account the effect of the control delay and therefore it gives reliable results only for low values of the cycle period.

In [52] the effects due to the presence of a sample and hold circuit and a cycle period delay in the digital control of MCs have been investigated using a small signal analysis combined with a frequency domain analysis. It has been shown that, depending on the system parameters, the cycle period value affects more or less the power limit. The presence of unstable operation in MCs has been also documented in [25], where the same small signal analysis as proposed in [18],[53] has been used. In particular, the effect of filtering differently the magnitude and the phase angle of the input voltage vector has been investigated. The existence of potential unstable operating conditions has been experimentally proved, emphasizing the influence of the system parameters.

In the first part of this chapter a complete analysis of the MC stability taking account of all the system parameters including the input voltage filter and the effects of the digital control is presented. The analysis is developed in

the frequency domain, using a small signal analysis similar to that carried out in [52]. The new contribution is the analytical approach proposed for the analysis of MC stability, which makes it possible to demonstrate the existence of possible unstable operating conditions and to emphasize which parameters may affect, more or less, the stability power limit. It has been verified that, besides the system parameters, also the power losses must be considered in order to predict the stability limit of matrix converter.

Despite of its completeness, the proposed method uses a small-signal analysis that makes difficult the interpretation of the physical phenomena related to instability.

During the study of instability phenomena, initially, it is possible to observe small high frequency oscillations superimposed on the input voltages. Then, owing to the effects of these oscillations on the calculations of the duty-cycles, the amplitude of the voltage oscillations increases preventing the normal operation.

In the second part of this chapter a different approach is presented for the analysis of the MC stability, which is based on a large signal analysis carried out in the frequency domain. The main advantage of this approach is the easy comprehension of the instability origin and the possibility to relate the amplitude of the input voltage oscillations to the operating conditions.

As the proposed analysis is based on a large-signal model, it is possible to investigate the non-linear behaviour of MCs in the case of large input voltage perturbations. This allows explaining phenomena that have not been clearly understood until now, such as the unstable behaviour of MCs in terms of limit cycles.

Several numerical simulations are presented showing current and voltage waveforms under stable and unstable operating conditions. Finally, experimental results carried out on a MC prototype are given for supporting the theoretical analysis and for proving the effect of different filtering methods applied to the input voltages.

5.2. Input/Output Matrix Converter Performance

The whole system, which is composed by a power supply, a second order input R-L-C filter, and a matrix converter feeding a R-L passive load, is represented in Fig. 5.1, where space vector notation is used for the

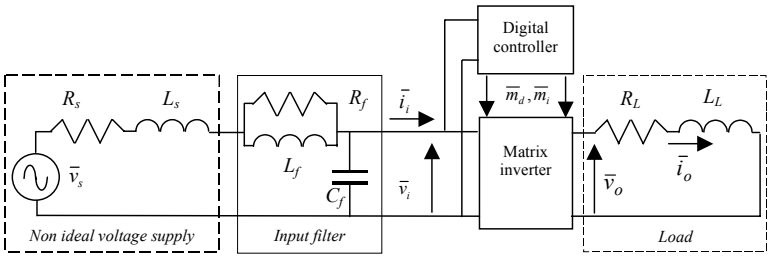

Fig. 5.1 - Basic matrix converter scheme.

representation of the system variables.

In this paragraph the main equations related to the system represented in Fig. 5.1 will be introduced. As usual, the analytical developments are carried out neglecting the effects of the switching harmonics, considering for the output voltages and input currents their average values over a cycle period T_p.

The variable t, s and z will be used to distinguish between the time domain, the Laplace domain and the domain of the sampled signal, respectively.

With reference to Fig. 5.1, the equation for the input side of the converter, written in the Laplace domain, is as follows:

$$\bar{v}_{eq}(s) = \overline{Z}(s)\bar{i}_i(s) + \bar{v}_i(s) \tag{5.1}$$

where $\bar{v}_{eq}(s)$ and $\overline{Z}(s)$ are the equivalent voltage and the impedance of the voltage source and the input filter, considered as a single bipole.

The equation of the output side of the converter can be expressed as follows

$$\bar{i}_o(s) = \overline{Y}(s)\bar{v}_o(s) \tag{5.2}$$

where $\overline{Y}(s)$ is the admittance of the passive linear load.

The input-output relationships (2.35)-(2.36) of the matrix converter, written using the duty-cycle space vectors $\overline{m}_d$ and $\overline{m}_i$ [7], are here reported for convenience:

$$\overline{v}_o(t) = \frac{3}{2}\left[\overline{m}_i^*(t)\overline{v}_i(t) + \overline{m}_d(t)\overline{v}_i^*(t)\right] \tag{5.3}$$

$$\bar{i}_i(t) = \frac{3}{2}\left[\overline{m}_i(t)\bar{i}_o(t) + \overline{m}_d(t)\bar{i}_o^*(t)\right]. \tag{5.4}$$

The symbol '*' is used to represent complex conjugate variables.

If the input current vector is kept in phase with the input voltage vector, the problem of the determination of the duty-cycle space vectors is completely solved by the following equations:

$$\overline{m}_{d,ref}(t) = \frac{\overline{v}_{o,ref}(t)}{3\overline{v}_i^*(t)} \tag{5.5}$$

$$\overline{m}_{i,ref}(t) = \frac{\overline{v}_{o,ref}^*(t)}{3\overline{v}_i^*(t)}. \tag{5.6}$$

where $\overline{v}_{o,ref}(t)$ is the reference output voltage.

Unfortunately, at any instant t the duty-cycles $\overline{m}_d(t)$ and $\overline{m}_i(t)$ cannot have exactly the values $\overline{m}_{d,ref}(t)$ and $\overline{m}_{i,ref}(t)$ because the digital controller, which measures the input voltages and calculate (5.5) and (5.6) at each cycle period, applies the new switching configurations only at the beginning of the next cycle period, thus introducing a time delay. This means that $\overline{m}_d(t)$ and $\overline{m}_i(t)$ are delayed with respect to the desired values.

The model represented in Fig. 5.2 has been developed to take into account the effects of the control system delay. S&H is a sample and hold device, z^{-1} is the delay operator and ZOH a zero-order hold.

It should be noted that, using this model, $\overline{m}_d(t)$ and $\overline{m}_i(t)$ in (5.3) and (5.4) are constant during a cycle period T_p, while the input voltage vector

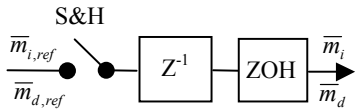

Fig. 5.2 - System used to represent the effect of the digital controller.

$\overline{v}_i(t)$ and the output current vector $\overline{i}_o(t)$ are free to change.

According to Fig. 5.2, the relationship between $\overline{m}_d(t)$ and $\overline{m}_{d,ref}(t)$ or between $\overline{m}_i(t)$ and $\overline{m}_{i,ref}(t)$ can be described through the transfer function $\overline{D}(s)$ in the Laplace domain given by

$$\overline{D}(s) = \frac{\overline{m}_d(s)}{\overline{m}_{d,ref}(s)} = \frac{\overline{m}_i(s)}{\overline{m}_{i,ref}(s)} = \left(\frac{1 - e^{-T_p s}}{T_p s} \right) e^{-T_p s} . \tag{5.7}$$

In (5.7) the term inside the brackets is related to the sampling and reconstruction processes, whereas the exponential term outside the brackets is due to the delay introduced by the digital controller.

In order to study the stability of the system, it is opportune to linearize the system equations around a steady-state operating point corresponding to balanced and sinusoidal supply voltages.

5.3. Steady-State Operating Conditions with Balanced and Sinusoidal Supply Voltages

In steady-state operating conditions, with balanced and sinusoidal supply voltages, the input voltages and the reference output voltages can be represented by means of rotating space vectors with constant magnitudes, as follows:

$$\overline{V}_i(t) = \overline{V}_i \, e^{j\omega_i t} \tag{5.8}$$

$$\overline{V}_{o,ref}(t) = \overline{V}_{o,ref} \, e^{j\omega_o t} \tag{5.9}$$

where ω_i and ω_o are the input and output angular frequency, respectively.

Substituting (5.8) and (5.9) in (5.5) and (5.6), leads to the following steady-state expressions for $\overline{m}_{d,ref}(t)$ and $\overline{m}_{i,ref}(t)$:

$$\overline{M}_{d,ref}(t) = \frac{\overline{V}_{o,ref}}{3\overline{V}_i^*} \, e^{j(\omega_i + \omega_o)t} \tag{5.10}$$

$$\overline{M}_{i,ref}(t) = \frac{\overline{V}_{o,ref}^{*}}{3\overline{V}_{i}^{*}} e^{j(\omega_i - \omega_o)t} . \tag{5.11}$$

The actual values of the duty-cycle space vectors $\overline{M}_d$ and $\overline{M}_i$ could be calculated applying (5.7) to (5.10) and (5.11), respectively. It is worth noting that the delay introduced by the digital filter on the fundamental harmonics at frequencies ω_i and ω_o can be ignored and the actual values of the duty-cycle space vectors $\overline{M}_d$ and $\overline{M}_i$ can be assumed equal to their reference values $\overline{M}_{i,ref}$ and $\overline{M}_{d,ref}$. On the basis of this assumption, substituting (5.10) and (5.11) in (5.3), and taking (5.8) into account, it is possible to verify that also the output voltage can be assumed equal to its reference value

$$\overline{V}_o(t) = \overline{V}_{o,ref}(t) . \tag{5.12}$$

As a consequence, the steady-state output current vector can be expressed as

$$\bar{I}_o(t) = \overline{Y}(\omega_o)\overline{V}_{o,ref} e^{j\omega_o t} = \bar{I}_o e^{j\omega_o t} \tag{5.13}$$

where

$$\bar{I}_o = \frac{2}{3} \bar{\gamma} P_{id} \frac{\overline{V}_{o,ref}}{V_{ref}^2} \tag{5.14}$$

$$\bar{\gamma} = \frac{\overline{Y}(\omega_o)}{\mathrm{Re}\{\overline{Y}(\omega_o)\}} \tag{5.15}$$

$$P_{id} = \frac{3}{2} \overline{V}_{o,ref}(t) \cdot \bar{I}_o(t) . \tag{5.16}$$

In (5.14) and (5.16) P_{id} is the power delivered to the load by an ideal matrix converter in which $\overline{V}_o(t) = \overline{V}_{o,ref}(t)$.

5.4. Small Signal Equations

The stability analysis is performed under the assumption that a small perturbation $\Delta\overline{v}_i$ is superimposed on the input voltage space vector.

The linearization of the set of equations (5.1)-(5.7) around the steady-state operating point defined by (5.8)-(5.16) leads to the following set of small-signal equations:

$$0 = \overline{Z}(s)\Delta\bar{i}_i(s) + \Delta\bar{v}_i(s) \tag{5.17}$$

$$\Delta\bar{i}_o(s) = \overline{Y}(s)\Delta\bar{v}_o(s) \tag{5.18}$$

$$\Delta\bar{v}_o(t) = \frac{3}{2}\left[\overline{V}_i(t)\,\Delta\overline{m}_i^*(t) + \Delta\bar{v}_i(t)\,\overline{M}_i^*(t) + \Delta\bar{v}_i^*(t)\,\overline{M}_d(t) + \overline{V}_i^*(t)\,\Delta\overline{m}_d(t)\right] \tag{5.19}$$

$$\Delta\bar{i}_i(t) = \frac{3}{2}\left[\bar{I}_o(t)\,\Delta\overline{m}_i(t) + \bar{I}_o^*(t)\,\Delta\overline{m}_d(t) + \Delta\bar{i}_o(t)\,\overline{M}_i(t) + \Delta\bar{i}_o^*(t)\,\overline{M}_d(t)\right] \tag{5.20}$$

$$\Delta\overline{m}_{d,ref}(t) = -\frac{\overline{V}_{o,ref}(t)}{3\left[\overline{V}_i^*(t)\right]^2}\,\Delta\bar{v}_i^*(t) \tag{5.21}$$

$$\Delta\overline{m}_{i,ref}(t) = -\frac{\overline{V}_{o,ref}^*(t)}{3\left[\overline{V}_i^*(t)\right]^2}\,\Delta\bar{v}_i^*(t) \tag{5.22}$$

$$\Delta\overline{m}_d(s) = \overline{D}(s)\Delta\overline{m}_{d,ref}(s) \tag{5.23}$$

$$\Delta\overline{m}_i(s) = \overline{D}(s)\Delta\overline{m}_{i,ref}(s)\,. \tag{5.24}$$

The small signal equations (5.17)-(5.24) have been determined under the assumption that the supply voltage and the reference output voltage vector are not subjected to perturbations, namely

$$\Delta\bar{v}_s = 0 \tag{5.25}$$

$$\Delta\bar{v}_{o,ref} = 0\,. \tag{5.26}$$

Fig. 5.3 shows the equivalent circuit described by (5.17). As can be seen, the matrix converter acts as a non-linear harmonic current generator.

In order to determine the variation of the input current due to the perturbation of the input voltage, the system of equations (5.17)-(5.24) has to be solved. For this purpose, it is necessary to substitute the expression of $\Delta\bar{i}_o(s)$, given by (5.18) and (5.19), in (5.20), taking (5.8), (5.9) and (5.21)-(5.24) into account. To simplify the analysis, the low-pass filtering action of the load can be assumed high enough to neglect the output current variations

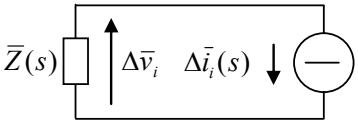

Fig. 5.3 - Equivalent circuit of the system for small signal analysis.

due to the output voltage variations, yielding

$$\Delta\overline{i}_o = 0\,. \tag{5.27}$$

Under this assumption, substituting (5.12), (5.14), (5.21)-(5.24) in (5.20) leads to the following expression for the variation of the input current in the Laplace domain:

$$\Delta\overline{i}_i(s) = -\frac{2}{3}\frac{P_{id}}{\left[\overline{V}_i^*\right]^2}\,\overline{D}_{eq}(s)\Delta\overline{v}_i^c(s-2j\omega_i) \tag{5.28}$$

where $\Delta\overline{v}_i^c(s)$ is the Laplace transform of $\Delta\overline{v}_i^*(t)$ and $\overline{D}_{eq}(s)$ is defined by

$$\overline{D}_{eq}(s) = \frac{1}{2}\left[\overline{\gamma}\,\overline{D}(s-j\omega_o) + \overline{\gamma}^*\,\overline{D}(s+j\omega_o)\right]. \tag{5.29}$$

The superscript "c" applied to the function $\Delta\overline{v}_i$ is used to represent the Laplace transform of the conjugate of $\Delta\overline{v}_i$. More details on this mathematical representation, that will be used in the following, can be found in Appendix C. It can be verified that for angular frequencies much higher than ω_o, $\overline{D}_{eq}(j\omega) \cong \overline{D}(j\omega)$.

It is possible to determine the fundamental equation that must be satisfied by the input voltage variation substituting (5.28) in (5.17), yielding

$$-\frac{2}{3}\,\overline{Z}(s)\overline{D}_{eq}(s)\frac{P_{id}}{\left[\overline{V}_i^*\right]^2}\,\Delta\overline{v}_i^c(s-2j\omega_i) + \Delta\overline{v}_i(s) = 0\,. \tag{5.30}$$

In the previous equation there are two unknowns, which are $\Delta\overline{v}_i$ and $\Delta\overline{v}_i^c$. Hence, to solve the problem, a further equation is needed. This equation can be found by applying the operator "c" to (5.30), leading to

$$-\frac{2}{3}\overline{Z}^{c}(s)\overline{D}_{eq}^{c}(s)\frac{P_{id}}{\overline{V}_{i}^{2}}\Delta\overline{v}_{i}(s+2j\omega_{i})+\Delta\overline{v}_{i}^{c}(s)=0\,. \tag{5.31}$$

To simplify (5.30) and (5.31) it is useful to introduce a rotating reference frame synchronous with the supply voltage, which is completely defined substituting the variable s with

$$s=u+j\omega_{i}\,. \tag{5.32}$$

The following set of equations, written in matrix form, can be determined introducing (5.32) in (5.30) and (5.31), yielding:

$$\boldsymbol{M}(u,P_{id})\begin{bmatrix}\Delta\overline{v}_{i}(u+j\omega_{i})\\ \Delta\overline{v}_{i}^{c}(u-j\omega_{i})\end{bmatrix}=\begin{bmatrix}0\\0\end{bmatrix} \tag{5.33}$$

where

$$\boldsymbol{M}(u,P_{id})=\begin{bmatrix}1 & -\frac{2}{3}\overline{Z}_{eq}(u+j\omega_{i})\frac{P_{id}}{(\overline{V}_{i}^{*})^{2}}\\ -\frac{2}{3}\overline{Z}_{eq}^{c}(u-j\omega_{i})\frac{P_{id}}{\overline{V}_{i}^{2}} & 1\end{bmatrix} \tag{5.34}$$

and

$$\overline{Z}_{eq}(s)=\overline{Z}(s)\overline{D}_{eq}(s)\,. \tag{5.35}$$

By means of the previous analytical developments, the small signal equations (5.17)-(5.24) have been summarized by (5.33)-(5.35), which completely describe the system response due to a small input voltage variation.

Analyzing (5.35) it can be concluded that the behaviour of the system is described by the equivalent grid impedance $\overline{Z}_{eq}$, given by a combination of the actual impedance and the transfer function of the delay introduced by the digital controller.

5.5. Stability Analysis

Due to presence of the controller delay, the system stability cannot be analyzed through the determination of the system poles, because the

characteristic equation does not have a polynomial form. The instability phenomena that can be observed in matrix converters are generally characterized by the presence of sinusoidal oscillations superimposed to the input voltage. Therefore it is possible to determine an equation representing the necessary condition for the existence of unstable operation writing (5.33) in the form of an harmonic balance. For this purpose the variable $u = j\omega$ must be introduced in (5.33) yielding

$$\boldsymbol{M}(j\omega, P_{id})\begin{bmatrix} \Delta\overline{v}_i(j\omega + j\omega_i) \\ \Delta\overline{v}_i^c(j\omega - j\omega_i) \end{bmatrix} = \begin{bmatrix} 0 \\ 0 \end{bmatrix}. \tag{5.36}$$

The set of equations (5.37) has a non-trivial solution only if the determinant of $\boldsymbol{M}$ is zero, leading to the following constraint equation:

$$\overline{\Gamma}(\omega)\left(\frac{2}{3}\frac{P_{id}}{V_i^2}\right)^2 = 1 \tag{5.37}$$

where

$$\overline{\Gamma}(\omega) = \overline{Z}_{eq}(j\omega + j\omega_i)\overline{Z}_{eq}^{c}(j\omega - j\omega_i)\,. \tag{5.38}$$

A necessary condition for (5.37) to be verified is the existence of an angular frequency ω_r satisfying the following constrain equation:

$$\arg\overline{\Gamma}(\omega_r) = 0\,. \tag{5.39}$$

According to (5.39), for ω equal to ω_r the function $\overline{\Gamma}(\omega)$ is a real positive number, having the dimension of the square of an impedance. It is then useful to define a new equivalent resistance given by

$$R_{res} = \sqrt{\overline{\Gamma}(\omega_r)}\,. \tag{5.40}$$

Substituting (5.40) in (5.37) and solving for P_{id} leads to the following value of the ideal power limit:

$$P_{id,lim} = \frac{3}{2}\frac{V_i^2}{R_{res}}\,. \tag{5.41}$$

As can be seen from (5.41), the maximum power limit is proportional to

the square of the input voltage and to the inverse of the equivalent resistance R_{res}.

To outline how the stability analysis can be applied, an example is discussed in the following.

The first step is to plot $\overline{\Gamma}(\omega)$ as a function of ω. The most significant range of frequencies is centred around the resonance frequency of the input L-C filter (including the grid inductance too), as it corresponds to the highest magnitudes of the function $\overline{\Gamma}(\omega)$. Fig. 5.4 shows the behaviour of $\overline{\Gamma}(\omega)$ with reference to the parameters given in Tab. 5.1 and for a cycle period T_p of 80μs.

Fig. 5.4(a) shows the magnitude of $\overline{\Gamma}(\omega)$, whereas the argument of $\overline{\Gamma}(\omega)$, normalized in the range [-π, π], is shown in Fig. 5.4(b). It can be noted that the argument of $\overline{\Gamma}(\omega)$ equals zero for several angular frequencies, i.e. $\omega_r^{'}$ and $\omega_r^{''}$. Obviously, the stability power limit has to be evaluated with reference to the worst case, corresponding to the highest magnitude of $\overline{\Gamma}(\omega)$. Among all the solutions, $\overline{\Gamma}(\omega)$ assumes the maximum value for $\omega = \omega_r^{'}$, as can be verified in Fig. 5.4(a). Then, the equivalent resistance R_{res} must be calculated assuming $\omega_r = \omega_r^{'}$ in (5.40). Once R_{res} is known, the stability power limit can be determined by means of (5.41).

In order to emphasize how the delay of the digital controller can improve the stability power limit, a further example is discussed with reference to an ideal controller with a cycle period T_p=0. In this case the behaviour of $\overline{\Gamma}(\omega)$ is illustrated in Fig. 5.5. The stability power limit, corresponding to the angular frequency $\omega_r^{'''}$, is sensibly lower compared with the one determined

TABLE 5.1 - SYSTEM PARAMETERS

Supply	Filter	Load
V_S = 110 V(rms), $\omega_i = 2\pi$ 50 rad/s, R_S = 0.55 Ω, L_S=0.90 mH	L_f = 1.16 mH, C_f= 4.5 μF R_f = 300 Ω	R_L= 8.2 Ω, L_L = 1.3 mH, $\omega_o = 2\pi$ 100 rad/s

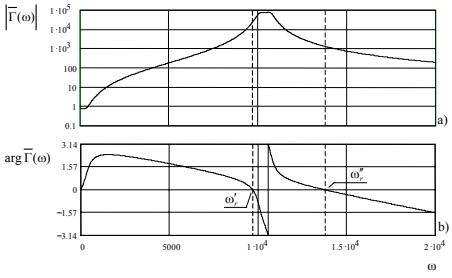

Fig. 5.4 – Behaviour of $\overline{\Gamma}(\omega)$ for the system parameters of Tab. I, with the effects of the digital controller delay, a) magnitude, b) argument .

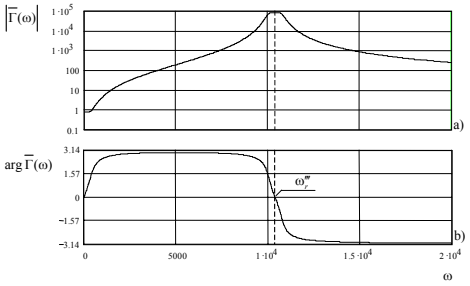

Fig. 5.5 – Behaviour of $\overline{\Gamma}(\omega)$ for the system parameters of Tab. I, without the effects of the digital controller delay, a) magnitude, b) argument .

for a non-ideal controller. It is clear, comparing Fig. 5.5 to Fig. 5.4, that the delay introduced by the digital controller has the effect to modify the $\arg\overline{\Gamma}(\omega)$ curve, whereas the magnitude is practically the same in both cases.

Owing to the delay, the argument of $\overline{\Gamma}(\omega)$ shown in Fig. 5.4(b) reaches zero at $\omega_r^{'}$, that is much lower than $\omega_r^{'''}$. As a consequence, also the equivalent resistance R_{res} is lower, leading to a higher stability power limit. Further details on the effect of the digital delay have been discussed in [52].

5.6. Small Signal Equations Introducing a Digital Filter

The power limit can be sensibly improved if the calculation of the duty cycles is carried out by filtering the matrix converter input voltages [24].

The equation of this filter, written in terms of Laplace transform, can be expressed as:

$$\overline{v}_{if}(s) = \overline{F}(s)\,\overline{v}_i(s) = \frac{1}{1+\tau(s-j\omega_i)}\,\overline{v}_i(s) \tag{5.42}$$

where $\overline{v}_{if}(s)$ is the Laplace transform of the filtered input voltage vector.

Owing to the discretization introduced by the digital controller, the transfer function $\overline{F}(s)$ in (5.42) can be only approximated by a Z-transform $\overline{F}_d(z)$. The expression of $\overline{F}_d(z)$ varies on the basis of the method used to

obtain the discrete-time formulation. The expression of $\overline{F}_d(z)$ used in this chapter is given in Appendix D. On the other hand, the analysis is developed in the Laplace domain, then it is necessary to represent $\overline{F}_d(z)$ in terms of Laplace transform, introducing the transfer function $\overline{F}_a(s)$. It is known that the expression of $\overline{F}_a(s)$ can be determined from $\overline{F}_d(z)$ introducing $z = e^{Ts}$, leading to

$$\overline{F}_a(s) = \overline{F}_d(e^{Ts}). \tag{5.43}$$

On the basis of (5.43), the variation of the filtered voltage in terms of Laplace transform can be approximated as follows:

$$\Delta\overline{v}_{if}(s) = \overline{F}_a(s)\Delta\overline{v}_i(s) \tag{5.44}$$

The approximation consists in neglecting the harmonic components of $\Delta\overline{v}_i(s)$ at a frequency comparable with or greater than the sampling frequency. In the system under study this assumption can be made because the input filter is of low-pass type.

Using the same procedure described in Paragraph 5.4, in which the input voltage variation $\Delta\overline{v}_i(s)$ is replaced by $\Delta\overline{v}_{if}(s)$, leads to the following expression for the input current variation:

$$\Delta\overline{i}_i(s) = -\frac{2}{3}\frac{P_{id}}{\left[\overline{V}_i^*\right]^2}\overline{D}_{eq}(s)\overline{F}_a^c(s-2j\omega_i)\Delta\overline{v}_i^c(s-2j\omega_i). \tag{5.45}$$

It can be noted that (5.45) corresponds to (5.28), the only difference is the presence of the transfer function $\overline{F}_a^c(s-2j\omega_i)$ which multiplies the term $\overline{D}_{eq}(s)$. As a consequence, the stability analysis carried out in Paragraph 5.5 is still valid provided that the equivalent impedance (5.35) is replaced with the following expression:

$$\overline{Z}_{eq}(s) = \overline{Z}(s)\overline{D}_{eq}(s)\overline{F}_a^c(s-2j\omega_i). \tag{5.46}$$

The presence of the transfer function $\overline{F}_a^c(s-2j\omega_i)$ modifies the equivalent impedance reducing its magnitude and changing its argument. If the filter is

correctly designed, this effect determines a reduction of the equivalent resistance (5.40) with an effective improvement of the stability power limit.

5.7. Model for the MC Losses

The power limit that can be calculated by means of the equations presented in the previous paragraphs is generally lower than that achievable in experimental tests. This because several factors, such as the iron losses in the inductances, or the power losses of the converter, may increase the damping effect of the real system, thus preventing unstable oscillations to arise.

In this paragraph a simplified method to represent the effects of the converter power losses on the system stability is proposed.

A non-ideal converter can be generally represented using a simplified model composed by an ideal converter and two generators that take into account the converter power losses, i.e. switching losses and conduction losses. The converter model that will be used in this chapter is represented in Fig. 5.6.

The output voltage is usually lower than the reference voltage since there is a voltage drop on the static switches. This voltage drop mainly determines the amount of the conduction losses $p_{cd}(t)$, and the voltage $\bar{v}_{cd}$ can be defined as follows:

$$\bar{v}_{cd}(t) = \frac{2}{3}\frac{p_{cd}(t)}{\left|\bar{i}_o(t)\right|^2}\bar{i}_o(t)\,. \tag{5.47}$$

Due to the switching losses $p_{sw}(t)$, the current at the input side of the non-ideal converter is generally higher than that of the ideal converter. This

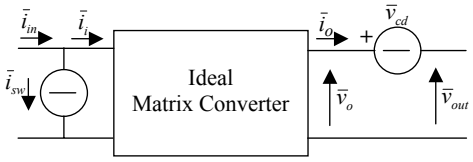

Fig. 5.6 - Basic scheme of a non-ideal matrix converter.

behaviour can be modelled with a current generator $\bar{i}_{sw}$ defined by

$$\bar{i}_{sw}(t) = \frac{2}{3}\frac{p_{sw}(t)}{\left|\overline{v}_i(t)\right|^2}\overline{v}_i(t). \tag{5.48}$$

The voltage generator in (5.47) and the current generator in (5.48) are defined so that they absorb an active power equal to p_{cd} and p_{sw}, respectively.

The presence of the power losses must be included in the small signal equations with the aim of predicting the power limit with more accuracy. In order to linearize (5.47) and (5.48), it is firstly necessary to determine the equations of the system in steady-state operating conditions with balanced and sinusoidal supply voltages. It is useful to represent the steady-state values of p_{cd} and p_{sw} introducing two equivalent resistances as follows

$$P_{cd} = \frac{3}{2}R_{cd}I_o^2. \tag{5.49}$$

$$P_{sw} = \frac{3}{2}\frac{V_i^2}{R_{sw}}. \tag{5.50}$$

Substituting (5.49) in (5.47) yields

$$\overline{V}_{cd}(t) = R_{cd}\bar{I}_o(t) \tag{5.51}$$

which demonstrates that at the fundamental frequency the conduction losses have the same effect as an additional resistance R_{cd} connected in series with the load. Therefore, (5.13)-(5.17) are still valid if the load admittance at angular frequency ω_o is replaced by the following expression:

$$\overline{Y}_{eq}(j\omega_o) = \frac{\overline{Y}(j\omega_o)}{1 + R_{cd}\overline{Y}(j\omega_o)}. \tag{5.52}$$

According to this approach, the main effect of the conduction losses is the reduction of the steady-state load current and, consequently, of the input current. The presence of switching losses, instead, does not modify anyone of the steady-state equations determined in Paragraph 5.15. Once the steady-state conditions have been determined, in order to proceed along with the linearization of (5.47) and (5.48), a model for the converter losses is needed.

The switching losses are proportional to the input voltage and the output

current, while the conduction losses are proportional to the output current [54]. Then, the simplest model for the converter losses can be represented by the following equations:

$$p_{cd}(t) = k_{cd}\, i_o \tag{5.53}$$

$$p_{sw}(t) = k_{sw} v_i\, i_o \tag{5.54}$$

where k_{cd} and k_{sw} are constant.

Taking (5.54) and (5.55) into account, the small signal equations corresponding to (5.47) and (5.48) are as follows:

$$\Delta\overline{v}_{cd} = 0 \tag{5.55}$$

$$\Delta\overline{i}_{sw}(t) = \frac{P_{sw}}{3V_i^2}\Delta\overline{v}_i(t) - \frac{P_{sw}}{3(\overline{V}_i^*(t))^2}\Delta\overline{v}_i^*(t) \tag{5.56}$$

The result expressed in (5.55) is justified by the fact that, according to (5.27), the variation of the output current is negligible.

In (5.56) the switching losses P_{sw} appear in both terms. In the first term the switching losses can be expressed through (5.50), whereas in the second term it is convenient to express the switching losses as a percentage of P_{id} introducing the ratio ε (Appendix E) defined as

$$\varepsilon = \frac{P_{sw}}{P_{id}}\,. \tag{5.57}$$

In this way it will be possible to define an equivalent impedance $\overline{Z}_{eq}(s)$ similar to (5.35) and (5.46). Taking (5.57) and (5.50) into account, (5.56) can be rewritten in the Laplace domain as follows:

$$\Delta\overline{i}_{sw}(s) = \frac{1}{2R_{sw}}\Delta\overline{v}_i(s) - \frac{\varepsilon P_{id}}{3(\overline{V}_i^*)^2}\Delta\overline{v}_i^c(s - 2j\omega_i)\,. \tag{5.58}$$

The equivalent circuit of the switching losses represented by (5.58) is shown in Fig. 5.7.

The equivalent circuit of the whole system can be determined combining the equivalent circuit of Fig. 5.7 with the basic circuit of Fig. 5.3, leading to Fig. 5.8.

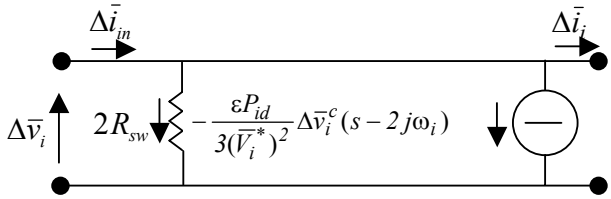

Fig. 5.7 - Equivalent circuit of the switching losses for small signal analysis.

It can be noted that the effect of the power losses can be described with a resistance connected in parallel with the input impedance and with a current generator. Fig. 5.8 can be simplified substituting the two current generators with an equivalent single current generator $\Delta\bar{i}_g$, as shown in Fig. 5.9. Taking (5.45) into account, $\Delta\bar{i}_g$ can be expressed as

$$\Delta\bar{i}_g(s) = -\frac{2P_{id}}{3(\bar{V}_i^*)^2}\left(\frac{\varepsilon}{2} + \bar{D}_{eq}(s)\bar{F}_a^c(s-2j\omega_i)\right)\Delta\bar{v}_i^c(s-2j\omega_i) \qquad (5.59)$$

The only difference between (5.59) and (5.45) is the presence of the term $\varepsilon/2$ added to the term $\bar{D}_{eq}(s)\bar{F}_a^c(s-2j\omega_i)$. Consequently, the stability analysis carried out in Paragraph 5.5 is still valid provided that the equivalent impedance (5.46) is replaced with the following expression:

$$\bar{Z}_{eq}(s) = \left(\bar{Z}(s)\,//\,2R_{sw}\right)\left(\bar{D}_{eq}(s)\bar{F}_a^c(s-2j\omega_i) + \frac{\varepsilon}{2}\right) \qquad (5.60)$$

It can be verified that the magnitude of the function $\bar{\Gamma}(\omega)$, developed through (5.60), is reduced owing to the presence of the resistance $2R_{sw}$ connected in parallel with the input impedance. This effect leads to an

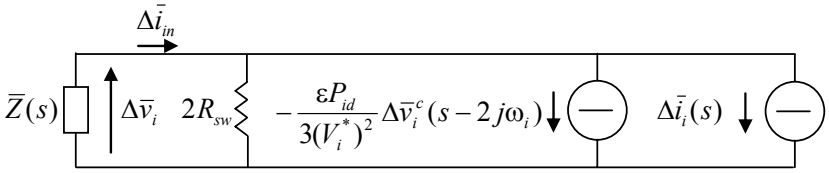

Fig. 5.8 - Equivalent circuit of a non-ideal matrix converter for small signal analysis.

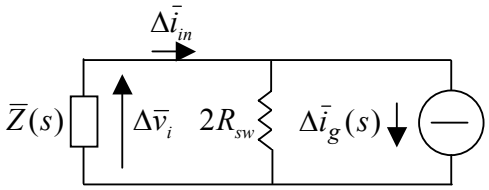

Fig. 5.9 - Equivalent circuit of a non-ideal matrix converter with a single current generator.

improvement of the stability power limit as will be shown in the next paragraphs.

In order to perform numerical and experimental tests on the stability of matrix converters feeding a constant load, it is more opportune to use as variable the output-to-input voltage transfer ratio q instead of P_{id}.

Combining (5.13)-(5.16) and (5.41) and solving for q leads to the following value of the limit voltage transfer ratio:

$$q_{lim} = \frac{1}{\sqrt{R_{res}\,\mathrm{Re}\left\{\overline{Y}_{eq}(j\omega_o)\right\}}}. \tag{5.62}$$

It is evident in (5.62) that, as the conduction power losses reduce the equivalent load admittance, they increase the limit voltage transfer ratio.

5.8. Simulation Results

In order verify the theoretical results obtained in the previous paragraphs, the behaviour of the system represented in Fig. 5.1 has been tested by numerical simulations.

For this purpose, the electronic circuit analysis program MICRO-CAP 7.0 has been adopted. In this program it is possible to use accurate models of the power switches and then to improve the simulation reliability. The numerical simulations take into account the switching behaviour of the matrix converter and the delay related to the digital implementation of the control algorithm.

The control strategy adopted for the matrix converter is the SVM technique, with a double-sided switching pattern [7] and a cycle period of 80 μs. The values of the system parameters are shown in Tab. 5.1.

Firstly, the effect of the power losses has been neglected and the equations

found in Paragraphs 5.16 and 5.17 have been used to evaluate the limit voltage transfer ratio for different values of the cut-off frequency $f_{cut\text{-}off}=1/(2\pi\tau)$ of the input voltage digital filter. The corresponding results are shown by the curve a) of Fig. 5.10.

Several simulations have been performed to check the validity of this stability curve using ideal switches. For instance, Fig. 5.11 shows the behaviour of the converter for $q = 0.37$ and $f_{cut\text{-}off} = 300$ Hz (corresponding to a time constant $\tau = 0.53$ ms), which is represented by the point 1 in Fig. 5.10.

Fig. 5.11(a) shows the steady-state waveform of the input voltage of the matrix converter. The steady-state waveforms of the line current and load current are illustrated in Figs. 5.11(b) and (c), respectively. As is possible to see, all the waveforms are sinusoidal and characterized by a small ripple, due to the high switching frequency of the matrix converter.

Then, the voltage transfer ratio has been changed to 0.47 (point 2 in Fig. 5.10) and the corresponding converter behaviour is shown in Fig. 5.12. Fig. 5.12(a) shows the waveform of the input voltage, whereas the waveforms of the line current and load current are illustrated in Figs. 5.12(b) and 5.12(c), respectively. In these operating conditions the input voltage and the line current waveforms are heavily distorted, showing large oscillations at about 1.75 kHz.

This behaviour is due to the predicted instability phenomena that occur

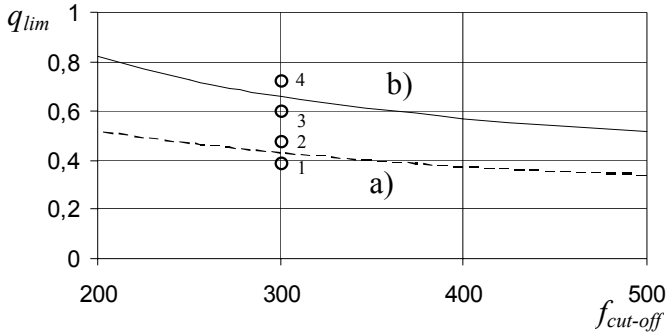

Fig. 5.10 - Limit voltage transfer ratio versus cut-off frequency of the input voltage digital filter with the system parameters given in Tab. I. a) without converter power losses, b) with converter power losses.

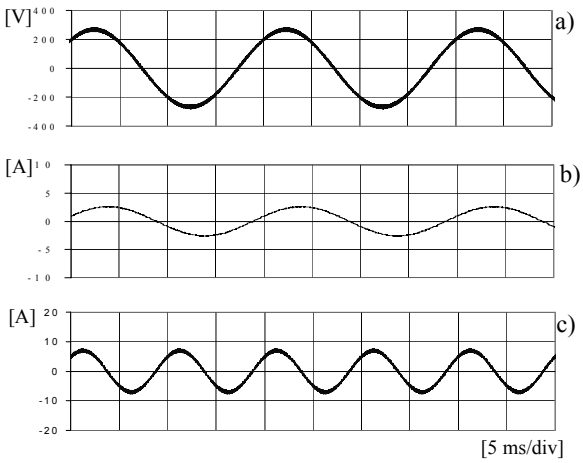

Fig. 5.11- Numerical results without the contribution of the converter power losses. Behavior of the matrix converter for $f_{cut\text{-}off}$ = 300 Hz and q = 0.37, a) input phase-to-phase voltage, b) line current, c) output current.

as the voltage transfer ratio exceeds the stability limits shown in Fig. 5.10. It is important to note that this unstable operation can be observed even if the switching frequency (12.5 kHz) is much higher than the resonance frequency of the input L-C filter (1.65 kHz).

These results are in agreement with the stability limits determined by the theoretical analysis. Fig. 5.10 gives a limit voltage transfer ratio of 0.43 at $f_{cut\text{-}off}$ = 300 Hz. In the case of Fig. 5.11, corresponding to the point 1 of Fig. 5.10, the voltage transfer ratio is lower than the limit value, and the system is stable. In the case of Fig. 5.12, corresponding to the point 2 in Fig. 5.10, the voltage transfer ratio is higher than the limit value, and the system becomes unstable. Any small perturbation, due to the switching effects or coming from input/output side, causes the system to leave the stable operating point.

It should be noted that in spite of the large oscillations at the input side, the waveform of the load current is nearly sinusoidal, as can be seen in Fig. 5.11(c), because of the fast adaptation of the duty-cycles, based on the on-line measurement of the input voltages.

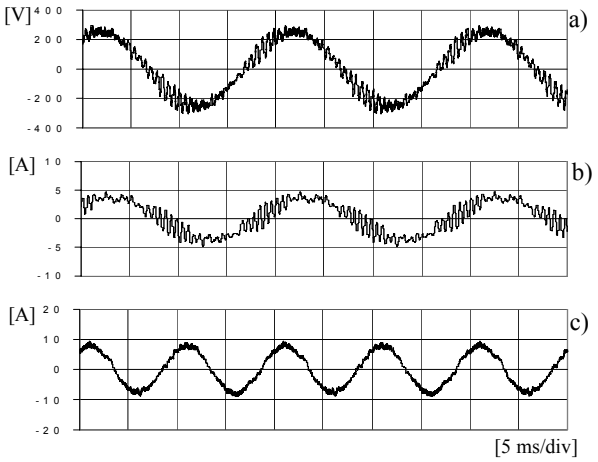

Fig. 5.12- Numerical results without the contribution of the converter power losses. Behavior of the matrix converter for $f_{cut\text{-}off} = 300$ Hz and $q = 0.47$, a) input line-to-line voltage, b) line current, c) load current.

Fig. 5.13(a), (b) and (c) show the numerical results achieved in the same operating conditions as in Fig. 5.12, but considering the power losses of the switching devices. To take into account the power losses, the model of the converter has been modified and improved using the models of real switches.

As can be seen, the use of non-ideal switches introduces a damping effect on input voltage and current oscillations, and a higher power can be delivered to the load before reaching the unstable operation. Comparing Figs. 5.12 and 5.13, it is evident that the converter power losses improve the system stability.

The curve b) in Fig. 5.10 represents the limit voltage transfer ratio taking the converter power losses into account. According to [54] and [55], it is assumed that the converter power losses are composed by 30% of switching losses and by 70% of conduction losses. This situation corresponds to a ratio δ (Appendix E) equal to 2.33.

For given values of switching frequency and load parameters, the converter efficiency depends on the output voltage. Due to the small value of the power delivered to the load (between 1-2 kW), for the theoretical calculations the efficiency has been assumed variable between 75% and 85%, and increasing with the voltage transfer ratio.

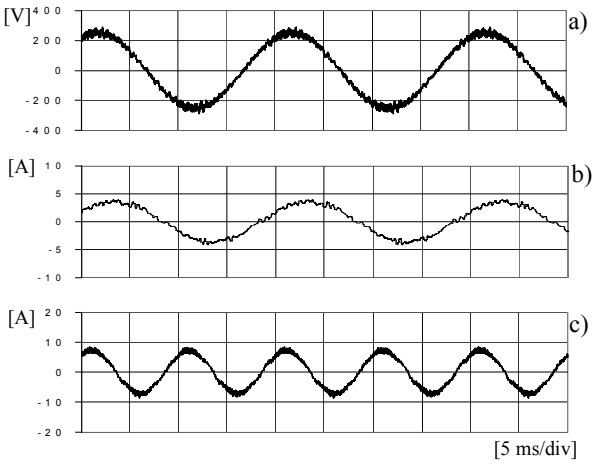

Fig. 5.13- Numerical results with the contribution of the converter power losses. Behavior of the matrix converter for $f_{cut\text{-}off} = 300$ Hz and $q = 0.47$, a) input line-to-line voltage, b) line current, c) load current.

As can be seen from Fig. 5.10, the converter power losses have a strong stabilizing effect and give an effective contribution to the system stability improvement.

5.9. Experimental Results

In order to verify the proposed theoretical approach for the MC stability, a prototype of a three-phase to three-phase matrix converter has been used to supply a linear passive R-L load. The matrix converter is realized using the FM35E12KR3 IGBT module produced by EUPEC. The control algorithm is implemented on the platform C6000, a floating-point digital signal processor provided by Texas Instruments. The switching frequency is 12.5 kHz, corresponding to a cycle period of 80 μs. The converter is fed by a voltage transformer with variable voltage transfer ratio to adjust the input voltage to a value of about 110 V rms. A L-C filter is connected at the input side of the converter. The parameters of filter, supply and load correspond to those reported in Tab. 5.1.

Several tests have been performed, for different values of the cut-off frequency of the input voltage digital filter and for different values of the

voltage transfer ratio.

Fig. 5.14 shows the behaviour of the matrix converter for $f_{cut\text{-}off} = 300$ Hz and $q = 0.6$. Fig. 5.14(a) represents the input voltage, Fig. 5.14(b) the line current and Fig. 5.14(c) the load current, respectively. It is evident that the system is stable, and only a small ripple due to the switching operation can be seen.

In Fig. 5.15, the voltage transfer ratio has been increased up to 0.7. As can be seen, the system becomes unstable, with appreciable oscillations on both input voltage and line current. The frequency of these oscillations is about 1700 Hz.

This results are in good agreement with the proposed theoretical approach. In fact, the situation of Fig. 5.14 corresponds to point 3 in Fig. 5.10, that is inside the stability region, whereas the situation of Fig. 5.15 corresponds to point 4, that is outside the stability region.

It is important to make a final remark on the use of the mathematical model proposed in this Chapter. The system parameters should be exactly known in order to determine the power stability limit with sufficient accuracy. Even small errors on the parameters values may lead to appreciable mismatching between theoretical and experimental results.

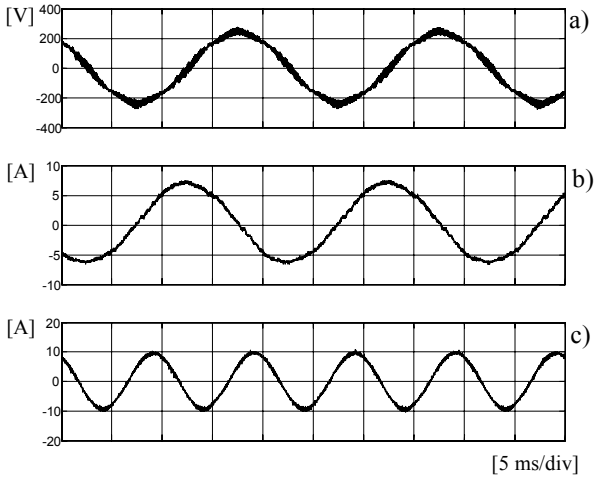

Fig. 5.14 - Experimental tests. Behavior of the matrix converter for $f_{cut\text{-}off} = 300$ Hz and $q = 0.6$, a) input line-to-line voltage, b) line current, c) load current.

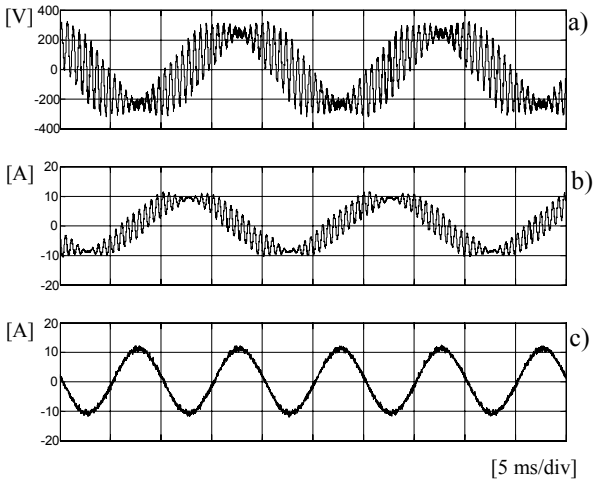

Fig. 5.15 - Experimental tests. Behavior of the matrix converter for $f_{cut\text{-}off}$ = 300 Hz and $q = 0.7$, a) input line-to-line voltage, b) line current, c) load current.

However, the proposed approach has the merit of emphasizing the mathematical relationships between the power stability limit and the system parameters, being a useful tool for the comprehension of the phenomena which occur in matrix converters.

5.10. Stability Analysis Based on a Large Signal Model

When instability phenomena are observed in MCs, as the output power is increased over a limit value, initially, small low frequency oscillations superimposed on the input voltages take place. Then, owing to the effects of these oscillations on calculations of the duty-cycles, the amplitude of the voltage oscillations increases preventing the normal operation.

Despite of its completeness, the analysis presented in the first part of this chapter uses a small-signal approach [56], making difficult to interpret the physical phenomena related to instability.

In the second part of this chapter a new approach is presented for the analysis of the MC stability, which is based on a large signal analysis carried out in the frequency domain. The main advantage of this approach is the easy comprehension of the instability origin and the possibility to relate the amplitude of the input voltage oscillations to the operating conditions.

As the proposed analysis is based on a large-signal model, it is possible to investigate the non-linear behaviour of MCs in the case of large input voltage perturbations. This allows one to explain phenomena that have not been clearly understood until now, such as the unstable behaviour of MCs in terms of limit cycles.

Several numerical simulations are presented showing current and voltage waveforms under stable and unstable operating conditions. Finally, experimental results carried out on a MC prototype are given for supporting the theoretical analysis and for proving the effect of different filtering methods applied to the input voltages. It is expected that these results will be useful in the design of matrix converter systems in the future.

5.11. Equations of the System

As is known, the matrix converter allows not only the control of the output voltages, but also of the phase angle of the input current vector.

If the switches are assumed ideal and the converter power losses are neglected, the input current vector can be expressed in terms of the power p_o delivered to the load as shown in (1.4):

As usual, the input current vector is supposed to be in phase with the actual input voltage vector, determining instantaneous unity input power factor,

$$\overline{\psi}_{ref} = \overline{v}_i \,. \tag{5.63}$$

Substituting (3) in (1.4) leads to the following expression for the input current:

$$\overline{i}_i = \frac{2}{3}\frac{p_o(t)}{\overline{v}_i^*} \,. \tag{5.64}$$

The magnitude of the input current space vector depends on the output power level and the input voltage vector.

With reference to Fig. 5.1, the equation for the input side of the MC, written in the Fourier domain, is reported in (5.1).

The behaviour of the system at the input side is completely described by (4.1) and (5.1) once the output power is assigned.

A. Expression of the Input Voltage

In order to introduce the problem of the stability of matrix converter, it is opportune to discuss the results of some numerical simulations. For this purpose, the electronic circuit analysis program MICRO-CAP 7.0 has been adopted. In this program it is possible to use accurate models of the power switches and then to improve the simulation reliability. The numerical simulations take into account the switching behaviour of the matrix converter and the delay related to the digital implementation of the control algorithm. The control strategy adopted for the matrix converter is the SVM technique, with a double-sided switching pattern [7] and a cycle period of 80 μs. The values of the system parameters are shown in Tab. 5.2.

The behaviour of a matrix converter in stable operating conditions is shown in Fig. 5.16 referring to a input-to-output voltage transfer ratio $q = 0.4$. Fig. 5.16(a) shows the steady-state waveform of the input voltage of the matrix converter. The steady-state waveforms of the line current and load current are illustrated in Figs. 5.16(b) and 5.16(c), respectively. As can be seen, all the waveforms are sinusoidal and characterized by a small ripple, due to the high switching frequency of the matrix converter.

Then, the voltage transfer ratio is changed to $q = 0.50$ and the corresponding converter behaviour is shown in Fig. 5.17. Fig. 5.17(a) shows the waveform of the input voltage, whereas the waveforms of the line current and load current are illustrated in Figs. 5.17(b) and 5.17(c), respectively. In these operating conditions the input voltage and the line current waveforms are heavily distorted, showing large oscillations at about 2.2 kHz. This behaviour is due to the predicted instability phenomena that occur as the voltage transfer ratio is increased and the output power exceeds the stability limits. It is important to note that this unstable operation can be observed even if the switching frequency (12.5 kHz) is much higher than the resonance frequency of the input L-C filter (1.7 kHz).

TABLE 5.2 - SYSTEM PARAMETERS

Supply	**Filter**	**Load**
$V_S = 110$ V(rms), $\omega_i = 2\pi\ 50$ rad/s, $R_S = 0.2\ \Omega$, L_S=0.70 mH	$L_f = 1.16$ mH, C_f= 4.5 μF $R_f = 300\ \Omega$	R_l= 8.3 Ω, $L_l = 1.3$ mH, $\omega_o = 2\pi\ 100$ rad/s

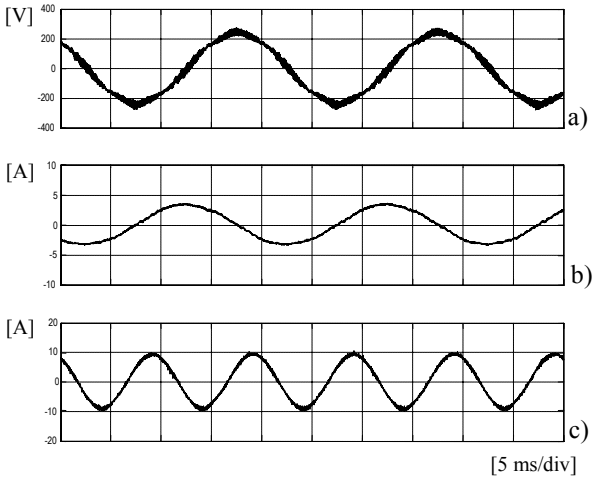

Fig. 5.16 - Simulation result - Behavior of the matrix converter for $q = 0.4$, a) input line-to-neutral voltage, b) line current, c) load current.

A detailed analysis of Fig. 5.17(a) and 5.17(b) reveals that the oscillations superimposed on the input voltage and line current fundamental components do not have constant amplitude. The amplitude, instead, varies periodically from zero to a maximum value and the frequency of its modulation is exactly double with respect to input source frequency. This phenomenon, widely known in wave physics, is usually referred as "beating" and it is determined by the sum of at least two separate harmonics with close frequencies.

The spectrum of the input voltage corresponding to Fig. 5.17(a) is shown in Fig. 5.18. As can be seen, apart from the fundamental component at 50 Hz, there are two harmonics respectively at 2130 Hz and 2230 Hz. The switching harmonics at 12.5 kHz, outside the visible frequency range, are negligible.

As a consequence, in order to define a large signal model of matrix converter, it is necessary to represent the input voltage vector as the sum of a fundamental component and two harmonics at high frequency, as follows:

$$\overline{v}_i(t) = \left(\overline{V}_i + \overline{V}_{dir} e^{j\omega_r t} + \overline{V}_{inv} e^{-j\omega_r t}\right) e^{j\omega_i t} \tag{5.65}$$

where $\overline{V}_i$ is the Fourier coefficient of the fundamental component at angular frequency ω_i, $\overline{V}_{dir}$ and $\overline{V}_{inv}$ are the Fourier coefficients of the harmonics at

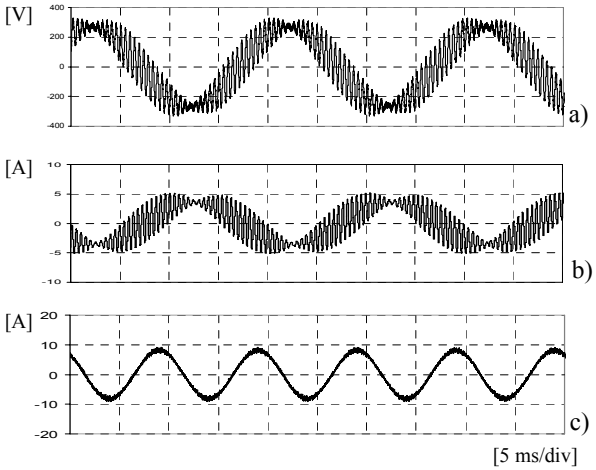

Fig. 5.17 - Simulation results - Behavior of the matrix converter for $q = 0.5$, a) input line-to-neutral voltage, b) line current, c) load current.

angular frequencies $\omega_i+\omega_r$ and $\omega_i-\omega_r$. The frequency ω_r, that the numerical simulations demonstrate to be close to the resonance angular frequency of the input L-C filter, is unknown and has to be determined.

When the system is stable, obviously $\overline{V}_{dir}$ and $\overline{V}_{inv}$ are zero. However, voltage source perturbations or random noise, acting as excitation sources, could force $\overline{V}_{dir}$ and $\overline{V}_{inv}$ to assume values different from zero for a while. If the system behaviour is stable, as soon as the temporary excitation disappears, the system returns to the original operating conditions after a

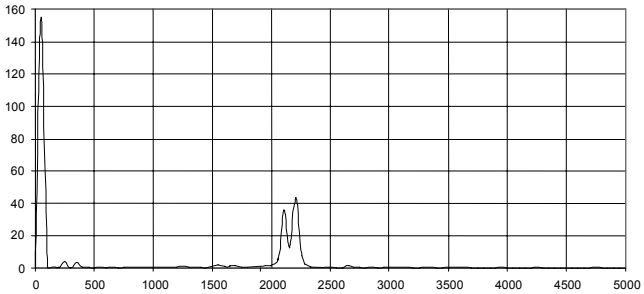

Fig. 5.18 - Simulation results - Spectrum of the input line-to-neutral voltage for $q = 0.5$.

short transient. Otherwise, if the voltage transfer ratio is greater than a limit value, as in the case shown in Fig. 5.17, the system present steady-state oscillations with finite-amplitude superimposed on the input voltages and currents.

B. Expression of the Input Current

In order to find the power stability limit, it is necessary to determine the effects on the input current produced by the distorted voltage (5.65). The input current is completely defined once the output power waveform is assigned. In this paragraph the output power is assumed constant, i.e.

$$p_o(t) = P_{id} \tag{5.66}$$

where P_{id} is the reference value for the power delivered to the load. Fig. 5.19 shows the block diagram of the system with constant output power.

In Appendix F it is shown that the input current can be approximated by means of the following harmonics:

$$\bar{i}_i(s) = \left(\bar{I}_i + \bar{I}_{dir} e^{j\omega_r t} + \bar{I}_{inv} e^{-j\omega_r t}\right) e^{j\omega_i t} \tag{5.67}$$

where

$$\bar{I}_i = \frac{2}{3}\frac{P_{id}}{V_i^2}\frac{\overline{V_i}}{\overline{\delta}} \tag{5.68}$$

$$\bar{I}_{dir} = \frac{1}{3}\frac{P_{id}}{V_{dir}^2}\overline{V}_{dir}\left(1 - \frac{1}{\overline{\delta}}\right) \tag{5.69}$$

$$\bar{I}_{inv} = \frac{1}{3}\frac{P_{id}}{V_{inv}^2}\overline{V}_{inv}\left(1 - \frac{1}{\overline{\delta}}\right). \tag{5.70}$$

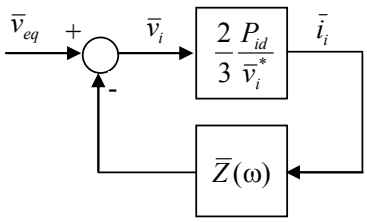

Fig. 5.19 - Block diagram of the system with constant output power.

In (5.69)-(5.70) $\overline{\delta}$ is defined as

$$\overline{\delta} = \sqrt{1 - 4\left(\frac{\overline{V}_{dir}\overline{V}_{inv}}{\overline{V}_i^2}\right)^*} \,. \tag{5.71}$$

There are in general two solutions for the root square of a complex number. Therefore, it is important to note that (5.71) must be intended as the solution in the right half of the complex plane (i.e. with positive real part).

In (5.67) high order harmonics due to switching effects have been ignored, because the input L-C filter acts as a low pass filter.

C. Determination of the Oscillation Magnitudes

In order to determine the magnitudes of the current and voltage oscillations, (5.1) can be written for the specific cases $\omega = \omega_i$, $\omega = \omega_i + \omega_r$, $\omega = \omega_i - \omega_r$, as emphasized in (5.65) and (5.67), leading to the following system of equations:

$$\overline{v}_{eq}(\omega_i) = \overline{Z}(\omega_i)\overline{I}_i + \overline{V}_i \tag{5.72}$$

$$0 = \overline{Z}(\omega_i + \omega_r)\overline{I}_{dir} + \overline{V}_{dir} \tag{5.73}$$

$$0 = \overline{Z}(\omega_i - \omega_r)\overline{I}_{inv} + \overline{V}_{inv} \,. \tag{5.74}$$

The system of equations (5.72)-(5.73) together with (5.68)-(5.70) completely describe the behaviour of the system composed of the matrix converter, the grid and the input L-C filter, either for stable or unstable operating conditions.

5.12. Stability Analysis

The stability analysis involves the determination of solutions of the system of equations (5.72)-(5.74). To simplify the problem, the magnitude of $\overline{V}_i$ can be considered known and close to that of the source voltage. In such a way, only (5.73) and (5.74) are necessary to determine $\overline{V}_{dir}$, $\overline{V}_{inv}$ and ω_r.

Substituting (5.69)-(5.70) in (5.73)-(5.74) and solving for $\overline{V}_{dir}$ and $\overline{V}_{inv}$

leads to the following explicit form for the equations of the system:

$$\left[\overline{Z}(\omega_i + \omega_r)\frac{P_{id}}{3V_{dir}^2}\left(1 - \frac{1}{\overline{\delta}}\right) + 1\right]\overline{V}_{dir} = 0 \tag{5.75}$$

$$\left[\overline{Z}(\omega_i - \omega_r)\frac{P_{id}}{3V_{inv}^2}\left(1 - \frac{1}{\overline{\delta}}\right) + 1\right]\overline{V}_{inv} = 0 \tag{5.76}$$

As can be seen, (5.75)-(5.76) always present the trivial solution

$$\overline{V}_{dir} = \overline{V}_{inv} = 0 \tag{5.77}$$

that corresponds to stable, steady-state operating conditions.

Non-trivial solutions for $\overline{V}_{dir}$ and $\overline{V}_{inv}$ can be found solving the following system of equations, which can be obtained dividing (5.75)-(5.76) by $\overline{V}_{dir}$ and $\overline{V}_{inv}$, respectively:

$$\overline{Z}(\omega_i + \omega_r)\frac{P_{id}}{3V_{dir}^2}\left(1 - \frac{1}{\overline{\delta}}\right) = -1 \tag{5.78}$$

$$\overline{Z}(\omega_i - \omega_r)\frac{P_{id}}{3V_{inv}^2}\left(1 - \frac{1}{\overline{\delta}}\right) = -1 \ . \tag{5.79}$$

A. Determination of the Angular Frequency ω_r

To determine ω_r, (5.78) and (5.79) must be combined multiplying term by term (5.78) and the complex conjugate of (5.79), leading to

$$\overline{\Omega}^2(\omega_r)\left(\frac{P_{id}}{3V_{dir}V_{inv}}\left|1 - \frac{1}{\overline{\delta}}\right|\right)^2 = 1 \tag{5.80}$$

where

$$\overline{\Omega}(\omega_r) = \sqrt{\overline{Z}(\omega_i + \omega_r)\overline{Z}^*(\omega_i - \omega_r)} \ . \tag{5.81}$$

In (5.81) only the value in the right half of the complex plane has to be considered.

A necessary condition for (5.80) to be verified is the existence of an angular frequency ω_{r0} satisfying the following constrain equation:

$$\arg \overline{\Omega}^2(\omega_{r0}) = 0 \tag{5.82}$$

Equation (5.82) can be written also in the equivalent following form:

$$\arg \overline{\Omega}(\omega_{r0}) = 0 \tag{5.83}$$

According to (5.83), for $\omega_r = \omega_{r0}$ the function $\overline{\Omega}(\omega_r)$ is a real number, having the dimension of an impedance. It is then useful to introduce a new equivalent resistance $R_{res,}$ defined as

$$R_{res} = \left|\overline{\Omega}(\omega_{r0})\right|. \tag{5.84}$$

B. Determination of the Amplitude of the Harmonics

Dividing term by term (5.78) and (5.79) leads to the following relationship between the magnitude of $\overline{V}_{dir}$ and $\overline{V}_{inv}$:

$$\frac{\overline{Z}(\omega_i + \omega_{r0})}{\overline{Z}(\omega_i - \omega_{r0})} \frac{V_{inv}^2}{V_{dir}^2} = 1. \tag{5.85}$$

It is worth noting that (5.85) is not sufficient to find $\overline{V}_{dir}$ and $\overline{V}_{inv}$ in explicit form. However, a simple method based on a graphical approach can be used to determine $\overline{V}_{dir}$ and $\overline{V}_{inv}$. For this method it is useful to introduce the new variable $\overline{p}$, normalised product of the harmonic amplitudes, defined as

$$\overline{p} = \frac{\overline{V}_{dir}\overline{V}_{inv}}{\overline{V}_i^2}. \tag{5.86}$$

The magnitudes of $\overline{V}_{dir}$ and $\overline{V}_{inv}$ can be expressed in terms of $\overline{p}$ by solving (5.85) and (5.86) as follows

$$V_{dir} = V_i \sqrt{p} \left(\frac{Z(\omega_i - \omega_{r0})}{Z(\omega_i + \omega_{r0})} \right)^{\frac{1}{4}} \tag{5.87}$$

$$V_{inv} = V_i \sqrt{p} \left(\frac{Z(\omega_i + \omega_{r0})}{Z(\omega_i - \omega_{r0})} \right)^{\frac{1}{4}}. \tag{5.88}$$

As a conclusion, the knowledge of p and ω_{r0} is sufficient to determine the magnitude of both voltage harmonics.

In order to study the behaviour of p, it is convenient to rewrite (5.80) in the following form:

$$G\,A(\overline{p})^{-1} = 1 \tag{5.89}$$

where

$$G = \frac{2}{3}\frac{R_{res}P_{id}}{V_i^2} \tag{5.90}$$

$$A(\overline{p}) = \left[\frac{1}{2p}\left|1 - \frac{1}{\sqrt{1-4\overline{p}^*}}\right|\right]^{-1}. \tag{5.91}$$

It is worth noting that (5.89) can be interpreted as the characteristic equation of the closed-loop system represented by the block diagram shown in Fig. 5.20. G represents the forward gain, A the feedback non-linear attenuation and $\overline{p}$ has the meaning of a state variable.

It is demonstrated in Appendix G that the solutions of (5.78)-(5.79) are represented by the values of $\overline{p}$ defined by following parametric equation:

$$\overline{p}(\lambda) = \frac{1}{4}\left[1 - \frac{1}{\left(1+\lambda e^{j\beta}\right)^2}\right] \tag{5.92}$$

where λ is any positive real number and β is defined by

$$\beta = \arg\left\{\overline{Z}(\omega_i + \omega_{r0})\right\} = \arg\left\{\overline{Z}(\omega_i - \omega_{r0})\right\}. \tag{5.93}$$

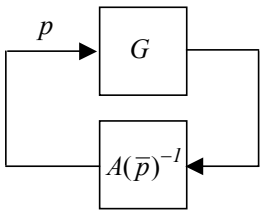

Fig. 5.20 - Block diagram of closed loop system equivalent to (5.89).

For any value of λ it is possible to calculate $\overline{p}$ and the corresponding value of $A(\overline{p})$. These couples of values $(p,\ A(\overline{p}))$ can be plotted on a graph with the values of p on the real axis and the values of $A(\overline{p})$ on the imaginary axis. In this way $A(\overline{p})$ can be plotted as a function of p.

The curves of $A(\overline{p})$ show only two types of behaviour, corresponding to $\cos\beta > 0$ and $\cos\beta < 0$.

Fig. 5.21(a) shows the curve of $A(\overline{p})$ for $\cos\beta > 0$. As can be seen, the diagram starts from the point $A=1$ at $p = 0$. According to (5.89) the determination of p can be performed by intersecting $A(\overline{p})$ with the straight line corresponding to the gain G, proportional to the power delivered to the load. If G is lower than 1, an intersection is possible (state p_0), but this solution is not stable. In fact, starting from the state p_0, a small decrease of p determines an increase of the attenuation, thus causing a further decrease of p toward the stable state $p = 0$. On the other side, a small increase of p determines a decrease of the attenuation, thus causing a further increment of p.

As a consequence, if G is lower than 1, for any disturbance of small amplitude $p < p_0$, the attenuation function A is greater than gain G and the disturbance tends to vanish. If G is greater than 1, the gain G is always greater than the attenuation function A and any small disturbance is indefinitely amplified.

Fig. 5.21(b) shows the curves of $A(\overline{p})$ corresponding to the case $\cos\beta < 0$.

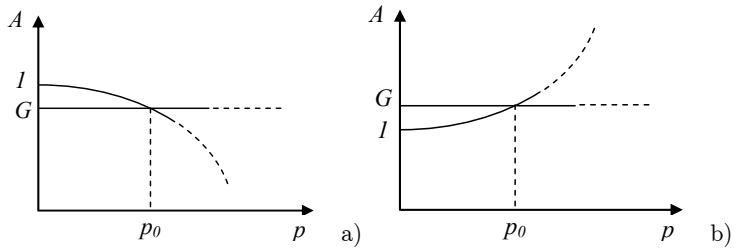

Fig. 5.21 - Curves of the attenuation A as a function of the variable p.
a) $\cos\beta > 0$, b) $\cos\beta < 0$.

In this case, no intersection between the straight line corresponding to the gain G and the curve A is possible if $G < 1$. Otherwise, if $G > 1$ the intersection corresponding to the state p_1 can be determined. It is important to note that this solution is stable, but the converter does not work correctly, as a value of p different from zero means that $\overline{V}_{dir}$ and $\overline{V}_{inv}$ have finite magnitude and the input voltage is distorted.

As a conclusion, in both cases the stability power limit corresponds to the condition G=1 and its value is

$$P_{lim} = \frac{3V_i^2}{2R_{res}}. \tag{5.94}$$

From a physical point of view, it is possible to describe the behaviour of the system in this way: a disturbance of the input voltage leads to a corresponding disturbance of the input current, that is proportional to the output power. The input L-C resonant filter amplifies the current disturbance and if the output power is sufficiently high, the system can reach a new steady state condition, but with distorted voltages.

5.13. Delay of the Digital Control

In Paragraph 5.17 it has been shown that the digital controller introduces a delay, that leads to two main consequences. The first one is that the controller does not keep the input current in phase with the input voltage. The second one is that the output power cannot be considered completely constant and equal to the desired value.

A. Delay Introduced on the Input Current Vector

As known from the control theory, the effects determined by a sample & hold process and by the delay of the digital controller can be approximately studied inserting the following transfer function in the block diagram of the system.

$$\overline{D}(\omega) = \left(\frac{1 - e^{-jT\omega}}{jT\omega}\right) e^{-jT\omega}. \tag{5.95}$$

In (5.95) the term inside the brackets is related to the sampling and

reconstruction processes, whereas the exponential term outside the brackets is due to the delay introduced by the digital controller. The block diagram of the system including the delay is shown in Fig. 5.22.

Comparing the block diagram of Fig. 5.19 with that of Fig. 5.22 it can be noted that the power limit (5.94), found in the previous paragraph, is still valid provided that $\overline{Z}(\omega)$ is replaced with the following equivalent impedance:

$$\overline{Z}_{eq}(\omega) = \overline{Z}(\omega)\overline{D}(\omega)\,. \tag{5.96}$$

The presence of the delay modifies the impedance mainly changing its argument. It can be verified that in a system with delays the angular frequency ω_{r0} is different from that of the same system without delays and generally corresponds to lower values of R_{res}. This causes an effective improvement of the stability power limit.

B. Variation of the Output Power due to Digital Control Delay

The output voltage can be expressed in terms of the input voltage by means of (5.3), where the duty-cycle space vector $\overline{m}_d$ and $\overline{m}_i$ are given by

$$\overline{m}_d = \frac{\overline{V}_{o,ref} e^{j\omega_o t}}{3\overline{v}^*_{im}(t)} \tag{5.97}$$

$$\overline{m}_i = \frac{\overline{V}^*_{o,ref} e^{-j\omega_o t}}{3\overline{v}^*_{im}(t)}\,. \tag{5.98}$$

In (5.97) and (5.98) $\overline{V}_{o,ref}$ is the reference output voltage vector with

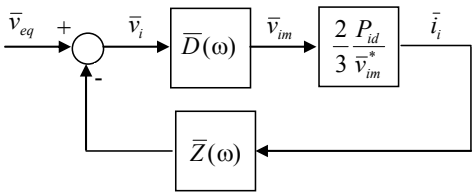

Fig. 5.22 - Block diagram of the system including the delay introduced by the digital controller.

angular frequency ω_o and $\overline{v}_{im}(t)$ is the input voltage measured by the digital controller and used to calculate the duty-cycles.

Substituting (5.97) and (5.98) in (5.3) leads to the following expression for the output voltage:

$$\overline{v}_o(t) = \overline{V}_{o,ref} e^{j\omega_o t} \operatorname{Re}\left\{ \frac{\overline{v}_i(t)}{\overline{v}_{im}(t)} \right\}. \tag{5.99}$$

If the effects of the delay are negligible, the measured voltage coincides with the actual voltage, namely

$$\overline{v}_{im}(t) = \overline{v}_i(t) \tag{5.100}$$

and (5.41) becomes:

$$\overline{v}_o(t) = \overline{V}_{o,ref} e^{j\omega_o t}. \tag{5.101}$$

Due to the delay, the measured voltage $\overline{v}_{im}$ is slightly different from the actual voltage $\overline{v}_i$. The explicit expression of the measured voltage can be found multiplying (5.65) by the transfer function $\overline{D}(\omega)$. In the time domain one finds

$$\overline{v}_{im}(t) = \left[\overline{V}_i + \overline{V}_{dir} \overline{D}(\omega_i + \omega_r) e^{j\omega_r t} + V_{inv} \overline{D}(\omega_i - \omega_r) e^{-j\omega_r t} \right] e^{j\omega_i t}. \tag{5.102}$$

Due to the inductive load, the output current is not sensitive to the output voltage harmonics at high frequency and can be expressed as follows:

$$\overline{i}_o(t) = \overline{Y}(\omega_o) \overline{V}_{o,ref} e^{j\omega_o t} \tag{5.103}$$

where $\overline{Y}(\omega)$ is the admittance of the load.

Therefore, the output power can be expressed as

$$p_o = \frac{3}{2} \overline{v}_o(t) \cdot \overline{i}_o(t) = P_{id} \operatorname{Re}\left\{ \frac{\overline{v}_i(t)}{\overline{v}_{im}(t)} \right\} \tag{5.104}$$

where P_{id} is the output power corresponding to the reference voltage, defined as

$$P_{id} = \frac{3}{2}\mathrm{Re}\left\{\overline{Y}(\omega_o)\right\}V_{o,ref}^2 . \tag{5.105}$$

The analysis presented in Paragraphs 5.23 and 5.24 should be now repeated assuming for p_o the expression (5.104) instead of (5.66) and taking (5.102) into account. For doing this, the mathematical developments are not simple and are not useful for the comprehension of the system behaviour.

However, with the aim to understand the changes that (5.104) determines in the power limit, it is opportune to linearize the system equations assuming that $\overline{V}_{dir}$ and $\overline{V}_{inv}$ have small magnitudes.

Instead of the non-linear system of equations (5.75)-(5.76), the analysis leads to the following system of equations, written in matrix form:

$$\boldsymbol{M}\begin{bmatrix}\overline{V}_{dir}\\ \overline{V}_{inv}^*\end{bmatrix} = \begin{bmatrix}0\\0\end{bmatrix} \tag{5.106}$$

where

$$\boldsymbol{M} = \begin{bmatrix} 1+\dfrac{\overline{Z}(\omega_i+\omega_r)}{R_{res}}\overline{m}_{11} & \dfrac{\overline{Z}(\omega_i+\omega_r)}{R_{res}}\overline{m}_{12} \\ \dfrac{\overline{Z}(\omega_i-\omega_r)^*}{R_{res}}\overline{m}_{21}^* & 1+\dfrac{\overline{Z}(\omega_i-\omega_r)^*}{R_{res}}\overline{m}_{22}^* \end{bmatrix}. \tag{5.107}$$

The coefficients of the matrix $\boldsymbol{M}$ are defined as follows

$$\overline{m}_{11} = \frac{1-\overline{D}(\omega_i+\omega_r)}{2} \tag{5.108}$$

$$\overline{m}_{12} = -\frac{1+\overline{D}^*(\omega_i-\omega_r)}{2}\frac{\overline{V}_i}{\overline{V}_i^*} \tag{5.109}$$

$$\overline{m}_{21} = -\frac{1+\overline{D}^*(\omega_i+\omega_r)}{2}\frac{\overline{V}_i}{\overline{V}_i^*} \tag{5.110}$$

$$\overline{m}_{22} = \frac{1-\overline{D}(\omega_i-\omega_r)}{2} \tag{5.111}$$

and R_{res} is now re-defined in the general form

$$R_{res} = \frac{3}{2}\frac{V_i^2}{P_{lim}}. \tag{5.112}$$

This equation is formally equivalent to (5.94). The system of equations (5.107) has non-trivial solutions only if the determinant of $\boldsymbol{M}$ is zero, leading to the following constraint equation:

$$R_{res}^2 + \overline{b}(\omega_r)R_{res} + \overline{c}(\omega_r) = 0 \tag{5.113}$$

where

$$\overline{b}(\omega_r) = \overline{Z}(\omega_i + \omega_r)\overline{m}_{11} + \overline{Z}^*(\omega_i - \omega_r)\overline{m}_{22}^* \tag{5.114}$$

$$\overline{c}(\omega_r) = \overline{Z}(\omega_i + \omega_r)\overline{Z}^*(\omega_i - \omega_r)\left[\overline{m}_{11}\overline{m}_{22}^* - \overline{m}_{12}\overline{m}_{21}^*\right]. \tag{5.115}$$

The equation (5.113) is of the second order and has two solutions $R_{res} = \overline{\Omega}_1$ and $R_{res} = \overline{\Omega}_2$, namely

$$\overline{\Omega}_{1,2}(\omega_r) = \frac{-\overline{b}(\omega_r) \pm \sqrt{\overline{b}^2(\omega_r) - 4\overline{c}(\omega_r)}}{2}. \tag{5.116}$$

As R_{res} in (5.112) is a real positive number, a necessary condition for (5.116) to be acceptable is the existence of an angular frequency ω_{r0} satisfying the following constrain equation:

$$\arg \overline{\Omega}_{1,2}(\omega_{r0}) = 0. \tag{5.117}$$

As can be noted, (5.117) is the general form of (5.83). After R_{res} is known, the power limit can be determined solving (5.54) for P_{lim}.

5.14. Improvement of the Stability Power Limit

The analysis described in the previous paragraphs gives important information for the improvement of the stability power limit. Equation (5.112) shows that the stability power limit is affected by the value of the resistance R_{res} that depends on the grid and input filter impedance and on the digital system delays.

Lower values of R_{res}, corresponding to higher power limits, can be obtained reducing the peak of resonance of $\overline{Z}(\omega)$, i.e. adding damping resistors. The

use of damping resistance in parallel with the filter inductance is described in [18] and [52]. A suitable value of this resistance allows the high frequency current harmonics to flow through the source leading to lower oscillations of the capacitor voltage. The damping effect and then the stability limit increases while reducing the value of the resistance. Unfortunately, this solution is effective for improving the MC stability but it is detrimental for the EMI requirements. Therefore, a compromise should be found between stability and input current quality.

Another important consideration for the improvement of the system stability is the fact that the delay introduced by the digital controller affects the angular frequency ω_r. The same result can be achieved if the calculation of the duty cycles is carried out by filtering the matrix converter input voltages [24]-[25].

5.15. Experimental Results

In order to verify the proposed theoretical approach for the MC stability, the same prototype presented in Paragraph 5.9 has been used. The matrix converter is realized using the FM35E12KR3 IGBT module produced by EUPEC. The control algorithm is implemented on the platform C6711, a floating-point digital signal processor provided by Texas Instruments. The switching frequency is 12.5 kHz, corresponding to a cycle period of 80 μs. The converter is fed by a voltage transformer with variable voltage transfer ratio to adjust the input voltage to a value of about 110 V rms. A L-C filter is connected at the input side of the converter. The parameters of filter, supply and load correspond to those reported in Tab. 5.2.

In order to perform experimental tests on the stability of a matrix converter feeding a constant passive load, it is more appropriate to use the output-to-input voltage transfer ratio q instead of P_{id}.

Combining (5.94), (5.105) and solving for q leads to the following value of the limit voltage transfer ratio:

$$q_{lim} = \frac{1}{\sqrt{R_{res}\,\mathrm{Re}\left\{\overline{Y}(\omega_o)\right\}}}\,. \tag{5.118}$$

Firstly, to validate the stability analysis, some experimental tests have

been performed to find the limit voltage transfer ratio.

Fig. 5.23 shows the behaviour of the matrix converter for $q = 0.39$. Fig. 5.23(a) represents the input voltage, Fig. 5.23(b) the line current and Fig. 5.23(c) the load current, respectively. It is evident that the system is stable, and only a small ripple due to the switching operation can be seen.

In Figs. 5.24 and 5.25, the voltage transfer ratio has been increased to 0.46 and 0.49 respectively. As can be seen, the system becomes unstable, with appreciable oscillations on both input voltage and line current.

The spectral analysis of the input voltage is given in Fig. 5.26 and shows that there are two main harmonics with frequencies of 2150 Hz e 2250 Hz, respectively. This result is in good agreement with the proposed theoretical approach, as the two frequencies differ for the double of the input frequency ($2\pi 50$ Hz = 100 Hz). In addition, the amplitude of the oscillations tends to increase with the output power as predicted by the stability analysis for the case with $\cos \beta < 0$.

In Tab. 5.3 the limit voltage transfer ratio calculated by means of the proposed theory is compared with the experimental limit value, namely $q \cong 0.45$.

The basic theory, that neglects both the effects caused by the delay,

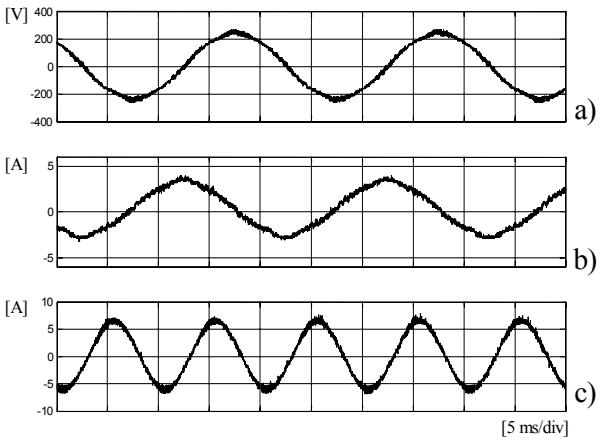

Fig. 5.23 - Experimental tests - Behavior of the matrix converter for $q = 0.39$, a) input line-to-line voltage, b) line current, c) load current.

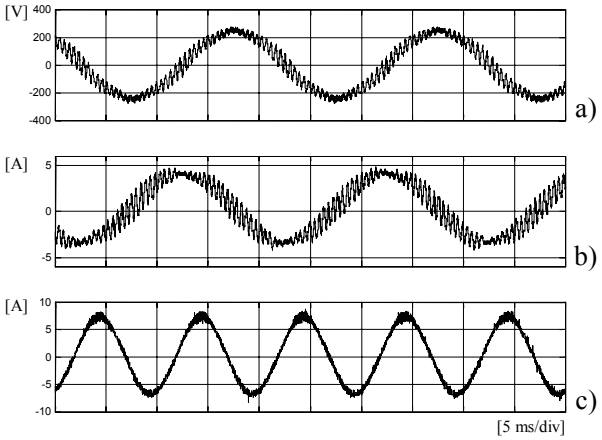

Fig. 5.24 - Experimental tests - Behavior of the matrix converter for $q = 0.46$, a) input line-to-line voltage, b) line current, c) load current.

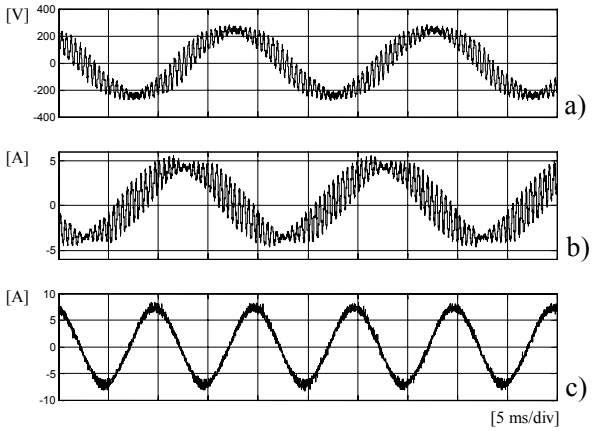

Fig. 5.25 - Experimental tests - Behavior of the matrix converter for $q = 0.49$, a) input line-to-line voltage, b) line current, c) load current.

predicts the possibility that the system becomes unstable, but with increasing voltage and current oscillations.

This is different from the behaviour experimentally observed, that presents finite-amplitude stable oscillations. The limit voltage transfer ratio calculated is 0.167, about half of the experimental value. This difference is probably due to the lower value of ω_r compared to that obtained in the

TABLE 5.3 - COMPARISON BETWEEN THEORETICAL RESULT AND EXPERIMENTAL TESTS

Mathematical model	$\frac{\omega_r}{2\pi}$	cos β	R_{res}	q_{lim}	Solution type
Basic theory (no delays and $P_o=P_{id}$)	1739	0.53	299	0.167	Unstable oscillations
Model with delays, but output power is assumed constant.	**1630** 2180	**0.98** -0.99	**158,9** 42,67	**0.230** 0.443	**Unstable oscillations** Stable oscillations
Model with $P_o=P_o(t)$	1616	0.39	133,0	0.251	Unstable oscillations
Complete model, with delays and $P_o=P(t)$	1007 **2182** 3142	0.75 **-0.99** -0.69	17.29 **42.17** 13,18	0.696 **0.446** 0.797	Unstable oscillations **Stable oscillations** Stable oscillations
Experimental tests	2200	-	-	**0.44**	**Stable oscillations**

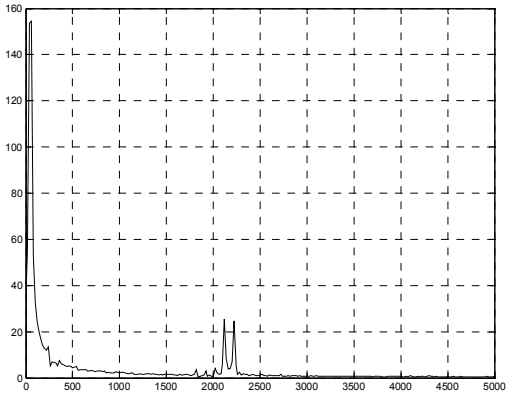

Fig. 5.26 - Experimental tests. Spectrum of the input line-to-neutral voltage during unstable operation of the converter.

experimental test.

Better results can be found if the delay introduced by the digital controller is taken into account. In this case, (5.83) presents several solutions. Obviously, the stability power limit has to be evaluated with reference to the worst case, corresponding to the lowest value of q_{lim}.

If the output power is assumed constant, q_{lim} results 0.230. However, the second solution (i.e. $q_{lim} = 0.443$, $\omega_r/2\pi = 2180$ Hz) presents a behaviour that is very close to that of the actual system. This means that it is essential to take the delay into account to describe the real system.

If the output power is not assumed constant and the effect of the delay on the input current displacement is neglected, then the limit voltage ratio increases to 0.251.

Finally, if both the effects caused by the delays of the digital controller are considered, the theory predicts the value 0.446 for the limit voltage transfer ratio that is just a little lower than the experimental value. In addition, the frequency and the behaviour of the oscillations are in good agreement with the experimental results. The small mismatching between theoretical predictions and experimental values may be ascribed to several factors, such as converter power losses and parameter uncertainties.

It is worth noting that this analysis does not consider the effect of the converter losses for the sake of brevity. The power limit that can be calculated by means of the equations presented in the previous paragraph is generally lower than that achievable in experimental tests. This is because the iron losses in the inductances or the power losses of the converter may increase the damping effect of the real system, thus preventing unstable oscillations to arise. The effect of the losses is more or less evident depending on the operating conditions and the system parameters. In particular, the damping effect could be very evident if the theoretical stability power limit would be small and comparable with the converter losses.

Another case in which the damping effect of the losses becomes evident is when the digital filter is used, and this is because the consequent power limit increase leads to higher losses as shown in [25].

Several tests have been performed, for different values of the time constant τ of the input voltage digital filter in order to evaluate the limit voltage transfer ratio. The discrete-time version of the digital filter is presented in Appendix D. The experimental results are reported in Fig. 5.27. The dashed area between the two curves represents an uncertainty region, where it is not possible to clearly state if the system is stable or unstable.

In fact, in experimental tests the unstable behaviour of the converter can be established only in case of input voltage and current oscillations higher than a threshold value. If the output power is not sufficiently greater than the stability limit, these oscillations are very small and can be confused with the natural disturbances due to the interaction between the switched current and the input L-C filter.

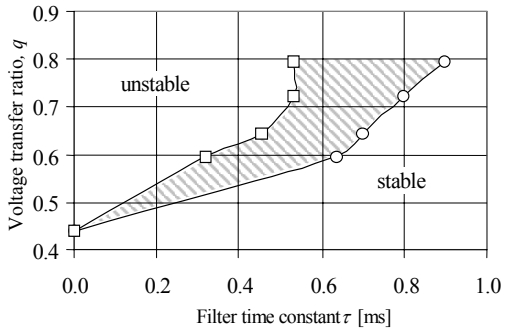

Fig. 5.27 - Experimental tests. Limit voltage transfer ratio as a function of the input digital filter τ.

The frequency of the oscillations was about 1850 Hz at $\tau = 0.9$ ms and moves toward higher values as τ decreases.

Additional tests were carried out considering digital filters of the 2nd and 3rd order. These filters were implemented using filters of first order in cascade. Fig. 5.28 shows in percent the increase of the limit voltage transfer ratio with respect to the case of first order filtering.

5.16. Conclusion

In the first part of this chapter a complete analysis of the stability of matrix converters has been carried out using a small signal analysis around a steady-state operating point. A complex mathematical model was necessary

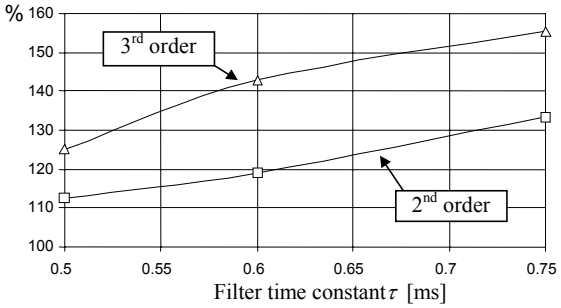

Fig. 5.28 - Experimental tests - Percentage of increment of the limit voltage transfer ratio for filters of 2nd and 3rd order.

to include all the system parameters and to emphasize their effect on the matrix converter stability. Particular attention has been paid to take the time delay introduced by digital controllers and the matrix converter power losses into account.

In the second part of this chapter, the analysis of the stability of matrix converters has been carried out using a large signal analysis based on the physical observation that the instability phenomena can be described as beatings.

The proposed analytical methods can be usefully adopted for the estimation of the maximum output power and for choosing among different input filter topologies. Furthermore they help understanding the operating principle of some common methods to increase the system stability, such as filtering the input voltages.

Finally, several experimental tests are reported to validate the theoretical approach.

Chapter 6

Quality of the Input Current

Abstract

This chapter deals with the quality of the input currents in matrix converters under input and output unbalanced conditions. Two control strategies of the input current displacement angle are presented and compared in order to emphasise their influence on the input current harmonic content. The first one is based on keeping the input current vector in phase with the input voltage vector. In the second one the input current displacement angle is dynamically modulated as function of positive and negative sequence components of the input voltages. In both cases the harmonic content and the three-phase RMS value of the input current have been evaluated analytically. In the second part of the chapter a general approach for the determination of the line current harmonic content in matrix converters is presented. The input disturbances, such as voltage unbalance and voltage harmonics, are considered as perturbations of the fundamental component, and a small-signal analysis is used to determine the spectrum of the line current. The proposed analytical approach has a general validity, because it takes the effects of the line and filter impedance into account, and can be usefully employed to evaluate the line current quality in

the point of common coupling for different filter topologies and supply distortions. Experimental results are given to confirm the analytical solution.

6.1. Introduction

As the matrix converter has no DC-link energy storage, any disturbance in the input voltages will be reflected in the output voltages. In particular, considering unbalanced input voltages, most of the modulation strategies introduce low order harmonics in the output voltages. The effects of unbalanced supply voltages have been already investigated in traditional converters [57]-[59], and recently some attention has been paid also to matrix converter [60]-[62].

In [61] a SVM algorithm for matrix converters has been presented which allows balanced output voltages to be generated, even under unbalanced supply conditions. As known, in the case of unbalanced supply voltages, the negative sequence components of the voltage system causes variation in magnitude and angular velocity of the input voltage vector. As a consequence, a simple synchronisation with the input voltages, as under balanced conditions, is no longer applicable and the input voltages have to be measured at each sampling instant. Owing to the angular velocity variation of the input voltage vector some problems arise in defining the input current displacement angle. In [61] the input current vector has been modulated in order to be, at any instant, in phase with the input voltage vector. In [62] the matrix converter analysis has been developed in order to take account of both input and output unbalance.

In the first part of this chapter an input current modulation strategy is proposed in order to reduce the harmonic content of the input current under unbalanced conditions and is compared to that described in [61]. The proposed control strategy is based on a dynamic modulation of the instantaneous displacement angle between input voltage and current vectors. The modulation law is determined as function of the magnitude and phase angle of positive and negative sequence components of the input voltages. The corresponding harmonic content, as well as the three-phase RMS value of the input current, has been determined analytically in the general case of input and output voltage unbalance.

A numerical simulation of the matrix converter has been carried out

assuming ideal switching devices. Some numerical results are presented in order to show the influence of input and output unbalance on the input current RMS value and input current harmonic content.

6.2. Input And Output Unbalance Representation

The input current of the matrix converter can be expressed as a function of the output power and the input voltage, as follows:

$$\bar{i}_i = \frac{4}{3}\frac{p_o\ \overline{\psi}}{\bar{e}_i\ \overline{\psi}^* + \bar{e}_i^*\ \overline{\psi}}. \tag{6.1}$$

Equation (6.1) is a general expression of the input current vector which can be further developed for any particular case. In the following the analysis will be focused on the development of (6.1) under input and output unbalanced conditions. In particular, for unbalanced supply voltages and sinusoidal conditions with period $T_i=2\pi/\omega_i$, the input line-to-neutral voltage vector can be written as

$$\bar{e}_i = \overline{E}_{ip} e^{j\,\omega_i\, t} + \overline{E}_{in}^*\ e^{-j\,\omega_i\, t} = \bar{e}_{ip} + \bar{e}_{in}^* \tag{6.2}$$

where $\overline{E}_{ip}$ and $\overline{E}_{in}$ are the time phasors of positive and negative symmetrical components of the line-to-neutral input voltages. It should be noted that, when a voltage unbalance is present, the negative sequence component causes the input voltage vector trajectory to change from circular to elliptical shape. This causes variations in input voltage vector magnitude and angular velocity.

By substituting (6.2) in (6.1) yields

$$\bar{i}_i = \frac{\frac{4}{3}p_o}{\left(\overline{E}_{ip}^* e^{-j\,\omega_i\, t} + \overline{E}_{in} e^{j\,\omega_i\, t}\right)\overline{\psi}\ + \left(\overline{E}_{ip} e^{j\,\omega_i\, t} + \overline{E}_{in}^* e^{-j\,\omega_i\, t}\right)\overline{\psi}^*}\,\overline{\psi}. \tag{6.3}$$

In order to make an analysis concerning balanced and unbalanced output conditions the effects due to the switching harmonics are neglected. Considering balanced output conditions the output power assumes a constant value. On the contrary, under unbalanced output conditions the output power can be in general expressed as the sum of a constant and an

alternating component. In this case the analysis requires the output quantities also to be expressed in terms of symmetrical components, as follows:

$$\bar{e}_o = \overline{E}_{op} e^{j\,\omega_o\, t} + \overline{E}^*_{on} e^{-j\,\omega_o t} \tag{6.4}$$

$$\bar{i}_o = \bar{I}_{op} e^{j\,\omega_o\, t} + \bar{I}^*_{on} e^{-j\,\omega_o t}\,. \tag{6.5}$$

Substituting (6.4) and (6.5) in (6.3) leads to the following expression for the input current vector:

$$\bar{i}_i = \frac{C_1 + \overline{C}_2\; e^{j\,2\,\omega_o\, t} + \overline{C}^*_2 e^{-j\,2\,\omega_o\, t}}{\left(\overline{E}^*_{ip} e^{-j\,\omega_i\, t} + \overline{E}_{in} e^{\,j\,\omega_i\, t}\right)\overline{\psi} \;+ \left(\overline{E}_{ip} e^{j\,\omega_i\, t} + \overline{E}^*_{in} e^{-j\,\omega_i\, t}\right)\overline{\psi}^*}\,\overline{\psi} \tag{6.6}$$

where the constants C_1 and $\overline{C}_2$ are given by

$$\begin{aligned} C_1 &= \overline{E}_{op}\;\bar{I}^*_{op} + \overline{E}_{on}\;\bar{I}^*_{on} + \overline{E}^*_{op}\;\bar{I}_{op} + \overline{E}^*_{on}\;\bar{I}_{on} \\ \overline{C}_2 &= \overline{E}_{op}\bar{I}_{on} + \overline{E}_{on}\bar{I}_{op} \end{aligned} \tag{6.7}$$

It can be shown that the constants C_1 and $\overline{C}_2$ are related to the mean value P_{om} and to the alternating component P_{oa} of the output power respectively, by the following relationships

$$C_1 = \frac{4}{3}\,P_{om}\;\;,\left|\overline{C}_2\right| = \frac{2}{3}\,P_{oa}\,. \tag{6.8}$$

Equations (6.3) and (6.6) show that the input current vector is influenced by the choice of the space vector $\overline{\psi}$ along which the input current is modulated. The choice of this space vector is important because it determines the input current harmonic content. The difference between the two modulation strategies described below is concerned with the choice of the space vector $\overline{\psi}$.

6.3. Constant Displacement Angle Between Input Voltage And Current Vectors (Method 1)

As explained above, with unbalanced supply voltage, the input voltage vector has variable angular velocity. Then, a possible modulation strategy

can be adopted in order to keep, at any instant, a constant displacement angle between input voltage and current vectors. In this case the input current vector direction can be defined by

$$\overline{\psi} = \overline{e}_i \; e^{-j\varphi_i} = \left(\overline{E}_{ip} \; e^{j\omega_i t} + \overline{E}^*_{in} e^{-j\omega_i t}\right) e^{-j\varphi_i} = \left(\overline{e}_{ip} + \overline{e}^*_{in}\right) e^{-j\varphi_i} \tag{6.9}$$

Fig. 6.1 shows the corresponding space vector representation in the d-q plane.

Introducing (6.9) in (6.6), after some manipulations leads to

$$\overline{i}_i = \frac{e^{-j\varphi_i}}{2\cos\varphi_i} \frac{C_1 + \overline{C}_2 e^{j2\omega_o t} + \overline{C}^*_2 e^{-j2\omega_o t}}{\left(\overline{E}^*_{ip} e^{-j\omega_i t} + \overline{E}_{in} e^{j\omega_i t}\right)} \tag{6.10}$$

Equation (6.10) clearly emphasises the influence of the input current displacement angle φ_i. Of course, assuming $\varphi_i = 0$ leads to the lowest value for the input current vector magnitude.

In order to evaluate the input current quality it is necessary to determine the harmonic content of the input current vector. For this purpose it is opportune to express by complex Fourier series the following term of (6.10)

$$\frac{1}{\left(\overline{E}^*_{ip} \; e^{-j\omega_i t} + \overline{E}_{in} \; e^{j\omega_i t}\right)} = \sum_{k=0}^{\infty} \overline{A}_{pk} \; e^{jk\omega_i t} + \sum_{k=1}^{\infty} \overline{A}^*_{nk} \; e^{-jk\omega_i t} \tag{6.11}$$

Rearranging (6.11) and equating terms with the same angular frequency it is possible to show that all even harmonic symmetrical components of the input current are identically null. The odd harmonic symmetrical components

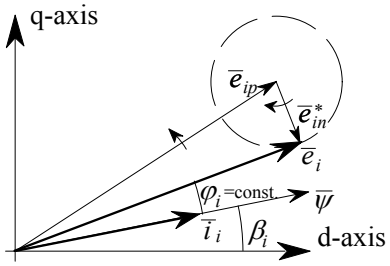

Fig. 6.1 - Space vector representation of Method 1.

for $\left|\overline{E}_{ip}\right| > \left|\overline{E}_{in}\right|$ are as follows:

$$\overline{A}_{pk} = \frac{1}{\overline{E}_{ip}^{*}}\left(-\frac{\overline{E}_{in}}{\overline{E}_{ip}^{*}}\right)^{\frac{k-1}{2}} \qquad k = 1, 3,... \tag{6.12}$$

$$\overline{A}_{nk} = 0 \qquad k = 1, 3,... \tag{6.13}$$

Taking the results obtained into account, (6.10) gives the input current vector in terms of complex Fourier series which can be expressed as

$$\bar{i}_i = \frac{e^{-j\varphi_i}}{2\cos\varphi_i}\left[\sum_{k=1,3}^{\infty}\frac{C_1}{\overline{E}_{ip}^{*}}\left(-\frac{\overline{E}_{in}}{\overline{E}_{ip}^{*}}\right)^{\frac{k-1}{2}} e^{jk\omega_i t} + \sum_{k=1,3}^{\infty}\frac{\overline{C}_2}{\overline{E}_{ip}^{*}}\left(-\frac{\overline{E}_{in}}{\overline{E}_{ip}^{*}}\right)^{\frac{k-1}{2}} e^{j(2\omega_o + k\omega_i)t} + \right.$$
$$\left. + \sum_{k=1,3}^{\infty}\frac{\overline{C}_2^{*}}{\overline{E}_{ip}^{*}}\left(-\frac{\overline{E}_{in}}{\overline{E}_{ip}^{*}}\right)^{\frac{k-1}{2}} e^{j(-2\omega_o + k\omega_i)t}\right] \tag{6.14}$$

As (6.14) shows, the harmonic content of $\bar{i}_i$ is represented by three series of harmonics which decay by the input unbalance degree u, which is defined as

$$u = \left|\overline{E}_{in}\right| \Big/ \left|\overline{E}_{ip}\right|. \tag{6.15}$$

The displacement angle φ_i has the same influence on all the current harmonic components. The magnitude of the harmonic components are related to the output power by means of the constants C_1 and $\overline{C}_2$. In particular the first series depends on the average value of the output power, while the second and third series depend on the amplitude of the output power alternating component. It should be noted that the third series may introduce sub-harmonic components depending on the difference between input and output frequency.

The harmonic content of the three line currents can be derived from the harmonic content of the input current vector.

A. Balanced Input - Unbalanced Output Conditions

Analysing (6.14) it is possible to verify that with balanced supply voltages (u=0), only the first harmonic component of each series will be present and the input current equation reduces to

$$\bar{i}_i = \frac{e^{-j\varphi_i}}{2\cos\varphi_i}\frac{1}{\overline{E}_{ip}^*}\left[C_1 e^{j\omega_i t} + \overline{C}_2 e^{j(2\omega_o+\omega_i)t} + \overline{C}_2^* e^{-j(2\omega_o-\omega_i)t}\right] \tag{6.16}$$

B. Unbalanced Input - Balanced Output Conditions

Under balanced output conditions the output power is constant and equals the input power. Considering unbalanced supply voltages, the input current cannot be balanced and sinusoidal. This can be verified rewriting (6.14) under such operating conditions ($\left|\overline{C}_2\right|$=0), leading to

$$\bar{i}_i = \frac{4}{3}\frac{e^{-j\varphi_i}}{2\cos\varphi_i}\left[\sum_{k=1,3}^{\infty}\frac{P_{om}}{\overline{E}_{ip}^*}\left(-\frac{\overline{E}_{in}}{\overline{E}_{ip}^*}\right)^{\frac{k-1}{2}} e^{jk\omega_i t}\right] \tag{6.17}$$

As it is possible to see, only the first series of (6.28) containing positive sequence harmonic components is present in this case. The input line currents, described by (6.31) are characterised by different waveforms but having equal RMS value.

C. Calculation of the Three-Phase RMS Value of the Input Current

Using the analytical relationships obtained it is possible to evaluate the three-phase RMS value of the input line currents which is defined as [63]

$$I_{RMS} = \sqrt{\frac{1}{T}\int_0^T \left(i_a^2 + i_b^2 + i_c^2\right)dt}\ . \tag{6.18}$$

The three-phase RMS value so defined is related to the Joule losses. Equation (6.18) can be expressed as function of positive and negative sequence components leading to

$$I_{RMS} = \sqrt{\frac{3}{2}}\sqrt{\sum_{k=0}^{\infty}\left|\bar{I}_{pk}\right|^2 + \sum_{k=1}^{\infty}\left|\bar{I}_{nk}\right|^2}\ . \tag{6.19}$$

Equation (6.19) is a general expression and can be further developed taking the results of (6.14) into account. If all the harmonic components in (6.14) have different harmonic order, (6.19) becomes

$$I_{RMS} = \sqrt{\frac{2}{3}} \frac{P_{om}}{\left|\overline{E}_{ip}\right|} \frac{1}{\sqrt{1-u^2}} \sqrt{1+\frac{1}{2}\frac{P_{oa}^2}{P_{om}^2}} \frac{1}{\cos\varphi_i} \tag{6.20}$$

The previous equation shows how the three-phase RMS value is affected by the input current displacement angle, the input unbalance degree and the output unbalance defined by the ratio between the alternating component and the mean value of the output power. From (6.20) it is possible to derive the three-phase RMS value of the input current vector for unity input power factor (φ_i=0), balanced supply voltages (u=0) and balanced output voltages (P_{oa}=0).

Equation (6.20) shows that operating the matrix converter with φ_i=0 leads to the lowest three-phase RMS value of the input current vector. It could be shown that this result is valid also considering any modulation strategy of φ_i.

6.4. Variable Displacement Angle Between Input Voltage And Current Vectors (Method 2)

As explained above, the harmonic content of the input current is strongly influenced by the choice of the input current reference angle. Analysing (6.20) we can note that a reduction of the harmonic content could be achieved applying a new modulation strategy of the input current displacement angle defined by the following expression

$$\overline{\psi} = \overline{E}_{ip}\, e^{j\,\omega_i\, t} - \overline{E}_{in}^{*}\, e^{-j\,\omega_i\, t} = \overline{e}_{ip} - \overline{e}_{in}^{*} \tag{6.21}$$

The space vector representation of this input current modulation is given in Fig. 6.2. As it is possible to see, due to the opposite angular velocity of $\overline{e}_{ip}$ and $\overline{e}_{in}^{*}$, a dynamic modulation of the input current displacement angle is obtained.

The implementation of the modulation law expressed by (6.21) is more complex with respect to that given by (6.9) being related to the positive and

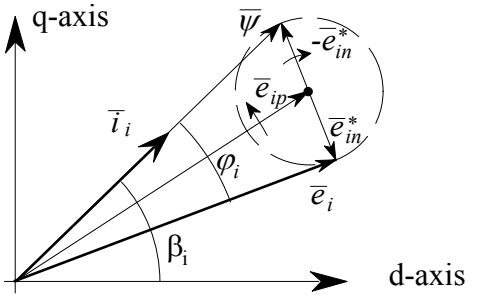

Fig. 6.2 - Space vector representation of Method 2.

negative sequence components of the input voltage. However, it can be shown that the modulation law expressed by (6.21) allows the elimination of the time dependent terms in the denominator of (6.6) which determine the presence of harmonic series in the input current. For this purpose, the analytical expression of the input current vector is obtained substituting (6.21) in (6.6). After some manipulations, it is possible to obtain the following equation

$$\bar{i}_i = \frac{C_1 + \overline{C}_2\, e^{j\,2\,\omega_o\,t} + \overline{C}_2^{*} e^{-j\,2\,\omega_o\,t}}{2\left(\overline{E}_{ip}\overline{E}_{ip}^{*} - \overline{E}_{in}\overline{E}_{in}^{*}\right)}\left(\overline{E}_{ip}\, e^{j\,\omega_i\,t} - \overline{E}_{in}^{*}\, e^{-j\,\omega_i\,t}\right) \tag{6.22}$$

By further developments of (6.22), the final expression for the input current becomes

$$\begin{aligned}\bar{i}_i = \frac{1}{2\left(\left|\overline{E}_{ip}\right|^2 - \left|\overline{E}_{in}\right|^2\right)}\Big[\, & C_1\overline{E}_{ip}e^{j\omega_i t} - C_1\overline{E}_{in}^{*}e^{-j\omega_i t} + \overline{C}_2\overline{E}_{ip}e^{j\,(2\,\omega_o+\omega_i)\,t} - \overline{C}_2\ \overline{E}_{in}^{*}\ e^{j\,(2\omega_o-\omega_i)\,t} + \\ & + \overline{C}_2^{*}\ \overline{E}_{ip}e^{j\,(-2\omega_o+\omega_i)\,t} - \overline{C}_2^{*}\ \overline{E}_{in}^{*}\ e^{j\,(-2\omega_o-\omega_i)\,t}\Big]\end{aligned} \tag{6.23}$$

Equation (6.23) shows that the input current harmonic content is reduced to a positive and a negative sequence fundamental component, plus two positive and two negative sequence harmonic components. Comparing Method 2 to Method 1 we can note that each series of (6.14) is substituted by a couple of terms in (6.23). In this way the high order harmonic components in the input current spectrum are eliminated.

A. Balanced Input - Unbalanced Output Conditions

In this case the equation of the input current vector can be obtained rewriting (6.23) with E_{in}=0, leading to

$$\bar{i}_i = \frac{1}{2\overline{E}_{ip}^*}\left[C_1 e^{j\omega_i t} + \overline{C}_2 e^{j(2\omega_o+\omega_i)t} + \overline{C}_2^* \, e^{j(-2\omega_o+\omega_i)t} \right] \tag{6.24}$$

By comparing (6.24) to (6.16) it appears that Method 2 is equivalent to Method 1 when operated with φ_i=0.

B. Unbalanced Input - Balanced Output Conditions

The use of Method 2 is particularly effective in the usual case of balanced output conditions ($\left|\overline{C}_2\right|$=0). In fact in this case (6.23) reduces to

$$\bar{i}_i = \frac{2}{3}\frac{P_{om}}{\left(\left|\overline{E}_{ip}\right|^2 - \left|\overline{E}_{in}\right|^2 \right)}\left[\overline{E}_{ip} e^{j\omega_i t} - \overline{E}_{in}^* e^{-j\omega_i t} \right] \tag{6.25}$$

As it is possible to see the current spectrum contains only the positive and the negative sequence fundamental component, so determining unbalanced but sinusoidal input line currents.

By comparing (6.25) to (6.17) the improvement achieved in the harmonic content of the input current using Method 2 is particularly evident.

C. Calculation of Input Current RMS Value

If all the harmonic components in (6.23) have different harmonic order, the three-phase RMS value of the input current becomes

$$I_{RMS} = \sqrt{\frac{2}{3}}\frac{P_{om}}{\left|\overline{E}_{ip}\right|}\frac{\sqrt{1+u^2}}{1-u^2}\sqrt{1+\frac{1}{2}\frac{P_{oa}^2}{P_{om}^2}} \tag{6.26}$$

Equation (6.26) shows how the three-phase RMS value is affected by the input unbalance degree and the output unbalance.

6.5. Numerical Simulations

Two different simulation models for the matrix converter have been used in the analysis. The first is based on the power balance equation, neglecting

the losses and switching effects of the converter.

In order to apply this model it is necessary to calculate the input voltage vector $\bar{e}_i$ for a given set of input voltages. Then, the input current vector $\bar{i}_i$ can be determined by (6.1) for a given output power P_o once the reference displacement angle of the input current is known. Finally the input line currents are readily evaluated and the harmonic content of $\bar{i}_i$ can be determined by numerical integration. The three-phase RMS value is calculated by (6.19).

For the numerical examples the following supply unbalance has been considered

$$\bar{E}_{ip} = 300 \text{ V } \underline{/\ 0°} \quad , \quad \bar{E}_{in} = 30 \text{ V } \underline{/\ 0°}$$

The input frequency is $f_i = 50$ Hz and the output frequency is $f_o = 80$ Hz.

6.6. Unbalanced Output Conditions

In the case of unbalanced output conditions the output voltages and currents have been assumed as follows

$$\bar{E}_{op} = 300/\sqrt{3} \text{ V } \underline{/\ -30°} \qquad \bar{E}_{on} = 0$$

$$\bar{I}_{op} = 208 \text{ A } \underline{/\ -67°} \qquad \bar{I}_{on} = 41.5 \text{ A } \underline{/\ -67°}$$

Fig. 6.3 shows the harmonic content of the input current vector when Method 1 is applied with unity input power factor (φ_i=0). As predicted by (6.14), three series of harmonics have been obtained. In Fig. 6.3, the three series are clearly denoted by different symbols. The first harmonic components of the series have frequency of -110 Hz, 50 Hz and 210 Hz. Note that negative values of frequency represent negative sequence harmonic components.

Fig. 6.4 shows the harmonic content of the input current vector when Method 2 is employed. Analysing Figs. 6.3 and 6.4 it appears that the new modulation strategy performs in order to transform each series of harmonics of Method 1, into a positive and a negative sequence component, having the same frequency of the first harmonics. The amplitudes and the frequencies of these harmonic components are in full agreement with that predicted by

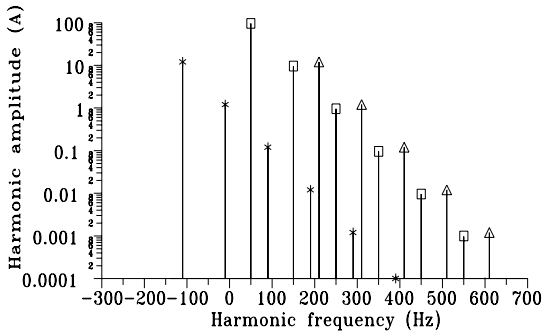

Fig. 6.3 - Input current spectrum, Method 1.

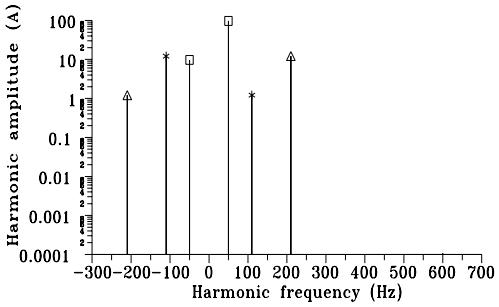

Fig. 6.4 - Input current spectrum, Method 2.

(6.23).

The three-phase RMS value of the input currents is 120 A for Method 1 and 121 A for Method 2. The same values have been obtained using (6.20) and (6.26) respectively. It can be noted that the reduction of the input current harmonic content has been obtained without appreciable increase of the input current three-phase RMS value.

6.7. Balanced Output Conditions

In order to emphasise the effectiveness of Method 2 an example with balanced output conditions has been investigated. The output voltages and currents have been assumed as follows

$$\overline{E}_{op} = 300/\sqrt{3}\ \text{V}\ \underline{/\ -30°} \qquad \overline{E}_{on} = 0$$

$$\bar{I}_{op} = 208\ \text{A}\ \underline{/\ -67°} \qquad \bar{I}_{on} = 0$$

Fig. 6.5 represents the input current spectrum using Method 1. In this figure it is possible to note the presence of a series of positive sequence harmonic components, as predicted by (6.17).

Fig. 6.6 represents the harmonic content obtained using Method 2. In this case the new modulation strategy determines sinusoidal input currents characterised by only a positive and a negative fundamental component, as it appears in (6.25). The three-phase RMS value of the input currents is 118 A for Method 1 and 119 A for Method 2.

Taking into account that Method 1 gives the lowest three-phase RMS

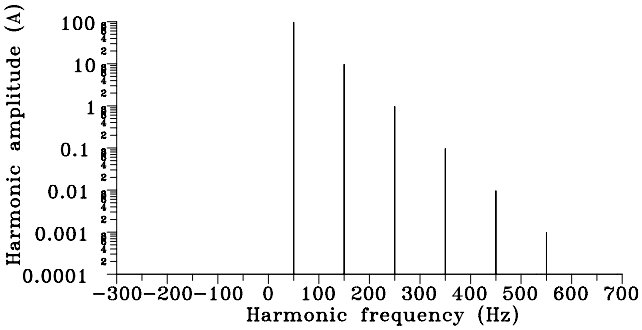

Fig. 6.5- Input current spectrum, Method 1.

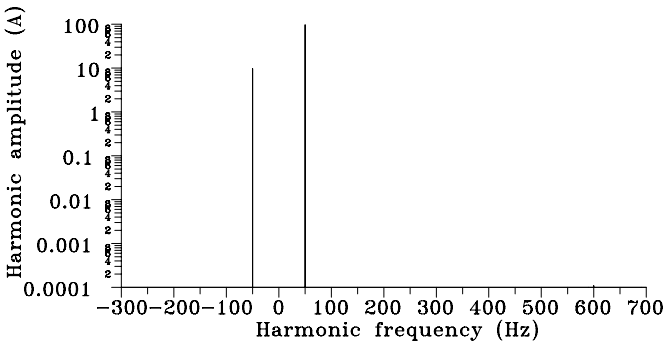

Fig. 6.6 - Input current spectrum, Method 2.

value for the input current, these results emphasise that, for acceptable unbalance degrees (u<0.1), Method 2 allows the input current harmonic elimination without appreciable increase of the three-phase RMS value.

The simulation model above described does not take into account the presence of the high frequency harmonic components due to the commutation processes. In order to take these phenomena into account a simulation model of the matrix converter has been implemented on the basis of the SVM algorithm. The matrix converter is constituted by ideal switches. The input terminals are connected to an ideal voltage source and the output terminal to a given R-L load.

In order to clearly show the switching effects, all the simulations have been performed assuming a switching frequency of 2 kHz. Figs. 6.7, 6.8 and 6.9 show the results obtained using Method 1, with unity input power factor. For display purposes the switched waveform of the input current shown in Fig. 6.7 is smoothed averaging the instantaneous values over each switching cycle period. Fig. 6.8 shows the waveforms of the three averaged input line

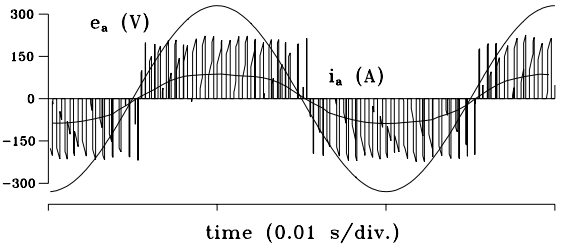

Fig. 6.7.- Input line-to-neutral voltage and line current

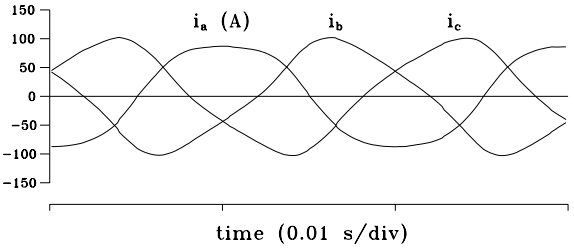

Fig. 6.8 - Averaged input line currents.

currents. It is possible to verify that the input line currents have the same RMS value even if they show different waveforms. Fig. 6.9 shows the harmonic content of the switched input currents. As it is possible to see, the higher amplitude harmonics correspond to those given in Fig. 6.5. The lower amplitude harmonics shown in Fig. 6.5 are, in Fig. 6.9, obscured by the switching harmonics.

Figs. 6.10, 6.11 and 6.12 show the numerical results obtained using Method 2, for the same operating conditions used for Method 1. Comparing Figs. 6.8 and 6.11 to Figs. 6.9 and 6.12 respectively it is evident the effect produced by the new modulation strategy which determines sinusoidal input currents, as predicted by (6.25). The presence of the negative sequence fundamental components determines different amplitude for the three input line currents. Fig. 6.12 shows the harmonic content of the switched input

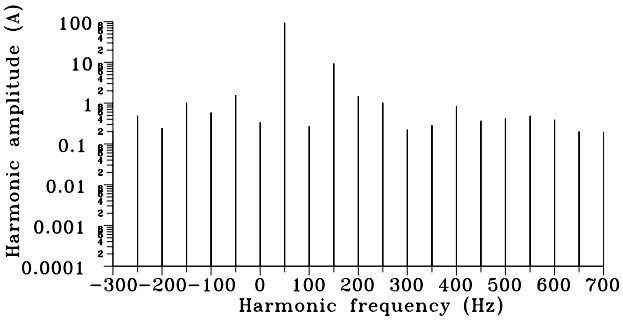

Fig. 6.9 - Input current spectrum.

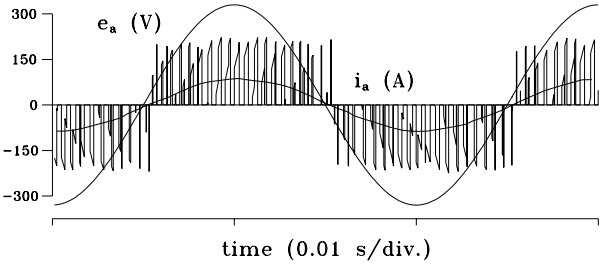

Fig. 6.10 - Input line-to-neutral voltage and line current.

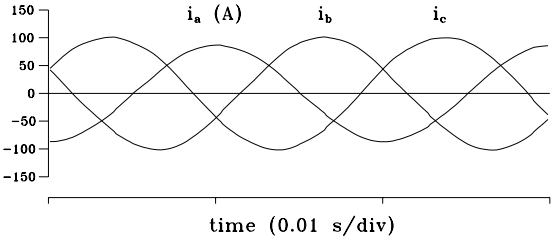

Fig. 6.11 - Averaged input line currents.

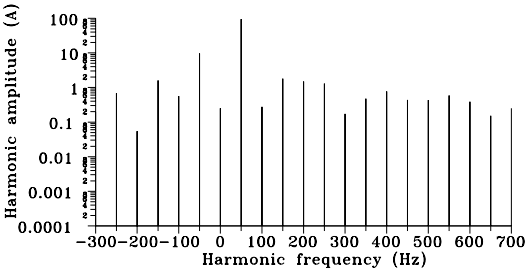

Fig. 6.12 - Input current spectrum.

currents. In this case also the higher amplitude harmonics match against the corresponding harmonics given in Fig. 6.6.

6.8. Preliminary Conclusions

Two input current modulation strategies for matrix converters have been analysed. The first one (Method 1) operates in order to keep the input current vector in phase with the input voltage vector. This strategy can be easily implemented requiring only the determination of the phase angle of the input voltage vector. Furthermore, it determines input currents with the lowest three-phase RMS value.

The second strategy (Method 2) is some more complicated to be implemented but it has the advantage concerning the possibility to reduce or eliminate the harmonic content of the input current. It has been shown that the improvement of the input current quality can be achieved without appreciable increase of the three-phase RMS value given by Method 1.

The two input current modulation strategies have been implemented using a SVM algorithm which ensures sinusoidal and balanced output voltages even under unbalanced input voltages.

For both strategies the input current harmonic spectrum and the three-phase RMS value have been determined analytically showing the influence of input and output unbalance conditions.

The validity of the theoretical analysis and the performance of the modulation algorithm have been confirmed by numerical simulations.

6.9. Introduction to the General Analysis of the Input Current

In the previous paragraphs two modulation strategies of the input current reference angle have been proposed in order to reduce the harmonic content of the input current under unbalanced supply voltages.

However, the supply voltages not only are usually unbalanced to some extent, but also show a typical distortion due to the presence of nonlinear loads connected to the grid. Hence, it is of practical interest to investigate the performance of MCs in these operating conditions as well [64], [65].

A general analysis on the input current for unbalanced and distorted input voltages was presented in [22].

Recently, industry has paid particular attention to this problem, that is important for EM compatibility and line current quality. In [66] the attention is focused on the input and output filters to meet the restrictive CISPR 11 standards, whereas an active damping has been proposed in [67] to reduce the line harmonics.

In the second part of this chapter, a general approach is developed in order to predict the spectrum of the line current of MCs controlled with the Space-Vector Modulation (SVM) technique in the case of unbalanced and non-sinusoidal supply voltages. The input current harmonic content is obtained with a small signal analysis of the system equations. In this way, it is possible to investigate the converter performance under any condition determined by input disturbances. The main advantage of the proposed approach is the possibility to consider the effects of the line and filter impedance, that can be important for detecting the resonant behaviours of the converter. The results of the analysis could be of considerable interest in

the design of the input filters.

6.10. Basic Equations

The system considered for the analysis is composed of a power supply, a second order input L-C filter, and a MC feeding a passive load. The system is the same shown in Fig. 5.1, where space vector notation is used for the representation of the system variables.

The input filter is generally needed to smooth the input currents and to satisfy the EMI requirements. It is also known that the design of the input filters is strictly related to the switching frequency [68]. If the input filter is well designed, current harmonics at frequencies greater or equal to the switching frequency are smoothed adequately.

In this paragraph the main equations related to the system represented in Fig. 5.1 will be introduced. The variables t and ω will be used to distinguish between the time domain and the Fourier domain respectively.

In the following, the analytical developments are carried out neglecting the effects of the switching harmonics, considering for the output voltages and input currents their average values over a cycle period T_p.

The input current modulation strategy keeps the input current vector in phase with the actual input voltage vector, determining instantaneous unity input power factor.

However, as shown in the beginning of this chapter, variants of this modulation strategies are possible to reject the input voltage disturbances, such as the one based on keeping the input current vector in phase with the fundamental component of input voltage vector instead of its instantaneous value [22].

Hence, it is convenient to consider the modulation vector as a function of the input voltage vector, and eventually of its derivatives and integrals, as follows:

$$\overline{\psi} = \overline{\psi}(\overline{v}, \frac{d\overline{v}}{dt}, \int \overline{v} dt)\,. \tag{6.27}$$

The equation for the input side of the MC, written in the Fourier domain, is as follows:

$$\overline{E}_{eq}(\omega) = \overline{Z}(\omega)\overline{i}(\omega) + \overline{v}(\omega) \tag{6.28}$$

where $\overline{E}_{eq}(\omega)$ and $\overline{Z}(\omega)$ are the Thevenin equivalent voltage and impedance of the voltage source and input filter.

For the particular case shown in Fig. 5.1, $\overline{E}_{eq}(\omega)$ and $\overline{Z}(\omega)$ can be expressed as functions of the line and filter parameters as follows:

$$\overline{E}_{eq}(\omega) = \frac{\overline{e}_s(\omega)}{1 + j\omega C_f \overline{Z}_{tot}(\omega)} \tag{6.29}$$

$$\overline{Z}(\omega) = \frac{\overline{Z}_{tot}(\omega)}{1 + j\omega C_f \overline{Z}_{tot}(\omega)} \tag{6.30}$$

where

$$\overline{Z}_{tot}(\omega) = R_s + j\omega L_s + \frac{j\omega L_f R_f}{j\omega L_f + R_f}. \tag{6.31}$$

The behaviour of the system at the input side is completely described by (1.4) and (6.28) once the converter power and the modulation law are assigned.

The line current, instead, depends on the filter topology. For the typical case shown in Fig. 5.1, the line current is

$$\overline{i}_L(\omega) = \frac{\overline{e}_s(\omega) - \overline{v}(\omega)}{\overline{Z}_{tot}(\omega)}. \tag{6.32}$$

As can be seen from (6.32), to determine the line current spectrum, it is necessary to know the spectrum of the input voltage vector. However, the input voltage depends on the current absorbed by the converter, due to the voltage drop on the impedance of the line and the filter.

For this reason, to determine the line current spectrum, it is necessary to solve the set of non-linear equations (1.4), (6.27) and (6.28). The solution of this problem will be presented in the following sub-sections.

A. Steady State Operating Conditions with Balanced and Sinusoidal Supply Voltages

In steady-state operating conditions, with balanced and sinusoidal supply

voltages, the input voltages can be represented by means of rotating space vectors with constant magnitudes as follows:

$$\overline{E}_{eq}(t) = \overline{E}_1 e^{j\omega_i t} \tag{6.33}$$

$$\overline{v}(t) = \overline{V}_1 e^{j\omega_i t} \tag{6.34}$$

where ω_i is the angular frequency of the voltage source.

In these operating conditions, the modulation vector coincides with the input voltage vector, as follows:

$$\overline{\psi}(t) = \overline{V}_1 e^{j\omega_i t} \quad . \tag{6.35}$$

B. Steady State Operating Conditions with Unbalanced and Non-sinusoidal Supply Voltages.

If the supply voltages are not balanced and sinusoidal, then (6.33)-(6.35) must be rewritten in the following form:

$$\overline{E}_{eq}(t) = \overline{E}_1 e^{j\omega_i t} + \Delta\overline{E}_{eq}(t) \tag{6.36}$$

$$\overline{v}(t) = \overline{V}_1 e^{j\omega_i t} + \Delta\overline{v}(t) \tag{6.37}$$

$$\overline{\psi}(t) = \overline{V}_1 e^{j\omega_i t} + \Delta\overline{\psi}(t) \tag{6.38}$$

where $\Delta\overline{E}_{eq}(t)$, $\Delta\overline{v}(t)$ and $\Delta\overline{\psi}(t)$ are the perturbations of each quantity with respect to its fundamental harmonic.

It is convenient to rewrite (6.37) and (6.38) in terms of new variables, that allow one to make easier the mathematical approach, as follows:

$$\overline{v}(t) = \overline{V}_1 e^{j\omega_i t}\left(1 + \overline{\varepsilon}(t)\right) \tag{6.39}$$

$$\overline{\psi}(t) = \overline{V}_1 e^{j\omega_i t}\left(1 + \overline{\gamma}(t)\right) \tag{6.40}$$

where

$$\overline{\varepsilon}(t) = \frac{\Delta\overline{v}(t)}{\overline{V}_1} e^{-j\omega_i t} \tag{6.41}$$

$$\overline{\gamma}(t) = \frac{\Delta\overline{\psi}(t)}{\overline{V}_1} e^{-j\omega_i t} \, . \tag{6.42}$$

As can be seen from (6.41) and (6.42), $\bar{\varepsilon}(t)$ and $\bar{\gamma}(t)$ represent the perturbations $\Delta\bar{v}(t)$ and $\Delta\bar{\psi}(t)$ written in p.u. in a reference frame synchronous with the fundamental component of the input voltage.

The expression of the input current can be found under the assumption that the perturbations $\Delta\bar{v}(t)$ and $\Delta\bar{\psi}(t)$ are small compared to the fundamental harmonics. Substituting (6.39) and (6.40) in (1.4) leads to the following expression of the input current, valid for small signals:

$$\bar{i}(t) = \frac{2}{3}\frac{P_o e^{j\omega_i t}}{\bar{V}_1^*}\left(1 + \frac{\bar{\gamma}(t) - \bar{\gamma}^*(t)}{2} - \frac{\bar{\varepsilon}(t) + \bar{\varepsilon}^*(t)}{2}\right) \tag{6.43}$$

where the symbol "*" is used to represent complex conjugate variables.

6.11. Small-Signal Equations in the Fourier Domain

In order to determine the spectrum of the line current, it is convenient to rewrite the equations shown in the previous paragraph in the Fourier domain.

Equations (6.36), (6.39)-(6.40) and (6.43) become

$$\bar{E}_{eq}(\omega) = \bar{E}_1\delta(\omega - \omega_i) + \Delta\bar{E}_{eq}(\omega) \tag{6.44}$$

$$\bar{v}(\omega) = \bar{V}_1\delta(\omega - \omega_i) + \bar{V}_1\bar{\varepsilon}(\omega - \omega_i) \tag{6.45}$$

$$\bar{\psi}(\omega) = \bar{V}_1\delta(\omega - \omega_i) + \bar{V}_1\bar{\gamma}(\omega - \omega_i) \tag{6.46}$$

$$\bar{i}(\omega) = \frac{2P_o}{3\bar{V}_1^*}\delta(\omega - \omega_i) + \Delta\bar{i}(\omega) \tag{6.47}$$

where $\delta(\omega)$ is the Dirac function and $\Delta\bar{i}(\omega)$ is defined as follows:

$$\Delta\bar{i}(\omega) = \frac{P_o}{3\bar{V}_1^*}\left[\bar{\gamma}(\omega - \omega_i) - \bar{\gamma}^c(\omega - \omega_i) - \bar{\varepsilon}(\omega - \omega_i) - \bar{\varepsilon}^c(\omega - \omega_i)\right]. \tag{6.48}$$

In (6.48) the superscript " ^{c} " applied to the functions $\bar{\gamma}$ and $\bar{\varepsilon}$ is used to represent the Fourier transform of the complex conjugate of $\bar{\varepsilon}(t)$ and $\bar{\gamma}(t)$, i.e. $\bar{\varepsilon}^*(t)$ and $\bar{\gamma}^*(t)$. Some details on this mathematical representation, that will be used in the following, can be found in Appendix C.

As can be seen from (6.48), the perturbation of the input current can be determined only if the modulation law is assigned. For sake of simplicity, it is convenient to suppose that the perturbation of the modulation vector is directly related to the perturbation of the input voltage vector, as follows:

$$\overline{\gamma}(\omega) = \overline{H}(\omega)\overline{\varepsilon}(\omega) \tag{6.49}$$

where $\overline{H}(\omega)$ is a transfer function that can be chosen by the designer. It is possible to show that (6.49) is rather general and comprises several well-known modulation laws of the input current as particular cases. For instance, a modulation strategy that keeps the modulation vector in phase with the input voltage is represented by

$$\overline{H}(\omega) = 1 \tag{6.50}$$

whereas, the modulation strategy that keeps the modulation vector in phase with the fundamental component of the input voltage is described by

$$\overline{H}(\omega) = 0\,. \tag{6.51}$$

Substituting (6.26) in (6.25) leads to the following expression for the input current disturbance:

$$\Delta\overline{i}(\omega) = \frac{P_o}{3\overline{V}_1^*}\left[\left(\overline{H}(\omega-\omega_i)-1\right)\overline{\varepsilon}(\omega-\omega_i) - \left(\overline{H}^c(\omega-\omega_i)+1\right)\overline{\varepsilon}^c(\omega-\omega_i)\right] \tag{6.52}$$

6.12. Determination of the Input Voltage

It is possible to determine the fundamental equations that must be satisfied by the fundamental component of the input voltage and its perturbation substituting (6.44), (6.45) and (6.47) in (6.28), and taking (6.52) into account. Equating the terms corresponding to the same frequencies leads to the following independent equations:

$$\overline{E}_1 = \frac{2\overline{Z}(\omega_i)P_o}{3\overline{V}_1^*} + \overline{V}_1 \tag{6.53}$$

$$\frac{\Delta\overline{E}_{eq}(\omega)}{\overline{V}_1} = \left\{\frac{\overline{Z}(\omega)P_o\overline{V}_1}{3V_1^2}\left[\left(\overline{H}(\omega-\omega_i)-1\right)+1\right]\overline{\varepsilon}(\omega-\omega_i)\right.$$

$$-\frac{\overline{Z}(\omega)P_o\overline{V}_1}{3V_1^2}\left(\overline{H}^c(\omega-\omega_i)+1\right)\overline{\varepsilon}^c(\omega-\omega_i)\Bigg\}\ . \tag{6.54}$$

Equation (6.53) allows the determination of the fundamental harmonic of the input voltage in terms of supply voltage, grid and filter impedance and power delivered to the load.

Equation (6.54) instead relates the input voltage perturbation to the supply voltage perturbation. It is evident that in (6.54) there are two unknowns, namely $\overline{\varepsilon}$ and $\overline{\varepsilon}^c$. To emphasize this aspect, (6.54) can be rewritten performing a frequency shift as follows:

$$\frac{\Delta\overline{E}_{eq}(\omega+\omega_i)}{\overline{V}_1}=\overline{A}(\omega)\overline{\varepsilon}(\omega)+\overline{B}(\omega)\overline{\varepsilon}^c(\omega) \tag{6.55}$$

where

$$\overline{A}(\omega)=\frac{\overline{Z}(\omega+\omega_i)P_0}{3V_1^2}\left[\overline{H}(\omega)-1\right]+1 \tag{6.56}$$

$$\overline{B}(\omega)=-\frac{\overline{Z}(\omega+\omega_i)P_0}{3V_1^2}\left[\overline{H}^c(\omega)+1\right]\ . \tag{6.57}$$

Hence, to solve (6.55), a further equation is needed. This equation can be found by applying the operator "c" to (6.55), leading to

$$\frac{\Delta\overline{E}_{eq}^c(\omega-\omega_i)}{\overline{V}_1^*}=\overline{B}^c(\omega)\overline{\varepsilon}(\omega)+\overline{A}^c(\omega)\overline{\varepsilon}^c(\omega)\,. \tag{6.58}$$

Solving (6.55) and (6.58) leads to the following expression for the perturbation of the input voltage:

$$\overline{\varepsilon}(\omega)=\frac{\overline{A}^c(\omega)\Delta\overline{E}_{eq}(\omega+\omega_i)}{\overline{D}(\omega)\overline{V}_1}-\frac{\overline{B}(\omega)\Delta\overline{E}_{eq}^c(\omega-\omega_i)}{\overline{D}(\omega)\overline{V}_1^*} \tag{6.59}$$

where

$$\overline{D}(\omega)=\overline{A}(\omega)\overline{A}^c(\omega)-\overline{B}(\omega)\overline{B}^c(\omega)\ . \tag{6.60}$$

Once the input voltage perturbation is known from (6.59) and (6.45), it is

possible to derive the expression of the line current by means of (6.32).

6.13. Expression of the Input Voltage in Terms of Harmonics

In the previous paragraphs it has been shown how to calculate the Fourier transform of the input voltage, and consequently of the line current, in a very general form.

However, the most common case is the one with supply harmonics having frequencies multiple of the fundamental one, as follows

$$\Delta\overline{E}_{eq}(\omega) = \sum_{k=-\infty, k\neq 1}^{\infty} \overline{E}_k \delta(\omega - k\omega_i) \ . \tag{6.61}$$

Substituting (6.31) in (6.59) and taking (6.45) into account, leads to the following expression of the input voltage vector in the time domain:

$$\overline{v}(t) = \overline{V}_1 e^{j\omega_i t} + \sum_{k=-\infty, k\neq 1}^{\infty} \overline{V}_k e^{jk\omega_i t} \tag{6.62}$$

where

$$\overline{V}_k = \frac{\overline{A}^c\big((k-1)\omega_i\big)}{D\big((k-1)\omega_i\big)}\overline{E}_k - \frac{\overline{V}_1}{\overline{V}_1^*}\frac{\overline{B}\big((k-1)\omega_i\big)}{D\big((k-1)\omega_i\big)}\overline{E}_{2-k}^* \ . \tag{6.63}$$

Assuming that the modulation strategy is the one keeping the input current vector in phase with the input voltage vector, corresponding to (6.50), the explicit expression of (6.63) is as follows

$$\overline{V}_k = \frac{\overline{E}_k + \dfrac{2}{3}\dfrac{P_o}{\overline{V}_1^{*2}}\overline{Z}\big(k\omega_i\big)\overline{E}_{2-k}^*}{1 - \left(\dfrac{2}{3}\dfrac{P_o}{V_1^2}\right)^2 \overline{Z}\big(k\omega_i\big)\overline{Z}^*\big((2-k)\omega_i\big)}, \ k \neq 1 \ . \tag{6.64}$$

The line current can be expressed as a Fourier series as follows

$$\overline{i}_L(t) = \sum_{k=-\infty}^{\infty} \overline{I}_{L,k} e^{jk\omega_i t} \tag{6.65}$$

where

$$\bar{I}_{L,k} = \frac{\overline{E}_k - \overline{V}_k}{\overline{Z}_{tot}(k\omega_i)}. \tag{6.66}$$

As can be seen from (6.64), the *k-th* harmonic of the input voltage, and consequently the line current, is a weighted value of the *k-th* and the (2-*k*)-*th* harmonics of the supply voltage. This result is not new, and was already found in [22]. However, it is remarkable that the weights depends on the line and filter impedance, and the converter power as well.

This result can be important for the design of the input L-C filters, as its resonant frequency should be chosen far enough from the frequency of the supply voltage harmonics.

6.14. Experimental Results

In order to verify the theoretical analysis of the input current, a prototype of MC was used to supply a passive R-L load.

The control algorithm was implemented on the TMS320F2812, a fixed point DSP manufactured by Texas Instruments. The cycle period was 125 μs, corresponding to a switching frequency of 8 kHz.

The converter is fed by a voltage transformer with variable voltage transfer ratio to adjust the input voltage to a value of about 115 V_{rms}. Three capacitors of 40 μF are wyse-connected at the input side of the converter. The other parameters concerning the filter, the supply and load are reported in Tab. 6.1.

Firstly, the supply voltages, that show a small amount of distortion and unbalance, were sampled and their spectrum was determined. The magnitude and the phase of the main harmonics of the supply voltage are listed in Tab. 6.2, whereas its spectrum is shown in Fig. 6.13.

Then, the converter was activated, and the line currents and the input voltages were sampled and stored.

The waveforms of the three line-to-neutral input voltages are shown in Fig. 6.14(a), whereas the waveforms of the three line currents are shown in Fig. 6.14(b).

As can be seen from Fig. 6.14(b), the line currents are distorted to some extent. There are two main reasons for this distortion. The first one is that, despite a constant output power, the input currents of the MC cannot be

TABLE 6.1 - SYSTEM PARAMETERS

$\omega_i = 2\pi 50$ rad/s
L_s+$L_f = 1$ mH, $R_f = 300\ \Omega$
$C_f = 40\ \mu$F
$R_s = 0.2\ \Omega$
$P_i = 497$ W
$\omega_o = 2\pi 150$ rad/s
$T_c = 125\ \mu$s.

TABLE 6.2
MAIN HARMONICS OF THE VOLTAGE SUPPLY

Order	Magnitude [V]	Phase [Deg.]
1	93.57	0
3	0.11	+126
5	0.10	+160
7	0.88	-42
-1	1.10	+30
-5	2.18	-20
-7	0.32	+62

sinusoidal if the input voltages are unbalanced or non-sinusoidal. The second reason is that the capacitor of the L-C input filter tends to enhance the harmonic distortion that is present in the supply voltage.

The spectrum of the input voltage vector and of the line current vector, in p.u. of the fundamental component, is shown in Figs. 6.15(a) and 6.15(b). As can be seen, according to the theory exposed, supply harmonics of order k lead to input voltage and line current harmonics of order k and $2-k$.

To validate the proposed analytical approach, the spectrum of the line current must be compared with the one that can be calculated with (6.66).

It is worth noting that, before (6.66) is used, $\overline{V}_1$ must be preliminary determined solving (6.53), then the input voltage harmonics $\overline{V}_k$ must be calculated with (6.64).

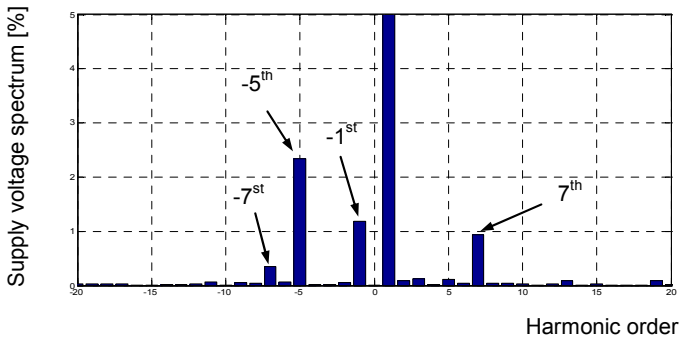

Fig. 6.13 – Experimental results. Spectrum of the supply voltage vector $\overline{e}_s$ in per cent of the fundamental component.

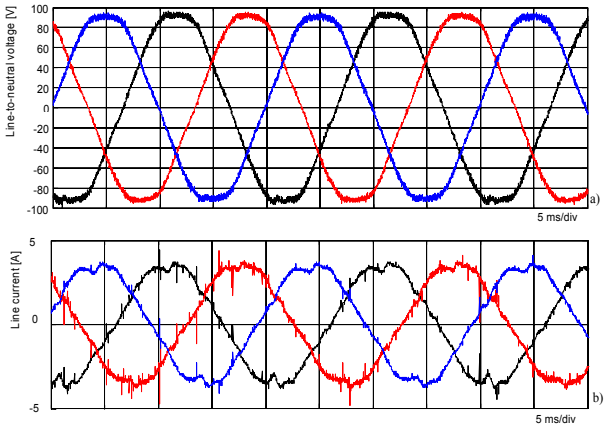

Fig. 6.14 – Experimental tests. Sampled waveforms of the line-to-neutral voltages (a) and of the line currents (b).

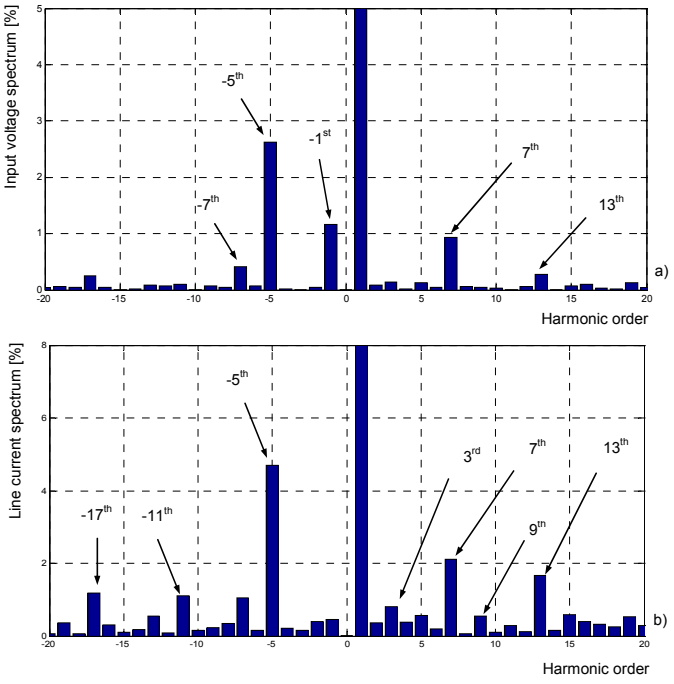

Fig. 6.15 – Experimental result. a) Spectrum of the input voltage vector, in percent of the fundamental component. b) Spectrum of the line current vector, in percent of the fundamental component.

The expected spectrum of the line current is shown in Fig. 6.16. As can be seen, there is a good agreement between theoretical and experimental results.

The proposed analytical approach is valid if power absorbed by the MC is constant. To verify this assumption, it can be noted that the waveform of the output current, shown in Fig. 6.17, is almost sinusoidal, except for the typical ripple due to SVM. This guarantees that the output power, and thus the input power, is rather constant.

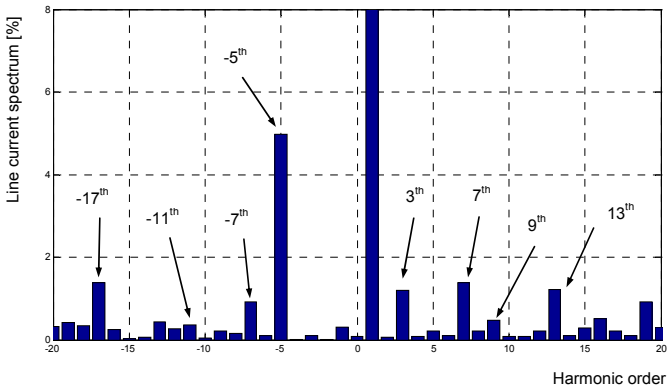

Fig. 6.16 – Theoretical result. Spectrum of the line current, in per cent of the fundamental component.

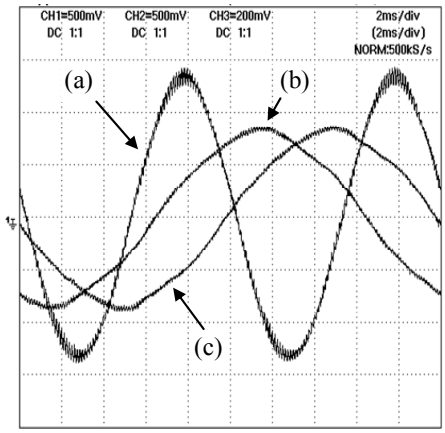

Fig. 6.17 - Experimental test. Typical waveforms. (a) Load current (2 A/div). (b) Line-to-line voltage V_{AB} (150 V/div). (c) Line-to-line voltage V_{AC} (150 V/div).

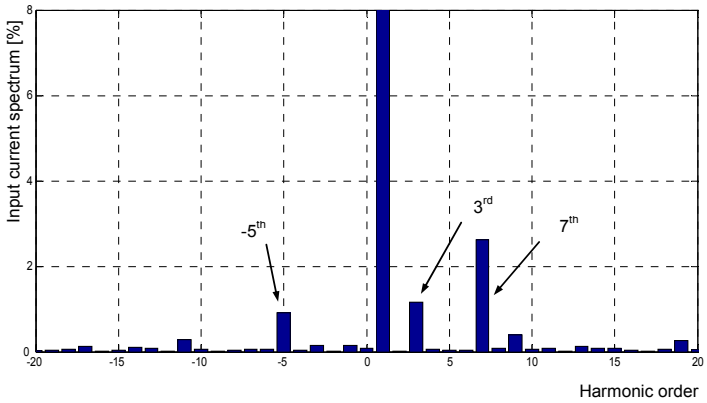

Fig. 6.18 - Theoretical result. Spectrum of the input current, in per cent of the fundamental component.

In order to emphasizes the effect of the line and filter impedance on the line current, the theoretical spectrum of the input current is shown in Fig. 6.18. It is calculated by means of (6.1) on the basis of the sampled values of the input voltages.

This result is the same that could be achieved assuming that the converter is fed by an ideal voltage source, without internal impedence and LC input filter.

It is worth noting that the spectra of the line and input currents are rather different, specially for the magnitude of the -5th and the 7th harmonics.

This means that, if the quality of the input current is investigated, the effect of the line and filter parameters cannot be ignored and the traditional analysis, based on the assumption that they are negligible, is not sufficiently accurate.

6.15. Conclusion

A theoretical method for the determination of the line current spectrum has been presented. The method is based on a small-signal analysis of the whole system in the Fourier domain and its main characteristic is that it takes the effect of the filter and line impedance into account.

In addition, it is rather general, because it allows the determination of the line current spectra for different input current modulation strategies.

The utility of the proposed analysis is mainly related to unbalanced and non-sinusoidal supply voltage and can be used for the design of the input filter.

The validity of the theoretical analysis has been confirmed by experimental tests.

Chapter 7

Electric Drives

Abstract

The control scheme of a speed-sensorless induction motor drive fed by a matrix converter is presented. The proposed scheme allows the motor to exploit the maximum torque in the whole speed range, and shows a reduced dependence on the motor parameters. The behaviour of the matrix converter is assessed by means of computer simulations and experimental results.

7.1. Introduction

Induction motor drives fed by MC can theoretically offer better performance than traditional drives based on voltage source inverters [69]. The main advantages that are often cited are the compactness, the bidirectional power flow and the higher current quality. In fact, the matrix converter is more compact than a voltage source inverter (VSI), since it does not require bulky capacitors (some small capacitors are present in the input high frequency filter and in the safety diode clamp). In addition, breaking resistances are not necessary, since the power flow during breaking can be reverted, thus leading to a regenerative operation. Finally, the input currents are sinusoidal and the power factor is near unity.

However, the use of MC poses some problems. First of all, to obtain a good quality of the output currents, the input voltages should be constantly measured in order to adapt the duty-cycles of the output voltages in presence

of input voltage harmonics or disturbances [22]. When the power delivered to the load is constant, this closed-loop scheme has been proved to be unstable, depending on the value of the output power and the parameters of the input filter and the grid. In fact, as soon as the output power exceeds a limit value, voltage and current oscillations arise at the input of the converter [56].

Secondly, MC bidirectional switches cause an higher voltage drop compared to VSI power switches, since the output current has to pass through two components in series, usually an IGBT and a diode. In addition, the switch commutation is a complex process that introduces dead-times similar to those of voltage source inverters. These converter nonlinearities, together with the sensor offsets, could affect the estimation of the voltage applied to the load [12], [70].

Finally, some studies have shown that the quality of the input current deteriorates if the source voltage is unbalanced or distorted. The same happens if the load current is distorted or unbalanced [22].

All these aspects should be taken into account when assessing the performance of an electric motor drive fed by a MC.

Some paper describing drives based on MC have already been presented. Initially, the researchers turned their attention to the solution of the hardware problems, such as the construction of the bidirectional switches or the process of current commutation. Then, the compactness of MC suggested the possibility to integrate the converter and the motor in a single unit, in order to reduce the costs and to increase the overall efficiency [71], [72].

On the other hand, some researches were made to transfer the existing control techniques for voltage source inverters to MCs, such as constant V/Hz, field-oriented control and direct torque control [48], [73]-[75].

Electric drives are often requested to deliver constant power at speeds higher than the rated one. However so far the performance of drives fed by MC and operating in the field-weakening region has not been examined in details.

When the induction motors are used for applications at high speed, it is desirable to retain the maximum torque capability in the field weakening region. Several papers about this issue were presented for drives fed by traditional VSI [76]-[80]. According to these field weakening algorithms, the optimal flux value of the motor should be updated by means of look-up

tables or explicit expressions containing the motor parameters and quantities such as the motor speed, the motor currents, the dc-link voltage and the requested torque. However, the performance of these algorithms is strictly related to the accuracy by which the parameters are known. In addition, the drive performance in the high speed range may depend on the correct determination of the base speed, which is function of the actual dc-link voltage and the overload capability.

As a consequence, new methods for compensating the parameter variations and the uncertainties of the models have been investigated. Among these, some adaptive schemes have been proposed in order to provide a suitable estimation of the varying parameters [81]-[84]. These methods provide good drive performance to the detriment of the complexity of the control scheme and the regulator tuning.

A suitable method for robust field weakening is to determine the optimal flux level using closed-loop schemes that analyze the motor behaviour, rather than look-up tables or explicit expressions containing the motor parameters. From this point of view, interesting contributions towards robust field weakening strategies were proposed in [85]-[88]. According to these papers, the flux is adjusted on the basis of the supply voltage requested by the regulators. If the requested voltage is greater than the available one, the field weakening algorithm reduces the flux. Furthermore, suitable control strategies allows the motor to exploit the maximum torque in the whole speed range, namely the motor current is kept equal to the maximum current in the constant power speed range, and is lower in the decreasing power speed range.

In this chapter, a field weakening scheme for induction motor drives fed by a MC is presented and assessed.

The proposed scheme allows the motor to exploit the maximum torque capability in the whole speed range and exhibits a reduced dependence on the motor parameters and the base speed. In addition, it does not require any complex calculation of the flux level or look-up tables.

The traditional field-oriented control utilizes the stator current components as control variables. The d-component of the stator current acts on the rotor flux, whereas the q-component is proportional to the motor torque. In the proposed rotor-flux-oriented control scheme the main control

variables are the stator flux components instead of the stator current components. This basic choice simplifies the control scheme and simplifies the tuning of the regulators.

Since the motor is fed by a MC, all the advantages provided by this type of converter (compactness, bi-directional power flow, good quality of input and output currents) are inherited by the whole drive.

The feasibility of the motor drive (including the robust field weakening algorithm) is confirmed through simulations and experimental tests.

7.2. Machine Equations

The behaviour of the induction machine can be described in terms of space vectors by the following equations written in a reference frame synchronous with the rotor flux:

$$\bar{v}_s = R_s \bar{i}_s + j\omega \bar{\varphi}_s + \frac{d\bar{\varphi}_s}{dt} \tag{7.1}$$

$$0 = R_r \bar{i}_r + j(\omega - \omega_m)\bar{\varphi}_r + \frac{d\bar{\varphi}_r}{dt} \tag{7.2}$$

$$\bar{\varphi}_s = L_s \bar{i}_s + M \bar{i}_r \tag{7.3}$$

$$\bar{\varphi}_r = L_r \bar{i}_r + M \bar{i}_s \tag{7.4}$$

$$T = -\frac{3}{2} p \bar{i}_r \cdot j\bar{\varphi}_r \,. \tag{7.5}$$

where p is the pole pairs number, ω is the angular speed of the rotor flux vector, ω_m is the rotor angular speed in electric radians, and "·" denotes the scalar product.

Solving (7.3) and (7.4) with respect to $\bar{i}_s$ and $\bar{i}_r$, and substituting in (7.2) and (7.5) yields

$$0 = -\left(\frac{R_r M}{\sigma L_s L_r}\right)\bar{\varphi}_s + \left[\frac{R_r}{\sigma L_r} + j(\omega - \omega_m)\right]\bar{\varphi}_r + \frac{d\bar{\varphi}_r}{dt} \tag{7.6}$$

$$T = \frac{3}{2} p \frac{M}{\sigma L_s L_r} \overline{\varphi}_s \cdot j\overline{\varphi}_r \tag{7.7}$$

where the parameter σ is defined as follows:

$$\sigma = 1 - \frac{M^2}{L_s L_r} \quad . \tag{7.8}$$

The reference frame orientation is chosen so that the d-axis has the direction of the rotor flux vector. Hence (7.6) can be rewritten in terms of d and q components as follows:

$$\frac{\sigma L_r}{R_r} \frac{d\varphi_r}{dt} + \varphi_r = \frac{M}{L_s} \varphi_{sd} \tag{7.9}$$

$$(\omega - \omega_m)\varphi_r = \frac{R_r M}{\sigma L_s L_r} \varphi_{sq} . \tag{7.10}$$

Also (7.7) can be rewritten as follows

$$T = \frac{3}{2} p \frac{M}{\sigma L_s L_r} \varphi_r \varphi_{sq} \quad . \tag{7.11}$$

As can be seen, these equations are quite similar to the corresponding equations of the traditional field oriented control based on d-q stator current components. In fact the rotor flux depends only on φ_{sd}, whereas the motor torque is proportional to φ_{sq}.

In steady-state operation, (7.1), (7.3) and (7.9) become

$$\overline{V}_s = R_s \overline{I}_s + j\omega \overline{\varphi}_s \tag{7.12}$$

$$\varphi_{sd} = L_s I_{sd} \tag{7.13}$$

$$\varphi_{sq} = \sigma L_s I_{sq} \tag{7.14}$$

$$\varphi_r = \frac{M}{L_s} \varphi_{sd} . \tag{7.15}$$

These steady-state equations will be utilized for the analysis of the maximum torque capability.

7.3. Maximum Torque Capability In The Field Weakening Region

In the high-speed range the motor performance is limited by the maximum inverter voltage, the inverter current rating and the machine thermal rating.

The maximum voltage magnitude $V_{s,max}$ that the inverter can apply to the machine is related to the input voltage amplitudes and the modulation strategy. Using Space Vector Modulation (SVM) the maximum magnitude of the stator voltage vector is

$$V_{s,max} = \frac{\sqrt{3}}{2} v_i \,. \tag{7.16}$$

The voltage limit and the current limit can be represented by the following inequalities:

$$v_s \leq V_{s,max} \tag{7.17}$$

$$i_s \leq I_{s,max} \,. \tag{7.18}$$

Inequalities (7.17) and (7.18) sensibly influence the motor behaviour, especially at high speed. It is known that the operation of an induction motor can be divided into three speed ranges, namely the low speed range (region I), the constant-power speed range (region II) and the decreasing-power speed range (region III).

In region I, the current limit and the rated flux level determine the operating point corresponding to the maximum torque.

The beginning of region II is defined as the voltage required to inject the maximum current reaches $V_{s,max}$. In region II, it is necessary to reduce the stator flux magnitude to keep the back emf approximately constant. Therefore the operating point corresponding to the maximum torque requires a rotor flux magnitude lower than the rated one, and the magnitudes of the stator current vector and stator voltage vector are equal to the limit values $I_{s,max}$ and $V_{s,max}$ respectively. As the torque is inversely proportional to the rotor speed, the power delivered to the load is nearly constant.

Finally, in region III the available voltage is not sufficient to inject the maximum current and the power delivered to the load decreases nearly proportionally with the rotor speed.

It is evident that the maximum torque capability is a consequence of the

voltage and current limits.

In order to determine the operating point corresponding to the maximum torque, when the stator voltage is equal to $V_{s,max}$, it is opportune to introduce the angle α between the stator flux vector and the rotor flux vector, as follows:

$$\varphi_{sd} = \varphi_s \cos \alpha \tag{7.19}$$

$$\varphi_{sq} = \varphi_s \sin \alpha. \tag{7.20}$$

Combining (7.11), (7.15), (7.19) and (7.20), it is possible to express the motor torque as follows

$$T = \frac{3}{4} p \frac{M^2}{\sigma L_s^2 L_r} \varphi_s^2 \sin 2\alpha \ . \tag{7.21}$$

At high speed, the voltage drop on the stator resistance is small and (7.12) can be approximated as

$$V_{s,max} \cong \omega \varphi_s \ . \tag{7.22}$$

Combining (7.22) and (7.21) leads to the following expression of the torque in the high speed region:

$$T \cong \frac{3}{4} p \frac{M^2}{\sigma L_s^2 L_r} \left(\frac{V_{s,max}}{\omega} \right)^2 \sin 2\alpha \ . \tag{7.23}$$

From (7.23) it is clear that for any value of ω, the maximum torque is produced when the stator flux and the rotor flux vectors are delayed by an angle of 45°, i.e. φ_{sq} is equal to φ_{sd}.

However, when the maximum torque is delivered to the load, the current could be greater than $I_{s,max}$. In fact, according to (7.13) and (7.14), the stator current components are related to the corresponding stator flux components.

Since the magnitude of the stator current vector must not exceed the maximum current $I_{s,max}$, a limitation strategy should be present to prevent the flux request $\varphi_{sq,req}$ from reaching too high values.

If i_{sd} is the d-component of the current corresponding to the flux φ_{sd}, in order to guarantee that the current limit (7.18) is satisfied, the absolute value

of i_{sq} cannot be greater than the following value:

$$i_{sq,available} = \sqrt{I_{s,max}^2 - i_{sd}^2} \ . \tag{7.24}$$

As a consequence, due to (7.14), the flux component φ_{sq} cannot be grater than the following limit value:

$$\varphi_{sq,available} = \sigma L_s \ i_{sq,available}. \tag{7.25}$$

In conclusion, the maximum torque compatible with the constraints (7.17) and (7.18) is given in any operating condition by the following value of φ_{sq}:

$$\varphi_{sq,max} = \min\left\{ \varphi_{sd}, \varphi_{sq,available} \right\} \ . \tag{7.26}$$

This fundamental relationship will be used by the field weakening algorithm to achieve the maximum torque operation.

7.4. Control Algorithm

The torque control block diagram, including the proposed field weakening strategy, is shown in Fig. 7.1. It is worth noting that the subscript "req" in Fig. 7.1 is used for the output quantities of the regulators, whereas the subscript "ref" denotes the reference signals at the input of the regulation loops.

The control scheme is implemented in a reference frame synchronous with the rotor flux vector, like traditional field oriented controls. It is assumed that a suitable observer estimates $\overline{\varphi}_s$, $\overline{\varphi}_r$, and the angular frequency ω of the rotor flux vector.

A. Torque Control

The motor torque is controlled by comparing the torque reference T_{ref} with the estimated torque T. On the basis of the torque error, the PI regulator (a) produces a torque request by adjusting the q-component of the stator flux, according to (7.11). Therefore, if the reference torque is higher than the actual torque, the PI regulator (a) tends to increase the $\varphi_{q,req}$, otherwise it tends to decrease it.

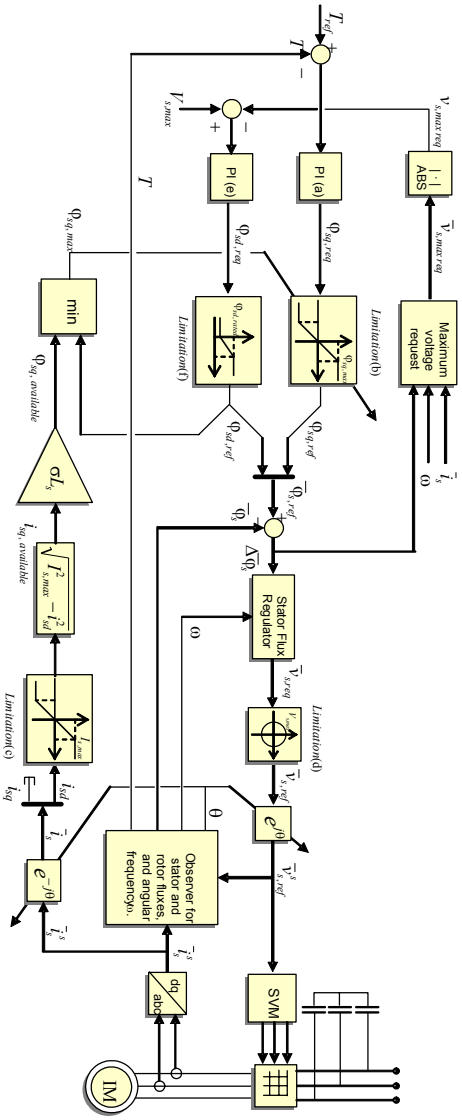

Fig. 7.1- Block diagram of the torque control scheme, including the field weakening strategy.

B. Control of Rotor and Stator Fluxes

The rotor flux is controlled by adjusting the d-component of the stator flux, according to (7.9).

In region I, the d-component of the stator flux is constant and has the rated value $\varphi_{sd,rated}$. At higher speeds, instead, it is reduced by the field weakening algorithm, as described in Paragraph 7.5.

The stator flux regulator behaves as a proportional controller, with some additional terms compensating the stator back-EMF and the voltage drop caused by the stator resistance. The stator flux regulator equation can be expressed as follows:

$$\bar{v}_{s,req} = R_s \bar{i}_s + j\omega\bar{\varphi}_s + \frac{\bar{\varphi}_{s,ref} - \bar{\varphi}_s}{\tau} \tag{7.27}$$

where $1/\tau$ represents the gain of the controller.

Combining (7.27) and (7.1), i.e. $\bar{v}_s = \bar{v}_{s,req}$, leads to the following equation, expressing the dynamic behaviour of the stator flux vector:

$$\tau \frac{d\bar{\varphi}_s}{dt} + \bar{\varphi}_s = \bar{\varphi}_{s,ref} \quad . \tag{7.28}$$

According to (7.28), in order to obtain fast flux transients, and consequently a high torque dynamic, it is necessary to adopt small values of τ.

The limitation block (d) ensures that the voltage reference satisfies the voltage constraint (7.17), namely the voltage reference vector lies inside a circle with radius $V_{s,max}$.

The behaviour of the limitation block (d) is described by the following equation:

$$\bar{v}_{s,ref} = \begin{cases} \bar{v}_{s,req} & if \left|\bar{v}_{s,req}\right| \le V_{s,max} \\ \dfrac{\bar{v}_{s,req}}{\left|\bar{v}_{s,req}\right|} V_{s,max} & if \left|\bar{v}_{s,req}\right| > V_{s,max} \end{cases} . \tag{7.29}$$

According to (7.29), if the requested voltage is greater than $V_{s,max}$ the limitation block (d) performs a proportional reduction of its magnitude, but preserves the angular phase.

Finally, the reference voltage vector in the stator reference frame is calculated by means of the operator $e^{j\theta}$, where θ is the phase angle of the

rotor flux vector with respect to the stationary reference frame.

C. Maximum Torque Capability

In order to guarantee the maximum torque capability, the flux request has to be lower than $\varphi_{sq,max}$ given by (7.26). This task is performed by the limitation block (b), shown in details in Fig. 7.2. At low speed this block does not limit φ_{sq} for usual overload conditions.

It is interesting to note that, at high speed, the limitation block (b) prevents instability phenomena by limiting the torque reference (i.e. $\varphi_{sq,ref}$) to values lower than the maximum achievable torque, according to (7.26). In fact, without the limitation block (b), an excessive torque request causes an increase of the requested voltage, which in turn yields to a reduction of φ_{sd} and of the produced torque. This behaviour proceeds leading to a progressive reduction of the stator flux until the motor stops.

7.5. Field Weakening Algorithm

Several field weakening strategies are possible for induction motor drives, as reported in the introduction. However, the best results are obtained using closed-loop controllers based on the principle of reducing the flux reference as soon as the voltage request becomes greater than the available voltage.

This principle can be implemented according to the block diagram shown in Fig. 7.3. As can be seen, the stator flux regulator compares the flux reference with the corresponding estimated value and establishes the voltage that has to be applied to the motor. When the motor operating point is very close to the field weakening region, the voltage request may become greater than the limit voltage $V_{s,max}$. A negative difference between the limit voltage

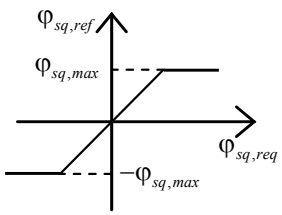

Fig. 7.2 – Limitation block (b) for the q-component of the stator flux vector.

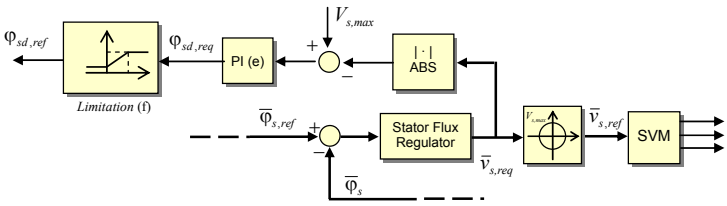

Fig. 7.3- Block diagram of the field weakening controller based on the saturation of the voltage regulator.

and the amplitude $v_{s,req}$ of the requested voltage means that the back-emf is too high and the flux level should be reduced. This task is performed by the PI regulator (e), that integrates the difference $V_{s,max} - v_{s,req}$. If this difference is negative, the flux request decreases; otherwise, the flux level increases up to the rated value defined in the limitation block (f). Fig. 7.4 shows the behaviour of the limitation block (f) in details, where $\varphi_{sd,rated}$ and $\varphi_{sd,min}$ are the rated and the minimum admissible value of the d-component of the stator flux, respectively.

It is worth noting that in the field weakening region, owing to the integral part of the regulator (e), the amplitude of the voltage request tends to equal the limit voltage. From this point of view, the field weakening control scheme is very similar to an anti-windup scheme preventing a voltage request greater than the available voltage.

Although the scheme of Fig. 7.3 allows the motor to fully utilize the supply voltage, it has an inherent drawback related to the fact that fast variations of the torque demand in region II and III lead to undesired flux transients which delay the torque response. In fact this scheme is based on selecting $\varphi_{sd,ref}$ so that the voltage required to produce the demanded torque

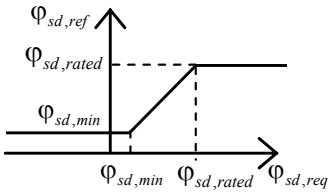

Fig. 7.4 – Limitation block (f) for the *d*-component of the stator flux vector.

satisfies the voltage limit. For example, when a torque variation is required in region II or III, the control system, as a consequence of the corresponding variation of the requested voltage, changes $\varphi_{sd,ref}$, thus causing undesired transients of the rotor flux.

To avoid this problem, the scheme of Fig. 7.3 should be modified in order to change the basic principle for the selection of the flux level. In particular, the flux level should be always set to the value required to generate the maximum achievable torque at any operating speed. In this way any demand of torque variations within the admissible values is achieved without changing φ_{sd} but only φ_{sq}. This new field weakening strategy is implemented as shown in Fig. 7.1.

For a given value of the d-component of the stator flux, and consequently of the rotor flux, the maximum torque is achieved when $\varphi_{sq,ref} = \pm\varphi_{sq,max}$. Taking this equation into account, the voltage required to generate the maximum torque can be determined from (7.27) as follows:

$$v_{sd,max\ req} = R_s i_{sd} - \omega_{max}\left(\operatorname{sign}\varphi_{sq}\right)\varphi_{sq,max} + \frac{\varphi_{sd,ref} - \varphi_{sd}}{\tau} \tag{7.30}$$

$$v_{sq,max\ req} = R_s i_{sq,max} + \omega_{max}\varphi_{sd} + \frac{\varphi_{sq,ref} - \varphi_{sq}}{\tau} \tag{7.31}$$

where $i_{sq,max}$ is defined as follows

$$i_{sq,max} = \frac{\varphi_{sq,max}}{\sigma L_s} \tag{7.32}$$

and ω_{max} is the corresponding angular frequency of the rotor flux, expressed by

$$\omega_{max} = \omega + \left(\operatorname{sign}\varphi_{sq}\right)\frac{R_r}{\sigma L_r}\frac{\varphi_{sq,max} - \left|\varphi_{sq}\right|}{\varphi_{sd}}. \tag{7.33}$$

It is worth noting that in practical applications it is possible to approximate ω_{max} with ω and therefore the knowledge of the rotor parameters is not necessary.

The main advantage of the proposed field weakening scheme is the

independence from the base speed and a fast torque response in the field weakening region.

7.6. Flux and Torque Observers

A. Flux Observer

The aim of the flux observer is the determination of stator flux and phase angle of the rotor flux, which are necessary for the field oriented control of the induction machine. The flux observer operates in the stator reference frame. In the following the subscript "s" will be used to identify quantities expressed in the stator reference frame.

The stator flux is determined integrating the stator voltage:

$$\overline{\varphi}_s^s = \int \left(\overline{v}_s^s - R_s \bar{i}_s^s\right) dt \ . \tag{7.34}$$

The rotor flux can be estimated as follows

$$\overline{\varphi}_r^s = \frac{L_r}{M}\left(\overline{\varphi}_s^s - \sigma L_s \bar{i}_s^s\right) . \tag{7.35}$$

The phase angle θ of the rotor flux vector, necessary for the field oriented control, can be derived from (7.35) as follows

$$\theta = \arg \overline{\varphi}_r^s = \arg\left(\overline{\varphi}_s^s - \sigma L_s \bar{i}_s^s\right) . \tag{7.36}$$

It is evident from (7.34) that the estimation of the stator flux vector can be affected by stator resistance mismatch, sensor offsets and the inverter non-linearity (inverter dead-times, voltage drop on the conducting switches, etc.). However, at high speed, and hence in the field weakening region, the estimation error is lower than that at low speed, because the input voltage becomes the most important term in the right-hand side of (7.34).

The estimation error on the phase angle θ depends on the stator flux estimation error, the mismatch on the leakage inductance σL_s and the offset of the current sensors. The leakage inductance shows moderate variations with the stator currents and it will be assumed practically constant.

In conclusion, the stator flux observer depends only on two machine parameters, namely R_s and σL_s, but the effects of this dependence can be

considered negligible in the high speed range. On the contrary, in order to obtain good performance at low speed, it is preferable to adopt a closed-loop flux estimator, that could reduce the effect of parameter mismatch and sensor offsets [79].

B. Estimation of the Angular Frequency of the Rotor Flux Vector

The angular frequency ω needed in (7.27) and (7.33) is obtained by means of the following equation:

$$\omega = \left(\frac{d}{dt} \frac{\overline{\varphi}_r}{|\overline{\varphi}_r|} \right) \cdot j \left(\frac{\overline{\varphi}_r}{|\overline{\varphi}_r|} \right) . \tag{7.37}$$

The angular frequency ω is insensitive to disturbance and noise that usually affect the stator flux and the stator currents, owing to the filtering action applied to the rotor flux. When this action is not adequate, an additional low-pass filter can be applied to (7.37).

C. Torque Observer

The torque can be estimated from the measurements of the stator current and the estimation of the stator flux, as follows:

$$T = \frac{3}{2} p \left(\bar{i}_s \cdot j \overline{\varphi}_s \right). \tag{7.38}$$

As can be seen, the torque estimation does not require explicitly any motor parameters, excepts the pole pairs.

7.7. Simulation Results

Preliminarily, some numerical simulations have been carried out to confirm the effectiveness of the field weakening strategy. The motor parameters are reported in Tab. 7.1, and the load is supposed to be only inertial.

Fig. 7.5 shows the motor behaviour in response to a step command of the motor torque (the figure does not include the end of the transient). Vertical dash-dotted lines delimit the three regions of operation of the induction motor. Initially, the torque delivered to the load is zero, the motor is at standstill and the stator flux corresponds to the rated value. As the torque

TABLE 7.1 – MOTOR PARAMETERS

P_{rated}	=	0.25	kW	R_s	=	14.6	Ω
$I_{s,\ rated}$	=	1.16	A_{rms}	R_r	=	16	Ω
$V_{s,rated}$	=	220	V_{rms}	L_s	=	701	mH
ω_s	=	2π50	rad/s	L_r	=	701	mH
p	=	1		M	=	53	mH

command is applied, the motor starts up.

The q-component of the stator flux requested by the PI regulator (a) is limited to the value $\varphi_{sq,max}$, corresponding to a stator current equal to $I_{s,max}$. As soon as $v_{s,max\ req}$ reaches the voltage limit, the field weakening algorithm decreases the d-component of the stator flux. As a consequence of the reduction of the magnetizing current, the q-component of the stator current,

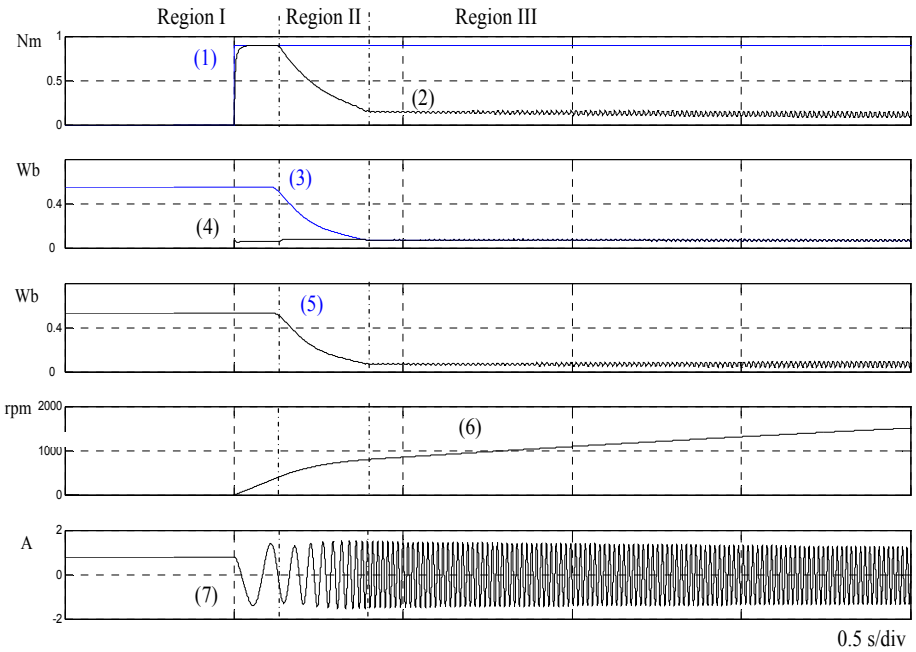

Fig. 7.5 – Computer simulation. Starting transient from 0% up to 600% of the base speed after the application of the rated torque. Main motor quantities. 1) Torque reference. 2) Estimated torque. 3) $\varphi_{sd,ref}$. 4) $\varphi_{sq,ref}$. 5) Rotor flux. 6) Motor speed. 7) Stator current.

proportional to $\varphi_{sq,ref}$, increases, making it possible to keep the stator current equal to the limit current in region II. As soon as the motor enters in region III, the current decreases and the maximum value of $\varphi_{sq,ref}$ is set equal to $\varphi_{sd,ref}$.

Fig. 7.6 shows the motor behaviour after a torque reduction from 100% of the rated torque to 50% of the rated torque in region II. As can be seen, immediately after the torque decreases, the voltage delivered to the loads is lower than $V_{s,max}$, but this voltage margin does not mean that φ_{sd} should increase. In fact the motor continues accelerating and φ_{sd} decreases without unwanted transients. This behaviour could not be achieved without changing the basic scheme of the field weakening strategy of Fig.7.3 as proposed in

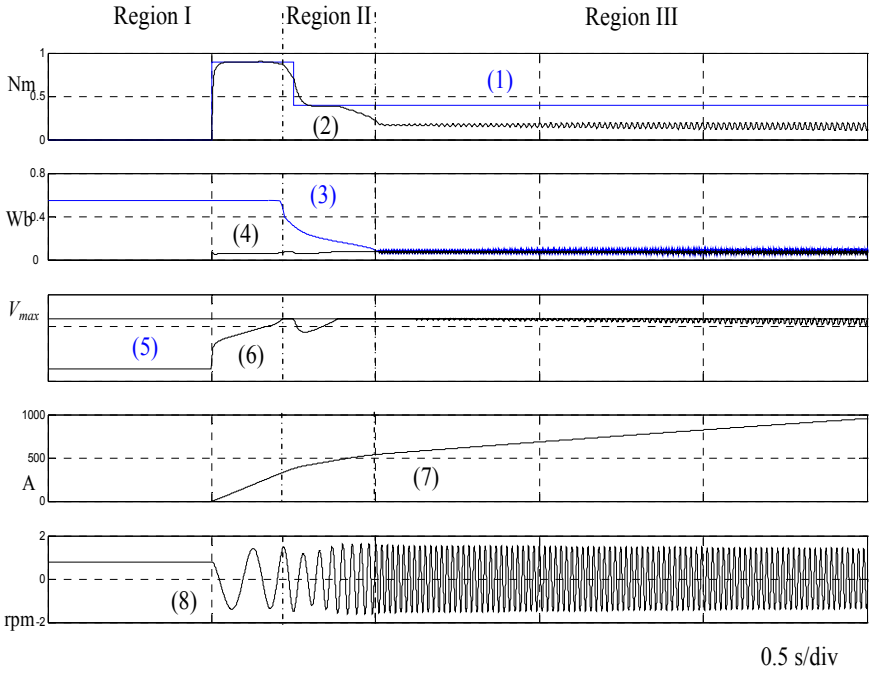

Fig. 7.6 – Computer simulation. Torque reduction from 100% of the rated torque to 50% of the rated torque in region II during an acceleration transient. Main motor quantities. 1) Torque reference. 2) Estimated torque. 3) $\varphi_{sd,ref}$. 4) $\varphi_{sq,ref}$. 5) $V_{s,max}$. 6) v_s. 7) Motor speed. 8) Stator current.

Fig. 7.1.

7.8. Experimental Results

A complete drive system has been realized to verify the feasibility of the proposed control scheme. The experimental set-up consists of a MC inverter and a 250 W, 2-pole squirrel cage induction motor. The motor parameters are the same ones reported in Tab. 7.1. The test motor is coupled to a separately excited DC machine, 3000 rpm. The control algorithm is implemented on a Digital Signal Processor (DSP) TMS320C28. The cycle period of the control scheme, including the field weakening algorithm, is 125 μs.

Some tests have been carried out to investigate the drive performance in the field weakening region. In order to limit the test bench speed to safe values, the motor has been fed with a reduced voltage, i.e. 25% of the rated voltage, so leading to a rated speed of about 700 rpm.

Fig. 7.7 shows the motor behaviour during a transient from 90% up to 600% of the rated speed (the figure does not include the end of the transient). As can be seen, the motor behaves as expected, namely the

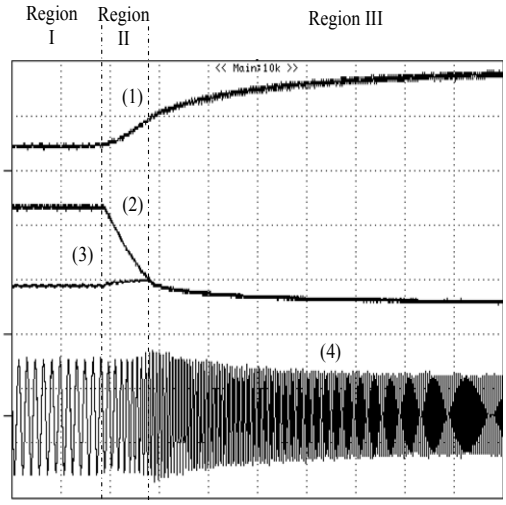

Fig. 7.7 – Experimental test. Speed transient from 90% to 600% of the base speed. 1) Estimated speed (1500 rpm/div). 2) $\varphi_{sd,ref.}$ (0.25 Wb/div). 3) $\varphi_{sq,ref.}$ (0.25 Wb/div). 4) Stator current (1.5 A/div).

current is constant in region II and decreases in region III.

Some tests were carried out to assess the dynamic performance of the motor drive. In Figs. 7.8 and 7.9 the behaviour during a transient after a

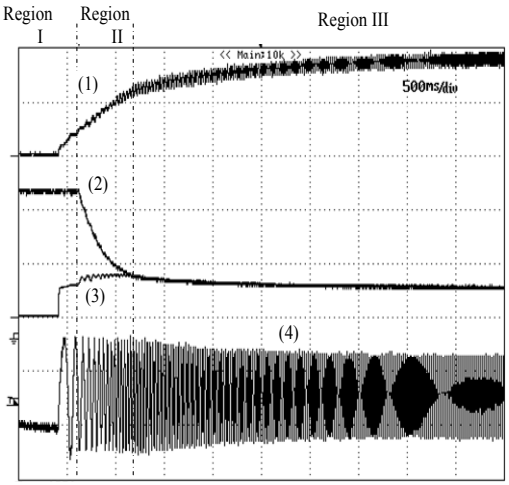

Fig. 7.8 – Experimental test. Starting transient from 0% up to 600% of the base speed. Main motor quantities. 1) Estimated speed (1500 rpm/div). 2) $\varphi_{sd,ref}$ (0.25 Wb/div). 3) $\varphi_{sq,ref.}$ (0.25 Wb/div). 4) Stator current (1.5 A/div).

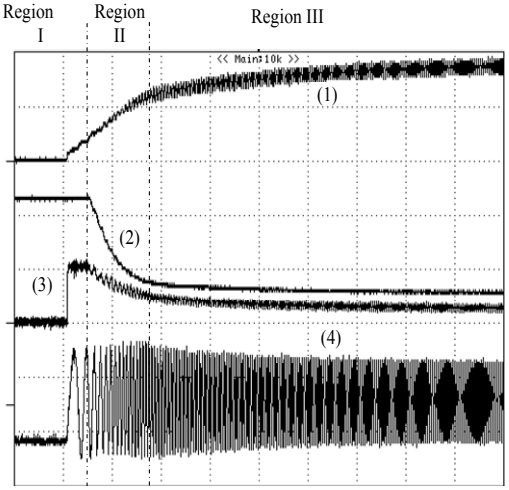

Fig. 7.9 – Experimental test. Starting transient from 0% up to 700% of the base speed. Main motor quantities. 1) Estimated speed (1500 rpm/div). 2) $\varphi_{sd,ref}$ (0.25 Wb/div). 3) Estimated torque (0.8 Nm/div). (4) Stator current (1.5 A/div).

torque step is shown. The experimental results are in good agreement with the computer simulations shown in Fig. 7.5. In particular $\varphi_{sq,ref}$, constant in region I, slightly increases in region II, keeping the stator current equal to the limit value.

Some tests have been carried out to evaluate the capability of the control system to increase the flux during a deceleration transient.

Fig. 7.10 shows the motor behaviour when the speed decreases from about 500% to 90% of the base speed. The deceleration is obtained by increasing the breaking torque generated by the DC machine operating as a load. It can be verified that, as the speed decreases, the control algorithm increases smoothly the flux reference $\varphi_{sd,ref}$ up to the rated value.

Finally, the quality of the input and output currents have been assessed. Fig. 7.11 shows the waveform of a load current, whereas Fig. 7.12 shows the waveforms of the line currents for two different load conditions. As can be seen, all the waveforms are nearly sinusoidal and the harmonic content is negligible.

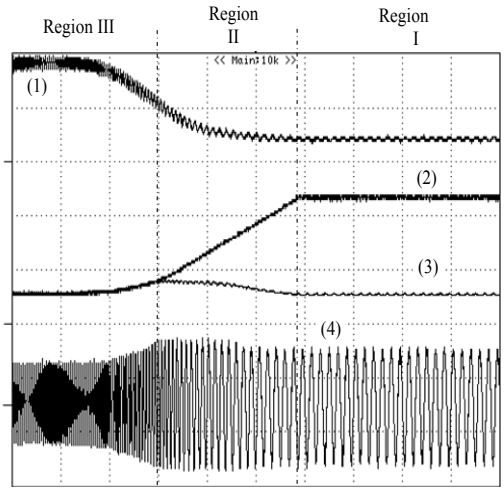

Fig. 7.10 – Experimental test. Breaking transient from 500% down to 90% of the base speed. Main motor quantities. 1) Estimated speed (1500 rpm/div). 2) $\varphi_{sd,ref}$ (0.25 Wb/div). 3) $\varphi_{sq,ref.}$ (0.25 Wb/div). (4) Stator current (1.5 A/div).

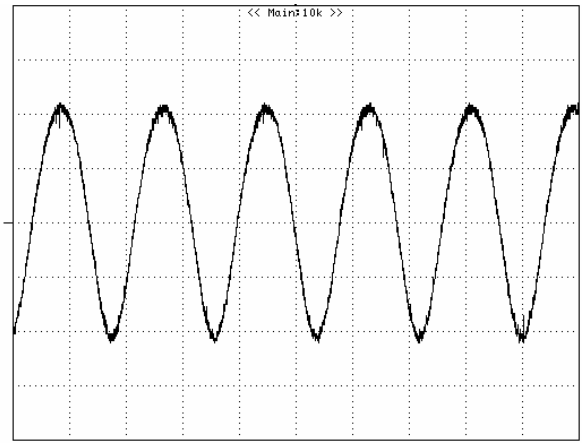

Fig. 7.11 – Experimental test. Load currents (0.75 A/div).

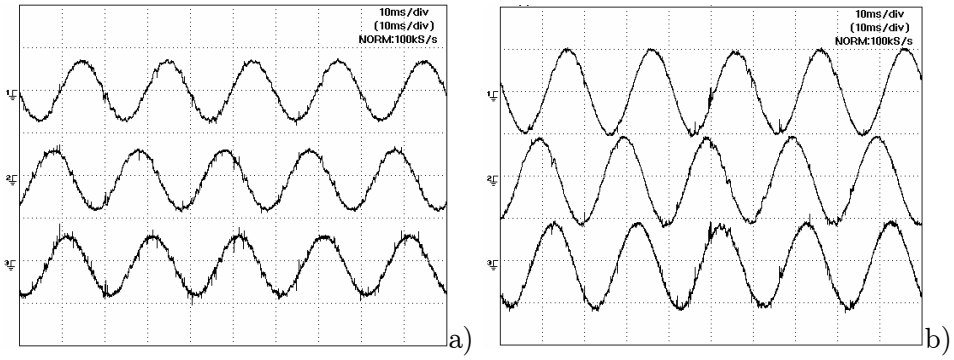

a) b)

Fig. 7.12 – Experimental test. Input currents for two different load conditions (2.5 A/div). Motor operating at the base speed, at 30% of the rated torque (a) or at the rated torque (b).

7.9. Conclusion

A control strategy for field weakening operation of speed-sensorless induction motor drives fed by MC is analyzed in this chapter.

The control system scheme utilizes the stator flux components as control variables and decreases the d-component of the stator flux as the voltage corresponding to the maximum torque achievable at a given speed tends to exceed the maximum voltage.

The control scheme allows a smooth transition into and out of the field

weakening mode, exploiting the maximum torque capability of the machine over the whole operating speed range.

The main advantages of proposed field weakening algorithm are: i) reduced dependence on machine parameters, ii) no need of calculation of the base speed, which in general depends on the machine parameters, motor current and available voltage, iii) fast torque response, also in the field weakening region.

The effectiveness of the proposed control scheme has been verified by computer simulations and experimental tests.

Appendix A

The algorithm for the selection of λ and $\overline{m}_o$ in the general case is presented in this Appendix.

The first step is to determine which triangle vertex should coincide with a duty-cycle space vector. This can be done by means of Fig. A.1, that reports the vertex names as a function of the sector of $\overline{\psi}_{ref}$. If the indexes 1,2,3 are associated to the vertex A, B and C respectively, the position of the selected vertex in the d-q plane can be represented by means of the space vector $\frac{2}{3}\exp\left(j2\pi(\nu-1)/3\right)$, where ν is defined in Fig. A.1.

Then, the modulation algorithm determines which duty-cycle space vector among $\overline{m}_1, \overline{m}_2$ and $\overline{m}_3$ should coincide with the vertex previously selected. For this purpose, the index n of the searched duty-cycle space vector is reported in Table A.1. As can be seen, the index n depends on the sector occupied by the reference output voltage and the input current. The sectors of the reference output voltage are represented in Fig.A.2.

The duty-cycle space vector $\overline{m}_n$ must satisfy the following constraint:

$$\overline{m}_n = \frac{2}{3} e^{j\frac{2}{3}\pi(\nu-1)} \tag{A1}$$

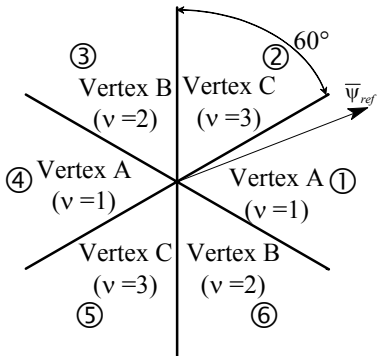

Fig. A.1 – Graphic table for the selection of the triangle vertex coinciding with a duty cycle space vector among $\overline{m}_1$, $\overline{m}_2$ and $\overline{m}_3$ as a function of the desired direction of the input current.

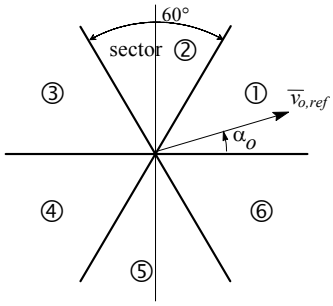

Fig. A.2 - Sectors of the output reference voltage vector.

Substituting (18), written for k=n in (A1), and solving for $\overline{m}_o$, leads to the following expression:

$$\overline{m}_o = \frac{2}{3} e^{j\frac{2}{3}\pi(\nu-1)} - \overline{A}_n - \lambda \overline{B}_n . \qquad \text{(A2)}$$

By substituting (A2) in (3.2) the following general expressions for the remaining duty-cycle space vectors, as a function of λ, can be found:

$$\overline{m}_k = \overline{A}_k - \overline{A}_n + \lambda\left(\overline{B}_k - \overline{B}_n\right) + \frac{2}{3} e^{j\frac{2}{3}\pi(\nu-1)} \ (k=1,2,3 \text{ and } k \neq n). \qquad \text{(A3)}$$

TAB. A.1 – INDEX n OF THE DUTY-CYCLE SPACE VECTOR PLACED ON A TRIANGLE VERTEX

		SECTOR OF THE DESIRED INPUT CURRENT	
		1 - 3 - 5	2 - 4 - 6
SECTOR OF THE REFERENCE OUTPUT VOLTAGE	1	1	3
	2	2	3
	3	2	1
	4	3	1
	5	3	2
	6	1	2

With reference to the example of Fig. 3.2, (A3) represent the parametric equations of the straight lines r and s.

The next step of the modulation algorithm consists in the determination of the six values of λ that bring a duty-cycle space vector to a triangle side. These values can be determined by solving each of the six following linear equations:

$$\overline{m}_k \cdot e^{j\frac{2\pi h}{3}} + \frac{1}{3} = 0 \qquad (k \neq n,\ h=0,1,2) \tag{A4}$$

Among these six values of λ, in this analysis, the one corresponding to the minimum absolute value is adopted for the modulation law. The selected value coincides with the values λ_p or λ_n previously defined.

Appendix B

To determine the time required by $\bar{i}_{rip}$ to virtually cover the distance between C and A, the following equation can be used:

$$\overline{BA} + \overline{CB} + \overline{AC} = 0 \tag{B1}$$

where the expression of $\overline{BA}$, $\overline{CB}$ and $\overline{AC}$ are those given in Tab. 3.5.

Substituting and solving for δ' leads to

$$\delta' = \frac{\delta_1\left(\overline{v}_1 - \overline{v}_{o,ref}\right)\cdot \overline{v}_{o,ref} + \delta_2\left(\overline{v}_2 - \overline{v}_{o,ref}\right)\cdot \overline{v}_{o,ref}}{v_{o,ref}^2}. \tag{B2}$$

Similarly, for δ'' one obtains:

$$\delta'' = \frac{\delta_3\left(\overline{v}_3 - \overline{v}_{o,ref}\right)\cdot \overline{v}_{o,ref} + \delta_4\left(\overline{v}_4 - \overline{v}_{o,ref}\right)\cdot \overline{v}_{o,ref}}{v_{o,ref}^2}. \tag{B3}$$

Appendix C

In this Appendix some definitions involving Laplace transform are presented, which are used in the stability analysis.

Let be $\bar{f}(s)$ the Laplace transform of the generic vector $\bar{f}(t)$, defined as follows:

$$\bar{f}(s) = \int_0^\infty \bar{f}(t) e^{-st} dt \,. \tag{C1}$$

The superscript 'c' is used for the Laplace transform of $\bar{f}^*(t)$, defined as

$$\bar{f}^c(s) = \int_0^\infty \bar{f}^*(t) e^{-st} dt \,. \tag{C2}$$

It can be verified that the following relationships exist between $\bar{f}(s)$ and $\bar{f}^c(s)$:

$$\bar{f}^c(s) = \bar{f}^*(s^*) \tag{C3}$$

$$\bar{f}^{c*}(s^*) = \bar{f}(s) \tag{C4}$$

Appendix D

A transfer function of a filter in the time domain can be approximated in the discrete-time by using several expressions.

In Chapter 5, (5.42) has been approximated by means of the following difference equation:

$$\overline{v}_{if}(k) = \overline{a}_1 \overline{v}_{if}(k-1) + \overline{b}_0 \overline{v}_i(k) + \overline{b}_1 \overline{v}_i(k-1) \tag{D1}$$

where

$$\overline{a}_1 = 1 + \left(-\frac{1}{\tau} + j\omega_i\right)T + \frac{1}{2}\left(-\frac{1}{\tau} + j\omega_i\right)^2 T^2 \tag{D2}$$

$$\overline{b}_0 = \frac{T}{2\tau} \tag{D3}$$

$$\overline{b}_1 = \frac{T}{2\tau}\left[1 + \left(-\frac{1}{\tau} + j\omega_i\right)T\right]. \tag{D4}$$

that can be represented with the following Z-transform:

$$\overline{F}_d(z) = \frac{\overline{b}_0 + \overline{b}_1 z^{-1}}{1 - \overline{a}_1 z^{-1}}. \tag{D5}$$

Appendix E

The ratio ε can be more easily characterized by the knowledge of the converter efficiency (η) and the conduction losses to switching losses ratio (δ). The converter efficiency is given by

$$\eta = \frac{P_{out}}{P_{in}} = \frac{P_{id} - P_{cd}}{P_{id} + P_{sw}} \tag{E1}$$

which can be rewritten as follows

$$\eta = \frac{1 - \delta\varepsilon}{1 + \varepsilon} \tag{E2}$$

where

$$\delta = \frac{P_{cd}}{P_{sw}}. \tag{E3}$$

Appendix F

The input current can be expressed as a sum of harmonics. To obtain this result, it is necessary to substitute (5.65) in (5.64) and to take (5.66) into account. It follows:

$$\bar{i}_i = \bar{f}(t)e^{j\omega_i t} \tag{F1}$$

where

$$\bar{f}(t) = \frac{2}{3}\frac{P_{id}}{\overline{V}_i^* + \overline{V}_{dir}^* e^{-j\omega_r t} + \overline{V}_{inv}^* e^{j\omega_r t}} \tag{F2}$$

The function $\bar{f}(t)$ is periodic and can be expressed as a Fourier series as follows:

$$\bar{f}(t) = \sum_{k=-\infty}^{\infty} \overline{F}_k e^{jk\omega_r t} \tag{F3}$$

where

$$\overline{F}_k = \frac{\omega_r}{2\pi}\int_{-\frac{\pi}{\omega_r}}^{\frac{\pi}{\omega_r}} \bar{f}(t)e^{-j\frac{2\pi}{\omega_r}kt}\,dt\,. \tag{F4}$$

An approximated form for $\bar{f}(t)$ can be derived from (F3) neglecting the

terms with order greater then 1, as follows

$$\bar{f}(t) \cong \overline{F}_{-1} e^{-j\omega_r t} + \overline{F}_0 + \overline{F}_1 e^{j\omega_r t} . \qquad \text{(F5)}$$

The explicit form of $\overline{F}_{-1}$, $\overline{F}_0$ and $\overline{F}_1$ can be calculated by means of (F4) for k = -1, 0 and 1 respectively. Substituting (F5) in (F1) leads to (5.67) and the expressions of $\overline{F}_{-1}$, $\overline{F}_0$ and $\overline{F}_1$ coincides with those given in (5.68), (5.69) and (5.70).

Appendix G

To derive (5.92), (5.78) must be written in the following form:

$$Z(\omega_i + \omega_r)e^{j\beta}\frac{P_o}{3V_{dir}^2}\left(1-\frac{1}{\overline{\overline{\delta}}}\right) = -1\,. \tag{G1}$$

Rearranging the terms of (G1) leads to this equivalent equation:

$$\left(1-\frac{1}{\overline{\overline{\delta}}}\right) = -\lambda e^{-j\beta} \tag{G2}$$

where λ is the real positive parameter defined as

$$\lambda = \frac{3V_{dir}^2}{Z(\omega_i + \omega_r)P_o}\,. \tag{G3}$$

Finally, combining (G2), (5.71) and (5.86) and solving for $\overline{p}$ leads to (5.92).

References

Preface

[1] Alesina, M. Venturini, "Solid-state power conversion: a fourier analysis approach to generalized transformer synthesis," IEEE Trans.Circuits and Systems, vol. 28, No. 4, pp. 319-330, April 1981.

[2] A. Alesina, M. G. B. Venturini, "Analysis and design of optimum-amplitude nine-switch direct ac-ac converters," IEEE Trans. Power Electronics, vol. 4, pp. 101-112, January 1989.

[3] P. D. Ziogas, S.I. Khan, M.H. Rashid, "Analysis and design of forced commutated cycloconverter structures with improved transfer characteristics," IEEE Trans. Industrial Electronics, vol. 1E-33, No. 3, pp. 271-280, August 1986.

[4] L. Huber, D. Borojevic, "Space vector modulator for forced commutated cycloconverters," Proc. IEEE PESC Conf., San Diego, (USA), 1989, pp. 871-876.

[5] L. Huber, D. Borojevic, "Space vector modulated three-phase to three-phase matrix converter with input power factor correction," IEEE Trans. on Industry Applications, Vol. 31, No. 6, November/ December 1995, pp. 1234-1246.

[6] D. Casadei, G. Grandi, G. Serra, A. Tani, "Space vector control of matrix converters with unity input power factor and sinusoidal input/output waveforms," Proc. EPE Conference, Brighton (UK), 13-16 September 1993, vol. 7, pp. 170-175.

[7] D. Casadei, G. Serra, A. Tani, **L. Zarri**, "Matrix converter modulation strategies: a new general approach based on space-vector representation of the switch state," IEEE Trans. Industrial Electronics, Vol. 49, No. 2, pp. 370-381, April 2002.

[8] C. Klumpner, P. Nielsen, I. Boldea,; F. Blaabjerg,: "New solutions for a low-cost power electronic building block for matrix converters," IEEE Trans. on Industrial Electronics, Vol. 49 , No. 2, Apr. 2002, pp. 336 - 344.

[9] J. Mahlein, J. Weigold, O. Simon, "New concepts for matrix converter design," IEEE IECON-01, 29 Nov-2 Dec. 2001, Denver, USA, vol. 2, pp.1044-1048.

[10] M. Bland, L. Empringham, P. W. Wheeler, J. C. Clare, "Comparison of calculated and measured switching losses in direct ac-ac converters," IEEE PESC Conf 2001, pp. 1096-1101.

[11] Jun-Koo Kang, H. Hara, E. Yamamoto, E. Watanabe, "Analysis and evaluation of bi-directional power switch losses for matrix converter drive," Record of the Industry Applications Conference 2002, 13-18 Oct. 2002, pp. 438 - 443 vol.1.

[12] P.W. Wheeler, J. C. Clare, L. Empringham, "A vector controlled MCT matrix converter induction motor drive with minimized commutation times and enhanced waveform quality," Proc. of IEEE IAS 2002, Vol. 1 , 13-18 Oct. 2002, pp. 466 - 472.

[13] K.G. Kerris, P.W. Wheeler, J.C. Clare, L. Empringham, "Implementation of a matrix converter using p-channel MOS-controlled thyristors, Power Electronics and Variable Speed Drives", 2000. Eighth International Conference on IEE Conf. Publ. No. 475 , 18-19 Sept. 2000, pp. 35 - 39.

[14] P.W. Wheeler, J.C. Clare, L. Empringharn, M. Bland, M. Apap "Gate drive level intelligence and current sensing for matrix converter current commutation", IEEE Trans. on Industrial Electronics, Vol. 49 , No. 2 , April 2002, pp. 382 - 389.

[15] D. Casadei, A. Trentin, M. Matteini, M. Calvini, "Matrix Converter Commutation Strategy using both output current and input voltage sign measurement", EPE 2003, 2-4 Sept., Toulouse, France, paper 1101, CD-ROM.

[16] J. Mahlein, J. Igney, J. Weigold, M. Braun, O. Simon, "Matrix converter commutation strategies with and without explicit input voltage sign measurement", IEEE Trans. Industrial Electronics, vol. 49, No.2, pp. 407-414, April 2002.

[17] P. Nielsen, F. Blaabjerg, J. K. Pedersen, "New Protection Issues of a Matrix Converter: Design Considerations for Adjustable-Speed Drives", IEEE Trans. on Ind. App., vol. 35, n. 5, Sept./Oct. 1999, pp. 1150-1160.

Chapter 1

[18] D. Casadei, G. Serra, A. Tani, "Stability analysis of electrical drives fed by matrix converters," in Proc. IEEE-ISIE, L'Aquila, Italy, Jul. 2002, pp.1108-1113.

[19] D. Casadei, G. Serra, A. Trentin, **L. Zarri**, M. Calvini, "Experimental analysis of a matrix converter prototype based on new IGBT modules," IEEE ISIE 2005, June 20-23, 2005, Dubrovnik, Croatia, Vol. II, pp. 559-564.

[20] C. Klumpner, F. Blaabjerg, "Short term braking capability during power interruptions for integrated matrix converter motor drives," IEEE Trans. on Power Electronics, Vol. 19, No. 2, March 2004, pp. 303-311.

[21] D. Casadei, G. Serra, A. Tani, "Reduction of the input current harmonic content in matrix converters under input/output un-balance," IEEE Trans. on IE, vol. 45, n. 3, June 1998, pp. 401-411.

[22] D. Casadei, G. Serra, A. Tani, "A general approach for the analysis of the input power quality in matrix converters," IEEE Trans. on PE, vol. 13, n. 5, September 1998, pp. 882-891.

[23] F. Blaabjerg, D. Casadei, C. Klumpner, M. Matteini, "Comparison of two current modulation strategies for matrix converters under unbalanced input voltage conditions," IEEE Trans. on IE, vol. 49, n. 2, April 2002, pp. 289-296.

[24] D. Casadei, G. Serra, A. Tani, **L. Zarri**, "Effects of input voltage measurement on stability of matrix converter drive system," IEE Proceedings on Electric Power Applications, vol. 151, No. 4, July 2004, pp. 487-497.

[25] F. Liu, C. Klumpner, F. Blaabjerg, "Stability analysis and experimental evaluation of a matrix converter drive," in Proc. IECON, Roanoke, VA, Nov. 2003, pp. 2059-2065.

[26] L. Malesani, L. Rossetto, P. Tenti, P. Tomasin, "AC/DC/AC PWM converter with reduced energy storage in the DC link," IEEE Trans-actions on Industry Applications, vol. 31 , no.2 , March-April 1995, pp. 287 - 292.

[27] S. Bernet, S. Ponnaluri, R. Teichmann, "Design and loss comparison of matrix converters and voltage-source converters for modern AC drives," IEEE Transaction on Industrial Electronics, vol. 49, no.2 , April, 2002, pp. 304-314.

[28] M. Apap, J.C. Clare, P.W. Wheeler, M.Bland, K. Bradley, "An approach to the analysis on efficiency and device control power loss distribution for matrix converters," Proceedings of EPE Conference, 2003, ISBN: 90-75815-07-7, no. 509, pp. 1-8.

[29] D.Casadei, G.Grandi, C.Rossi, A.Trentin, **L.Zarri**, "Comparison between back-to-back converter and matrix converter based on the thermal stress of the switches", in Proc. IEEE ISIE, May 4-7 2004, Ajaccio, France, ISBN 0-7803-8305-2 (on cd-rom, file sf-001304.pdf).

Chapter 2

[30] M.J. Maytum, D. Colman: "The implementation and future potential of the venturini converter," in Proc. Drives, Motors and Controls, 1983, pp. 108-117.

[31] G. Roy, G.E. April: "Cycloconverter operation under a new scalar control algorithm," in Proc. IEEE PESC. Conf., Milwaukee (WI), 1989, pp. 368-375.

[32] L. Huber, D. Borojevic: "Space vector modulation with unity input power factor for forced commutated cycloconverters," in Proc. IEEE IAS Conf., pp. 1032-1041, 1991.

[33] O. Simon, M. Braun: "Theory of vector modulation for matrix converters," Proc. EPE Conference, Graz (Austria), 27-29 August 2001.

Chapter 3

[34] L. Huber, D. Borojevic, "Digital modulator forced commutated cyclo converters with input power factor correction", in Proc. IEEE PESC Conf., 1992, pp. 518-523.

[35] P. Nielsen, F. Blaabjerg, J.K. Pedersen, "Space vector modulated matrix

converter with minimized number of switchings and a feedforward compensation of input voltage unbalance", in Proc. PEDES Conf., 1996, pp. 833-839.

[36] L. Helle, S. Munk-Nielsen, "A novel loss reduced modulation strategy for matrix converters", in Proc. IEEE PESC Conf., 2001, pp. 1102-1107.

[37] M. Apap, J.C. Clare, P.W. Wheeler, K.J. Bradley, "Analysis and comparison of AC-AC matrix converter control strategies", in Proc. IEEE PESC Conf., 2003, Vol. 3, pp. 1287-1292.

[38] L. Helle, K.B. Larsen, A.H. Jorgensen, S. Munk-Nielsen, "Evaluation of modulation schemes for three-phase to three-phase matrix converters," IEEE Trans. Industrial Electroncs, Vol. 51, No. 1, pp. 158-171, February 2004.

[39] D. Casadei, G. Serra, A. Tani, **L. Zarri**, "Effects of the switching strategy on the input power quality of matrix converters," IEEE Power Tech 2003, 23-26 June 2003, Bologna, Italy, Vol. 1, 8 pp.

[40] J.Igney, M. Braun, " A New Matrix Converter Modulation Strategy Maximizing the Control Range," PESC 2004, June 20-25, Aachen, Germany, Vol. 3, pp. 2875-2880

[41] D. Casadei, G. Serra, A. Tani, **L. Zarri**, "A novel modulation strategy for matrix converters with reduced switching frequency based on output current sensing," PESC 2004, June 20-25, Aachen, Germany, Vol. 3, pp. 2373-2379, ISBN: 07803-8400-8, IEEE Catalog Number 04CH37551C, CD-ROM, 2373˙11393.pdf.

[42] D. Casadei, G. Serra, A. Tani, **L. Zarri**, "Theoretical and experimental analysis for the RMS current ripple minimization in induction motor drives controlled by SVM technique," IEEE Trans. on IE, Vol. 51, No.4, pp.1056-1066, Oct. 2004.

Chapter 4

[43] T. Lipo, P. Krause: "Stability analysis of a rectifier-inverter induction motor drive," IEEE Trans. on PAS, PAS-88, vol. 1, 1969, pp. 55-66.

[44] M.M. Ahmed, J.A. Taufiq, C.J. Goodman, M. Lockwood: "Electrical instability in a voltage source inverter-fed induction motor at a constant speed," IEE Proc. B, vol. 133, No. 4, 1986, pp. 299-307.

[45] B. Mellit, J. Allan: " Stability characteristics of a constant power chopper controller for traction drives," IEE Proc. B, vol. 1, No. 3, 1978, pp. 100-104.

[46] S. Chandrasekaran, D. Borojevic, D.K. Lindner: "Input filter interaction in three phase AC-DC converters," in Proceedings of PESC, 1999, pp. 987-992.

[47] R. Czarnecki, K. Hasse, A.M. Walczyna: "Input filter stability of drives fed from voltage inverters controlled by direct flux and torque control methods," IEE Proc. Electr. Power Appl., Vol. 143, No. 5, September 1996, pp. 396-402.

[48] D. Casadei, G. Serra, A. Tani: "The Use of Matrix Converters in Direct Torque Control of Induction Machines," in Proceedings of IECON, Aachen (Germany), August 31 - September 4 1998, Vol. 2, pp. 744-749.

[49] P.W. Wheeler, J. Rodriguez, J. C. Clare, L. Empringham, "Matrix Converter. A technology review," IEEE Transactions of Industrial Electronics, vol.49, no.2, April, 2002, pp. 276-288

[50] Yanhui Xie, Yongde Ren, "Implementation of DSP-based three-phase AC-AC matrix converter," Proc. of IEEE APEC '04, vol. 2 , 2004, pp. 843 - 847.

[51] C.L. Neft, C.D. Schauder: "Theory and Design of a 30-HP Matrix Converter," IEEE Trans. on IA, Vol. 38, No. 3, May-June 1992, pp. 546-551.

[52] D. Casadei, G. Serra, A. Tani, **L. Zarri**, "Analysis of digital implementation effects on matrix converter stability," Proc. EPE'03, Toulouse, France, 2-4 September 2003, ISBN 90-75815-07-7, CD-ROM, 0894.pdf.

Chapter 5

[53] D. Casadei, G. Serra, A. Tani, **L. Zarri**, "Improvement of the stability of electrical drives fed by matrix converters," IEE Seminar on Matrix Converters, April 2003, Birmingham, pp. 3/1-3/12.

[54] M. Bland, L. Empringham, P. W. Wheeler, J. C. Clare, "Comparison of calculated and measured switching losses in direct AC-AC converters," Proc. IEEE-PESC Conf., 2001, 17-21 Jun. 2001, Vancouver, BC , Canada, Vol. 2, pp. 1096-1101.

[55] J. K. Kang, H. Hara, E. Yamamoto, E. Watanabe, "Analysis and evaluation of bi-directional power switch losses for matrix converter drive," Proc. IEEE-IAS 2002, Pittsburgh, USA, 13-18 Oct. 2002, vol.1, pp. 438-443.

[56] D.Casadei, G.Serra, A.Tani, A.Trentin, **L.Zarri**, "Theoretiecal and experimental investigation on the stability of matrix converters," IEEE Trans. Ind. Electron., vol. 52, no. 5, pp. 1409-1417, October 2005.

[57] M. H. Rashid, A. I. Maswood, "Analysis of three-phase AC-DC converters under unbalanced supply conditions," IEEE Trans. on Ind. App., Vol. 24. No. 3 May/June 1988, pp. 449-455.

[58] M. Sakui, H. Fujita, "Calculation of harmonic currents in a three-phase convertor with unbalanced power supply conditions," IEE Proc.-B, Vol. 139, No. 5, Sept. 1992, pp. 478-484.

[59] L. Moran, P. D. Ziogas, G. Joos, "Design aspects of synchronous PWM rectifier-inverter systems un-der unbalanced input voltage conditions," IEEE Trans. on Ind. App., Vol. 28 No. 6, Nov./Dec. 1992, pp. 1286-1293.

[60] P. Enjeti, X. Wang, "A critical evaluation of harmonic generated by forced commutated cyclo con-verter under unbalance," Proc. of IAS 1990, pp. 1162-1166.

[61] D. Casadei, G. Grandi, G. Serra, A. Tani, "Analysis of space vector modulated matrix converter under unbalanced supply voltages," Proc. of SPEEDAM'94, 8-10 June, 1994, Taormina (Italy), Proceedings pp. 39-44.

[62] D. Casadei, G. Serra, A. Tani, P. Nielsen, "Performance of SVM controlled matrix converter with input and output unbalanced conditions," Proc. of EPE-95, Sevillle, 18-21 Sept. 1995, Proceedings Vol. II, pp. 628-633.

[63] A. Ferrero, G. Superti-Furga, "A unified approach to unbalance three-phase systems under non-sinusoidal conditions: some definitions," Proc. 4-th Conference on Harmonics in Power Systems, Budapest (Hungary), October 1990, pp.32-37.

[64] D. Zhou, K. Sun, L. Huang, "Evaluation of matrix converter operation in abnormal conditions," Proc. of ICEMS 2003, Beijing, China, 9-11 Nov., 2003, vol. 1, pp. 402-406.

[65] Y.Mei, K.Sun, D. Zhou, L. Huang, "Analysis and comparison of matrix converter operation under abnormal input voltage conditions," Proc. of IPEMC, Xian, China, 14-16 Aug. 2004, vol. 3, pp. 1311-1315.

[66] K.Yamada, T. Higuchi, E.Yamamoto, H.Hara, T.Sawa, "Integrated filters and their combined effects in matrix converter," Proc. of IAS 2005, Hong Kong, 2-6 Oct. 2005, vol.2, pp. 1498-1503.

[67] J.K. Kang, H.Hara, E. Yamamoto, E. Watanabe, J. Oyama et al., "Input harmonics damping for high power quality applications of matrix converter," Proc. of IAS 2003, Salt Lake City, 12-16 Oct 2003, pp.1498-1503.

[68] P.Wheeler, D. Grant, "Optimised input filter design and low-loss switching techniques for a practical matrix converter," IEE Proc. Electric Power Applications, vol. 144, no.1, January 1997, pp. 53-60.

Chapter 7

[69] E. Watanabe, S. Ishii., E, Yamamoto, H. Hara, J. Kang, Ahmet M. Hava, "High performance motor drive using matrix converter," 2000, pp.7/1-7/6.

[70] Kyo-Beum Lee, F. Blaabjerg, "Improved sensorless vector control for induction motor drives fed by a matrix converter using nonlinear modeling and disturbance observer," IEEE Trans. of Energy Conversion, Vol. 21, No. 1, March 2006, pp. 52-58.

[71] C. Klumpner , P. Nielsen, I. Boldea, F. Blaabjerg, "A new matrix converter motor (MCM) for industry applications," IEEE Trans. on Ind. Elect., Vol. 49, No. 2, April 2002, pp.325-335.

[72] Junichi Itoh, I. Sato, A. Odaka, H. Ohguchi, H. Kodachi, N. Eguchi, "A novel approach to practical matrix converter motor drive system with reverse blocking IGBT," IEEE Trans. on PE, Vol. 20, No. 6, Nov. 2005, pp.1356-1362.

[73] Kyo-Beum Lee, F. Blaabjerg, "Reduced-order extended Luenberger observer based sensorless vector control driven by matrix converter with nonlinearity compensation," IEEE Trans. on Industrial Electronics, Vol.53, No.1, February 2006, pp. 66-74.

[74] K. Sun, L Huang, K. Matsuse, T. Ishida, "Combined control of matrix converter fed induction motor drive system," Proc. of IAS 2003, 12-16 Oct. 2003, Vol. 3, pp. 1723-1729.

[75] T. Podlesak, D. Katsis, P. Wheeler, J. Clare, L. Empringham, M. Bland, "A 150 kVA vector-controlled matrix converter induction motor drive," IEEE Trans. on Ind. App., Vol. 41, No. 3, May/June 2005, pp. 841-847.

[76] X. Xu, D. W. Novotny, "Selection of the flux reference for induction machine drives in the field weakening region," IEEE Trans. on Ind. App. Vol 28, No 6, Nov. - Dec. 1992, pp. 1353-1358.

[77] S.H.Kim, S.K. Sul, "Maximum torque control of an induction machine in the field weakening region," IEEE Trans. on. Ind. Appl., Jul./Aug. 1995, Salt Lake City, USA, vol.31, No.4, pp. 787-794.

[78] G. Griva, F. Profumo, M. Abrate, A. Tenconi, D. Berruti, "Wide speed

range DTC drive performance with new flux weakening control," Conf. Rec. PESC-98, 17-22 May 1998, Fukuoka, Japan, vol. 2, pp. 1599-1604.

[79] D. Casadei, F. Profumo, G. Serra, A. Tani, **L. Zarri**, "Performance analysis of a speed-sensorless induction motor drive based on a constant-switching-frequency DTC scheme," IEEE Trans. on Ind. App., Vol. 39, NO. 2, March/April 2003, pp. 476-484.

[80] H. Grotstollen, J.Wiesing, "Torque capability and control of a saturated induction motor over a wide range of flux weakening," IEEE Trans. on Ind. Elec., vol. 42, no. 4, Aug. 1995, pp. 374-381.

[81] R. J. Kerkman, T. M. Rowan, D. Leggate, "Indirect field-oriented control of an induction motor in the field-weakening region," IEEE Trans. on Ind. Applications, Vol. 28, No. 4, July / August 1992, pp. 850-857.

[82] E. Levi, M. Wang, "A speed estimator for high performance sensorless control of induction motors in the field weakening region," IEEE Trans. on Power Electronics, Vol.17, No. 3, May 2002, pp. 365-378.

[83] M.S. Huang and C.M. Liaw, "Transient performance improvement control for IFO induction motor drive in field-weakening region," IEE Proc.-Electr. Power Appl., Vol. 150, No. 5, September 2003, pp. 521-530.

[84] M.Ho Shin, D.S. Hyun, S. B. Cho, "Maximum torque control of stator-flux-oriented induction machine drive in the field-weakening region," IEEE Trans. on Ind. App., Vol. 38, No. 1, January/February 2002, pp. 117-121.

[85] A. Biinte, H. Grotstollen, P. Krafka, "Field weakening of induction motors in a very wide region with regard to parameter uncertainties," PESC 96, Vol. 1, 26-27 June 96, pp. 944-950.

[86] S.H. Kim, S.K. Sul, "Voltage control strategy for maximum torque operation of an induction machine in the field weakening region," IEEE Trans. on Ind. El., Vol. 44, No.4, Aug. 1997, pp. 512-518.

[87] D. Casadei, G. Serra, A. Tani, **L. Zarri**, "Robust flux weakening operation of induction motor drives based on stator flux vector control," Proc. of ICEM 2006, XVII International Conference on Electrical Machines, Chania, Crete Island, Greece, September 2-5, 2006, paper PMM2-15 on CD-ROM, pp. 489/1- 489/6.

[88] H. Abu-Rub, H. Schmirgel,. Holtz, "Sensorless control of induction motors for maximum steady-state torque and fast dynamics at field weakening," IAS 2006, Tampa, Florida, 8-12 October 2006, Paper N.IAS03P, ISBN: 1-4244-0365-0.